

---

# Data-driven identification and modelling of coherent dynamics in turbulent flows

---

vorgelegt von

**Diplom-Ingenieur  
Moritz Alexander Sieber**

ORCID:0000-0002-8150-4977

an der Fakultät V – Verkehrs- und Maschinensysteme der

**Technischen Universität Berlin**

zur Erlangung des akademischen Grades

**Doktor der Ingenieurwissenschaften  
– Dr.-Ing. –**

genehmigte Dissertation

Promotionsausschuss:

Vorsitzende: Prof. Dr.-Ing. Neda Djordjevic

Gutachter: Prof. Dr.-Ing. Kilian Oberleithner  
Prof. Dr.-Ing. Christian Oliver Paschereit  
Prof. Dr. Nicolas Noiray  
Prof. Dr. Kunihiko Taira

Tag der wissenschaftlichen Aussprache: 10. November 2020

Berlin 2021



## *Vorwort*

Ich möchte hier allen danken, die mich im Laufe der letzten Jahre dabei unterstützt haben, diese Dissertation zu vollenden. Zu aller erst gilt ein sehr großer Dank meiner Frau Laura, welche mich immer großartig unterstützt und motiviert hat und mir besonders in den letzten anstrengenden Zeiten den Rücken freigehalten hat, sodass ich Ruhe zum Schreiben finden konnte. Meinen Eltern möchte ich ebenfalls besonders danken, da sie mir ein freies Ausleben meiner Neugier und Interessen ermöglicht haben, welches mich im Laufe der Zeit unweigerlich in die Naturwissenschaften gezogen hat.

Ein besonderer Dank gilt Kilian Oberleithner für die exzellente fachliche Unterstützung und die Geduld, die er mit mir und meinen Analysen hatte. In gleichem Maße möchte ich Oliver Paschereit danken, dass er mir diese Promotion ermöglicht hat, wobei ich mich eigenständig und ausführlich einem Forschungsthema konnte. Den vielen Kolleginnen und Kollegen am Institut möchte ich hier auch für die vielen Unterstützungen und die schöne Zusammenarbeit danken, insbesondere Lothar Rukes, Stefan Vey, Christoph Strangfeld, Navid Nayeri, Dominik Wassmer, Phoebe Kuhn, David Holst, Finn Lückhoff, Udo Schwadtke, Florian Ostermann, Dirk Wieser, Mathew Lennie, Katharina Göckeler, Thoralf Reichel, David Marten, Sebastian Schimek, Steffen Terhaar, Folker Hirthammer und Henning Lang.

Furthermore, I would like to thank the scientists outside the Institute who, through cooperation and professional discussions, have made a significant contribution to the development of the work, especially Bernd Noack, Robert Martinuzzi, Michael Stöhr, Maarten Vanierschrot, Alexander Kuhn and Hans-Christian Hege.

Special thanks are also expressed to the external reviewers Nicolas Noiray and Kuni-hiko Taira who were willing to contribute to the extensive evaluation of the work.

Berlin, Juli 2020

Moritz Sieber



## Zusammenfassung

Diese Dissertation befasst sich mit methodischen Ansätzen für die titulierte Identifikation und Modellierung kohärenter Dynamiken in turbulenten Drallstrahlen. Die Identifikation betrifft dabei die Entwicklung einer neuen Methode zur modalen Zerlegung von Messdaten. Diese erlaubt eine präzise Isolierung einzelner strömungsdynamischer Phänomene von komplexen Strömungen mit interagierenden und überlagerten Dynamiken. Die Modellierung bezieht sich auf die Anwendung stochastischer Methoden zur Beschreibung der Interaktion von deterministischen und stochastischen Dynamiken in turbulenten Strömungen. Diese ist wesentlich, um die experimentell beobachteten Phänomene beschreiben zu können. Nicht explizit titulierte, aber ein weiterer wesentlicher Punkt der Arbeit ist die Darstellung der Wirbelstrukturen, die durch die kohärenten Dynamiken entstehen.

Die Arbeit befasst sich ausschließlich mit der Analyse von Messdaten, wobei die Analyse von Zeitreihen die primäre Quelle für die Interpretation der Daten ist. Die modale Zerlegung der Daten liefert dabei die Grundlage für eine reduzierte Repräsentation der Phänomene in komplexen räumlich-zeitlichen Strömungen. Die Untersuchungen und Methoden fokussieren sich nicht auf eine bestimmte Strömung, der Schwerpunkt der Untersuchungen liegt aber bei der Analyse von Drallströmungen. Dabei wird insbesondere die dominante helikale Mode, welche auf Grund einer globalen Instabilität im Drallstrahl entsteht, untersucht.

Der Anspruch der Arbeit ist die Entwicklung und Beschreibung von robusten Methoden zur Analyse von Messdaten und einer darauf basierenden Identifikation von relevanten strömungsdynamischen Phänomenen. Die weiterführende Modellierung der Dynamiken erlaubt dabei eine Interpretation der zu Grunde liegenden hydrodynamischen Instabilitäten. Dadurch kann aus einfachen Messungen ein genaues Bild der dominanten Dynamiken und der physikalischen Parameter einer Strömung gewonnen werden.

Die Anwendung der Methoden an verschiedenen Konfigurationen des Drallstrahls zeigt deutlich wie aus stationären Messungen die primären und sekundären Dynamiken dieser Strömung identifiziert werden können. Die Modellierung der dominanten helikalen Mode durch ein stochastisches dynamisches System erlaubt weiterhin eine präzise Bestimmung der Wachstumsrate der zu Grunde liegenden Instabilität. Die Beschreibung der Wachstumsrate in Abhängigkeit verschiedener Kontrollparameter erlaubt eine genaue Charakterisierung der Bifurkation, welche mit der Instabilität verknüpft ist.

Die Arbeit liefert damit wichtige neue Erkenntnisse zum Auftreten der helikalen Mode in turbulenten Drallstrahlen. Darüber hinaus zeigen die neu entwickelten und angepassten Methoden einen vielversprechenden Ansatz zur Analyse anderer Strömungen. Die Erkenntnisse, die sich allein für den Drallstrahl ergeben haben, zeigen ein großes Potential zur exakteren Beschreibung bekannter und Entdeckung neuer Phänomene.



## *Abstract*

This dissertation deals with methodological approaches for the titled identification and modelling of coherent dynamics in turbulent swirling jets. The identification concerns the development of a new method for the modal decomposition of measurement data. This allows precise isolation of single fluid dynamic phenomena from complex flows with interacting and superimposed dynamics. The modelling refers to the application of stochastic methods to describe the interaction of deterministic and stochastic dynamics in turbulent flows. This is essential to describe the experimentally observed phenomena. Not explicitly titled, but another essential point of the work is the visualisation of the vortex structures created by the coherent dynamics.

The work deals exclusively with the analysis of measurement data, whereby the analysis of time series is the primary source for the interpretation of the data. The modal decomposition of the data provides the basis for a reduced representation of the phenomena in complex spatio-temporal flow data. The investigations and methods do not target a specific flow, but the focus of the investigation is on the analysis of swirling flows. In particular, the dominant helical mode, which arises due to a global instability in the swirl jet, is investigated.

The aim of the thesis is the development and description of robust methods for the analysis of measurement data and the identification of relevant flow dynamic phenomena. Further modelling of the dynamics allows an interpretation of the underlying hydrodynamic instabilities. Thus, a precise picture of the dominant dynamics and the physical parameters of a flow can be obtained from relatively simple measurements.

The application of the methods to different configurations of the swirling jet clearly shows how the primary and secondary dynamics of this flow can be identified from stationary measurements. The modelling of the dominant helical mode by a stochastic dynamical system also allows a precise determination of the growth rate of the underlying instability. The description of the growth rate as a function of various control parameters allows a precise characterisation of the bifurcation associated with the instability.

The work thus provides important new insights into the occurrence of the helical mode in turbulent swirling jets. Furthermore, the newly developed and adapted methods show a promising approach for the analysis of other flows. The results obtained for the swirling jet alone show great potential for a more precise description of known and the discovery of new phenomena.



# Contents

<b>Vorwort</b>	<b>iii</b>
<b>Zusammenfassung</b>	<b>v</b>
<b>Abstract</b>	<b>vii</b>
<b>Contents</b>	<b>ix</b>
<b>List of Figures</b>	<b>xi</b>
<b>Nomenclature</b>	<b>xiii</b>
<b>1 Introduction and Motivation</b>	<b>1</b>
<b>2 Modal decomposition fundamentals</b>	<b>5</b>
2.1 Derivation of SPOD from Lumley’s initial POD formulation . . . . .	6
2.1.1 The classical POD . . . . .	7
2.1.2 The common POD . . . . .	7
2.1.3 The spectral POD (SPOD) . . . . .	8
2.2 Time- vs. frequency-domain SPOD . . . . .	11
2.3 Overview of different SPOD approaches . . . . .	13
2.4 Relation of time-delay embedding and SPOD . . . . .	15
<b>3 Publications</b>	<b>19</b>
3.1 Spectral proper orthogonal decomposition . . . . .	20
3.2 Advanced Identification of Coherent Structures in Combustors . . . . .	51
3.3 Transient Mechanisms of Bi-Stable Flame Shape Transitions in a Combustor	64
3.4 Stochastic modelling of global instability in a turbulent swirling jet . . . . .	77
3.5 Impact of density stratification on the global mode in a swirling jet . . . . .	110
<b>4 Discussion</b>	<b>127</b>
4.1 SPOD for the analysis of flow dynamics . . . . .	127
4.1.1 Relation between different SPOD variants . . . . .	127
4.1.2 Coping with nonlinear interactions and stochastic disturbances . . . . .	128
4.1.3 Principal disadvantage of modal decompositions . . . . .	129
4.2 Coherent structures in turbulent flows . . . . .	130
4.2.1 Observation of hydrodynamic instabilities in a turbulent flow . . . . .	130
4.2.2 Discrepancies between modal, phase averaged and instantaneous flow structures . . . . .	131
4.2.3 Difference between measurement noise and turbulent perturbations	131
4.3 The dominant modes in a turbulent swirling jet . . . . .	132
4.3.1 Observed modes and mode interactions in a swirling jet . . . . .	132
4.3.2 Stochastic modelling for the entire SPOD spectrum . . . . .	133

4.3.3	Control parameters of the PVC bifurcation . . . . .	135
4.3.4	Explanation of experimental observations by a subcritical bifurcation	135
4.4	Concluding Remarks . . . . .	138
<b>A</b>	<b>SPOD related supplements</b>	<b>141</b>
A.1	Decomposition of experimental data from a turbulent jet . . . . .	141
A.2	Boundary conditions for the SPOD filter . . . . .	143
A.3	Decomposition of generic noisy data . . . . .	146
A.4	Effect of filter variation on the SPOD . . . . .	149
A.5	Mathematical derivations . . . . .	151
A.5.1	Conversion of the modes from time- to frequency-domain . . . . .	152
A.5.2	Conversion of the SPOD snapshot correlation . . . . .	152
	<b>Bibliography</b>	<b>155</b>
	<b>Associated Publications</b>	<b>161</b>

# List of Figures

1.1	The Kármán vortex street across multiple scales . . . . .	2
1.2	Global mode in a swirling jet . . . . .	4
2.1	Classification of different POD approaches . . . . .	14
4.1	SPOD mode spectrum with mode ranking according to coherence and growth rate . . . . .	134
4.2	Probability density functions of the PVC . . . . .	136
4.3	Possible bifurcation scenarios in isothermal and stratified swirling jets . .	137
A.1	SPOD spectrum for the frequency- and time-domain decomposition . . .	142
A.2	Spatial mode shapes for the frequency- and time-domain SPOD . . . . .	143
A.3	Surface plot of the entire time-domain SPOD mode . . . . .	144
A.4	Comparison of different boundary conditions . . . . .	145
A.5	Generic data sequence representing an amplified travelling wave . . . . .	147
A.6	Scatter plot of estimated system dynamics . . . . .	148
A.7	Frequency error and amplification error over SNR for different filter sizes	150
A.8	Visualisation of the time-domain SPOD spectrum . . . . .	151



# Nomenclature

## *Latin letters*

$a$	temporal (S)POD coefficient
$D$	nozzle diameter
$i$	complex unit $\sqrt{-1}$
$k$	spatial wavenumber
$m$	azimuthal mode number
$\mathbf{I}$	identity matrix
$M$	number of spatial points
$N$	number of snapshots
$N_f$	size of the SPOD filter
$\mathbf{R}$	spatial correlation matrix
$\mathbf{C}$	snapshot correlation matrix
$\mathbf{S}$	filtered snapshot correlation matrix
$u, v$	velocity fields (arbitrary component)
$x, y, z$	Cartesian coordinates
$\mathbf{X}, \mathbf{Y}$	collection of data in a snapshot matrix

## *Greek letters*

$\lambda$	(S)POD mode energy
$\mu$	DMD eigenvalue
$\Phi$	spatial (S)POD mode
$\omega$	angular frequency
$\sigma$	amplification rate
$\tau$	local time scale in a temporal subset

## *Subscripts*

$()_{j-l}$	mode numbers
$()_x$	x-component of the velocity
$()_y$	y-component of the velocity
$()_z$	z-component of the velocity

## *Superscripts*

$\dot{()}$	time derivative of a function
$()'$	shifted time or coordinate in a cross correlation
$()^T$	transpose of a matrix
$()^*$	complex conjugate
$\overline{()}$	temporal mean of a variable
$\hat{()}$	time domain representation of the SPOD

$\tilde{()}$  frequency domain representation of the SPOD

### *Abbreviations*

<b>BC</b>	<b>B</b> oundary <b>C</b> ondition
<b>DMD</b>	<b>D</b> ynamic <b>M</b> ode <b>D</b> ecomposition
<b>FTLE</b>	<b>F</b> inite <b>T</b> ime <b>L</b> yapunov <b>E</b> xponent
<b>LDA</b>	<b>L</b> aser <b>D</b> oppler <b>A</b> nemometry
<b>LSA</b>	<b>L</b> inear <b>S</b> tability <b>A</b> nalysis
<b>PDF</b>	<b>P</b> robability <b>D</b> ensity <b>F</b> unction
<b>PIV</b>	<b>P</b> article <b>I</b> mage <b>V</b> elocimetry
<b>POD</b>	<b>P</b> roper <b>O</b> rthogonal <b>D</b> ecomposition
<b>POP</b>	<b>P</b> rincipal <b>O</b> scillation <b>P</b> attern
<b>PSD</b>	<b>P</b> ower <b>S</b> pectral <b>D</b> ensity
<b>PVC</b>	<b>P</b> recessing <b>V</b> ortex <b>C</b> ore
<b>SNR</b>	<b>S</b> ignal to <b>N</b> oise <b>R</b> atio
<b>SPOD</b>	<b>S</b> pectral <b>P</b> roper <b>O</b> rthogonal <b>D</b> ecomposition

*Für Valentina*



## Chapter 1

# Introduction and Motivation

The perception of coherent structures in fluid motion has always been driven by the observation of phenomena in nature. This goes back to the earliest records in drawings by Leonardo da Vinci, where visual perception by the naked eye was the only viable option Kemp, 2019. Due to the intuitive notion of coherent structures, an exact mathematical definition has always been problematic because it does not correspond to the personal experiences of all researchers and therefore collides with some aspects of individual realities. The narrative by George (1988) from a panel discussion with John Lumley at the 1982 APS DFD Meeting describes the situation aptly: "Lumley who, drawing from a U.S. Supreme Court decision on pornography, pointed out that like pornography, coherent structures are hard to define but you know one when you see it." More profoundly Lumley (1970) stated that: "...coherence represents the extent of correlation between the Fourier components of two signals, ignoring difference in phase...". These two citations coarsely encompass the conception of coherent structures in this work.

The understanding of coherent structures in turbulent flows is fundamental for research and engineering (Holmes et al., 2012). The presence of ordered and periodic structures in a turbulent flow has a big impact on mixing, reaction and fluid structure interactions. Other than the stochastic, undirected motions that are generally associated with turbulence, the organised, periodic motions of coherent structures accumulate and direct the kinetic energy of the flow. This can cause the flow and a coupled mechanical or acoustic system to resonate or show other undesirable dynamic phenomena. The collapse of the Tacoma narrows bridge (July 1, 1940) dramatically demonstrated a resonance catastrophe due to fluid dynamic oscillations. However, such oscillatory motion enables the formulation of deterministic models that describe and predict the onset and dynamics of coherent structures in the flow.

The occurrence of oscillatory motions due to hydrodynamic instabilities is well understood for laminar flows (Landau & Lifshitz, 1987; Oertel & Delfs, 1996). There, the oscillations develop from a steady base flow, which allows an accurate description of the dynamics from an infinitesimal perturbation of the flow. In a turbulent flow, there is no steady flow on which an instability develops. It constitutes a continuous spectrum of stochastic perturbations, where hydrodynamic instabilities grow on top. Nevertheless, the dominant coherent structures in laminar and turbulent flows often exhibit very similar spatial structures. This is clearly seen for the Kármán vortex street, which is similarly observed in laboratory and atmospheric scales, as presented in figure 1.1. The similarity of the spatial structures leads to the assumption that the underlying fluid dynamics are

similar as well. Actually, many of the analytical approaches developed for laminar flows can be used in a similar way for turbulent flows, if an appropriate closure for neglected stochastic fluctuations is considered. The modelling of hydrodynamic instabilities and the proper account of the effect of turbulent fluctuations is one central aspect of this thesis. More specifically, the dynamics observed in measurement data are used to calibrate empirical dynamical systems. Ultimately, the parameters of the dynamical system reflect the physical properties of the underlying flow state.

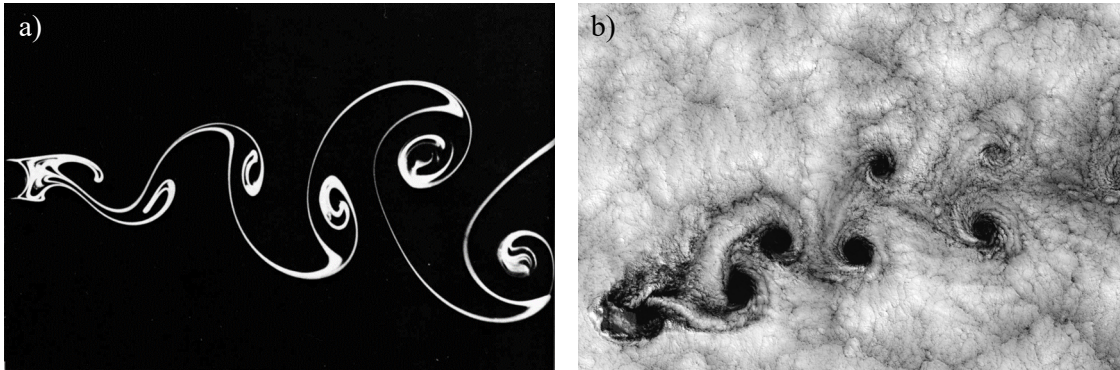


FIGURE 1.1: The Kármán vortex street across multiple scales: a) Behind a cylinder at  $Re = 140$  by Sadatoshi Tenada (Van Dyke, *An Album of Fluid Motion*). b) Behind the Juan Fernandez Islands at  $Re \approx 10^9$  (Bob Cahalan, NASA GSFC).

A secondary topic, directly related to modelling, is the identification of coherent structures from data. There is a seamless transition between structures at different scales and frequencies in a turbulent flow. The accurate identification of coherent structures and a meaningful separation of interacting dynamics is decisive to enable the interpretation of the dynamics in time. One of the most promising approaches for this task is the proper orthogonal decomposition (POD), which was developed from the transfer of statistical methods to the field of fluid dynamics by Lumley (Lumley, 1967; Lumley, 1970). Since then, many variants of the POD were developed independently, all of which aim to improve the results for particular applications and flow configurations. This independent development of methods, however, lacks some general framework and nomenclature to understand the relations between the methods. The situation was further complicated by another extension of the POD that was developed within this work. The more formal classification of the method into existing approaches, which is given at the beginning of the thesis, should reduce this confusion.

A large part of this thesis is about methods for the identification and modelling of coherent structures. Thereby, the focus is not so much the fluid dynamics innovation or mathematical reasoning. It is rather the accumulated experience in data processing that is condensed into an engineering best practice approach to flow data analysis. The methods are developed in the context of measurement data analysis of highly turbulent flows. Therefore, they are robust against measurement uncertainties and strong turbulent perturbations. There might be other approaches that perform better in other experimental or numerical settings. However, personal experience suggests that the presented methods are an advisable way to avoid pitfalls and misinterpretations when analysing coherent structures in turbulent flows.

The three main topics that are addressed in this work are (i) the identification of coherent structures, (ii) the interpretation of their temporal dynamics, and (iii) the presentation of spatial structures. For this purpose, the spatio-temporal dynamics of the flow is basically considered in a modal decomposition (Taira et al., 2017). The observations of the flow are split into a sum of spatial modes and temporal coefficients. In this context, a coherent structure is typically associated with one mode (pair), which enables the investigation of the temporal dynamics by the inspection of the time evolution of a single mode coefficient. The further interpretation of flow physics is based exclusively on the temporal development of a few mode-coefficients. The step back to the spatial manifestation of the coherent structure is disrupted by the interpretation of the flow as a superposition of different modes. The effect of a mode on the flow field is often only apparent from its interaction with the remaining modes. Therefore, a reconstruction of the flow is necessary to interpret the spatial structures. These are further clarified by the computation of Lagrangian coherent structures in the reconstructed flow (Haller, 2015).

The methods are demonstrated in this thesis for various experimental flow configurations. Most of them consist of swirling jets from swirl-stabilised combustors or generic experimental configurations. Swirling jets exhibit a global hydrodynamic instability that is controlled mainly by the swirl intensity (Liang & Maxworthy, 2005). The bifurcation is largely independent of the Reynolds number, which allows one to investigate it at high Reynolds numbers resulting in highly turbulent flows. This results in the presence of secondary dynamics and stochastic perturbations of the flow that will be studied in detail. The extensive study of the global mode in this work enables fundamental new insights into the related dynamics of the swirling jet. The recurring examination of one specific flow with different methods further illustrates the overarching methodological approach of the work.

The general motivation for the consecutive methods in this thesis is the establishment of a relation between the known coherent dynamics from laminar flows and the coherent dynamics observed in turbulent flows. This aims to invert the apparent relation between the coherent structures of laminar and turbulent flows, visible from the images shown in figure 1.1. The flow visualisations in figure 1.2 shows the initial and terminal stage of the process that is established in this work. The smoke visualisation (figure 1.2 a) gives the fully turbulent flow that exhibits a large scale coherent structure but also turbulent perturbations at various scales. The finite-time Lyapunov exponent image (figure 1.2 b) represents the isolated coherent structure that is obtained from measurements of the turbulent flow. Without going into further detail here, a similarity of the coherent structures is evident. The two steps involved in this graphical representation of the process are the identification of coherent structures and the representation of spatial structures. The third aspect of the thesis is the investigation of temporal dynamics to retain information about the flow physics.

The time-domain analysis of measured dynamics is the essential approach for the interpretation of flow physics in the present thesis. This involves the simple inspection of the temporal development of mode coefficients, spectral measures of mode coherence, and the development of models that replicate the dynamics. For the modelling of the coherent dynamics in turbulent flows, the perturbation of the dynamics by the turbulent

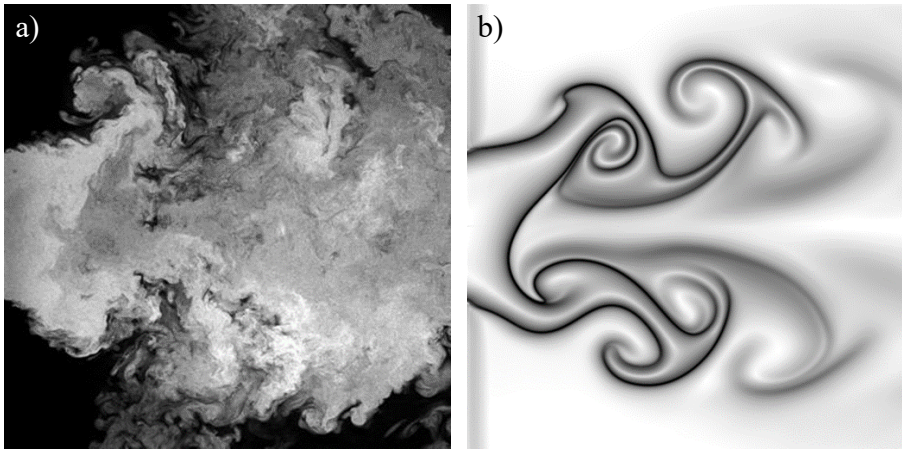


FIGURE 1.2: Global mode in a swirling jet at  $Re = 20000$  : a) smoke visualisation b) finite time Lyapunov exponent.

fluctuations must be considered. This is the central aspect that is discussed in the work in connection with the development of stochastic models.

The present thesis is a cumulative work that spans five publications with diverse experimental investigations and method developments. Beyond the general introduction given here, there is no further introduction to the topics. Further introductions are given in the individual publications according to the areas covered.

In chapter 2, a more general classification of the spectral proper orthogonal decomposition (SPOD) is given, which is an extension of the POD that is developed within the thesis and further described in section 3.1. The publications that are part of the thesis are presented in chapter 3, where a short profile of each publication is given upfront to facilitate the classification within the thesis. General topics of the thesis and further findings are discussed in chapter 4. They are separated into topics regarding the SPOD (section 4.1), the stochastic perturbations (section 4.2), and the fluid dynamics of the swirling jet (section 4.3).

## Chapter 2

# Modal decomposition fundamentals

This chapter gives a general classification of the spectral proper orthogonal decomposition (SPOD) presented by Sieber et al. (2016c) (see section 3.1). Due to the cumulative format of this thesis, the methods are not collectively presented in the first part of this work. Therefore, the reader who is not familiar with modal decompositions should rather consider reading the introductory paper by Taira et al. (2017) or the more profound review of Rowley & Dawson (2017) first. A comprehensive introduction to the field of modal decompositions and the formulation of reduced order models is further provided by the textbook of Holmes et al. (2012).

The reader who is already familiar with modal decompositions or who just returned after the lecture of the proposed literature is further suggested to read the article presented in section 3.1 before continuing with the current chapter. This chapter refers in some points to that article, and its previous lecture is recommended for better understanding. Due to the fixed form of the cumulative thesis the correct order could not be retained in this document. The following derivations give further details and specific aspects that were not clear at the time the paper was published. In a slightly different form, the following derivations can also be found in an unpublished preprint (Sieber et al., 2017) that was rejected for publication due to irreconcilable disagreements during the review.

In the original introduction of the SPOD (see section 3.1), the method was proposed as an extension of the classical snapshot POD, where the SPOD overcomes some limitations of the POD. The SPOD was motivated by data analysis and was proven to be a very useful tool to process experimental data. From a numerical point of view, the SPOD is a snapshot POD with an additional filter operation applied to the correlation matrix. The correlation matrix might be thought of as a condensed representation of all the dynamics of the investigated flow – a dynamic fingerprint. The diagonalisation of this matrix provides a basis for the snapshot POD (Sirovich, 1987), which comprises the optimum building blocks of the matrix. However, the correlation matrix does not only contain coherent flow dynamics but also stochastic fluctuations and measurement noise. Within the SPOD approach, the matrix is filtered to attenuate the random part while leaving the coherent dynamics unaffected, therewith, to separate the coherent fluctuations from stochastic ones. It was observed that the stochastic contributions in the matrix appear as random variations, whereas the coherent structures appear as diagonal streaks in the matrix. The filter takes advantage of these properties, but it is only inspired by empirical considerations and does not withstand a rigorous analytical derivation. It is rather

shown from experimental and numerical data that the SPOD provides better assignment of specific fluid dynamic phenomena to individual modes (Sieber et al., 2016a; Ribeiro & Wolf, 2017) in situations where snapshot POD tends to mix several dynamics into single modes. Moreover, SPOD compensates for partially recorded phenomena, shows superior noise rejection, and provides smooth dynamics that facilitate mode interpretation (Stöhr et al., 2017).

Another prominent POD variant is the *frequency-domain* POD (Glauser et al., 1987; Citriniti & George, 2000; Gudmundsson & Colonius, 2011), which was recently also referred to as *spectral* POD (Taira et al., 2017; Towne et al., 2018; Schmidt et al., 2018). This approach goes back to the more general form of POD introduced by Lumley (Lumley, 1967; Lumley, 1970). The key aspect of this frequency-domain approach is that a stationary time series is considered, for which the cross-correlation tensor takes a special form that guarantees the existence of its Fourier transform. A detailed discussion of this topic is given by Towne et al. (2018) including a review on the approximation of this spectral cross-correlation tensor from actual data using Welch's method. This approach comprises a division of a long time series into short segments, where each segment is Fourier transformed in time and POD is applied to the Fourier coefficients at a specific frequency. The approach provides a very clean separation of coherent structures in the broadband spectrum of turbulent jets (Gudmundsson & Colonius, 2011).

In this section, the SPOD will be put in a more general context to reveal its relation to other currently developed POD-based approaches. The POD concept of Lumley (Lumley, 1967; George, 1988) is revisited, which considers the coupled space and time correlation instead of their separation. This will draw the connections between SPOD and the frequency-domain POD outlined in the previous paragraph. It will be shown that both approaches rely on the same assumptions and that they are the time- and frequency-domain representation of the same decomposition. Therefore, the two approaches will be named time-domain SPOD (tdSPOD), when referring to the matrix filter operation and frequency-domain SPOD (fdSPOD), when referring to the segmentation and Fourier transform in time.

## 2.1 Derivation of SPOD from Lumley's initial POD formulation

The general concept of POD evolved from the collection of stochastic methods for velocity data by Lumley (1970). This classical POD approach was overshadowed by extensive publications on a simplified POD version proposed by Sirovich (1987) and thoroughly described in the book of Holmes et al. (2012). According to the retrospective of George (2017), POD gained little acceptance in the beginning, despite its obvious capabilities in describing coherent structures of turbulent flows (George, 1988). One major obstacle has always been the collection of sufficient data to obtain converged statistics.

### 2.1.1 The classical POD

Starting with the decomposition proposed by Lumley (1967), we seek the space time correlation function

$$R_L(x, x', t, t') = \langle u_k(x, t)u_k^*(x', t') \rangle, \quad (2.1)$$

where  $\langle \rangle$  refers to the ensemble average over repeated observations  $(\cdot)_k$  of a stationary flow  $u$  (\* indicates the adjoint). It is obvious that a statistically relevant number of repeated observations from spatially and temporally resolved data implies a very large amount of data (George, 2017). From the correlation function  $R_L$ , the POD modes  $\Phi$  are obtained by solving the *Lumley integral equation*

$$\iint R_L(x, x', t, t')\Phi_k(x', t')dx'dt' = \lambda_k\Phi_k(x, t), \quad (2.2)$$

which reduces to the commonly known discretised formulation of eigenvalue decomposition. The obtained POD modes yield the flow decomposition

$$u_j(x, t) = \sum_k \alpha_{jk}\Phi_k(x, t), \quad (2.3)$$

where the mode coefficients  $\alpha_{jk}$  account for the specific mode amplitude of a certain realisation of the flow in the ensemble. The POD mode shapes  $\Phi_k(x, t)$  depend on space and time, which enables the capture of all possible space-time properties of coherent structures. In the following, mode shapes and mode coefficients will be abbreviated as modes and coefficients, respectively. Note that throughout this article integration is always assumed across the entire observed domain and recorded period. More details about the treatment of domain boundaries can be found in appendix A.2.

The actual computation of the classical POD is rarely feasible due to the large amount of required data. In the investigation of Gordeyev & Thomas (2013) it was used to optimally describe the transition from natural to forced flow states. The *temporal* POD, as it was named there, was shown to provide a good basis for simple low order models that describe the flow transition.

### 2.1.2 The common POD

To reduce the necessary amount of data, the time instance at which a *snapshot* of the flow is recorded can be treated as an observation of the statistical ensemble. Therefore, the temporal dependency of the modes is neglected and, in contrast to (2.1), only the spatial correlation function is considered (Holmes et al., 2012, p. 68)

$$R(x, x') = \langle u(x, t_k)u^*(x', t_k) \rangle. \quad (2.4)$$

A specific property of this approach is the separation of temporal and spatial dependencies of the flow into spatial modes and temporal coefficients

$$u(x, t) = \sum_k a_k(t) \Phi_k(x). \quad (2.5)$$

This approach is commonly referred to as POD (Berkooz et al., 1993; Holmes et al., 2012; Taira et al., 2017), which is somehow diffuse as it is just a variant of the originally proposed POD (Lumley, 1967). George (2017), therefore, termed it *snapshot POD* as it considers only isolated snapshots and ignores any temporal correlation between them. However, this term usually refers to the computational shortcut via the snapshot correlation (see equation (2.6)) that was proposed by Sirovich (1987). To avoid further naming confusion, this approach is still called POD.

The separation of space and time might contradict the entangled space-time correlations of turbulent flows; however, it provides a mathematical ansatz that tremendously simplifies the governing equations employing a Galerkin projection (Noack et al., 2003). An extensive description of possible reduced-order modelling and detailed properties of the POD is collected in Holmes et al. (2012). Moreover, the numerical implementation of POD allows for the exchange of spatial correlation with a snapshot correlation that leads to a much faster computation for typical flow data (Sirovich, 1987).

As shown by Aubry (1991), the exchange between spatial and temporal correlation is not only possible in the discrete but also in the continuous case, given that the data in spatial and temporal domain belong to the space of square-integrable functions. Accordingly, the solution of integral equation  $\int C(t, t') a(t') dt' = \lambda a(t)$  with the snapshot correlation function

$$C(t, t') = \int u(x, t) u^*(x, t') dx \quad (2.6)$$

provides the coefficients  $a(t)$  that likewise provide the modes  $\Phi(x)$  by expanding the temporal evolution of the data by the coefficients (see also (2.14)). The perfect symmetry between the temporal and spatial expansion inspired Aubry (1991) to name this approach bi-orthogonal decomposition. The computation of the POD from temporally uncorrelated snapshots through correlation (2.6), as proposed by Sirovich (1987), is commonly referred to as snapshot POD.

### 2.1.3 The spectral POD (SPOD)

The following section gives an alternative formulation to the POD that accounts for the temporal evolution of the flow without the need for vast amounts of data. The approach adopts the segmentation of time series that is used in Welch's method to estimate the power spectral density from limited data. The approach is commonly used for spectral averaging and was also applied to POD analysis (e.g. Citriniti & George (2000) and Taira et al. (2017)). However, in contrast to these applications, no Fourier transform of the segments is employed here. To include this methodology in the present derivation, we use a temporal weighting (window) function that is multiplied with the time series to isolate a segment.

The derivation is started from the previous formulation (2.1) but we seek to compute the temporal correlation as well as ensembles from a long time series. Therefore, we introduce a short time scale  $\tau$  within which the flow is correlated and a window function  $w(\tau)$  that accounts for the observation horizon  $T$ . The window function is taken to be a Gaussian function  $w(\tau) = \exp(-(\tau/T)^2)$ . The time series is segmented into windows centred at discrete time steps  $t_k$  constituting the observed ensembles. Consecutive segments may also overlap to an arbitrary extend. By inserting the two time scales into (2.1), the space-time-correlation function reads

$$\widehat{R}(x, x', \tau, \tau') = \langle u(x, t_k + \tau)w(\tau)u^*(x', t_k + \tau')w^*(\tau') \rangle \quad (2.7)$$

$$= \int u(x, t + \tau)w(\tau)u^*(x', t + \tau')w^*(\tau')dt, \quad (2.8)$$

where in the second expression the ensemble average is replaced by a time average. The change from a discrete ensemble to continuous integration corresponds to the maximal overlap of consecutive time segments. Note that the increase of the overlap and consequent addition of correlated ensembles does not change the resulting POD modes. The assumption of uncorrelated ensembles (snapshots), as noted in various related publications, is only due to the minimisation of computational costs (Sirovich, 1987).

The step from an ensemble average to continuous time integration requires that the flow is stationary and that the investigated time series is long enough to allow the flow to pass every possible state. This restriction is actually not mandatory since the following derivations can also be realised for an ensemble average. However, the nomenclature and derivations become much more compact due to this step.

The correlation function  $\widehat{R}$  also depends on the weighting function and the observation horizon  $T$ . Compared to the other variables, this is a rather weak dependency given that the observation horizon  $T$  is large enough (see appendix A.4). The observation horizon and weighting function can be considered similar to the window size and weighting used in Welch's method for spectral estimation.

Equivalent to (2.2), the POD modes are derived from the integral equation

$$\iint \widehat{R}(x, x', \tau, \tau')\widehat{\Phi}_k(x', \tau')dx'd\tau' = \lambda_k\widehat{\Phi}_k(x, \tau). \quad (2.9)$$

The resulting modes  $\widehat{\Phi}(x, \tau)$  are not only functions of space but also represent the temporal evolution across a time window given by  $w(\tau)$ .

The short time coordinate  $\tau$  together with the spatial coordinate may also be considered as a space-time coordinate  $\xi = [x, \tau]$ , which is similar to delay embedding, or the initial dot formulation of Lumley (1967) (using a  $'\cdot'$  as a placeholder for arbitrary coordinates). This reduces the expressions above to a normal POD in  $\xi$  and  $t$ . Therefore, we can follow the argumentation of Aubry (1991) to compute the POD coefficients from the temporal correlation, instead of the modes from the  $x$ - $\tau$ -correlation. Similarly, the argumentation of Sirovich (1987) would apply for the ensemble-averaged case (2.7) to enable the decomposition via the snapshot correlation matrix.

The temporal correlation function for the SPOD formulation reads

$$\widehat{S}(t, t') = \iint u(x, t + \tau)w(\tau)u^*(x, t' + \tau)w^*(\tau)dx d\tau \quad (2.10)$$

$$= \int w^2(\tau)C(t + \tau, t' + \tau)d\tau. \quad (2.11)$$

The simplification from (2.10) to (2.11) is due to the proposed Gaussian weighting and use of (2.6). Writing the equation for discrete time instances  $t = k\Delta t$ ,  $t' = l\Delta t$  and  $\tau = j\Delta t$  using appropriate quadrature, the correlation matrix reads

$$\widehat{S}_{k,l} = \sum_{j=-N_f}^{N_f} g_j C_{k+j, l+j}. \quad (2.12)$$

This expression is the filtered version of the snapshot correlation matrix that was proposed in Sieber et al. (2016c). This analogy implies that the coefficients  $g_j = w^2(j\Delta t)$  are the previously introduced SPOD filter coefficients that specify a discrete filter of extend  $1 + 2N_f$ . Hence, the SPOD concept outlined here is a generalisation of the approach in Sieber et al. (2016c).

After this detour to the discrete variables (more can be found in Sieber et al. (2016c)) we proceed with the continuous formulation of the snapshot correlation matrix given in (2.11). The corresponding SPOD coefficients are determined by solving

$$\int \widehat{S}(t, t')\widehat{a}_k(t')dt' = \lambda_k\widehat{a}_k(t). \quad (2.13)$$

The coefficients  $\widehat{a}_k(t)$  form an orthogonal basis in time domain and are scaled to match  $\int \widehat{a}_k(t)\widehat{a}_l(t)dt = \lambda_k\delta_{kl}$ . The SPOD modes that also extend in the  $\tau$  direction are determined from the convolution

$$\widehat{\Phi}_k(x, \tau) = \frac{1}{\lambda_k} \int \widehat{a}_k(t)u(x, t + \tau)w(\tau)dt \quad (2.14)$$

and are likewise orthonormal with  $\iint \widehat{\Phi}_k(x, \tau)\widehat{\Phi}_l^*(x, \tau)dx d\tau = \delta_{kl}$ . Finally, for the decomposition of the original flow data only the mode centred at  $\tau = 0$  is required, reading

$$u(x, t) = \sum_{k=1}^N \widehat{a}_k(t)\widehat{\Phi}_k(x, \tau = 0). \quad (2.15)$$

These partial modes are not necessarily orthogonal (Sieber et al., 2016c). The complete mode, that extends in  $\tau$  forms an orthogonal basis according to inner product introduced in equation (2.8). Accordingly, they form an orthogonal spatio-temporal mode basis that has a compact support in time as defined by the temporal window function  $w(\tau)$ .

The reduction of the temporal mode to the  $\tau = 0$  part may seem arbitrary. However, if we consider the coefficients  $\widehat{a}_k(t)$  to form an orthogonal basis of the time domain over which the flow is considered, the construction of the spatial mode (2.14) evaluated at  $\tau = 0$  is a projection of the original data on the temporal basis  $\widehat{a}_k(t)$  (because  $w(0) = 1$ ). The spatial mode  $\widehat{\Phi}_k(x, \tau = 0)$  constitutes the coefficients of this temporal basis that

enable the re-composition (2.15).

Similar to (2.14), the SPOD coefficients are derived from the modes by the convolution

$$\hat{a}_k(t) = \iint \hat{\Phi}_k(x, \tau) u^*(x, t + \tau) w^*(\tau) dx d\tau, \quad (2.16)$$

which is in contrast to the snapshot POD coefficients, where  $a_k(t) = \int \Phi_k(x) u^*(x, t) dx$ . The comparison of the two expressions shows the essential differences between POD and SPOD. While the coefficients of the POD only reflect the temporal correlation that is present in the data at a certain time, the SPOD involves a temporal convolution across the short time  $\tau$  and, therefore, maintains the temporal continuity.

## 2.2 Time- vs. frequency-domain SPOD

In the previous section, a decomposition was described that combines aspects of the classical POD and the snapshot POD and was shown to be equivalent to the time-domain SPOD formulation proposed in Sieber et al. (2016c). In this section, the relation to the frequency-domain SPOD is shown, which has been applied in several previous studies (Glauser et al., 1987; Citriniti & George, 2000; Gudmundsson & Colonius, 2011). Frequency-domain SPOD is likewise related to the classical POD where the spatio-temporal correlation is considered. It builds on the fact that, for statistically stationary flows, the correlation (2.1) does no longer depend on actual time, but only on time differences (Lumley, 1967; George, 1988). This allows to perform the correlation in the frequency domain, and thus, for each frequency separately.

The computation of the frequency-domain correlation (cross spectral density) from finite data is usually realised using Welch's method (Welch, 1967). As will be shown, this methodology of frequency-domain SPOD is largely the same as for the time-domain SPOD. It likewise involves the segmentation and weighting of a long time series with the additional step of a Fourier transformation in time  $\tau$ . The comparison is not intended to show similarities between the ideal frequency-domain SPOD and time-domain SPOD, but the analogy between the applied methods that use segmentation and weighting in the time domain.

The frequency-domain SPOD was originally proposed as a variation of the classical POD that incorporates knowledge about homogeneous coordinate directions, which reduces those directions to harmonic functions (Lumley, 1967; George, 1988). For a homogeneous temporal coordinate, the correlation function is supposed to be calculated from different realisations of the flow which were Fourier transformed in time

$$\tilde{R}(x, x', \omega) = \langle \tilde{u}_k(x, \omega) \tilde{u}_k^*(x', \omega) \rangle, \quad (2.17)$$

where a specific frequency  $\omega$  is considered. According to the recent survey of Towne et al. (2018), the computation of  $\tilde{R}$  is adequately approximated using Welch's method. This means taking segments of a long time series as statistical ensembles for the correlation that are weighted and Fourier transformed in time. In the present nomenclature, these

segments are expressed as

$$\tilde{u}_k(x, \omega) = \int u(x, t_k + \tau) w(\tau) e^{-i\omega\tau} d\tau, \quad (2.18)$$

where  $i$  indicates the imaginary unit. Insertion of (2.18) in (2.17) and replacing the ensemble average with a continuous time integration, analogously to the derivation of (2.8), results in

$$\tilde{R}(x, x', \omega) = \int \int u(x, t + \tau) w(\tau) e^{-i\omega\tau} d\tau \int u^*(x', t + \tau') w^*(\tau') e^{i\omega\tau'} d\tau' dt \quad (2.19)$$

$$= \iint \hat{R}(x, x', \tau, \tau') e^{i\omega(\tau' - \tau)} d\tau d\tau', \quad (2.20)$$

where the integrals are rearranged from (2.19) to (2.20) such that the correlation function (2.8) is isolated. Accordingly, the frequency-domain correlation function is either given by the correlation of the Fourier transformed velocity signal (2.19) or by the Fourier transform of the time-domain correlation function (2.20).

Again, the step from ensemble average to continuous time integration is not mandatory. The relations above and the following derivations can also be shown for an ensemble-averaged correlation.

From the correlation function, the frequency-dependent modes  $\Phi_k(x, \omega)$  are simply obtained from the integral equation

$$\int \tilde{R}(x, x', \omega) \tilde{\Phi}_k(x', \omega) dx' = \lambda_k(\omega) \tilde{\Phi}_k(x, \omega). \quad (2.21)$$

The derivations in appendix A.5.1 further show that the modes that result from the frequency-domain SPOD are identical to the Fourier transform of the time-domain modes, which reads as

$$\tilde{\Phi}_k(x, \omega) = \int \hat{\Phi}_k(x, \tau) e^{-i\omega\tau} d\tau. \quad (2.22)$$

This relation is valid as long as the investigated data are statistically stationary, which gives a correlation function that only depends on time differences, giving  $\hat{R}(x, x', \tau, \tau') = \hat{R}(x, x', \tau' - \tau)$  (George, 1988). The shown relation between the modes from time-domain SPOD and frequency-domain SPOD is based on several assumptions and is only demonstrated analytically and not for discrete finite length data. Nonetheless, the analysis of experimental data with both SPOD versions given in appendix A.1 shows that relation (2.22) holds, at least, for the dominant coherent structures.

Analogously to the conversion from spatial (2.8) to snapshot correlation (2.10) for the time-domain SPOD, the frequency-domain SPOD can also be deduced from the coefficients instead of the modes. By changing the integration of (2.19) from time to space and seeking the cross-correlation between  $t$  and  $t'$ , the frequency-domain snapshot correlation function is obtained as

$$\tilde{S}(t, t', \omega) = \int \int u(x, t + \tau) w(\tau) e^{i\omega\tau} d\tau \int u^*(x, t' + \tau') w^*(\tau') e^{-i\omega\tau'} d\tau' dx. \quad (2.23)$$

The snapshot correlation function, analogously to (2.13), allows to compute the coefficients of the SPOD decomposition and provides a shortcut to compute the modes for data sets in which the number of grid points is much larger than the number of snapshots. This conversion was equivalently shown by Towne et al. (2018) for the case of ensemble-averaged correlations (2.17). Equation (2.23) can be rearranged to

$$\tilde{S}(t, t', \omega) = \iint C(t + \tau, t' + \tau') w(\tau) w^*(\tau') e^{i\omega(\tau - \tau')} d\tau d\tau', \quad (2.24)$$

where the integrals are rearranged and the snapshot correlation function  $C$  is isolated as previously in (2.11). This shows that, similarly to the spatial correlation function (2.19) and (2.20), the snapshot correlation function in the frequency domain can either be obtained by the correlation of the Fourier transformed velocity (2.23) or the Fourier transform of the POD snapshot correlation function (2.24). However, the Fourier decomposition of the POD snapshot correlation function  $C$  is not trivial since it involves a transform in the direction  $(\tau - \tau')$  and the subsequent average of the Fourier coefficients in the  $(\tau + \tau')$  direction. The averaging of correlation function  $C$  in the  $(\tau + \tau')$  direction is also pursued for the time-domain SPOD (2.11) and can therefore be factored out (see appendix A.5.2) to simplify (2.24) to

$$\tilde{S}(t, t', \omega) = \int \hat{S}(t + \tau/2, t' - \tau/2) w(\tau) e^{-i\omega\tau} d\tau. \quad (2.25)$$

The inversion of this transformation is given by

$$\hat{S}(t, t') = \int \tilde{S}(t, t', \omega) d\omega, \quad (2.26)$$

which allows for the interchange between the time- and frequency-domain SPOD for the snapshot correlation.

## 2.3 Overview of different SPOD approaches

In this section, an analytical framework is presented that links several concurrent POD approaches. Figure 2.1 shows a graphical representation of these different POD variants. Each column refers to a different POD approach, while the rows list the corresponding correlation functions, modes, and coefficients.

As can be seen in the upper rows of figure 2.1, the fundamental difference between snapshot POD and SPOD is the treatment of the space-time correlation. For the snapshot POD, spatial structure and temporal evolution are separated in a product approach, which may lead to unphysical modes. The SPOD, instead, considers the spatio-temporal evolution of the modes across a short period. The differences between snapshot POD and SPOD can be understood as such that snapshot POD reveals statistically similar states among all recorded instances, whereas SPOD reveals similar space-time trajectories within the recorded data set. The snapshot correlation functions that are sketched in the mid-row of figure 2.1 do not exhibit these differences in such a clear way. Nevertheless, their representation highlights the close relation between the different approaches

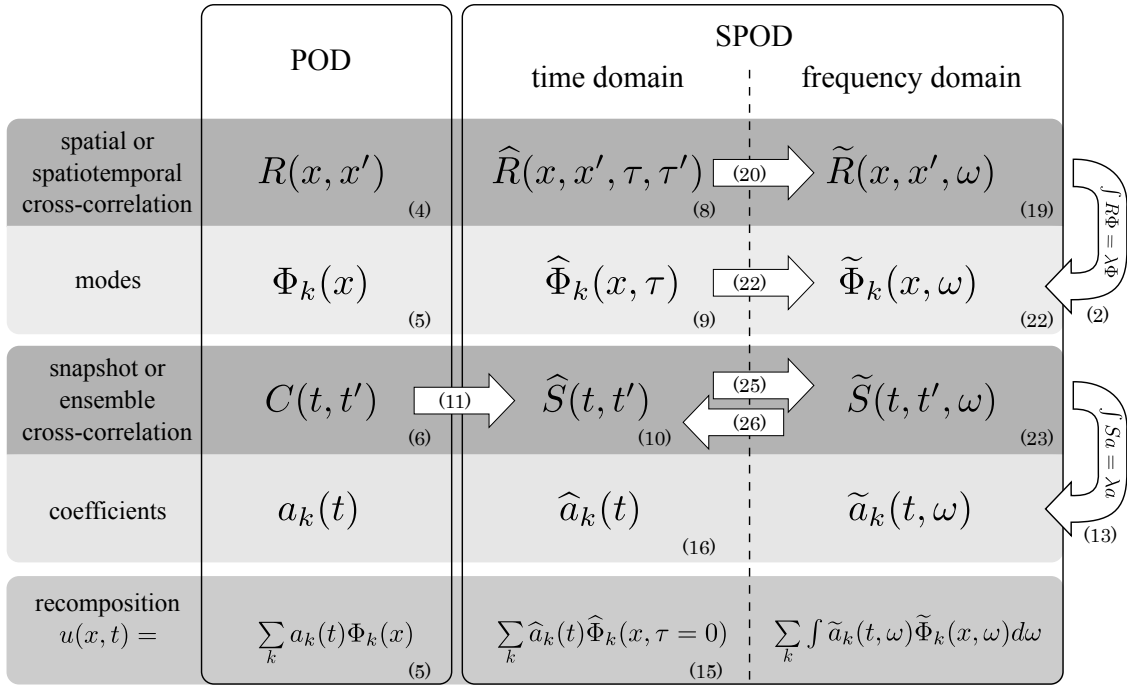


FIGURE 2.1: Classification of different POD approaches by the dependencies of the functions on the governing variables. The numbers in brackets (x) indicate the corresponding equations in the current chapter (2.x). The horizontal arrows indicate possible conversions of the functions.

and outlines numerical shortcuts to compute the SPOD through a simple manipulation of the snapshot correlation functions.

Despite their similarities, there are conceptual differences between the time- and frequency-domain SPOD, which are of relevance for specific applications. The re-composition of the flow from the modes and coefficients, given in the bottom row of figure 2.1, shows that the time-domain SPOD allows for a re-composition that is very similar to the snapshot POD, while the frequency-domain SPOD requires an additional integration along all frequencies. Therefore, time-domain SPOD is more suitable for reduced-order modelling, however, we have to keep in mind that the reduced modes ( $\tau = 0$ ) do not necessarily form an orthogonal basis. The frequency-domain SPOD separates the flow into pure harmonic contributions that have trivial dynamics but give additional constraints that are beneficial to characterise broadband dynamics.

Interestingly, in the relevant literature, the frequency-domain SPOD appears to be mainly applied to flows with convective instabilities (amplifier type flow, e.g. free jets, boundary layers), whereas the snapshot POD and time-domain SPOD seem to be favourably applied to flows with global instabilities (oscillator type flow, e.g. cylinder wake, cavity flow). This distinctive selection of methods relates to the prior expectations about the properties of the modal decomposition. The options are either the spectral purity provided by the frequency-domain SPOD or the modal sparsity () provided by the time-domain SPOD and snapshot POD. For amplifier type flows, a dispersed spectrum of modes is expected and therefore the spectral purity is preferred. Instead, an oscillator flow is expected to have sparse dynamics, which are desired to be captured by the decomposition with as few modes as possible. The better understanding of the two SPOD

variants gives the freedom to fade between the strict classifications and therefore may help to reveal new flow structures.

## 2.4 Relation of time-delay embedding and SPOD

Time-delay embedding is a method to enrich the information that can be extracted from limited observations of a system. It builds on Takens (1981) embedding theorem, which states that the state of a continuous chaotic attractor can be reconstructed from a single-measurement time-series. Accordingly, a single measurement is enriched with time-delayed measurements to form a larger basis. Delay embedding has shown to improve flow control (Brunton & Noack, 2015), stochastic estimation (Lasagna et al., 2013) and reduced-order modelling (Brunton et al., 2017). In the context of meteorological data analysis, POD is known as empirical orthogonal function (EOF) and the use of delay embedding is referred to as extended EOF (Chen & Harr, 1993).

In the following, the close relation between the delay embedding and the short time-scale  $\tau$  introduced in section 2.1 is shown. For this purpose, the continuous framework of the previous sections is left and the observation of  $P$  spatial points taken at  $N$  discrete time instances is considered. A single flow snapshot is represented by the vector  $\mathbf{u}(t_i) = [u(x_1, t_i), u(x_2, t_i), \dots, u(x_P, t_i)]^T$ .

The relation between delay embedding and the SPOD is first presented graphically to get an idea of the matrix dimensions and the transformation between the different approaches. Therefore, the snapshot matrix is given by

$$\mathbf{X}_0 = [\mathbf{u}(t_1) \ \mathbf{u}(t_2) \ \cdots \ \mathbf{u}(t_{n-1}) \ \mathbf{u}(t_n)] \quad (2.27)$$

and graphically represented as

$$\mathbf{X}_0 = [\mathbf{u}(t_1) \ \mathbf{u}(t_2) \ \dots \ \mathbf{u}(t_n)] = \begin{array}{c} \color{red}{\rule{0.5cm}{0.5pt}} \\ \color{orange}{\rule{0.5cm}{0.5pt}} \\ \color{yellow}{\rule{0.5cm}{0.5pt}} \\ \color{green}{\rule{0.5cm}{0.5pt}} \\ \color{blue}{\rule{0.5cm}{0.5pt}} \\ \color{purple}{\rule{0.5cm}{0.5pt}} \\ \color{brown}{\rule{0.5cm}{0.5pt}} \end{array}.$$

Accordingly, the snapshot correlation matrix is represented by a simple matrix product  $\mathbf{C} = \mathbf{X}_0^T \mathbf{X}_0$  with the following graphical representation:

$$\begin{array}{c} \color{red}{\rule{0.5cm}{0.5pt}} \\ \color{orange}{\rule{0.5cm}{0.5pt}} \\ \color{yellow}{\rule{0.5cm}{0.5pt}} \\ \color{green}{\rule{0.5cm}{0.5pt}} \\ \color{blue}{\rule{0.5cm}{0.5pt}} \\ \color{purple}{\rule{0.5cm}{0.5pt}} \\ \color{brown}{\rule{0.5cm}{0.5pt}} \end{array}^T \begin{array}{c} \color{red}{\rule{0.5cm}{0.5pt}} \\ \color{orange}{\rule{0.5cm}{0.5pt}} \\ \color{yellow}{\rule{0.5cm}{0.5pt}} \\ \color{green}{\rule{0.5cm}{0.5pt}} \\ \color{blue}{\rule{0.5cm}{0.5pt}} \\ \color{purple}{\rule{0.5cm}{0.5pt}} \\ \color{brown}{\rule{0.5cm}{0.5pt}} \end{array} = \begin{array}{c} \color{blue}{\rule{0.5cm}{0.5pt}} \\ \color{purple}{\rule{0.5cm}{0.5pt}} \end{array} \mathbf{C}$$

Furthermore, time-delayed and time-advanced instances of the snapshot matrix are introduced as

$$\mathbf{X}_2 = [0 \ 0 \ \mathbf{u}(t_1) \ \mathbf{u}(t_2) \ \cdots \ \mathbf{u}(t_{n-3}) \ \mathbf{u}(t_{n-2})], \quad (2.28)$$

$$\mathbf{X}_1 = [0 \ \mathbf{u}(t_1) \ \mathbf{u}(t_2) \ \cdots \ \mathbf{u}(t_{n-2}) \ \mathbf{u}(t_{n-1})], \quad (2.29)$$

$$\mathbf{X}_{-1} = [\mathbf{u}(t_2) \ \mathbf{u}(t_3) \ \cdots \ \mathbf{u}(t_{n-1}) \ \mathbf{u}(t_n) \ 0], \quad (2.30)$$

$$\mathbf{X}_{-2} = [\mathbf{u}(t_3) \ \mathbf{u}(t_4) \ \cdots \ \mathbf{u}(t_{n-1}) \ \mathbf{u}(t_n) \ 0 \ 0], \quad (2.31)$$

where zero padding is used to fill in missing data. Zero padding is chosen as continuation at the boundaries to give a proper illustration, but the derivation is not necessarily limited to this. Furthermore, the introduction of time-advanced instances in addition to the time-delayed instances is only due to the symmetry of the SPOD. They constitute only a shift of the reference time frame and are not strictly required for the derivation. In the graphical illustration, these time-delayed and time-advanced instances correspond to a column shift in the snapshot matrix:

$$\mathbf{X}_2 = \begin{array}{|c|} \hline \text{---} \\ \hline \end{array} \quad \mathbf{X}_1 = \begin{array}{|c|} \hline \text{---} \\ \hline \end{array} \quad \mathbf{X}_0 = \begin{array}{|c|} \hline \text{---} \\ \hline \end{array} \quad \mathbf{X}_{-1} = \begin{array}{|c|} \hline \text{---} \\ \hline \end{array} \quad \mathbf{X}_{-2} = \begin{array}{|c|} \hline \text{---} \\ \hline \end{array}$$

All time-shifted instances of the snapshot matrix are collected in a large delay-embedded state matrix reading

$$\mathbf{X} = \begin{bmatrix} \mathbf{X}_2 \\ \mathbf{X}_1 \\ \mathbf{X}_0 \\ \mathbf{X}_{-1} \\ \mathbf{X}_{-2} \end{bmatrix}. \quad (2.32)$$

The snapshot correlation matrix computed from this state matrix is assumed to be equivalent to the filtered correlation matrix, requiring that  $\mathbf{X}^T \mathbf{X} = \mathbf{S}$ . Graphically, this reads

$$\begin{array}{cccccc} \mathbf{X}_2^T & \mathbf{X}_1^T & \mathbf{X}_0^T & \mathbf{X}_{-1}^T & \mathbf{X}_{-2}^T & \\ \hline \text{---} & \text{---} & \text{---} & \text{---} & \text{---} & \\ \hline \end{array} \begin{array}{c} \mathbf{X}_2 \\ \mathbf{X}_1 \\ \mathbf{X}_0 \\ \mathbf{X}_{-1} \\ \mathbf{X}_{-2} \end{array} = \mathbf{S}$$

which can also be represented as the addition of correlations of all time-delayed instances

$$\begin{array}{cccccc} \mathbf{X}_2^T & \mathbf{X}_1^T & \mathbf{X}_0^T & \mathbf{X}_{-1}^T & \mathbf{X}_{-2}^T & \\ \hline \text{---} & \text{---} & \text{---} & \text{---} & \text{---} & \\ \hline \end{array} \begin{array}{c} \mathbf{X}_2 \\ \mathbf{X}_1 \\ \mathbf{X}_0 \\ \mathbf{X}_{-1} \\ \mathbf{X}_{-2} \end{array} + \begin{array}{cccccc} \mathbf{X}_1^T & \mathbf{X}_0^T & \mathbf{X}_{-1}^T & \mathbf{X}_{-2}^T & & \\ \hline \text{---} & \text{---} & \text{---} & \text{---} & & \\ \hline \end{array} \begin{array}{c} \mathbf{X}_1 \\ \mathbf{X}_0 \\ \mathbf{X}_{-1} \\ \mathbf{X}_{-2} \end{array} + \begin{array}{cccccc} \mathbf{X}_0^T & \mathbf{X}_{-1}^T & \mathbf{X}_{-2}^T & & & \\ \hline \text{---} & \text{---} & \text{---} & & & \\ \hline \end{array} \begin{array}{c} \mathbf{X}_0 \\ \mathbf{X}_{-1} \\ \mathbf{X}_{-2} \end{array} + \begin{array}{cccccc} \mathbf{X}_{-1}^T & \mathbf{X}_{-2}^T & & & & \\ \hline \text{---} & \text{---} & & & & \\ \hline \end{array} \begin{array}{c} \mathbf{X}_{-1} \\ \mathbf{X}_{-2} \end{array} + \begin{array}{cccccc} \mathbf{X}_{-2}^T & & & & & \\ \hline \text{---} & & & & & \\ \hline \end{array} \begin{array}{c} \mathbf{X}_{-2} \end{array} = \mathbf{S}$$

This it is obvious that the time shift in the snapshot matrix causes only a diagonal shift of the original correlation matrix  $\mathbf{C}$ . As a result, the time-shifted correlation matrix  $\mathbf{S}$  is a sum of diagonally shifted instances of matrix  $\mathbf{C}$ :

The sum of these shifted matrices can also be represented by a 2D convolution with an identity matrix that has the size of the time delay

where the convolution is nothing but the filter along the diagonals introduced with the SPOD.

The formal expression of this derivation reads more concisely as

$$\mathbf{S} = \mathbf{X}^T \mathbf{X} = \sum_{k=-2}^2 \mathbf{X}_k^T \mathbf{X}_k, \quad (2.33)$$

where the elements of the matrix  $\mathbf{S}$  are given by

$$S_{i,j} = \sum_{k=-2}^2 \mathbf{u}(t_{i+k})^T \mathbf{u}(t_{j+k}) = \sum_{k=-2}^2 g_k C_{i+k,j+k}, \quad (2.34)$$

with the basic snapshot correlation

$$C_{k,l} = \sum_{p=1}^P u(x_p, t_k) u(x_p, t_l) \quad (2.35)$$

and  $\mathbf{g} = [1 \ 1 \ 1 \ 1 \ 1]$ . This is the same as the representation of the filtered correlation matrix given in equation (2.12), which corresponds to an SPOD with a box filter of size 2 if the normalisation of the filter is omitted.

The derivation can also be provided in agreement with the notation introduced in the Hankel alternative view of Koopman (HAVOK) by Brunton et al. (2017). Therefore,  $M$  time-delay instances of the snapshot matrix are collected in a block-Hankel matrix  $\mathbf{H}$ , reading

$$\mathbf{H} = \begin{bmatrix} \mathbf{u}(t_1) & \mathbf{u}(t_2) & \cdots & \mathbf{u}(t_{N-M}) \\ \mathbf{u}(t_2) & \mathbf{u}(t_3) & \cdots & \mathbf{u}(t_{N-M+1}) \\ \vdots & \vdots & \ddots & \vdots \\ \mathbf{u}(t_M) & \mathbf{u}(t_{M+1}) & \cdots & \mathbf{u}(t_N) \end{bmatrix}. \quad (2.36)$$

The snapshot correlation of this matrix is again supposed to be equivalent to the filtered SPOD matrix  $\mathbf{S} = \mathbf{H}^T \mathbf{H}$ , which can likewise be described by the element-wise summation

$$S_{k,l} = \sum_{j=1}^M \sum_{p=1}^P u(x_p, t_{k+j}) u(x_p, t_{l+j}). \quad (2.37)$$

Again, the right hand side of (2.37) can be simplified by replacing the inner sum with the basic snapshot correlation (2.35), which gives

$$S_{k,l} = \sum_{j=1}^M C_{k+j,l+j}. \quad (2.38)$$

This reveals that the time-delay embedding is equivalent to a partial summation of the diagonals of  $C_{k,l}$ . Comparing this result to (2.12) shows that POD in combination with time delay embedding is equivalent to SPOD with a box filter ( $g_j = 1$  and  $N_f = (M - 1)/2$ ).

In addition to this correspondence, the SPOD has further unique characteristics. Such as that the SPOD, in contrast to time-delay embedding, includes a weighting of the delay with respect to the amount of delay relative to the centre coordinate. Moreover, delay embedding requires the construction of a very large Hankel matrix, while for SPOD the construction of this matrix is implicitly assumed but never really set up. Instead, the effect of the time-delay embedding is replicated by the filter applied to the correlation matrix. This saves computation time in case the number of snapshots is smaller than the number of spatial points multiplied by the embedding dimension ( $N < PM$ ).

## Chapter 3

# Publications

The publications that are part of this thesis are presented in chronological order as:

- 3.1 M. Sieber, C. O. Paschereit, & K. Oberleithner (2016d). “Spectral proper orthogonal decomposition”. *Journal of Fluid Mechanics* 792, pp. 798–828. DOI: [10.1017/jfm.2016.103](https://doi.org/10.1017/jfm.2016.103)
- 3.2 M. Sieber, C. O. Paschereit, & K. Oberleithner (2016b). “Advanced Identification of Coherent Structures in Swirl-Stabilized Combustors”. *Journal of Engineering for Gas Turbines and Power* 139.2, p. 021503. DOI: [10.1115/1.4034261](https://doi.org/10.1115/1.4034261)
- 3.3 M. Stöhr, K. Oberleithner, M. Sieber, Z. Yin, & W. Meier (2017). “Experimental Study Of Transient Mechanisms Of Bi-Stable Flame Shape Transitions In A Swirl Combustor”. *Journal of Engineering for Gas Turbines and Power*, V04BT04A063. DOI: [10.1115/1.4037724](https://doi.org/10.1115/1.4037724)
- 3.4 M. Sieber, C. O. Paschereit, & K. Oberleithner (2021a). “Stochastic modelling of a noise-driven global instability in a turbulent swirling jet”. *Journal of Fluid Mechanics* 916, A7. DOI: [10.1017/jfm.2021.133](https://doi.org/10.1017/jfm.2021.133)
- 3.5 M. Sieber, C. O. Paschereit, & K. Oberleithner (2021b). “Impact of density stratification on the global mode in a swirling jet: Stochastic modelling and Lagrangian coherent structures”. *International Journal of Heat and Fluid Flow* 90, p. 108820. DOI: <https://doi.org/10.1016/j.ijheatfluidflow.2021.108820>

The contribution of each publication to the dissertation is summarised at the beginning of every section under the following keywords:

**Methods** that are introduced in individual publications. The common methodological subjects are the development of the SPOD, the implementation of a stochastic model, and the visualisation of flow dynamics and flow structures.

**Results**, which are obtained from the application of the methods to measurement data. The investigated data are generally experimental data from different setups which are not all captured within the dissertation. The source of the data, the related experiments, and the general observations are summarised here.

**Physics** of fluid dynamic phenomena drawn from the results. The common fluid dynamic subject that is discussed in the superordinate work is the global mode in swirling jets. The contribution to the global picture of the swirling flow and the related instability is given here.

### 3.1 Spectral proper orthogonal decomposition

This article is published in an edited form in the Journal of Fluid Mechanics under the following reference: M. Sieber, C. O. Paschereit, & K. Oberleithner (2016d). “Spectral proper orthogonal decomposition”. *Journal of Fluid Mechanics* 792, pp. 798–828. DOI: [10.1017/jfm.2016.103](https://doi.org/10.1017/jfm.2016.103). The following is the accepted manuscript of the article. Reprinted with permission. This version is free to view and download for private research and study only. Not for re-distribution, re-sale or use in derivative works. ©Cambridge University Press.

The SPOD is presented in this work as a new method for the decomposition of velocity data from turbulent flows. The publication misses part of classification concerning similar POD variants. This is supplemented in the dissertation in chapter 2. The relations were not entirely clear at the time the paper was published but they developed in exchange with the scientific community.

**Methods:** The SPOD is derived from practical aspects of data processing. It is presented as an adjustable filter added to the classical snapshot POD. This allows a continuous fade from POD to Fourier decomposition. The pairing of linked modes that describe a common coherent structure is further introduced using a cross-spectral correlation based on the DMD.

**Results:** High-speed PIV data from different investigations at the chair of fluid dynamics are analysed to show the capabilities of the SPOD. The SPOD is opposed to POD and Fourier decomposition to highlight benefits of the new approach. The SPOD spectrum is introduced as a compact representation of the entire dynamics contained in a dataset.

**Physics:** Identification of a coherent structure through the separation of time scales between the fast oscillation and the slow variation in amplification rate and frequency. This is achieved by the short-time linearization through using the SPOD filter.

# Spectral proper orthogonal decomposition

Moritz Sieber<sup>†</sup>, C. Oliver Paschereit and Kilian Oberleithner

Institut für Strömungsmechanik und Technische Akustik  
 – Hermann-Föttinger-Institut –  
 Müller-Breslau Str. 8, D-10623 Berlin, Germany

(Received xx; revised xx; accepted xx)

The identification of coherent structures from experimental or numerical data is an essential task when conducting research in fluid dynamics. This typically involves the construction of an empirical mode base that appropriately captures the dominant flow structures. The most prominent candidates are the energy-ranked proper orthogonal decomposition (POD) and the frequency ranked Fourier decomposition and dynamic mode decomposition (DMD). However, these methods are not suited when the relevant coherent structures occur at low energies or at multiple frequencies, which is often the case. To overcome the deficit of these “rigid” approaches, we propose a new method termed Spectral Proper Orthogonal Decomposition (SPOD). It is based on classical POD and it can be applied to spatially and temporally resolved data. The new method involves an additional temporal constraint that enables a clear separation of phenomena that occur at multiple frequencies and energies. SPOD allows for a continuous shifting from the energetically optimal POD to the spectrally pure Fourier decomposition by changing a single parameter. In this article, SPOD is motivated from phenomenological considerations of the POD autocorrelation matrix and justified from dynamical system theory. The new method is further applied to three sets of PIV measurements of flows from very different engineering problems. We consider the flow of a swirl-stabilized combustor, the wake of an airfoil with a Gurney flap, and the flow field of the sweeping jet behind a fluidic oscillator. For these examples, the commonly used methods fail to assign the relevant coherent structures to single modes. The SPOD, however, achieves a proper separation of spatially and temporally coherent structures, which are either hidden in stochastic turbulent fluctuations or spread over a wide frequency range. The SPOD requires only one additional parameter, which can be estimated from the basic time scales of the flow. In spite of all these benefits, the algorithmic complexity and computational cost of the SPOD are only marginally greater than those of the snapshot POD.

## 1. Introduction and motivation

### 1.1. Contemporary methods for data reduction

Today’s high fidelity computational fluid dynamics (CFD) and high-end experimental data acquisition systems tend to produce vast amounts of data that are getting harder to interpret and overview. Methods to analyze such data are numerous and are always developing to stay in line with acquisition and computation systems. The most challenging data stem from turbulent flows that feature a huge range of temporal and spatial scales. A key challenge in turbulent flow data mining is the distinction of deterministic coherent motion from purely stochastic motion. Numerous methods exist that exploit the periodicity or energetic dominance of these coherent structures. These methods

<sup>†</sup> Email address for correspondence: moritz.sieber@fd.tu-berlin.de

range from classic Fourier decomposition to dynamic mode decomposition (DMD) and proper orthogonal decomposition (POD). The most prominent among them are shortly introduced in the following.

POD has been widely used since its introduction by Lumley (1970) and Sirovich (1987). It was applied in nearly every fluid dynamic field. Beyond fluid dynamics, this method is also known as singular value decomposition, principal component analysis or Karhunen-Loève expansion (Berkooz *et al.* 1993). The basic idea behind this method is to construct an optimal basis that represents most of the data variance with as few basis functions as possible. In context of POD the variance is turbulent kinetic energy. Therefore, the POD searches for the most energetic modes whereby coherent structures with high energy content are likely to be represented by POD basis functions (Holmes *et al.* 2012).

Another classical approach is the linear stochastic estimation introduced by Adrian & Moin (1988), where the readings of different sensors are related via a linear mapping. This is closely related to the extended POD (Boree 2003), also described in a unified framework (observable inferred decomposition) by Schlegel *et al.* (2012). In recent extensions of linear stochastic estimation, the use of time delays between the different sensors and also the use of one sensor at multiple time instances is pursued to separate periodic coherent structures from turbulent fluctuations (Durgesh & Naughton 2010; Lasagna *et al.* 2013). This approach was also used to improve the determination of harmonic POD modes from few pressure sensors (Hosseini *et al.* 2015). These utilisations of data from various time instances are also related to the temporal constraint used for the POD extension proposed in this article.

Targeting the temporal periodicity of the coherent structures, spectral methods like discrete Fourier transform (DFT) and the recently introduced DMD (Rowley *et al.* 2009; Schmid 2010) come into play. These methods commonly span the mode space according to fixed frequencies, which enables the identification of coherent structures within small spectral bandwidths. In contrast to the DFT, the DMD also distinguishes modes with respect to their linear amplification. The recently introduced extended DMD (Williams *et al.* 2015) tries to overcome the limitations encountered by the (linear) DMD approach when trying to decompose data from nonlinear systems. The idea is to use nonlinear functions that create observables of the data, which are *exactly* described by a linear system. This approach translocates the problem towards the identification of these nonlinear functions, which can be solved using the “kernel trick” that is common in machine learning. This paper presents an alternative approach, which extends POD to account for temporal dynamics in addition to energetic optimality.

### 1.2. *Why yet another method?*

After this short and incomplete review of data processing methods, one may ask if there is need for another method. The answer is probably no, so we take the most used method (POD) and bring it up to date for present research issues. The approach pursued here includes a simple yet effective extension to the classical POD, which leads to a more general method comprising POD and also the DFT. This approach unifies existing methods, but also offers possibilities beyond these. From the authors’ experience, the currently available methods often fail when applied to challenging flow data. These stem from flows with weak coherent structures where the recorded data have low signal to noise ratios, from flows with intermittent dynamics, or from flows featuring multi-modal interactions leading to frequency modulations, to name a few. In such cases, much effort is required to optimize the data processing until satisfactory results are obtained. The usual escape route is to focus on a certain spatial region or to apply suitable filters to pick out a certain wavelength or frequency range. This involves trial and error or

requires prior knowledge of the investigated flow. There is also the danger of cutting off a substantial portion of the data, leading to false interpretations. These procedures can be collected under the heading “identifying symmetries” as done by Holmes *et al.* (2012). The drawback of this approach is that the investigated flow must feature some symmetries and *they must be known a priori*. A recent application shows the huge variety of spatial and temporal filtering together with POD to separate different phenomena into different modes (Bourgeois *et al.* 2013), exemplifying the complexity of this approach.

The usage of spectral methods for highly turbulent flows is even more challenging than POD. The variable frequency of single coherent structures and intermittent occurrence of different structures with the same frequency hinders a proper decomposition. In terms of the DFT, averaging of spectra from multiple measurements or sensors is essential to get reliable results. Analogously, for the DMD, averaging over several events is an option to reject noise (Tu *et al.* 2014). Nonetheless, the results obtained with DFT and DMD suffer from limiting the temporal dynamics to single frequencies. Turbulent flows hardly ever feature discrete frequencies and it is not always valuable to restrict a single mode (flow phenomenon) to a single frequency. Coherent structures that feature significant phase jitter or frequency modulation are represented by many modes at similar frequencies. In contrast, the POD puts no temporal constraint on the modes. This can result in modes that represent flow phenomena occurring at largely different temporal scales. Thus, it is often hard to interpret these modes and draw meaningful conclusions from the temporal dynamics.

From our point of view, there is a big gap between the energetically optimal decomposition of POD and the spectrally clean decomposition of DFT or DMD. This gap will be bridged with the spectral proper orthogonal decomposition (SPOD) introduced in this article. This new method not only places itself somewhere in between these two extrema, but it allows for a continuous shifting from one to the other. The main idea is to apply a filter operation to the POD correlation matrix, which will force the POD towards clear temporal dynamic. Depending on the filter strength we continuously sweep from classic POD to DFT.

The remainder of this article is organized as follows: The proposed method is described in detail in §2. The reader is guided from snapshot POD via an in-depth interpretation of the correlation matrix towards the general description of the SPOD. In addition, a method is explained to identify coupled mode pairs describing a single coherent structure, which becomes handy when working with SPOD. In §3, the new method is demonstrated on three different experimental data sets. The results are compared against POD and DFT to point out the benefits of SPOD. In §4 the capabilities of SPOD are summarized, based on the findings from the application to experimental data.

## 2. Description and interpretation of the proposed method

### 2.1. Classical snapshot POD

To introduce the method and the nomenclature, the snapshot POD approach is described first. We start off with a decomposition of a data set into spatial modes and temporal coefficients:

$$u(\mathbf{x}, t) = \bar{u}(\mathbf{x}) + u'(\mathbf{x}, t) = \bar{u}(\mathbf{x}) + \sum_{i=1}^N a_i(t) \Phi_i(\mathbf{x}). \quad (2.1)$$

Note that only the fluctuating part  $u'(\mathbf{x}, t)$  is decomposed. It is split into a sum of spatial modes  $\Phi_i$  and mode coefficients  $a_i$ . A set of  $M$  spatial points recorded simultaneously over

4

*M. Sieber et al*

$N$  time steps is considered. To calculate the POD, the correlation matrix of this data set is needed. For data obtained from particle image velocimetry (PIV) or CFD, the number of spatial points is usually larger than the number of snapshots. The correlation matrix is then calculated between individual snapshots (temporal correlation). The alternative approach (spatial correlation) that applies for  $M \ll N$ , is detailed in appendix A. The correlation between two snapshots is calculated from an appropriate inner product  $\langle \cdot, \cdot \rangle$ , usually defined as the  $L^2$  inner product

$$\langle u(\mathbf{x}), v(\mathbf{x}) \rangle = \int_V u(\mathbf{x})v(\mathbf{x})dV, \quad (2.2)$$

where  $V$  specifies the spatial region or volume over which the correlation is integrated. The elements of the correlation matrix  $\mathbf{R}$  are given by

$$R_{i,j} = \frac{1}{N} \langle u'(\mathbf{x}, t_i), u'(\mathbf{x}, t_j) \rangle. \quad (2.3)$$

Matrix  $\mathbf{R}$  is of size  $N \times N$ .

The temporal coefficients  $\mathbf{a}_i = [a_i(t_1), \dots, a_i(t_N)]^T$  and mode energies  $\lambda_i$  are obtained from the eigenvectors and eigenvalues of the correlation matrix.

$$\mathbf{R}\mathbf{a}_i = \lambda_i\mathbf{a}_i; \quad \lambda_1 \geq \lambda_2 \geq \dots \geq \lambda_N \geq 0 \quad (2.4)$$

The subscript  $i$  refers to single eigenvalues, which are sorted in descending order. Since the  $\mathbf{a}_i$  are the eigenvectors of the real symmetric positive-definite matrix  $\mathbf{R}$ , they are orthogonal. Moreover, they are scaled with the energy of the single modes such that

$$\frac{1}{N}(\mathbf{a}_i, \mathbf{a}_j) = \lambda_i\delta_{ij}, \quad (2.5)$$

where  $(\cdot, \cdot)$  denotes the scalar product. The spatial modes are obtained from the projection of the snapshots onto the temporal coefficients

$$\Phi_i(\mathbf{x}) = \frac{1}{N\lambda_i} \sum_{j=1}^N a_i(t_j)u'(\mathbf{x}, t_j). \quad (2.6)$$

These modes are orthonormal by construction

$$\langle \Phi_i, \Phi_j \rangle = \delta_{ij}. \quad (2.7)$$

The formulation so far is perfectly in line with classical snapshot POD, which can also be computed by a singular value decomposition. However, since the SPOD requires a manipulation of the correlation matrix we retain the classical form.

## 2.2. Properties of the correlation matrix

The SPOD described in this article is essentially a filter applied to the correlation matrix  $\mathbf{R}$ . To offer a better understanding of this approach, the structure of the correlation matrix  $\mathbf{R}$  is inspected first.

Figure 1(a) shows the structure of the correlation matrix for the data set of a forced turbulent jet. The data were acquired with PIV inside a 2D-plane aligned with the jet axis. The considered flow shows strong vortex shedding at the forcing frequency (the acquisition frequency is 25 times the forcing frequency). The presence of these periodic patterns in the flow, and their convection within the observed flow field, lead to a diagonal, wave-like structure of the matrix. This is closely related to the periodicity of the auto-correlation coefficient. In fact, if the individual elements of the correlation matrix  $\mathbf{R}$  are

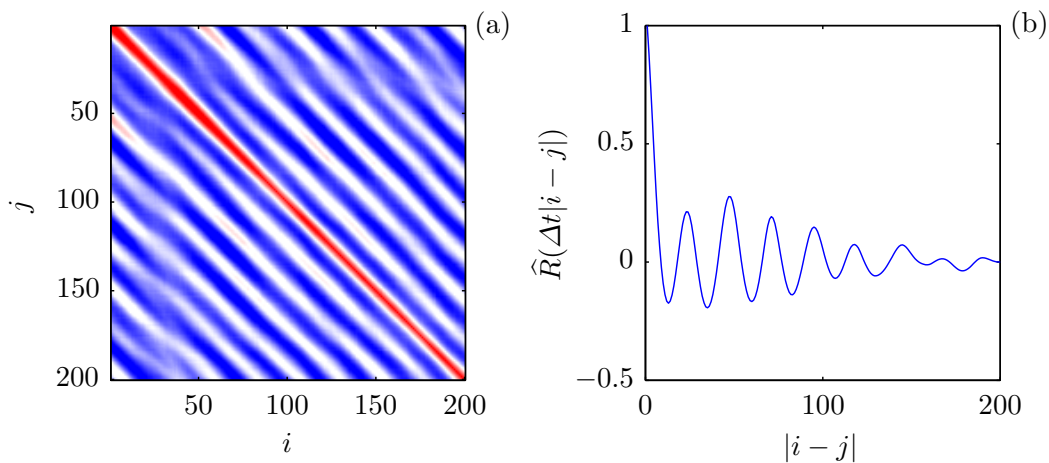


FIGURE 1. (a) Pseudo-color plot of the correlation matrix elements  $R_{i,j}$  and (b) the corresponding correlation coefficient  $\hat{R}$ . The displayed data are picked from PIV measurements of a forced turbulent jet.

summed up along the diagonals, we get the spatially averaged auto-correlation coefficient

$$\hat{R}(\tau) = \frac{\int_{\tau}^T \langle u'(\mathbf{x}, t), u'(\mathbf{x}, t - \tau) \rangle dt}{\int_0^T \langle u'(\mathbf{x}, t), u'(\mathbf{x}, t) \rangle dt}, \quad (2.8)$$

where the upper bound  $T$  is the length of the measured sequence. It is depicted in figure 1(b), showing the same periodicity as the correlation matrix. The auto-correlation coefficient itself represents the spectral content of different timescales and wavelengths and it is directly related to the power spectral density of the underlying data. However, it contains no information of the phase of individual frequencies, due to the reference of the signal to itself. This is why the elements along the diagonals of  $\mathbf{R}$  look so similar, as they represent only relative changes with respect to the time step on the main diagonal. Thus, increased similarity along the diagonals of  $\mathbf{R}$  is equivalent to an increased similarity of the dynamics of the underlying signal. This property will be discussed more deeply in section 2.4. The obvious consequence from these findings is: If we want to obtain smooth dynamics from the POD, we have to enforce the diagonal similarity of the correlation matrix. This is where we step into spectral POD.

### 2.3. General description of the SPOD

The yet so simple, but radical approach is a filter operating on the correlation matrix  $\mathbf{R}$ . To augment the diagonal similarity of  $\mathbf{R}$  a simple low-pass filter is applied along the diagonals. This results in a filtered correlation matrix  $\mathbf{S}$  with the elements given as

$$S_{i,j} = \sum_{k=-N_f}^{N_f} g_k R_{i+k,j+k}. \quad (2.9)$$

The filter above is just a symmetric finite impulse response filter with a filter coefficients vector  $\mathbf{g}$  of length  $2N_f + 1$ . The most simple approach would be a box filter, where all coefficients have the same value  $g_k = \frac{1}{2N_f+1}$ . In the examples discussed later, we use a Gaussian filter, which features a smooth response in time and frequency domain. Moreover, we choose a standard deviation as such that the filter gives the same cut-off

6

*M. Sieber et al*

frequency as a box filter with half the length. In fact, any kind of digital finite impulse response filter can be used here.

The further procedure of the SPOD is the same as for the classical POD. From the filtered correlation Matrix  $\mathbf{S}$  the temporal coefficients  $\mathbf{b}_i$  and mode energies  $\mu_i$  are obtained from the eigen decomposition

$$\mathbf{S}\mathbf{b}_i = \mu_i\mathbf{b}_i ; \quad \mu_1 \geq \mu_2 \geq \dots \geq \mu_N \geq 0. \quad (2.10)$$

The temporal coefficients are also scaled with the mode energy and they are still orthogonal

$$\frac{1}{N}(\mathbf{b}_i, \mathbf{b}_j) = \mu_i\delta_{ij}. \quad (2.11)$$

The spatial modes are finally obtained from the projection of the snapshots onto the temporal coefficients

$$\Psi_i(\mathbf{x}) = \frac{1}{N\mu_i} \sum_{j=1}^N b_i(t_j)u'(\mathbf{x}, t_j), \quad (2.12)$$

where these modes are no longer orthogonal. This property of the spatial modes is detailed in appendix B. The total energy of the data set is still represented by the decomposition ( $\sum \lambda_i = \sum \mu_i$ ), but the energy per mode is less for the first modes. Hence, increasingly plain temporal dynamics are obtained at the expense of spatial orthogonality and a dispersed SPOD spectrum. Nevertheless, the decomposition (as in (2.1))

$$u(\mathbf{x}, t) = \bar{u}(\mathbf{x}) + \sum_{i=1}^N b_i(t)\Psi_i(\mathbf{x}), \quad (2.13)$$

is still exact if all  $N$  SPOD modes are used for the re-composition.

If the filter size is extended over the entire time-series, the filtered correlation matrix converges to a symmetric Toeplitz matrix. This matrix has the form

$$S_{i,j} = \hat{R}(\Delta t|i - j|), \quad (2.14)$$

with the diagonals given by the average correlation coefficient (2.8). This special matrix is also known as the covariance matrix and its eigenvalues are tracing out the power spectral density of the underlying time series (Wise 1955). This equality is a part of Szegős theorem and it is valid for the limiting case where the number of samples approaches infinity. To discuss this feature for finite series, the treatment of the start and end of the time series must be clarified. At the boundaries of  $\mathbf{R}$ , the filter operation is not properly defined, since the symmetric filter lacks elements before and after the finite series. These elements can either be replaced by zeros or the time-series is assumed to be periodic. For the zero padded boundary,  $R_{i,j} = 0$  in (2.9) for any  $i$  or  $j$  that is outside of the domain  $[1, N]$ . In the case of periodic boundary conditions, indexing outside of the valid domain is mapped back into the domain by addition or subtraction of  $N$  (e.g.,  $R_{i,j} = R_{i-N,j}$  if  $i > N$ ). For periodic conditions and a box filter of the same size as the number of snapshots, a symmetric circulant matrix is obtained, where the eigenvalues and eigenvectors are given by the Fourier transform of the first row (Gray 2005). Hence, the DFT and the SPOD produce the same decomposition for this limiting case. For the Gaussian filter this limit is only exactly reached with a infinitely large filter size, but practically, the decomposition remains nearly constant for values  $N_f > N$ . In the following example of application, the DFT is calculated with  $N_f = N$  and a box filter.

The general SPOD approach and its placement with respect to the existing methods

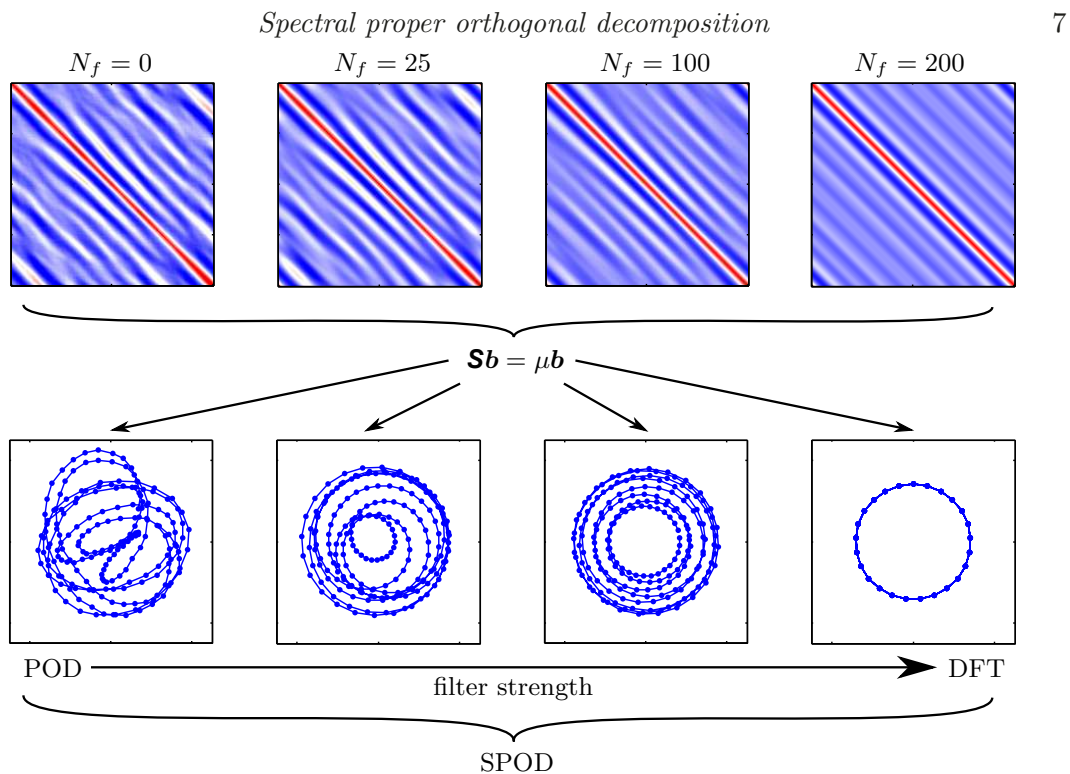


FIGURE 2. Schematic describing the main properties of the SPOD for increasing filter strength (from left to right). The top row shows pseudo-color plots of the filtered correlation matrix ( $\mathbf{S}$ ). The phase portraits of the corresponding first two modes ( $\mathbf{b}_1$  and  $\mathbf{b}_2$ ) that describe the dominant oscillations are shown below. The axes of the plots shown here are the same as for the plots in figure 1 and 16, respectively. The graphs are based on the data already presented in section 2.2 and the SPOD is calculated from 200 snapshots.

is graphically summarized in figure 2. The images in the first row show the filtered correlation matrix at different filter widths  $N_f$ . The images below depict the phase portraits of the leading two modes (compare figure 16). It is apparent that the increased diagonal similarity of the correlation matrix, which goes in hand with the increased filter width, successively limits the temporal variations of the mode amplitude and frequency until a stable limit cycle is reached. In summary, the SPOD allows for continuous fading from the energetically optimal POD to a purely spectral DFT. What happens in between these two limits is very promising, as will be shown later in this article.

#### 2.4. Spectral properties of the SPOD filter operation

Now provided with the continuous transition between POD and DFT, we may determine how the SPOD filter affects the resulting mode dynamics. In other words, we would like to know how the filter frequency response transfers into mode space. This enables the choice of an adequate filter size  $N_f$ , which is the crucial property of the introduced filter operation.

We consider the forced turbulent jet data already consulted in the previous section. In this flow the periodic shedding is strong and regular and it is represented by the same SPOD mode regardless of the filter setting. Furthermore, the flow is turbulent, showing sufficient jitter and broadband noise in the mode dynamics to demonstrate the effect of the SPOD filter. Figure 3 shows the spectrum of the most dominant SPOD mode coefficient  $b_1$  computed for different filter sizes  $N_f$ . According to these graphs, the SPOD operation applies a band-pass filter to the modal dynamics with the band centered

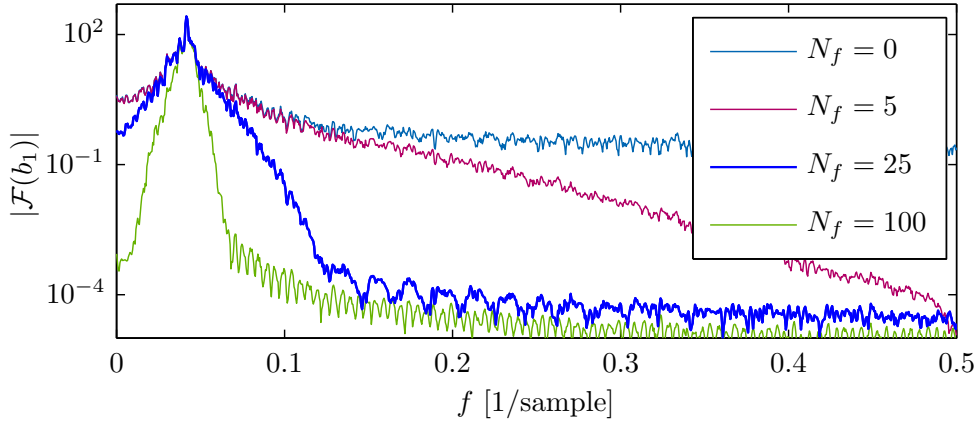


FIGURE 3. Magnitude of the frequency spectrum for the first SPOD mode for different filter widths  $N_f$ . The analyzed flow is the forced turbulent jet presented in figures 1 and 2.

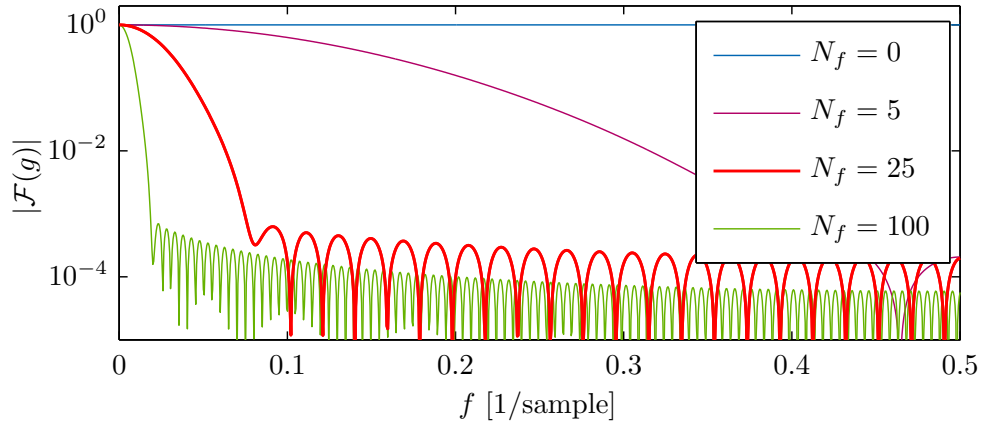


FIGURE 4. Magnitude of the SPOD filter frequency response for different filter widths  $N_f$ .

around the dominant frequency. The width of the band and the spectral attenuation is directly related to the filter width.

The spectral response of the filter coefficients  $\mathbf{g}$  that define the spectral constraint of the SPOD (2.9) are drawn in figure 4. As described in the previous section, these coefficients are chosen to represent a Gaussian filter with a typical low-pass characteristic, where the cutoff-frequency is related to the filter width as  $f_c \propto 1/N_f$ .

To evaluate the frequency response of the entire SPOD method, we compute the spectral attenuation of the SPOD with respect to POD and compare this to the frequency response of the filter coefficients. The spectral attenuation is calculated from the ratio of spectral magnitudes of the first SPOD ( $N_f = 25$ ) and POD ( $N_f = 0$ ) coefficients  $b_1$ . The results are shown in figure 5, where the graph of the filter frequency response must be shifted to compensate the difference between low- and band-pass filtering. Accordingly, both curves show nearly the same attenuation as well as the same characteristic stop-band ripples. In this adapted representation the spectral attenuation of the SPOD can be directly estimated from the filter coefficients. However, the SPOD shows a band-pass characteristic while the filter coefficients describe a low-pass filter. The frequency around which the band is centered is selected intrinsically by the SPOD.

The band-pass behavior of the SPOD is a direct consequence of the smoothing of the diagonal elements of the correlation matrix. As elaborated in appendix C for linear system

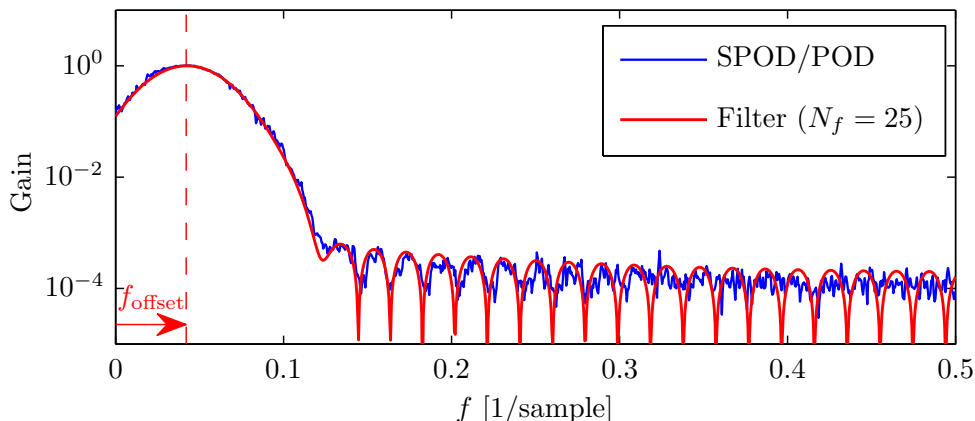


FIGURE 5. The spectral attenuation of the SPOD obtained from the ratio of the spectral magnitudes  $|\mathcal{F}(b_{N_f=0})|/|\mathcal{F}(b_{N_f=25})|$  and the response of the filter coefficients  $|\mathcal{F}(g)|$  (2.9). For the filter response the frequency axis is offset to match the modes center frequency.

dynamics, variations of the diagonal elements relate directly to variations of the frequency and amplification of the modes. Hence, the SPOD filter operation constrains the temporal variation of the mode frequency and amplification rate, but sets no limitations on the temporal mean frequency and amplitude. Thus, the SPOD filter averages out frequency variations which reduces the spectral bandwidth of the modes. With the selected low-pass filter coefficients, the smoothing intensity can be adjusted, which controls the bandwidth of the filter. However, the selection of a center frequency for this band-pass filter is data driven, which means the filter “snaps” to a dominant (coherent) fluctuation contained in the data.

Based on these conclusions, an adequate filter size  $N_f$  may be selected prior to the SPOD. Ideally, it should be a time span for which the dynamics of the coherent structures of interest exhibit constant dynamics. In practice, we found that suitable selections for this time span are the characteristic timescales of the flow. These are either one period of a dominant oscillation or the time that a structure needs to be convected a typical length-scale of the flow.

Based on the coefficient spectra shown in figure 3, it may seem that SPOD is just a method that is comparable to a subsequent band-pass filtering of POD modes, but the situation is substantially different. A posterior filtering of POD modes cut out parts of the temporal dynamics that are ignored in further investigations. In the case of the SPOD, the filter is applied prior to the decomposition. Hence, the filter shifts the dynamic content removed from one mode to the other modes. Therefore, the entire dynamic content is still represented in the decomposition, but it is redistributed among the modes (2.13). Moreover, the SPOD may “find” modes that were hidden in noise or mixed with other modes, which is not possible with a subsequent filter.

### 2.5. Identification of coupled modes

One crucial point in POD and SPOD is the identification of linked modes. Assuming the presence of periodic coherent structures, their dynamics are described by a pair of modes, analogue to the sine and cosine in the Fourier space or the real and imaginary part of DMD modes. They constitute the real and imaginary part of an analytical signal

$$\tilde{b}(t) = b_i(t) + ib_j(t) = A(t)e^{i\phi(t)}, \quad (2.15)$$

where  $A$  is the amplitude and  $\phi$ , the phase of the signal ( $i = \sqrt{-1}$ ). The coupling of such a mode pair is not given by the SPOD and it has to be identified a posteriori. Coupled modes typically show a similar amount of energy and pair in the POD spectrum (Oberleithner *et al.* 2011, 2014). For more complex dynamics with multiple energetic modes, the pairs are not easily identified and visual inspection of Lissayous figures and spatial modes is required. This manual procedure is cumbersome and by no means objective.

To provide an alternative, we propose an unbiased approach that gives a quantitative measure of the dynamic coupling of individual modes. The idea is to evaluate the mode coefficients cross spectra at  $\pi/2$  phase lag, in order to measure the spectral proximity. Mode pairs that describe a single structure must have the same spectral content, but are shifted by a quarter period. In the following, this spectral measure is also called harmonic correlation. Fourier decomposition and DMD were both considered to evaluate this harmonic correlation, but the DMD turned out to be more reliable for this task. The general procedure is schematically outlined in figure 6. From the depicted operations, the DMD and the mode coupling are discussed in this section.

For the DMD of the SPOD coefficients, their temporal evolution is assumed to be governed by a linear operator  $\mathbf{T}$

$$\mathbf{b}(t + \Delta t) = \mathbf{T}\mathbf{b}(t). \quad (2.16)$$

To approximate this operator, the SPOD coefficients are arranged in two matrices  $\mathbf{X} = [\mathbf{b}(0) \ \mathbf{b}(\Delta t) \ \dots \ \mathbf{b}((N-2)\Delta t)]$  and  $\mathbf{Y} = [\mathbf{b}(\Delta t) \ \mathbf{b}(2\Delta t) \ \dots \ \mathbf{b}((N-1)\Delta t)]$  (following the notation of Tu *et al.* (2014)). Hereafter, the operator is given by

$$\mathbf{T} = \mathbf{Y}\mathbf{X}^{-1}, \quad (2.17)$$

where  $\mathbf{X}^{-1}$  is the Moore-Penrose pseudoinverse of  $\mathbf{X}$ . Alternatively, this can be solved as a least squares problem, minimizing  $\|\mathbf{T}\mathbf{X} - \mathbf{Y}\|$ . To reject measurement noise in the identification procedure, only the ‘‘physical part’’ of the SPOD modes is considered for the calculation of the operator  $\mathbf{T}$ . That means, only the modes with acceptable signal to noise ratio should be considered. Therefore, the number of retained modes is calculated from the energy resolved by the SPOD, truncated after  $N_c$  modes, with

$$\mathcal{E}(N_c) = \frac{\sum_{k=1}^{N_c} \mu_k}{\sum_{k=1}^N \mu_k}. \quad (2.18)$$

In the examples shown later the modes are truncated around  $\mathcal{E}(N_c) = 0.95$ . This value depends on the signal to noise ratio of the considered measurement, which can be estimated from the POD spectrum (Raiola *et al.* 2015). Note that the number of retained modes increases for wider SPOD filters and corresponding flatter SPOD spectra ( $\mu_j$ ).

The DMD modes are obtained by the eigen-decomposition of matrix  $\mathbf{T}$  as

$$\mathbf{T}\mathbf{c}_i = \nu_i\mathbf{c}_i. \quad (2.19)$$

The eigenvalues  $\nu_i$  comprise the frequencies  $\omega_i$  and amplification-rates  $\sigma_i$  of the operator  $\mathbf{T}$  and are given by the logarithm of the eigenvalue  $\ln(\nu_i)/\Delta t = \sigma_i + i\omega_i$ . The eigenvectors  $\mathbf{c}_i$  hold the relative spectral content of the single SPOD coefficients with respect to these frequencies. More precisely, the element  $c_{i,j}$  of vector  $\mathbf{c}_i$  is the spectral content of the single mode coefficient  $b_j$  with respect to  $\nu_i$ . The actual modal representation is given by

$$b_j(t) = \sum_{i=1}^{N_c} c_{i,j} e^{(\sigma_i + i\omega_i)t}. \quad (2.20)$$

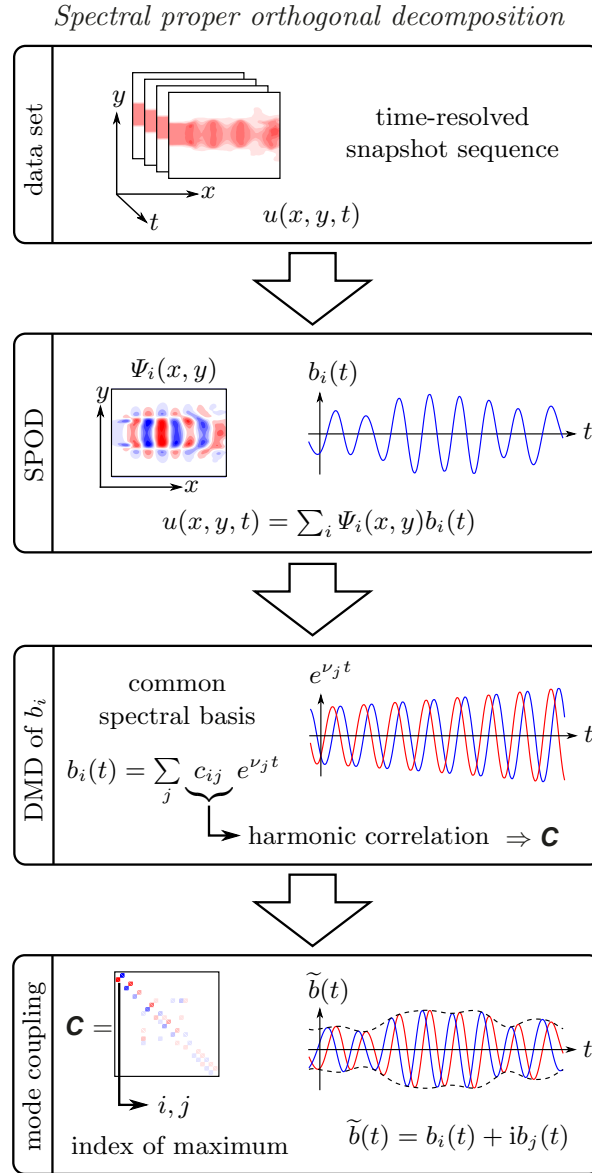


FIGURE 6. Schematic illustrating the main steps towards the identification of coupled modes (red and blue lines indicate real and imaginary parts of an analytic signal). The data displayed here were derived from measurements of a forced turbulent jet (see also figure 1).

It must be noted that this decomposition is only exact if  $N_c = N$ , whereas in the current approach  $N_c < N$ . Nevertheless, the decomposition gives a common spectral basis, which allows the ranking of spectral similarity of the temporal coefficients  $\mathbf{b}(t)$ . The developed proximity measure is given by

$$C_{i,j} = \text{Im} \left\{ \sum_{k=1}^{N_c} c_{k,i} c_{k,j}^* \text{sgn}(\text{Im}(\nu_k)) \right\}, \quad (2.21)$$

where  $*$  indicates the complex conjugate and the coefficients are normalized to  $(\mathbf{c}_i, \mathbf{c}_i) = 1$ . The sign function (sgn) in this expression accounts for the conjugate pairs that appear in the DMD spectrum (mirrored at the real axis).

For two modes to be coupled, they must have a similar spectral content, which is either shifted a quarter period forward or backward. This implies a positive or negative

imaginary part of the harmonic correlation (2.21), respectively, and coupled modes appear as peaks in the matrix  $\mathbf{C}$ . Hence, the row and column indices of the maximum of  $\mathbf{C}$  identify the first coupled SPOD modes. The corresponding row and column in  $\mathbf{C}$  are then set to zero and the next lower maximum is identified. This procedure is repeated until all modes are paired. It has to be noted that this approach also creates weakly correlated and possibly unphysical mode pairs.

Together with the identification of coupled modes, the procedure gives an average frequency of the coherent structure represented by the mode pair. Therefore, the eigenvalues  $\nu_k$  of the matrix  $\mathbf{T}$  are sorted in descending order with respect to their content for the identified mode pair  $\tilde{c}_k = c_{k,i}^2 + c_{k,j}^2$ . The frequency is given as the weighted sum of the eigenvalues

$$f = \frac{\sum_{i=1}^n \text{Im}\{\ln(\nu_i)\} \tilde{c}_i}{2\pi\Delta t \sum_{i=1}^n \tilde{c}_i}. \quad (2.22)$$

The weighting accounts for the relative energy content of a mode pair with respect to the single frequencies. In fact, only the most relevant eigenvalue ( $n = 1$ ) can be picked to determine the frequency, but for practical application it is recommended to use more than one eigenvalue as noise may corrupt them. For the examples discussed in the next chapter, we used an average over three eigenvalues ( $n = 3$ ) to get accurate results.

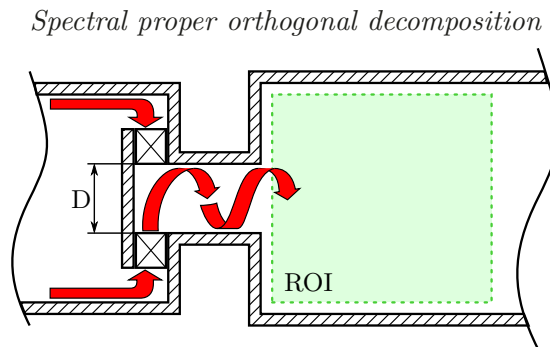
The coupled SPOD modes are considered as *one* complex mode (see equation (2.15) and figure 6) similar to the Fourier mode. The relative energy content of the identified modes is computed as

$$K = \frac{\mu_i + \mu_j}{\sum_{k=1}^{N_c} \mu_k}, \quad (2.23)$$

where  $i$  and  $j$  again refer to the indices of the coupled SPOD modes.

### 3. Applications to experimental data

In this chapter the SPOD is applied to three different data sets. All three examples originate from very different engineering problems, demonstrating the capability and broad applicability of SPOD. We consider the flow of a swirl-stabilized combustor, the wake of an airfoil with Gurney flap, and the flow field of a sweeping jet generated with a fluidic oscillator. All three flows were recorded with the same PIV measurement system. It consists of a Photron Fastcam SA 1.1 high-speed camera (1Mpixel at 2.7kHz double frame) and a Quantronix Darwin Duo laser (30mJ at 1kHz). The PIV data were processed with PIVview (PIVTEC GmbH) using standard digital PIV processing (Willert & Gharib 1991) enhanced by iterative multigrid interrogation (Soria 1996) with image deformation (Huang *et al.* 1993), (Raffel *et al.* 2007, pp. 146-158). Analyzing the present data sets with existing POD, DFT or DMD approaches caused some difficulties. As will be demonstrated, the SPOD is able to handle these shortcomings. The DMD and the DFT equally suffer from the restriction of the modes to narrow frequency bands, therefore we limit the following presentation to DFT. This choice is particularly handy as the DFT is a limiting case of the SPOD. We also performed DMD of the data presented here, where we found all DMD eigenvalues to lie in close proximity of the unit circle (distance  $< 10^{-6}$ ). This indicates that the DMD is nearly equivalent to the DFT. Rowley *et al.* (2009) stated that a DMD is identical to a DFT for periodic time-series, but from our observations it appears as if they are also almost identical for statistically stationary time-series. This supposition is based on the fact that none of the analyzed series is entirely periodic, but all are statistically stationary.



13

FIGURE 7. Experimental setup of the swirl stabilized combustor. Air enters from the left, passes a swirl generator and exits into the combustion chamber. Flow field measurements with PIV are conducted in the meridional plane as indicated by dashed square (ROI).

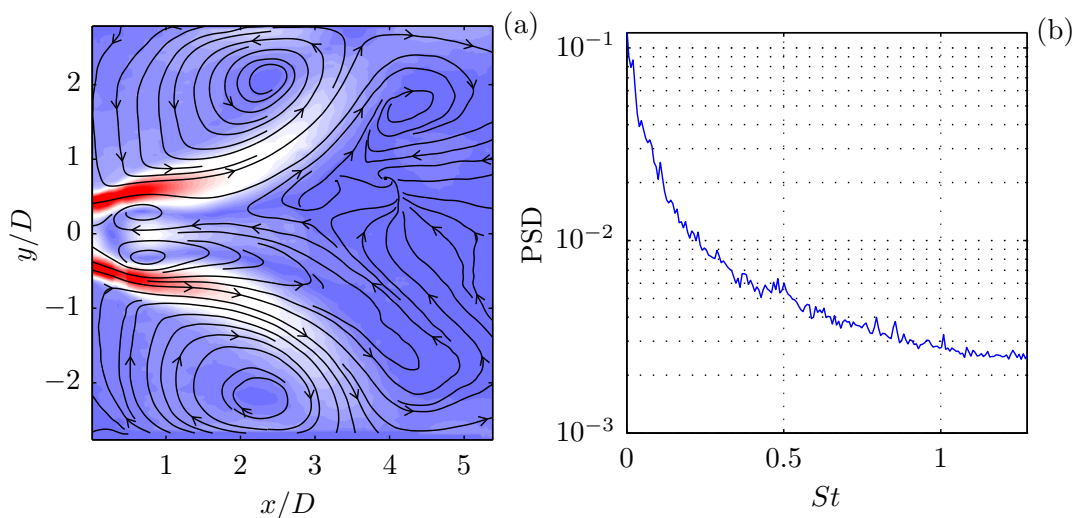


FIGURE 8. Swirl-stabilized combustor flow: Time-averaged flow field depicted by (a) contours of velocity magnitude and streamlines, and (b) spatially-averaged power spectral density.

### 3.1. Swirling jet undergoing vortex breakdown

At first, we consider the flow field of a swirl-stabilized combustor. Swirling jets are widely used in the gas turbine industry due to their capability of obstacle-free flame anchoring and enhanced mixing. The experimental setup to study these flows is sketched in figure 7. Swirl is generated by injecting fluid tangentially into a mixing tube that terminates in the combustion chamber. The cylindrical-shaped chamber is made of quartz glass to allow optical access for PIV. Flow measurements are conducted in the meridional section as indicated in the schematic. The case investigated here is non-reacting at a Reynolds number of 58 000 based on the nozzle diameter  $D$  and the bulk velocity at the nozzle exit. Additional details about the experimental setup can be found in Reichel *et al.* (2015).

The mean flow field and the spatially-averaged power spectral density (PSD) is depicted in figure 8, with the Strouhal number based on the same length and velocity scale as the Reynolds number ( $St = fD/u_{\text{bulk}}$ ). The flow exhibits a strong recirculation zone in the center, surrounded by an annular, strongly diverging jet. The cross-sectional jump at the combustion entrance creates an additional external recirculation zone between the jet and the confining walls. The spectral content of the flow is spread over all time scales and it decreases with increasing Strouhal number. The spectrum gives no indication of

any dominant coherent structure even though these flows typically feature helical global modes (Oberleithner *et al.* 2011).

Figure 9 (a), (b), and (c) illustrate the results from the SPOD for the filter lengths  $N_f = 0, 10, \text{ and } 2000$ , respectively. Note that the limiting cases  $N_f = 0$  and  $N_f = 2000$  produce results equivalent to those obtained with classical POD and DFT respectively, while the case in between represents the SPOD. Hence, this particular presentation concisely demonstrates the difference between POD, SPOD and DFT.

Each of the three cases in figure 9 show the so-called SPOD spectrum, where every mode pair is represented by a single dot. The size and color of the dots indicate the harmonic correlation of a mode pair  $C_{i,j}$ , according to equation (2.21). The frequency of a mode pair is determined according to (2.22) and the energy from the two eigenvalues relative to the total energy from (2.23). On the right side of every case in figure 9, three spatial modes  $\Psi_i(\mathbf{x})$  and the corresponding temporal coefficients  $b_i(t)$  are posed above each other. The spatial modes are visualized by the crosswise velocity component (in  $y$ -direction) together with streamlines of the time-averaged flow. They are numbered likewise in the SPOD spectrum and between the small mode plots. The plots are given without axis labels to allow a compact representation of the data, the section is the same as for the mean flow shown in figure 8(b). The time coefficients are represented by their power spectral density, where the time series is split into five (50% overlapping) sections, which are Fourier transformed and averaged. The horizontal dotted lines in the PSD plots indicate a spacing of three orders of magnitude ( $10^3$ ) and the  $y$ -axis is scaled logarithmically. The spectral averaging was also applied for the power spectra shown in figure 8(b) and in the subsequent PSD plots.

The POD (figure 9(a)) yields a broad spectrum of modes, where modes at lower Strouhal numbers have more energy. There are several modes with high harmonic correlation (diameter and color of the points), and high energy contents  $K$ . The spatial shape of the low-frequency mode (label 1) shows clear spatial symmetry and a limited spectral bandwidth ( $St \approx 0.1$ ). This mode is frequently observed in swirl-stabilized combustors and it is associated with a global hydrodynamic instability (Terhaar *et al.* 2015). From the four additional outstanding modes between  $St = 0.3$  and  $St = 0.8$ , we choose two for further investigation. Their spatial structures cannot be precisely assigned to a symmetric or anti-symmetric mode and they indicate mixtures of several spatial wavelengths. Accordingly, the mode spectra are broad and show only a slight hump at the frequencies indicated by the SPOD spectrum. The other modes around  $St = 0.5$ , which are not shown here, show similar spatial and spectral content.

Overall, the POD indicates the presence of a single mode at low frequency, together with other coherent structures that are not properly resolved. The most energetic mode (not inspected here) corresponds to a low frequency, large wavelength fluctuation, as indicated by the SPOD. Such slow changes of the mean flow are usually named shift modes (Luchtenburg *et al.* 2009; Hosseini *et al.* 2015). In this particular case the shift mode stems from weak movements of the vortex breakdown bubble.

Consider now the SPOD in figure 9(b), with a filter length  $N_f = 10$ ; From the SPOD spectra we identify three peaks at  $St = 0.09, 0.5$  and  $0.8$ . The first mode is the same as the one already identified by the POD, but its spectral content at higher frequencies is reduced. It describes a single-helical structure in the wake of the recirculation zone. The second identified mode exhibits a broad spectral peak at  $St = 0.5$ . Its spatial structure and Strouhal number match the global mode identified by Oberleithner *et al.* (2011). It is a single-helical mode linked to the precessing motion of the recirculation zone. The spatial structure of mode three suggests a double-helical shape. It is not a harmonic of the second mode, as their frequencies are not related.

## Spectral proper orthogonal decomposition

15

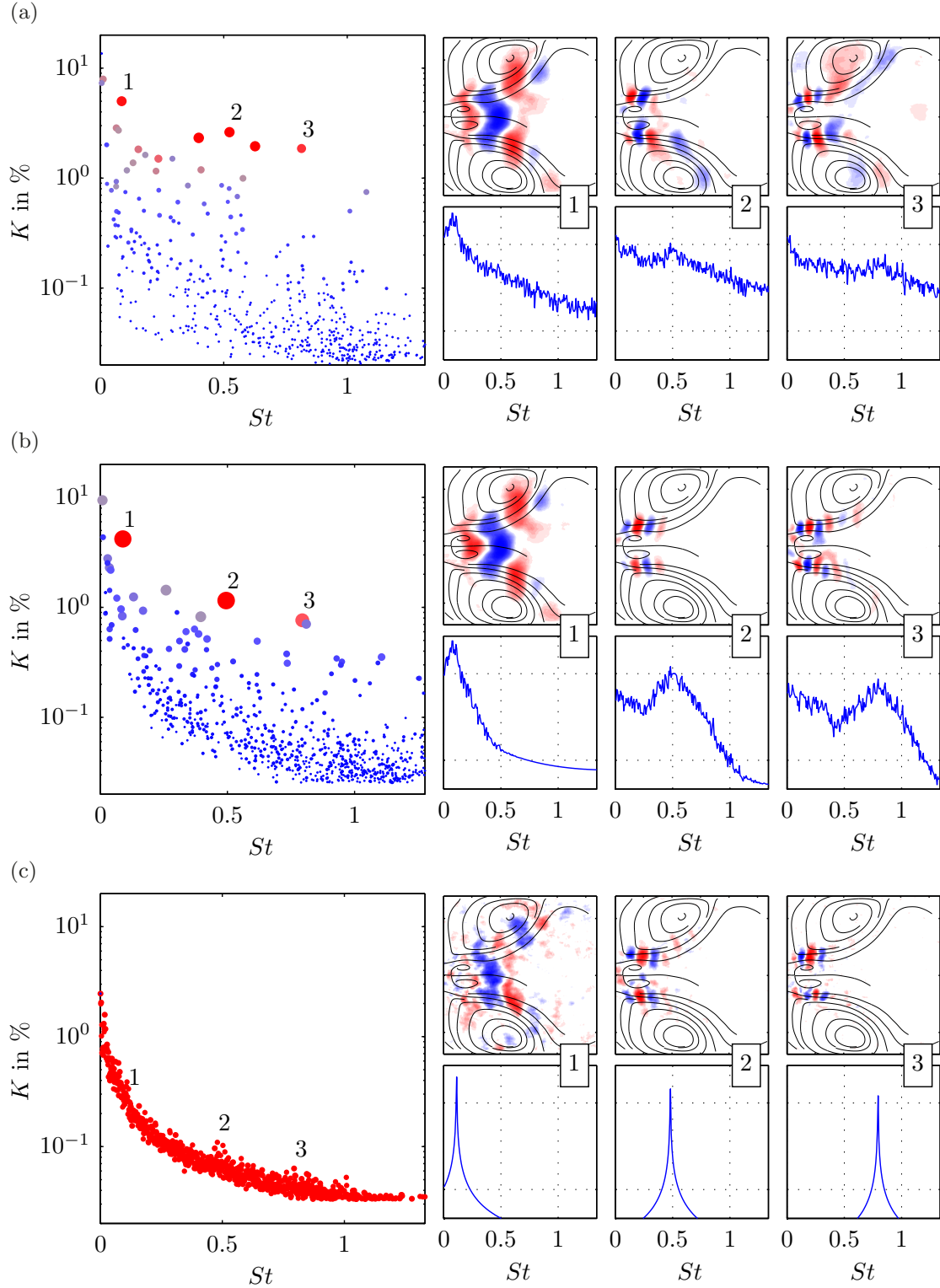


FIGURE 9. Swirling jet: Results from SPOD for different filter lengths (a)  $N_f = 0$  (POD), (b)  $N_f = 10$  (SPOD), and (c)  $N_f = 2000$  (DFT). For every filter length the SPOD spectrum is displayed as scatter plot (left), where a single dot indicates one mode pair (size and color  $C_{i,j}$  in (2.21)). For three selected pairs the spatial modes (upper row) and PSD of the temporal coefficient (lower row) are depicted. They are indicated by numbers in the SPOD spectrum, as well as between the small mode plots.

When the filter size is extended to its maximum, we get the the DFT (figure 9(c)) and the SPOD spectrum converges to the spatially-averaged PSD (figure 8(b)). The temporal coefficients converge to sines and cosines and all mode pairs show full harmonic correlation (uniform dot size in the SPOD spectrum). Since the selection based on harmonic correlation is impossible, we resort to the frequencies already known from the SPOD at  $N_f = 10$ . The spatial structures resemble the ones from figure 9(b), but they are corrupted by noise. Moreover, the spatial symmetries are no longer as clear as for the  $N_f = 10$  case. Note that the corresponding spectral peaks are broadened due to the averaging procedure, which is applied here only for consistency.

From this first example, we can point out some striking features of the SPOD. The SPOD is able to separate coherent fluctuation from stochastic turbulent fluctuations even though they both have the same energy contents (see the SPOD spectrum in figure 9(c)). The classical POD yields partially mixed structures that cannot be assigned to distinct flow phenomena, whereas the SPOD properly separates these structures and identifies them from harmonic correlations. The DFT instead shows the same structures at the identified frequencies, but they are corrupted with noise and the method itself would give no clue about the frequencies of interest.

The structures identified with the SPOD may also be found with the POD if the decomposition is applied to a subsection of the measured domain. Moreover, the exploitation of spatial symmetries prior to the POD decomposition usually provides good results for this type of flows (Terhaar 2015). Nevertheless, these alternative approaches would require prior knowledge of the shape or spatial extent of the structures, whereas the SPOD requires none of these.

All modes identified by the SPOD show clear spatial symmetries and distinct spectral peaks. The frequency and shape of the first mode coincide well with previous experimental observations in swirl-stabilized combustors (Terhaar *et al.* 2015). The second mode is very similar to the one observed in unconfined swirling jets (Oberleithner *et al.* 2011). However, the presence of these different modes in a single flow configuration raises the question about their physical relevance. To deal with this issue, we conducted a linear stability analysis of the underlying mean flow, following the procedure outlined by Oberleithner *et al.* (2015). This analysis similarly delivered three unstable modes whose frequencies and azimuthal and axial wavenumbers match the SPOD modes surprisingly well. To limit the scope of this paper the analysis is not further detailed here. One important parameter of the SPOD is the filter size  $N_f$ , which is twice the period of the second mode. The experiences gained throughout the first application show that a filter size of one to two periods of the mode of interest gives the best results.

### 3.2. Airfoil with Gurney flap

The second flow configuration considered here is the flow behind a pitched airfoil equipped with a Gurney flap. The experimental setup is shown in figure 10. It illustrates the working principle of the Gurney flap deployed at the pressure side of the airfoil. The flap creates additional lift (and drag), which can be used to locally control varying loads on large wind turbine airfoils (Bach *et al.* 2015a, 2014). The flow features around the Gurney flap are characterized by a single vortex that develops upstream of the flap and periodic shedding in its wake. The vortex upstream of the flap continuously grows up to a critical size, then it is shed into the wake, and it starts growing again. Here, a FX 63-137 airfoil at  $5^\circ$  angle of attack is investigated at a Reynolds number of 180 000 based on chord length. The reference length for the Strouhal number is the flap height, which is 3.6% of the chord. The measured region comprises only the wake of the airfoil capturing the dominant vortex shedding. More details about the experimental setup can be found

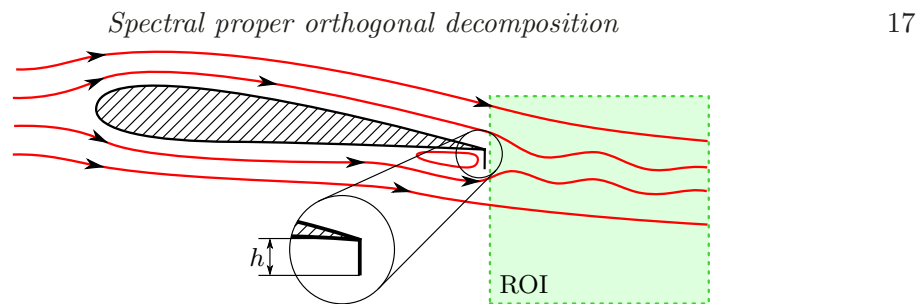


FIGURE 10. Schematic of the airfoil equipped with a Gurney flap at the trailing edge. Streamlines indicate the surrounding flow and the vortex upstream of the flap. The measured section (ROI) is a streamwise cut in the wake of the airfoil, capturing the periodic shedding behind the flap.

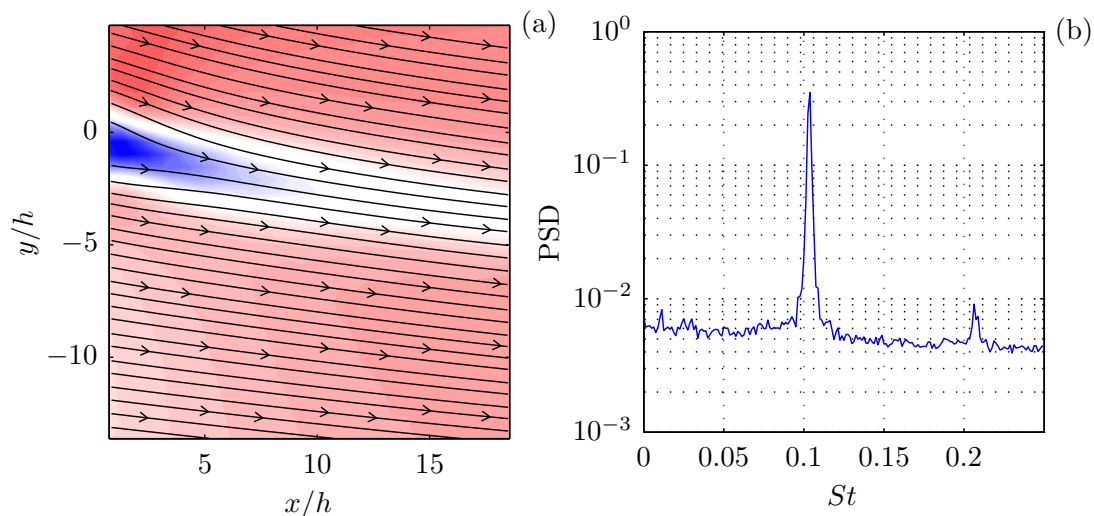


FIGURE 11. Wake of the airfoil with Gurney flap: Time-averaged flow field depicted by (a) contours of velocity magnitude and streamlines, and (b) spatially-averaged power spectral density. The origin of the coordinate system is located at the trailing edge.

in a preceding publication of these data (Bach *et al.* 2015b). The Strouhal number in the following results is calculated with the flap height  $h$  and the free stream velocity.

The mean flow shown in figure 11(a) reveals a velocity deficit in the wake of the Gurney flap, which generates the vortex shedding. The PSD (figure 11(b)) indicates strong oscillations at  $St = 0.105$  with a weak higher harmonic. In a previous investigation it was found that the vortex, which is shed from upstream of the flap causes an alteration of the periodic vortex shedding behind the flap (Troolin *et al.* 2006). Hot-wire measurements in the wake of the Gurney flap supported this assumption. The combination of a strong periodic flow pattern and the intermittent short-time events provides a formidable benchmark for the SPOD.

The presentation of the decomposition with the different methods is organized in the same way as for the previous example. The classic POD decomposition is shown in figure 12(a). The vortex shedding is represented by the most energetic POD mode with the highest harmonic correlation. The remaining modes show weak harmonic correlations and no distinct peak in the SPOD spectrum. The modes labeled 2 and 3 exhibit a broad spectral content with a spatial extent limited to the vicinity of the flap. There are additional modes with similarly compact spatial extent located further downstream. These compact modes describe the intermittent alteration of the vortex shedding during the passage of the single vortex that was generated upstream of the Gurney flap. An

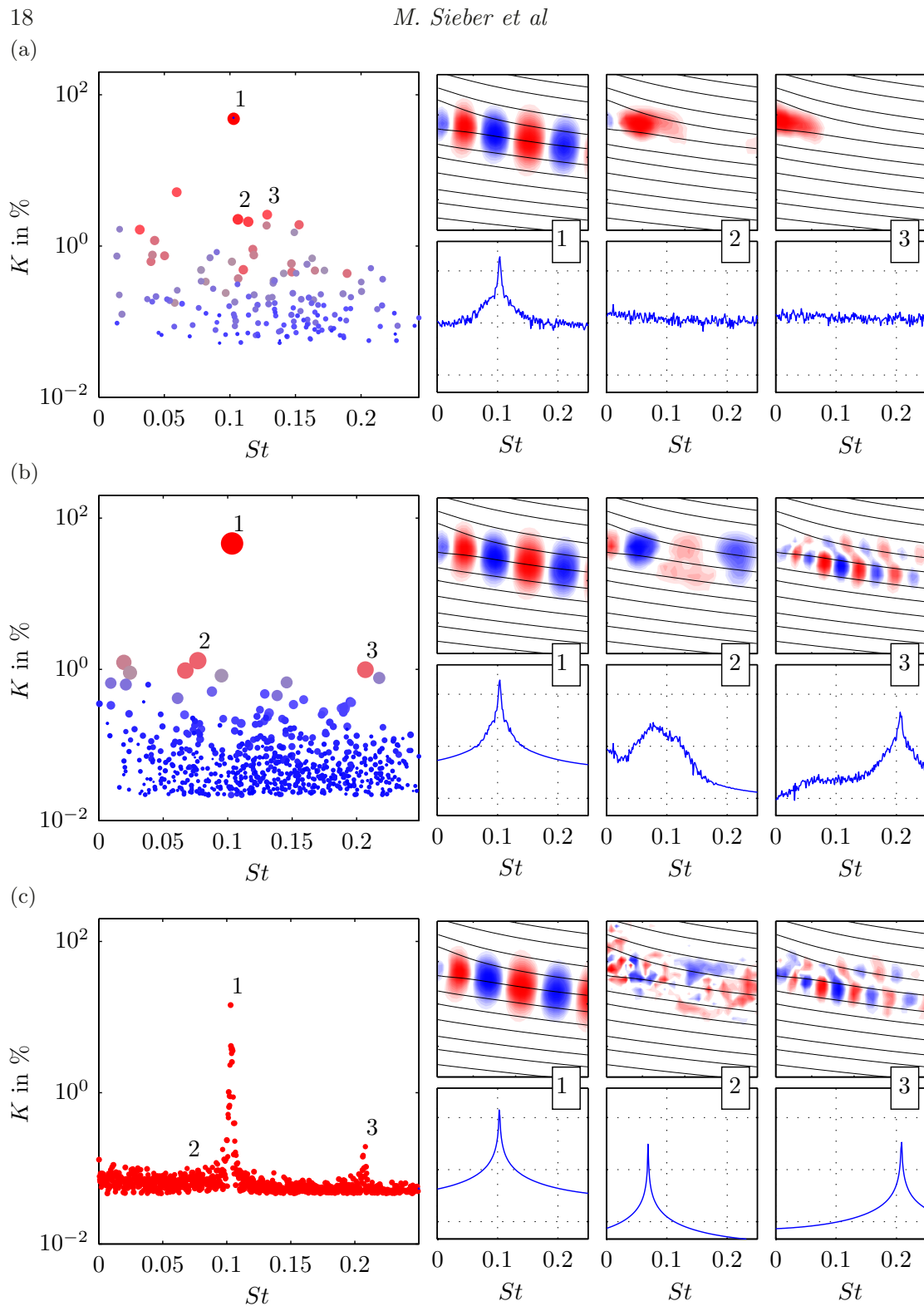


FIGURE 12. Airfoil with Gurney flap: Results from SPOD for different filter lengths (a)  $N_f = 0$  (POD), (b)  $N_f = 15$  (SPOD), and (c)  $N_f = 2000$  (DFT). For every filter length the SPOD spectrum is displayed as scatter plot (left), where a single dot indicates one mode pair (size and color  $C_{i,j}$  in (2.21)). For three selected pairs the spatial modes (upper row) and PSD of the temporal coefficient (lower row) are depicted. They are indicated by numbers in the SPOD spectrum, as well as between the small mode plots.

inspection of their time coefficients (not shown) reveals that these modes are only active one after another during one shedding period. Depending on the phase lag between the natural oscillation and the shedding of the upstream vortex, the developing wake vortex is either strengthened or weakened. The convection of this altered vortex is described by a spatial series of modes. The modes 2 and 3 represent only the upstream part of this convection, while the additional modes located further downstream (not shown) describe the subsequent motion. This behavior is indicated by a complex interaction of these modes and the periodic shedding modes, which is hard to identify in the POD expansion.

The SPOD yields a much clearer set of modes (figure 12(b)). In addition to the shedding mode, the SPOD also uncovers three other modes, which are offset from the rest. The two modes that appear at similar frequencies capture the alteration of the vortex shedding during the passage of the single vortex. Their mode shape is similar to the shedding mode, but with larger spatial wavelengths and lower frequencies (see mode 2 in figure 12(b)). The interaction of the upstream vortex with the vortex shedding increases the vortex size and thus the wavelength in the wake. Assuming a constant convection speed in the flow, this mode consequently has a lower frequency. In case of the SPOD the alteration of the vortex shedding is captured by a single mode (pair) and is thus much easier to interpret. The third mode represents the second harmonic of the vortex shedding with a clear spectral peak and clean spatial mode with twice the wavelength of the shedding mode. This higher harmonic is completely missed in the POD. The SPOD filter size  $N_f$  is equivalent to three shedding periods, which is approximately equal to the traveling time through the measurement domain.

The DFT shown in figure 12(c) reproduces the spectrum shown in figure 11(b). The natural mode and its higher harmonic can be identified from the spectral peaks. The corresponding mode shapes are similar to the SPOD, although the higher harmonic is corrupted with noise, resulting in a fragmented spatial mode. The DFT at the frequency of the second SPOD mode gives no indication of the structure identified before and the vortex-vortex interaction is completely missed. This is attributed to the fact that this phenomenon is highly intermittent with varying frequencies and amplitudes, which cannot be represented by a single-frequency mode. The same dilemma applies for the DMD.

For this example, the SPOD has shown its ability to separate dynamics with similar spatial structures and frequencies but very different energies. The spectral proximity and spatial similarity of the involved dynamics impede the application of POD. The modulation of the natural vortex shedding is represented by a natural mode with several intermittent modes. The DFT, however, with its single frequency modes does not capture the modulation of the shedding at all. The frequency constraint imposed by the SPOD is sharp enough to split the natural shedding from the modulation and soft enough to allow for frequency and amplitude variations. Hence the SPOD again gives easy access to dynamic features of the flow, which cannot be found with other common methods of similar algorithmic complexity. There may be feature tracking approaches capable of identifying the dynamics in this case, but they usually require more computational effort and might not be as versatile as the SPOD.

### 3.3. Fluidic oscillator

In this example, SPOD is applied to the flow field of the sweeping jet generated from a fluidic oscillator. This device is essentially a nozzle with feedback channels, which cause a self-sustained oscillation of the jet. Figure 13 shows the approximate geometry of this device and indicates the meandering shape of the sweeping jet. The shape and

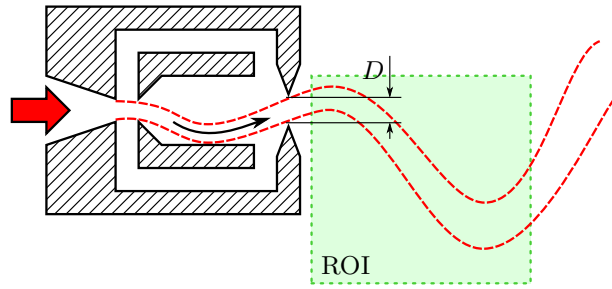


FIGURE 13. Schematic of the experimental setup with the fluidic oscillator. Air enters from the left, passes the oscillator and exits into the unconfined ambient air. The angle of the jet leaving the oscillator sweeps periodically up and down. The measured region (ROI) captures the meridional plane of the jet's near field. The oscillator has a square nozzle, hence the thickness of the jet normal to the plane is also  $D$ .

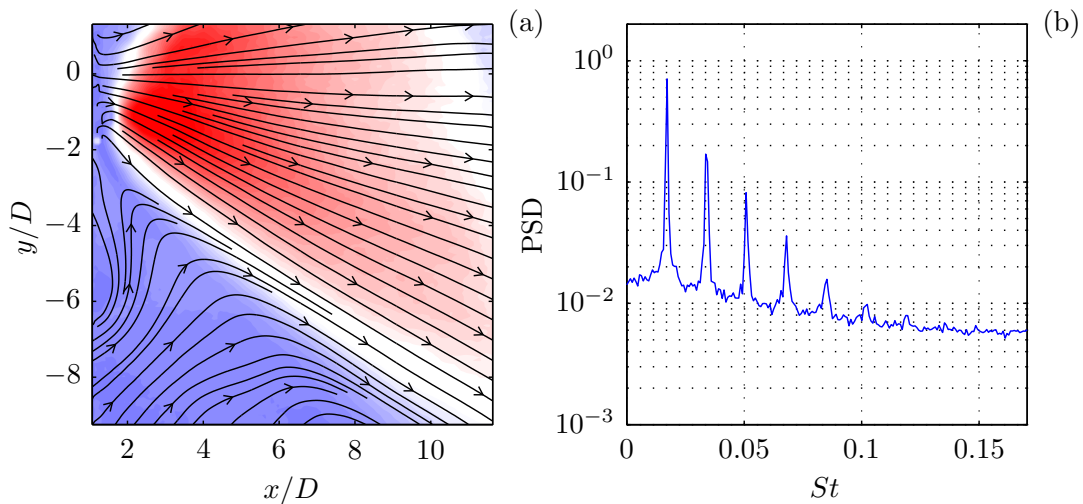


FIGURE 14. Fluidic oscillator: Time-averaged flow field depicted by (a) contours of velocity magnitude and streamlines, and (b) spatially-averaged power spectral density.

motion of the jet resemble a traveling wave. These devices are used for active flow control applications, where the sweeping motion of the jet allows a much wider actuator spacing resulting in less energy consumption (Woszidlo *et al.* 2014). The data presented here stem from an experimental setup investigating the spreading and entrainment of sweeping jets (Woszidlo *et al.* 2015; Ostermann *et al.* 2015b). The data are recorded at a Reynolds number of 37 000 based on the nozzle diameter  $D$  and the mean velocity in the nozzle. These scales are also used for later calculation of the Strouhal number. The mean velocity in figure 14(a) show that the PIV domain is moved off the jet center towards the lower half of the jet. Data points closer than  $x/D = 2$  were distorted due to laser light reflections. The spectral content averaged over the PIV domain (figure 14(b)) shows a narrow dominant peak and at least five higher harmonics. The narrow peaks indicate a stable operation at the fundamental frequency, while the additional peaks suggest more complex dynamics. The key challenge of this data set is to accurately reconstruct the sweeping jet dynamics from a truncated measurement domain.

Figure 15 shows the results from the SPOD for filter lengths  $N_f = 0, 30, \text{ and } 2000$ . As in the foregoing examples, these filter setting span the range between both limiting cases (from the POD to the DFT). The spectrum attained with the POD (figure 15(a)) reveals distinct modes at the fundamental frequency of the oscillator (labeled as 1) and

## Spectral proper orthogonal decomposition

21

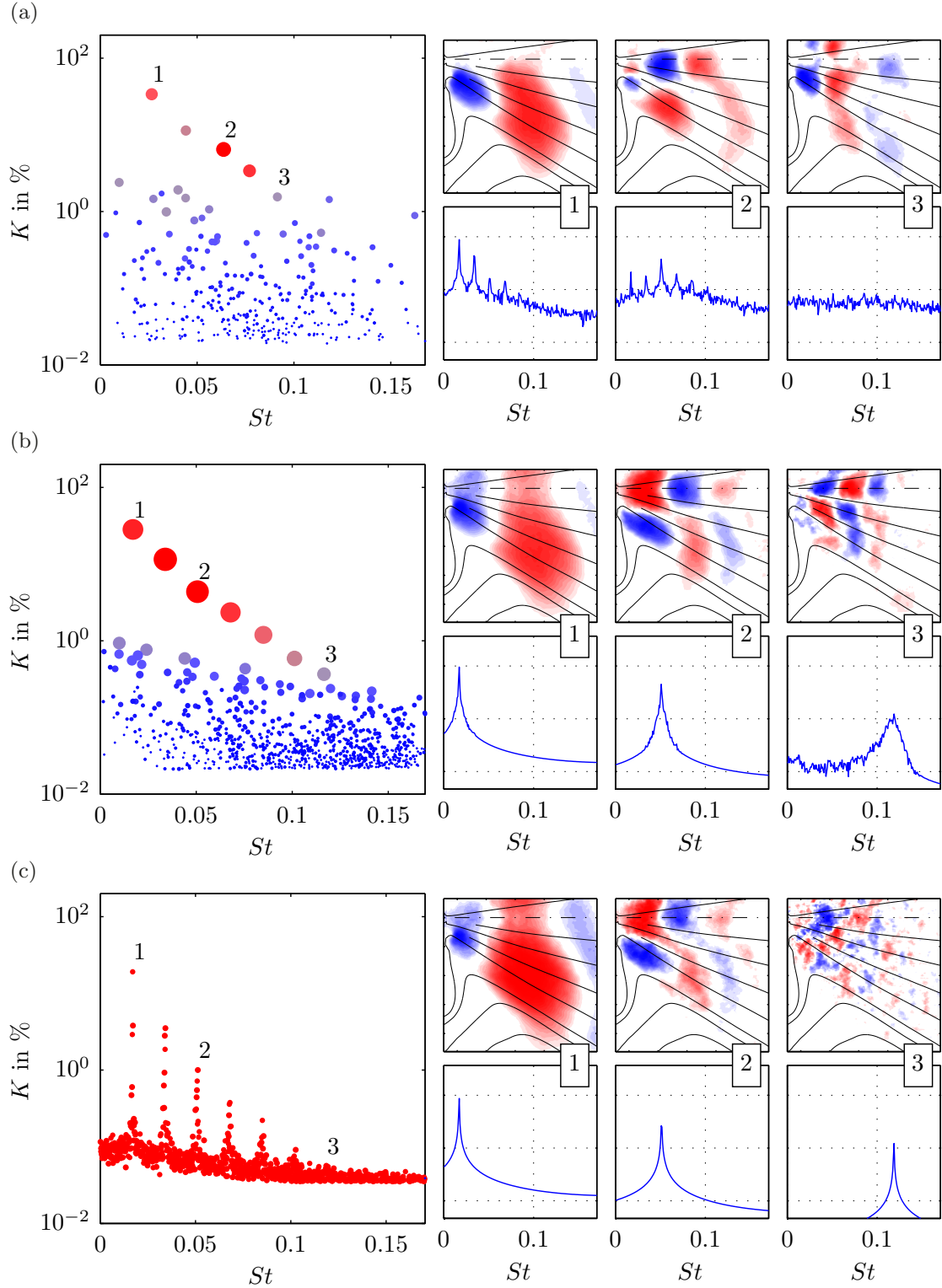


FIGURE 15. Fluidic oscillator: Results from SPOD for different filter lengths (a)  $N_f = 0$  (POD), (b)  $N_f = 30$  (SPOD), and (c)  $N_f = 2000$  (DFT). For every filter length the SPOD spectrum is displayed as scatter plot (left), where a single dot indicates one mode pair (size and color  $C_{i,j}$  in (2.21)). For three selected pairs the spatial modes (upper row) and PSD of the temporal coefficient (lower row) are depicted. They are indicated by numbers in the SPOD spectrum, as well as between the small mode plots. The centerline of is indicated by a dash dotted line.

at higher harmonics. The mode at the third harmonic frequency (labeled as 2) shows a surprisingly high harmonic correlation. The PSD of the mode coefficients reveal that each mode is not limited to a single frequency. The additional peaks in the PSD are partly attributed to the fact that only part of the jet is measured. During one oscillation period, the jet leaves and enters the measurement domain, creating sharp transitions in the time domain and thus a series of higher harmonics in the frequency domain. Due to the purely statistical POD approach, these higher harmonics appear in every mode coefficient, which contradicts the idea of a proper modal decomposition. The mode that seems to represent the fifth harmonic in the SPOD spectrum (labeled as 3) shows no distinct peak at all in the PSD of the coefficient. Thus, the POD of this data set does not provide a proper separation of the fundamental and higher harmonic contributions.

If the SPOD is applied instead, the fundamental and harmonic modes line up perfectly (figure 15(b)). Now, the harmonics are separated clearly up to the seventh harmonic. The spectral content and spatial shape are further examined for the fundamental, the third and seventh harmonic. The PSDs of the mode coefficients reveal narrow spectral bands. The corresponding mode shapes show an appropriate spatial symmetry, although the PIV domain is cropped shortly above the symmetry line. It is worth mentioning that the broad peak in the PSD of the seventh harmonic indicates considerable frequency jitter, while the mode shape remains remarkably smooth and symmetric.

The results obtained with the DFT are presented in figure 15(c). The peaks in the SPOD spectrum clearly indicate the fundamental and the first five higher harmonics. Their spatial shapes agree well with the SPOD modes, which is not surprising as these modes have narrow spectral bands. Note however that each peak is split into several DFT modes, which indicates slight frequency variation. This becomes crucial for the higher harmonics, where the frequency jitter is significant and the mode energy is low. For the seventh harmonic, the DFT fails to reproduce the structure seen in the SPOD (figure 15(b)). The frequency variations detected by the SPOD are simply too high and the mono-frequent energy content too low. This emphasizes the superior noise rejection of the SPOD.

In this example, the SPOD is superior to the POD and the DFT. The energy-ranked POD modes primarily suffer from the incompleteness of the data set. This is of immense importance as the relevant domain size is rarely known prior to a set of experiments, or POD analysis. The frequency-sharp DFT is insensitive to the domain size, but it fails to reconstruct weak modes with substantial noise and frequency jitter. The soft frequency constraint of the SPOD filter operation combines the advantages of both methods and generates a clear mode space. The SPOD generates modes with distinct frequencies and mode shapes for modes even weaker than the overall noise level.

For the fluidic oscillator, the DFT modes are nearly as accurate as those derived with the SPOD. The advantages of the SPOD are more obvious for less mono-frequent flow dynamics (see the previous examples). However, an additional advantage of the SPOD against the DFT is that it provides a reliable estimate of the oscillatory phase by accounting for the frequency jitter. Similar approaches, which also produce satisfactory results for the current case are described by Ostermann *et al.* (2015a), but again, the scope of SPOD is beyond this particular application. Figure 16(a,b) shows the phase portraits (Lissajous figures) of the temporal coefficients of the two most energetic POD ( $\mathbf{a}_i$ ) and SPOD ( $\mathbf{b}_i$ ) modes, respectively. The trajectory of the POD coefficients does not follow a clear circle that would indicate the limit-cycle. It rather follows a third of a circle and then collapses at one point. The coefficient of the SPOD modes follows a clear circle and the instantaneous phase and instantaneous frequency can consistently be deduced. A comparison of the first mode coefficient from both methods is shown in figure

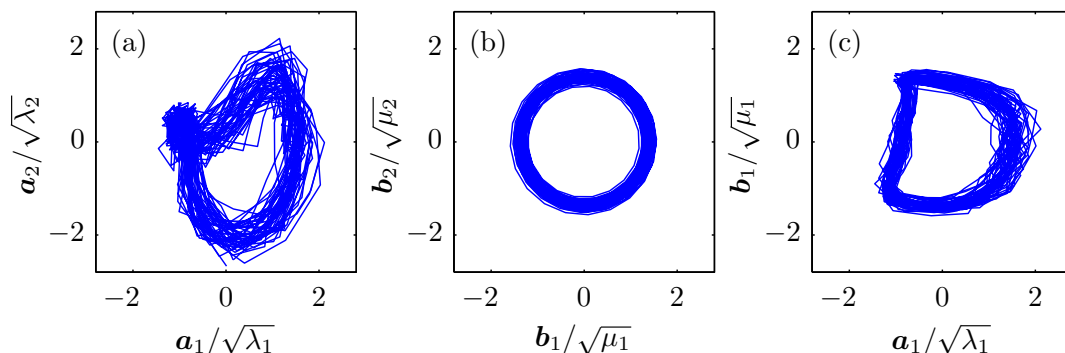


FIGURE 16. Phase portraits of first temporal coefficients from (a) POD, (b) SPOD, and (c) of both methods against each other.

16(c). It reveals that half of the period is cut out for the POD ( $\mathbf{a}_1$ ). This corresponds to the sweeping jet leaving the measurement domain, where the energy-based POD “sees” no jet. The SPOD properly recovers the temporal dynamics over the entire oscillation period. Furthermore, note that the SPOD produces coefficients with smooth temporal dynamics, while the POD coefficients show rather erratic movements. This is particularly important for reduced order modeling (Luchtenburg *et al.* 2009), phase averaging, and extended POD (Boree 2003). Practically, most of the further processing is eased if there is less noise.

## 4. Conclusions

### 4.1. Properties and capabilities of the proposed method

The SPOD is introduced as an extension of the POD for time-resolved data. This novel method involves a filter operation on the snapshot correlation matrix. The procedure is closely related to the classic snapshot POD with a negligible increase of algorithmic complexity and numerical costs. The SPOD filter allows for a continuous fading from the energetic optimality of POD to the spectral purity of DFT. It is conceptualized in a general form, with the POD and the DFT as the limiting cases. The concept of SPOD was developed through our experience with experimental data processing, and not from a constraint optimization problem. It arose from the desperate need for a method that applies to a wide range of turbulent flows at minimum user input. The SPOD is motivated based on theoretical considerations, where it is interpreted as a short time linearization of the flow dynamics.

The key feature of the SPOD is the smoothing along all diagonals of the correlation matrix. This filter operation is shown to constrain the amplitudes and frequencies of the SPOD modes. By setting the filter width, one gains control over the spectral bandwidth of the single modes. When the filter is set to the maximum length, the modes are assumed to be strictly periodic and the SPOD converges to the DFT.

The application of SPOD to the flow field of a swirl-stabilized combustor, an airfoil with Gurney flap and a fluidic oscillator revealed different advantageous features of the SPOD in comparison to POD or DFT. For every single case there exist other suitable methods, which may perform equally well as the SPOD, but none of them is as versatile as the proposed method.

The main advantages can be summarized as follows:

**Separation of structures:** The soft spectral constraint of the SPOD allows for a much better separation of individual fluid dynamic phenomena into single modes, whereas POD or DFT mix or spread them among several modes.

**Noise rejection:** SPOD is insensitive to noise and even recovers dynamics that are weaker than the overall noise level.

**Missing data compensation:** SPOD can eliminate the degradation of temporal dynamics of partially recorded phenomena, resulting from an improper choice of the measured region.

**Plain dynamics:** The mode coefficients are smooth in time and they feature adjustable variations of frequency and amplitude (set by the filter size).

The characteristics of the SPOD modes ease further processing such as the identification of linked modes, comparisons against other simultaneously acquired measurements (phase averaging or extended POD) and the identification of reduced order models. The SPOD may also provide a better basis for modal representation of snapshots as input for a DMD, as pursued in section 2.5.

#### 4.2. Concluding remarks

The SPOD has proven to be a reliable method to extract distinct phenomena from turbulent flows. It was not derived from purely mathematical considerations, but rather evolved from practical data processing. Nonetheless, the method has well defined upper and lower bounds and generates modes that can be easily interpreted. As shown in the considered examples, SPOD is a simple way to extract coherent structures from turbulent flows, where the POD or the DFT failed to provide valuable results. The SPOD constrains the spectral content, but retains the modal sparsity of the POD.

There are certainly plenty of other cases where this new method will ease the identification of hidden coherent structures. Its true benefit lies in the fact that only one assumption is made about the investigated flow dynamics, which is the filter timescale. This can also be understood as an inertia imposed on the mode dynamics, limiting the rate of change of the frequency and amplitude. The choice of this timescale can be assessed from the flow's dominant frequency or convective timescale, as shown in this article. The authors hope that the SPOD will give access to new fluid dynamical phenomena and enriches the available methods.

#### 4.3. Acknowledgment

The authors kindly acknowledge the stimulating discussions with Lothar Rukes and the generous provision of experimental data from Alena Bach and Florian Ostermann. The funding from the German Research Foundation (DFG Project PA 920/30-1) is also gratefully acknowledged.

## Appendix A. The spatial correlation version of SPOD

The original POD can either be calculated from a spatial or temporal correlation, which allows a computationally efficient calculation by restricting the size of the problem to the number of the snapshots or the number of grid points. Similarly, the SPOD has a spatial correlation counterpart, which is computationally more efficient if the number of snapshots is much larger than the number of grid points. This approach is slightly more

## Spectral proper orthogonal decomposition

25

complex and less intuitive than the snapshot version. Nevertheless, it is very valuable if long time series of few sensors are supposed to be decomposed into proper modes to perform an extended POD or to derive the phase of an oscillatory mode from the measurements. Assume a simultaneous multi point pressure measurement that shall be decomposed with SPOD. This series is decomposed as

$$P(x_i, t) = \bar{p}(x_i) + \sum_{s=1}^N b_s(t) \Psi_s(x_i), \quad (\text{A } 1)$$

where the number of measured positions  $M$  is much smaller than the number of samples  $N$ . The number of samples may easily reach a million or more, which complicates the solution in terms of memory requirements for the composition of the temporal correlation matrix and in terms of computational time for the solution of the eigenvalue problem. Therefore the temporal correlation described in section 2.3 is not feasible in this case. Instead, the spatial correlation should be employed, as outlined in this section. The multi time shift correlation tensor for the spatial SPOD reads

$$S_{i,j,k,l} = \frac{\sqrt{g_k g_l}}{MN \Delta t} \int p(x_i, t - k \Delta t) p(x_j, t - l \Delta t) dt \quad (\text{A } 2)$$

$$i, j = 1 \dots M ; k, l = -N_f \dots N_f,$$

where  $p = P - \bar{p}$  is the fluctuating part of the pressure and  $g_k$  are the filter coefficients. For numerical implementation this is reshaped to a matrix such that  $S_{i,j,k,l} = \tilde{S}_{(i+k*M), (j+l*M)}$ , but for the theoretical description the tensor notation is retained. The correlation tensor is decomposed in eigenvalues and eigenvectors, such that

$$\sum_{l=-N_f}^{N_f} \sum_{j=1}^M S_{i,j,k,l} \tilde{\Psi}_s(x_j, \tau_l) = \mu_s \tilde{\Psi}_s(x_i, \tau_k) ; \quad \mu_1 \geq \mu_2 \geq \dots \geq \mu_N \geq 0., \quad (\text{A } 3)$$

where  $\tau_k = k \Delta t$ . The eigenvector  $\tilde{\Psi}_s$  constitutes a discrete convolution filter, which is applied to the time series to obtain the mode coefficients

$$b_s(t) = \sum_{k=-N_f}^{N_f} \sum_{i=1}^M \sqrt{\frac{g_k}{M}} \tilde{\Psi}_s(x_i, \tau_k) p(x_i, t - \tau_k). \quad (\text{A } 4)$$

The spatial mode is the central part ( $\tau_k = 0$ ) of the convolution filter  $\Psi_s(x_i) = \tilde{\Psi}_s(x_i, 0)$ . The entire eigenvectors  $\tilde{\Psi}_s$  can be understood as a data driven filter bank, which allows for decomposition of time series into modal contributions. It might be applied to a single sensor, where each mode represents a certain spectral band of the signal. The principal approach is comparable to the empirical mode decomposition (Huang *et al.* 1998), but the SPOD can also handle multiple sensors. In case of multiple sensors, it gives excellent result when the phase of a dominant oscillation has to be reconstructed from pressure measurements. The approach outlined in this section is similar to the multi time delay POD phase estimation pursued by Hosseini *et al.* (2015).

In contrast to the snapshot version, the computational cost of the spatial version of SPOD scales with the filter size. It is only more efficient than the snapshot approach if  $M(2N_f + 1) < N$ .

## Appendix B. Properties of the SPOD modes

In section 2.3 it was shortly mentioned that the spatial SPOD modes are no longer orthogonal, which is only part of the truth. If the spatial mode  $\tilde{\Psi}$  (A 3) together with all of the temporally shifted instances is considered, they are orthonormal

$$\frac{1}{M} \sum_{l=-N_f}^{N_f} \sum_{k=1}^M \tilde{\Psi}_i(x_k, \tau_l) \tilde{\Psi}_j(x_k, \tau_l) = \delta_{i,j}. \quad (\text{B } 1)$$

The snapshot based calculation introduced in section 2.3, however, is restricted to the zero time delay ( $\tau = 0$ ) part of the spatial mode. Furthermore, the decomposition of the data into modal contributions is only feasible for time independent spatial modes. This limitation to one part of the the spatial mode  $\Psi_s(x_i) = \tilde{\Psi}_s(x_i, \tau = 0)$  introduces some imperfections. The selected modes for the decomposition are neither normal nor orthogonal

$$\frac{1}{M} \sum_{k=1}^M \Psi_i(x_k) \Psi_j(x_k) \neq \delta_{i,j}. \quad (\text{B } 2)$$

The loss of normality is a fact, whereas the norm of the spatial modes gives further insights to the data set. The norm

$$\zeta_i = \sqrt{\frac{1}{M} \sum_{k=1}^M \Psi_i^2(x_k)} \quad (\text{B } 3)$$

indicates how well a single mode is represented by the investigated data set.

With the application of the filter (2.9), an idealized correlation matrix is constructed that delivers modes, which are more or less captured by the initial data set. This fact is reflected by the deviation of the mode norm  $\zeta_i$  from one. Consider for example the measurement of the sweeping jet. There, the fundamental mode is only partially captured as shown in figure 16. With the SPOD, the missing data are completed and a SPOD mode pair with equal energy levels  $\mu_i$  is obtained. However, for the construction of the spatial modes the coefficients are projected onto the original data (2.12). There, the imperfect representation of one of the two modes re-enters the processing. For the sweeping jet's leading mode pair the norm  $\zeta_i$  of one mode is clearly below the other, but they approximately add up to one. Therefore, the eigenvalues  $\mu_i$  describe the idealized energy content of the single modes and the norm of the spatial mode  $\zeta_i$  corrects the deficits in comparison to the actual data set. The limiting SPOD cases (POD and DFT) do not show this deficits. The POD modes are already normalized  $\zeta_i = 1$  and for the DFT, the modes pair perfectly, while the norm of these pairs ( $i, j$ ) exactly add up to one ( $\zeta_i + \zeta_j = 1$ ).

## Appendix C. SPOD of linear dynamics

In this article a relation between the diagonal similarity of the correlation matrix and the dynamics of the underlying system is presumed but never discussed in detail. This section provides a better comprehension of the stated dynamics, which cause the diagonal similarity of the correlation matrix. Therefore, the term ‘‘similar dynamics’’ is replaced by ‘‘linear dynamics’’, whereby the temporal evolution of the investigated flow is locally governed by a linear, time invariant model. The term locally refers to a short and finite temporal extension, and it is closely related to the filter size  $N_f$ . The temporal evolution

of this system is given by

$$\frac{\partial \mathbf{u}(t)}{\partial t} = \mathbf{L}\mathbf{u}(t), \quad (\text{C1})$$

where the matrix  $\mathbf{L}$  is the system matrix describing the entire dynamics and the spatial points of the velocity field are organized as rows in  $\mathbf{u}(t) = [u(\mathbf{x}_1, t), \dots, u(\mathbf{x}_M, t)]^T$ . This approach may also be understood as the continuous time DMD. The linearized dynamics allow for the calculation of the velocity field at any time step from a reference snapshot  $\mathbf{u}_0 = \mathbf{u}(t=0)$  by the matrix exponential

$$\mathbf{u}(t) = e^{\mathbf{L}t}\mathbf{u}_0. \quad (\text{C2})$$

To allow further simplifications, we require the matrix  $\mathbf{L}$  to be normal. This allows for the decomposition  $\mathbf{L} = \mathbf{U}\mathbf{D}\mathbf{U}^*$ , where  $\mathbf{U}$  is a unitary matrix (eigenvectors of  $\mathbf{L}$ ),  $\mathbf{D}$  is a diagonal matrix (eigenvalues of  $\mathbf{L}$ ) and  $*$  means the conjugate transpose of a matrix (adjointed). Hereafter, equation (C2) becomes

$$\mathbf{u}(t) = e^{\mathbf{U}\mathbf{D}\mathbf{U}^*t}\mathbf{u}_0 = \mathbf{U}e^{\mathbf{D}t}\mathbf{U}^*\mathbf{u}_0. \quad (\text{C3})$$

The diagonal elements of the matrix  $\mathbf{D}$  contain the complex eigenvalues  $d_k$  of the system. Each of these eigenvalues contain the amplification rate  $\sigma$  and the frequency  $\omega$  of the related mode  $d_k = \sigma_k + i\omega_k$ . The diagonal matrix can be decomposed in amplification rate  $\mathbf{\Sigma}$  and frequency  $\mathbf{\Omega}$ , thus  $\mathbf{D} = \mathbf{\Sigma} + i\mathbf{\Omega}$ .

With the formulation in (C3), the inner product, which forms the elements of the correlation matrix, is simplified to

$$\begin{aligned} \langle u(\mathbf{x}, t_1), u(\mathbf{x}, t_2) \rangle &= \langle \mathbf{U}e^{\mathbf{D}t_1}\mathbf{U}^*\mathbf{u}_0, \mathbf{U}e^{\mathbf{D}t_2}\mathbf{U}^*\mathbf{u}_0 \rangle \\ &= \langle \mathbf{U}^*\mathbf{u}_0, e^{\mathbf{\Sigma}(t_1+t_2)+i\mathbf{\Omega}(t_2-t_1)}\mathbf{U}^*\mathbf{u}_0 \rangle. \end{aligned} \quad (\text{C4})$$

An inspection of the exponent in (C4) reveals that the inner product only depends on the sum and difference of time steps. According to this equation, the velocity fields are projected onto the subspace spanned by the linear operator  $\mathbf{U}^*\mathbf{u}_0$  and changes of the inner product are only governed by the eigenvalues of the system.

Within the context of the correlation matrix, we use the abbreviated nomenclature for the snapshots  $\mathbf{u}_i = \mathbf{u}(i\Delta t)$  and for the projected velocity  $\tilde{\mathbf{u}} = \mathbf{U}^*\mathbf{u}_0$ . The correlation matrix constructed around the neighborhood of snapshots  $\mathbf{u}_0$ , yields

$$\begin{aligned} \mathbf{S}_{\text{sub}} &= \begin{pmatrix} \langle \mathbf{u}_{-1}, \mathbf{u}_{-1} \rangle & \langle \mathbf{u}_0, \mathbf{u}_{-1} \rangle & \langle \mathbf{u}_1, \mathbf{u}_{-1} \rangle \\ \langle \mathbf{u}_{-1}, \mathbf{u}_0 \rangle & \langle \mathbf{u}_0, \mathbf{u}_0 \rangle & \langle \mathbf{u}_1, \mathbf{u}_0 \rangle \\ \langle \mathbf{u}_{-1}, \mathbf{u}_1 \rangle & \langle \mathbf{u}_0, \mathbf{u}_1 \rangle & \langle \mathbf{u}_1, \mathbf{u}_1 \rangle \end{pmatrix} \\ &= \begin{pmatrix} \langle \tilde{\mathbf{u}}, e^{-2\mathbf{\Sigma}\Delta t}\tilde{\mathbf{u}} \rangle & \langle \tilde{\mathbf{u}}, e^{-\mathbf{\Sigma}\Delta t-i\mathbf{\Omega}\Delta t}\tilde{\mathbf{u}} \rangle & \langle \tilde{\mathbf{u}}, e^{-2i\mathbf{\Omega}\Delta t}\tilde{\mathbf{u}} \rangle \\ \langle \tilde{\mathbf{u}}, e^{-\mathbf{\Sigma}\Delta t+i\mathbf{\Omega}\Delta t}\tilde{\mathbf{u}} \rangle & \langle \tilde{\mathbf{u}}, \tilde{\mathbf{u}} \rangle & \langle \tilde{\mathbf{u}}, e^{\mathbf{\Sigma}\Delta t-i\mathbf{\Omega}\Delta t}\tilde{\mathbf{u}} \rangle \\ \langle \tilde{\mathbf{u}}, e^{2i\mathbf{\Omega}\Delta t}\tilde{\mathbf{u}} \rangle & \langle \tilde{\mathbf{u}}, e^{\mathbf{\Sigma}\Delta t+i\mathbf{\Omega}\Delta t}\tilde{\mathbf{u}} \rangle & \langle \tilde{\mathbf{u}}, e^{2\mathbf{\Sigma}\Delta t}\tilde{\mathbf{u}} \rangle \end{pmatrix}. \end{aligned} \quad (\text{C5})$$

The actual properties of this complex expression are highlighted by showing just the factors for  $\mathbf{\Sigma}$  and  $i\mathbf{\Omega}$  in the exponents, given as

$$\mathbf{\Sigma} : \begin{bmatrix} -2 & -1 & 0 \\ -1 & 0 & 1 \\ 0 & 1 & 2 \end{bmatrix} \Delta t ; \quad i\mathbf{\Omega} : \begin{bmatrix} 0 & -1 & -2 \\ 1 & 0 & -1 \\ 2 & 1 & 0 \end{bmatrix} \Delta t. \quad (\text{C6})$$

It is perfectly visible that the changes of the correlation matrix along the diagonals are caused by amplification of modes, while changes along the anti-diagonals are caused by the modes' frequency. Therefore, the changes of the correlation matrix along the diagonal

are related to the modes amplitude and the crosswise changes are caused by the modes phase. The amplification rate can be assumed to be much smaller than the frequency, which allows a change in phase from a change in amplitude to be distinguished. Therefore, the correlation matrix generated by a linear system exhibits similar diagonals. Hence, a flow governed by linear dynamics shows the observed diagonal similarity in the correlation matrix.

If the amplification rate  $\sigma = 0$  and the frequency  $\omega = \text{constant}$ , a periodic oscillation with fixed amplitude is obtained. This constitutes the limiting DFT case, where the correlation matrix is perfectly constant along the diagonals. Thus, constant coefficients of the underlying system result in a perfectly diagonal matrix. In order to represent the variations in frequency and amplitude observed in the SPOD modes, the system parameters  $\sigma$  and  $\omega$  may change in time. These changes, however, will break the diagonal similarity of the correlation matrix. Therefore, the non-linearity and non-normality of the Navier-Stokes equations contribute to parameter variations of the linear system. The flow is assumed to behave like a linear normal system within the time scale of the filter and all non-linear and non-normal dynamics are represented by variations in  $\sigma$  and  $\omega$ . This kind of approach is also pursued in the generalized mean field model of Luchtenburg *et al.* (2009), where the mode interaction via the mean flow is represented by an interaction of linear oscillators through nonlinear coupling of model parameters. Hence, the SPOD filter might be understood as a smoothing (linearization) of the dynamics ( $\sigma \omega$ ) of the underlying system.

In this system dynamic framework, a relation between SPOD and DMD can be drawn. For the DMD the entire analyzed sequence is considered from the perspective of a linearized system. In the sense that a low-pass filter may also be described as a moving average, the SPOD may be understood as a moving DMD. The filter with  $N_f$  is the corresponding linearization horizon. Therefore, the eigenvalues of a short-term DMD may relate to the instantaneous dynamics ( $\sigma \omega$ ) of the SPOD modes.

## REFERENCES

- ADRIAN, R. J. & MOIN, P. 1988 Stochastic estimation of organized turbulent structure: homogeneous shear flow. *Journal of Fluid Mechanics* **190**, 531–559.
- BACH, A. B., BERG, R., PECHLIVANOGLU, G., NAYERI, C. & PASCHEREIT, C. O. 2015a Experimental Investigation of the Aerodynamic Lift Response of an Active Finite Gurney Flap. In *53rd AIAA Aerospace Sciences Meeting, AIAA SciTech*. American Institute of Aeronautics and Astronautics.
- BACH, A. B., LENNIE, M., PECHLIVANOGLU, G., NAYERI, C. N. & PASCHEREIT, C. O. 2014 Finite micro-tab system for load control on a wind turbine. *Journal of Physics: Conference Series* **524**, 012082.
- BACH, A. B., PECHLIVANOGLU, G., NAYERI, C. & PASCHEREIT, C. O. 2015b Wake Vortex Field of an Airfoil Equipped with an Active Finite Gurney Flap. In *53rd AIAA Aerospace Sciences Meeting, AIAA SciTech*. American Institute of Aeronautics and Astronautics.
- BERKOOZ, G., HOLMES, P. & LUMLEY, J. L. 1993 The Proper Orthogonal Decomposition in the Analysis of Turbulent Flows. *Annual Review of Fluid Mechanics* **25**, 539–575.
- BOREE, J. 2003 Extended proper orthogonal decomposition: a tool to analyse correlated events in turbulent flows. *Experiments in Fluids* **35** (2), 188–192.
- BOURGOIS, J. A., NOACK, B. R. & MARTINUZZI, R. J. 2013 Generalized phase average with applications to sensor-based flow estimation of the wall-mounted square cylinder wake. *Journal of Fluid Mechanics* **736**, 316–350.
- DURGESH, V. & NAUGHTON, J. W. 2010 Multi-time-delay LSE-POD complementary approach applied to unsteady high-Reynolds-number near wake flow. *Experiments in Fluids* **49** (3), 571–583.

- GRAY, R. M. 2005 Toeplitz and Circulant Matrices: A review. *Foundations and Trends in Communications and Information Theory* **2** (3), 155–239.
- HOLMES, P., LUMLEY, J. L., BERKOOZ, G. & ROWLEY, C. W. 2012 *Turbulence, Coherent Structures, Dynamical Systems and Symmetry*, 2nd edn. Cambridge and UK and New York: Cambridge University Press.
- HOSSEINI, Z., MARTINUZZI, R. J. & NOACK, B. R. 2015 Sensor-based estimation of the velocity in the wake of a low-aspect-ratio pyramid. *Experiments in Fluids* **56** (1).
- HUANG, H. T., FIEDLER, H. E. & WANG, J. J. 1993 Limitation and improvement of PIV: Part II: Particle image distortion, a novel technique. *Experiments in Fluids* **15** (4-5), 263–273.
- HUANG, N. E., SHEN, Z., LONG, S. R., WU, M. C., SHIH, H.H., ZHENG, Q., YEN, N.-C., TUNG, C. C. & LIU, H. H. 1998 The empirical mode decomposition and the hilbert spectrum for nonlinear and non-stationary time series analysis. *Proceedings of the Royal Society of London A: Mathematical, Physical and Engineering Sciences* **454** (1971), 903–995.
- LASAGNA, D., ORAZI, M. & IUSO, G. 2013 Multi-time delay, multi-point linear stochastic estimation of a cavity shear layer velocity from wall-pressure measurements. *Physics of Fluids* **25** (1), 017101.
- LUCHTENBURG, D. M., GÜNTHER, B., NOACK, B. R., KING, R. & TADMOR, G. 2009 A generalized mean-field model of the natural and high-frequency actuated flow around a high-lift configuration. *Journal of Fluid Mechanics* **623**, 283–316.
- LUMLEY, J. L. 1970 *Stochastic tools in turbulence, Applied mathematics and mechanics*, vol. v. 12. New York: Academic Press.
- OBERLEITHNER, K., RUKES, L. & SORIA, J. 2014 Mean flow stability analysis of oscillating jet experiments. *Journal of Fluid Mechanics* **757**, 1–32.
- OBERLEITHNER, K., SIEBER, M., NAYERI, C. N., PASCHEREIT, C. O., PETZ, C., HEGE, H.-C., NOACK, B. R. & WYGNANSKI, I. 2011 Three-dimensional coherent structures in a swirling jet undergoing vortex breakdown: stability analysis and empirical mode construction. *Journal of Fluid Mechanics* **679**, 383–414.
- OBERLEITHNER, K., STÖHR, M., SEONG, H. I., ARNDT, C. M. & STEINBERG, A. M. 2015 Formation and flame-induced suppression of the precessing vortex core in a swirl combustor: Experiments and linear stability analysis. *Combustion and Flame* **162** (8), 3100–3114.
- OSTERMANN, F., WOSZIDLO, R., GAERTLEIN, S., NAYERI, C. & PASCHEREIT, C. O. 2015a Phase-Averaging Methods for the Natural Flowfield of a Fluidic Oscillator. *AIAA Journal* **53** (8), 2359–2368.
- OSTERMANN, F., WOSZIDLO, R., NAYERI, C. & PASCHEREIT, C. O. 2015b Experimental Comparison between the Flow Field of Two Common Fluidic Oscillator Designs. In *53rd AIAA Aerospace Sciences Meeting, AIAA SciTech*. American Institute of Aeronautics and Astronautics.
- RAFFEL, M., KOMPENHANS, J., WERELEY, S. T. & WILLERT, C. E. 2007 *Particle image velocimetry: A practical guide*, 2nd edn. Heidelberg and New York: Springer.
- RAIOLA, M., DISCETTI, S. & IANIRO, A. 2015 On PIV random error minimization with optimal POD-based low-order reconstruction. *Experiments in Fluids* **56** (4).
- REICHEL, T. G., TERHAAR, S. & PASCHEREIT, O. 2015 Increasing Flashback Resistance in Lean Premixed Swirl-Stabilized Hydrogen Combustion by Axial Air Injection. *Journal of Engineering for Gas Turbines and Power* **137** (7), 071503.
- ROWLEY, C. W., MEZIC, I., BAGHERI, S., SCHLATTER, P. & HENNINGSON, D. S. 2009 Spectral analysis of nonlinear flows. *Journal of Fluid Mechanics* **641**, 115–127.
- SCHLEGEL, M., NOACK, B. R., JORDAN, P., DILLMANN, A., GRÖSCHEL, E., SCHRÖDER, W., WEI, M., FREUND, J. B., LEHMANN, O. & TADMOR, G. 2012 On least-order flow representations for aerodynamics and aeroacoustics. *Journal of Fluid Mechanics* **697**, 367–398.
- SCHMID, P. J. 2010 Dynamic mode decomposition of numerical and experimental data. *Journal of Fluid Mechanics* **656**, 5–28.
- SIROVICH, L. 1987 Turbulence and the dynamics of coherent structures: Part I: Coherent Structures. *Quarterly of Applied Mathematics* **45** (3), 561–571.
- SORIA, J. 1996 An investigation of the near wake of a circular cylinder using a video-based

- digital cross-correlation particle image velocimetry technique. *Experimental Thermal and Fluid Science* **12** (2), 221 – 233.
- TERHAAR, S. 2015 Identification and modeling of coherent structures in swirl stabilized combustors at dry and steam diluted conditions. PhD thesis, Technische Universität Berlin.
- TERHAAR, S., OBERLEITHNER, K. & PASCHEREIT, C. O. 2015 Key parameters governing the precessing vortex core in reacting flows: An experimental and analytical study. *Proceedings of the Combustion Institute* **35** (3), 3347–3354.
- TROOLIN, D. R., LONGMIRE, E. K. & LAI, W. T. 2006 Time resolved PIV analysis of flow over a NACA 0015 airfoil with Gurney flap. *Experiments in Fluids* **41** (2), 241–254.
- TU, J. H., ROWLEY, C. W., LUCHTENBURG, D. M., BRUNTON, S. L. & KUTZ, J. N. 2014 On dynamic mode decomposition: Theory and applications. *Journal of Computational Dynamics* **1** (2), 391–421.
- WILLERT, C. E. & GHARIB, M. 1991 Digital particle image velocimetry. *Experiments in Fluids* **10** (4).
- WILLIAMS, M. O., KEVREKIDIS, I. G. & ROWLEY, C. W. 2015 A Data-Driven Approximation of the Koopman Operator: Extending Dynamic Mode Decomposition. *Journal of Nonlinear Science* **25** (6), 1307–1346.
- WISE, J. 1955 The autocorrelation function and the spectral density function. *Biometrika* **42** (1-2), 151–159.
- WOSZIDLO, R., OSTERMANN, F., NAYERI, C. N. & PASCHEREIT, C. O. 2015 The time-resolved natural flow field of a fluidic oscillator. *Experiments in Fluids* **56** (6).
- WOSZIDLO, R., STUMPER, T., NAYERI, C. & PASCHEREIT, C. O. 2014 Experimental study on bluff body drag reduction with fluidic oscillators. In *52rd AIAA Aerospace Sciences Meeting, AIAA SciTech* . American Institute of Aeronautics and Astronautics.

## 3.2 Advanced Identification of Coherent Structures in Swirl-Stabilized Combustors

This article is published in an edited form in the Journal of Engineering for Gas Turbines and Power under the following reference: M. Sieber, C. O. Paschereit, & K. Oberleithner (2016b). “Advanced Identification of Coherent Structures in Swirl-Stabilized Combustors”. *Journal of Engineering for Gas Turbines and Power* 139.2, p. 021503. DOI: [10.1115/1.4034261](https://doi.org/10.1115/1.4034261). The following is the accepted manuscript of the article which is reprinted with permission of the American Society of Mechanical Engineers (ASME). This version is free to view and download for private research and study only. Not for re-distribution, re-sale or use in derivative works. ©2016 by ASME.

The publication shows an application example of the SPOD to reveal capabilities for the analysis of experimental data from combustion experiments.

**Methods:** The extended SPOD is presented in analogy to the extended POD that allows expanding additional measurements with the same expansion coefficients as the velocity data.

**Results:** High-speed PIV data from a swirl stabilised combustor with external forcing of an acoustic mode are analysed. The data originate from another project at the chair of fluid dynamics, which investigated the modelling of flame transfer functions. The SPOD allows an accurate separation of forced and natural flow dynamics without any external inputs. The interaction of natural and forced dynamics and their influence on the heat release of the flame is shown.

**Physics:** The natural helical mode and the forced axis-symmetric mode show a destructive interference. Thus, increasing external forcing suppresses the global mode. A secondary helical mode in the wake of the vortex breakdown is unaffected by the forcing.



## American Society of Mechanical Engineers

### ASME Accepted Manuscript Repository

#### Institutional Repository Cover Sheet

53

*First*

63

*Last*

ASME Paper Title: Advanced Identification of Coherent Structures in Swirl-Stabilized Combustors

Authors: Moritz Sieber, Christian Oliver Paschereit, Kilian Oberleithner

ASME Journal Title: Journal of Engineering for Gas Turbines and Power

Volume/Issue 139(2): 021503 (8 pages) Date of Publication (VOR\* Online) September 13, 2016

ASME Digital Collection URL: https://asmedigitalcollection.asme.org/gasturbinespower/  
article-abstract/139/2/021503/374397/

DOI: https://doi.org/10.1115/1.4034261

\*VOR (version of record)

## GTP-16-1246

### ADVANCED IDENTIFICATION OF COHERENT STRUCTURES IN SWIRL-STABILIZED COMBUSTORS

Moritz Sieber\*, Christian Oliver Paschereit and Kilian Oberleithner

Chair of Fluid Dynamics  
 – Hermann-Föttinger-Institut –  
 Technische Universität Berlin  
 Müller-Breslau-Str. 8, 10623 Berlin, Germany

#### ABSTRACT

We present an application of a newly introduced method to analyze the time-resolved experimental data from the flow field of a swirl-stabilized combustor. This method is based on classic proper orthogonal decomposition (POD) extended by a temporal constraint. The filter operation embedded in this method allows for continuous fading from the classic POD to the Fourier mode decomposition. This new method – called spectral proper orthogonal decomposition (SPOD) – allows for a clearer separation of the dominant mechanisms due to a clean spectral separation of phenomena. In this paper, the fundamentals of SPOD are shortly introduced. The actual focus is put on the application to a combustor flow. We analyze high-speed PIV measurements from flow fields in a combustor at different operation conditions. In these measurements, we consider externally actuated, as well as natural dynamics and reveal how the natural and actuated modes interact with each other. As shown in the paper, SPOD provides detailed insight into coherent structures in swirl flames. Two distinct PVC structures are found that are very differently affected by acoustic actuation. The coherent structures are related to heat release fluctuations, which are derived from simultaneously acquired OH\* chemiluminescence measurements. Besides the actuated modes, a low frequency mode was found that significantly contribute to the global heat release fluctuations.

#### NOMENCLATURE

$a$	Temporal SPOD mode coefficients
$c$	Correlation coefficient
$g$	SPOD filter coefficients
$I$	OH* chemiluminescence intensity
$\lambda$	SPOD mode energy
$M$	Number of spatial points
$N$	Number of snapshots
$N_f$	Size of the SPOD filter
$\Omega$	Spatial SPOD mode (chemiluminescence)
$\Phi$	Spatial SPOD mode (velocity)
$q$	Global heat release
$\mathbf{R}$	Correlation matrix
$\mathbf{S}$	Filtered correlation matrix
$St$	Strouhal number
$t$	Time
$\mathbf{v}$	Cartesian velocity vector $[u, v, w]^T$
$\mathbf{x}$	Cartesian coordinate vector $[x, y, z]^T$

#### INTRODUCTION

It's getting increasingly harder to identify the relevant information from the vast amount of data that is produced from recent measurement systems or computational fluid dynamics. Beside the mean quantities, the available time-resolved data put the focus towards dynamic phenomena in the flows. The dynamics of interest are usually related to large-scale periodic structures, also called coherent structures [1]. These are of major importance in

\*Address all correspondence to this author: moritz.sieber@tu-berlin.de

gas turbine combustors, since they interact with the flame and modulate the heat release of the combustor [2, 3].

In data of combustor flows and turbulent flows in general, the identification of coherent structures is aggravated by the occurrence of multiple different structure. Several dynamic structures may occur simultaneously, interact with each other and dis-/appear intermittently. In order to extract these structures from the data, modal decompositions are commonly used. There are two different approaches that can be employed to build such a modal basis for flow data. One of them is the POD [1], which provides a basis of modes that is optimal in terms of energy representation. The other approach includes the dynamic mode decomposition (DMD) [4, 5] or classical Fourier mode decomposition, where each mode is assigned to a single frequency. Both approaches are problematic when highly turbulent flows are investigated. The POD puts a strict focus on the maximization of the represented energy of a mode without any specification on the dynamic of these modes. This may result in the merging of multiple (e.g. less energetic) dynamical structures in a single POD mode. Moreover, the POD modes strongly depend on the snapshot ensemble and may differ between subsequent measurements, which hinder the comparison of decompositions from different measurements. The restriction to constant frequencies of single modes (DMD, Fourier) can eliminate this ambiguity, but at the cost of a much larger set of modes. Even slight frequency variations of a single flow structure are reflected by several modes at neighboring frequencies. In consequence, the modes represent less energy, resulting in lower signal to noise ratios of each single mode, which produces much noisier spatial modes.

An escape from this dilemma is provided by the spectral proper orthogonal decomposition (SPOD) [6], which unifies both approaches and allows for a continuous transition from the POD to the Fourier mode decomposition. Employing a soft spectral constraint, the SPOD permits frequency variations of single modes, while it still separates modes according to their spectral contents. The SPOD acts somewhat like a band-pass filter to the POD modes, but the bands are selected intrinsically by the flow dynamics.

In this paper, the SPOD is applied to Particle Image Velocimetry (PIV) data of a swirl-stabilized combustor. Natural flow dynamics as well as flows actuated at a constant frequency and several amplitudes are considered. Furthermore, a strategy is presented, which allows the inclusion of data that are measured simultaneously with the velocity. Here, data from OH\* chemiluminescence is used to demonstrate the procedure. The combined analysis of coherent velocity fluctuations and heat release rate fluctuations reveal the connection between the flame describing function and coherent structures.

This paper starts with the explanation of the experimental setup, followed by a description of the applied mathematical methods and the results obtained from the application of

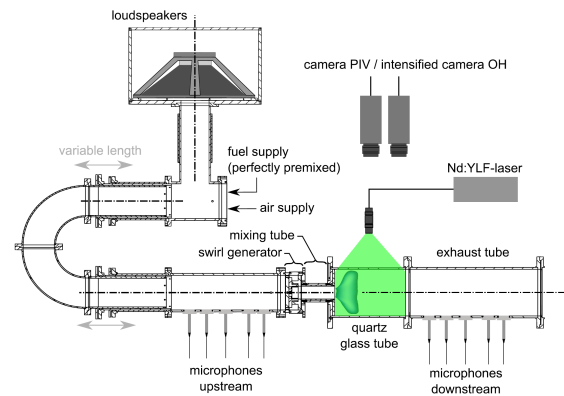


**FIGURE 1.** Sketch of the atmospheric combustion test-rig and measurement instrumentation

these methods. The final conclusions highlight the main findings gained from the application of SPOD to this highly turbulent reacting flow.

## EXPERIMENTAL SETUP

### Experimental Facility

The experimental data presented in this paper are obtained from an atmospheric combustion test-rig. A sketch of this setup together with the experimental apparatus is presented in fig. 1. A swirl-stabilized combustor is investigated at perfectly premixed conditions. Swirl is generated by injecting fluid tangentially into a mixing tube that terminates in the combustion chamber. For the considered experiments, the supplied air mass-flow is 100 kg/h, which results in a Reynolds number of around  $Re = 60\,000$ . The supplied air is not preheated. The combustor is operated with methane (natural gas) at an equivalence ratio of 0.7.

The test-rig allows for the actuation of streamwise acoustic waves using loudspeakers mounted upstream of the burner. In the present investigation, a forcing with constant frequency at different amplitudes is presented. The different amplitudes correspond to a modulation of the total flow by 10, 40 and 70% of the mean flow at the inlet ( $|u'|/\bar{u}$ ). The actuation frequency is 268Hz, which corresponds approximately to the maximum flame response at this operation conditions, according to measurements with the multi-microphone method [7].

### Data Acquisition

Inside the combustion chamber, the velocities and OH\*-chemiluminescence were recorded simultaneously with two synchronized high-speed cameras. Optical access to the combustion

GTP-16-1246

Sieber

chamber was enabled through a 200 mm diameter quartz glass pipe confining the flame.

Flow measurements were conducted by means of PIV in the meridional section as indicated in the schematic. The PIV system consists of a Photron Fastcam SA 1.1 high-speed camera (1Mpixel at 2.7kHz double frame) and a Quantronix Darwin Duo laser (30mJ at 1kHz). For each configuration, a set of 2000 images was recorded at a rate of 2000Hz. The PIV data were processed with PIVview (PIVTEC GmbH) using standard digital PIV processing [8] enhanced by iterative multigrid interrogation [9] with image deformation [10].

The chemiluminescence of the OH\* radicals was simultaneously recorded with a second Photron Fastcam SA 1.1. This was equipped with an image intensifier and an optical filter that restricts the observed wavelengths to 295-340nm.

### DATA ANALYSIS METHODOLOGY Spectral Proper Orthogonal Decomposition

The recently introduced SPOD is used to analyze the velocity and identify the coherent structures that occur in the considered flow. A detailed derivation and discussion of the SPOD can be found in [6]. Here, only the practical implementation is described. The SPOD is an offspring of the classical POD. Holmes et al. [1] provide full details on POD and recent publications from our group discuss the method in the context of swirling jets [11,12]. The application and computation of SPOD is generally comparable to classical POD, although there are some modifications in order to control the spectral properties of the decomposition.

The starting point of the SPOD is a decomposition of the velocity vector  $\mathbf{v}$  into a mean  $\bar{\mathbf{v}}$  and a fluctuating part  $\mathbf{v}'$  that is represented as a series, reading

$$\mathbf{v}(\mathbf{x}, t) = \bar{\mathbf{v}}(\mathbf{x}) + \sum_{i=1}^N a_i(t) \Phi_i(\mathbf{x}), \quad (1)$$

where  $\mathbf{x}$  denotes the coordinate vector and  $t$  the time. The decomposition consists of  $a_i$  temporal coefficients and  $\Phi_i$  spatial modes.

A set of  $M$  spatial points recorded simultaneously over  $N$  time steps is considered. To calculate the SPOD, the correlation matrix of this data set is needed, which is calculated between individual snapshots (temporal correlation). This is calculated from an appropriate inner product  $\langle \cdot, \cdot \rangle$ , defined as

$$\langle \mathbf{u}(\mathbf{x}), \mathbf{v}(\mathbf{x}) \rangle = \int_V \mathbf{u}(\mathbf{x}) \mathbf{v}^T(\mathbf{x}) dV, \quad (2)$$

where  $V$  specifies the spatial region or volume over which the correlation is integrated. The elements of the correlation matrix

$\mathbf{R}$  are given by

$$R_{i,j} = \frac{1}{N} \langle \mathbf{v}'(\mathbf{x}, t_i), \mathbf{v}'(\mathbf{x}, t_j) \rangle. \quad (3)$$

Matrix  $\mathbf{R}$  is of size  $N \times N$ .

In contrast to the classical POD algorithm, a filter is inserted at this point, which modifies the correlation matrix  $\mathbf{R}$ . To augment the diagonal similarity of  $\mathbf{R}$ , a simple low-pass filter is applied along the diagonals. This results in a filtered correlation matrix  $\mathbf{S}$ , with the elements given as

$$S_{i,j} = \sum_{k=-N_f}^{N_f} g_k R_{i+k, j+k}. \quad (4)$$

The filter above is just a symmetric finite impulse response filter with a filter coefficients vector  $\mathbf{g}$  of length  $2N_f + 1$ . The most simple approach would be a box filter, where all coefficients have the same value  $g_k = \frac{1}{2N_f + 1}$ . In this article, we use a Gaussian filter, which features a smooth response in time and frequency domain. Moreover, we choose a standard deviation as such that the filter gives the same cut-off frequency as a box filter with half the length.

The temporal coefficients  $\mathbf{a}_i = [a_i(t_1), \dots, a_i(t_N)]^T$  and mode energies  $\lambda_i$  are obtained from the eigenvectors and eigenvalues of the filtered correlation matrix.

$$\mathbf{S} \mathbf{a}_i = \lambda_i \mathbf{a}_i; \quad \lambda_1 \geq \lambda_2 \geq \dots \geq \lambda_N \geq 0 \quad (5)$$

The subscript  $i$  refers to single eigenvalues, which are sorted in descending order. The eigenvectors  $\mathbf{a}_i$  of  $\mathbf{S}$  are orthogonal and they are scaled with the energy of the single modes such that

$$\frac{1}{N} (\mathbf{a}_i, \mathbf{a}_j) = \lambda_i \delta_{ij}, \quad (6)$$

where  $(\cdot, \cdot)$  denotes the scalar product and  $\delta_{ij}$  the Kronecker delta. The spatial modes are obtained from the projection of the snapshots onto the temporal coefficients

$$\Phi_i(\mathbf{x}) = \frac{1}{N \lambda_i} \sum_{j=1}^N a_i(t_j) \mathbf{v}'(\mathbf{x}, t_j). \quad (7)$$

This spatial mode base is orthogonal if  $N_f = 0$ , which resembles the classic POD. The filter size  $N_f$  controls the spectral bandwidth of the individual modes, which allows a continuous transition from the classical POD to the Fourier decomposition. Thus,

the lower ( $N_f = 0$ ) and upper ( $N_f = N$ ) bound of the filter width correspond to the POD and Fourier decomposition, respectively. The best results are obtained when the filter width matches a characteristic time-scale of the flow. This can either be the period of a dominant oscillation or the characteristic length-scale divided by the characteristic velocity-scale.

The SPOD provides natural sorting of the spatial modes in terms of their turbulent kinetic energy  $\lambda_i$ . Another ranking is introduced by Sieber et al. [6] that is based on the cross spectra of mode pairs. This approach is based on the fact that a periodic coherent structure appears as a pair of modes in the decomposition. These pairs are identified by their level spectral coherence, which also delivers a ranking of periodic coherent structures.

### Extended SPOD of OH\* Chemiluminescence Data

Additional quantities that are recorded simultaneously with the velocities can also be represented in the modal basis of the SPOD. A simple way to accomplish this is the consideration of these quantities together with the velocity in an extended state vector of the flow. However, this approach requires a consistent implementation of these quantities into the inner product [13]. For the present case, a common measure for velocities measured within a planar field and line-integrated OH\*-chemiluminescence must be found. Since this would only allow for a flawed measure, we pursue another approach.

The extended POD introduced by Boree [14] enables to represent any kind of simultaneous measurement in the same basis as the POD. This approach can be similarly applied to the SPOD as will be shown here. The intensity of the OH\* chemiluminescence  $I$  is decomposed into a mean part  $\bar{I}$  and a fluctuating part  $I'$  that is represented as a series, reading

$$I(\mathbf{x}, t) = \bar{I}(\mathbf{x}) + I'(\mathbf{x}, t) = \bar{I}(\mathbf{x}) + \sum_{i=1}^N a_i(t) \Omega_i(\mathbf{x}). \quad (8)$$

Here, the same expansion coefficients  $a_i$  are used that are derived from the decomposition of the velocity field. Consequently, the OH\* modes  $\Omega_i$  are also obtained by the projection of the OH\* snapshots onto the coefficients, with

$$\Omega_i(\mathbf{x}) = \frac{1}{N\lambda_i} \sum_{j=1}^N a_i(t_j) I'(\mathbf{x}, t_j). \quad (9)$$

The spatial points  $\mathbf{x}$  do not require to be the same as those for which the velocity was measured. Moreover, the extended SPOD can also be applied to any other kind of simultaneous measurement.

### Correlation of Global Heat Release and Coherent Structures

The relation between the heat release and the coherent structures is quantified by a correlation measure. The global heat release  $q$  is obtained from the spatially integrated OH\* chemiluminescence, with

$$q(t) = \int_A I(\mathbf{x}, t) dA, \quad (10)$$

where  $A$  specifies the spatial integration area, which is taken to be the entire measured domain. The heat release is also represented by a mean and fluctuation part

$$q(t) = \bar{q} + q'(t). \quad (11)$$

The fluctuating part is correlated with the SPOD expansion coefficients to measure the contribution of the individual modes to the heat release fluctuations. It is given by

$$c_i = \frac{1}{N\sqrt{\lambda_i}} \sum_{j=1}^N a_i(t_j) q'(t_j). \quad (12)$$

In fact, this is just the extended SPOD of a single point signal.

## RESULTS

### The Mean Flow

The time-averaged flow is considered for the natural case without any actuation. The velocity field is depicted in fig. 2. It shows a typical conical vortex breakdown shape that corresponds to a V-flame [15, 16]. The crosswise extend of the measured domain reaches almost up to the combustor side walls, and the attachment (and deflection) of the jet at the wall is visible. The velocity field shows a large recirculation zone inside the conical jet. At the upstream end, this is delimited by a stagnation point on the jet axis. Two additional recirculation zones develop between the jet and the outer confinement.

In fig. 3, the mean OH\* intensity is depicted. An inverse Abel transformation is used to deduce the intensity in a plane from the line integrated intensities. Therefore, a rotational symmetry of the field is assumed. The OH\* distribution shows that this configuration features a V-shaped flame, which is anchored in the inner shear-layer shortly downstream of the combustor inlet.

### The Coherent Structures of the Natural Flow

The classical POD and the SPOD of the natural flow are contrasted in this section. This demonstrates best the increased performance of the SPOD. Both decompositions are calculated using the algorithm explained above, but with different filter widths

GTP-16-1246

Sieber

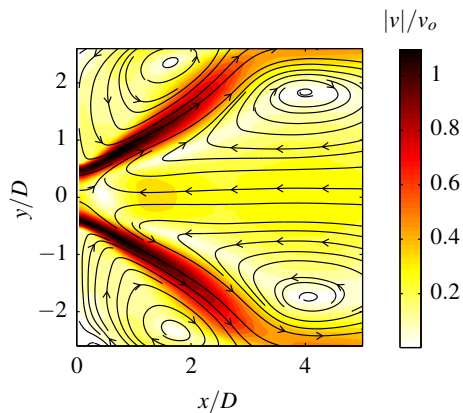


**FIGURE 2.** Natural mean velocity field (magnitude and streamlines)

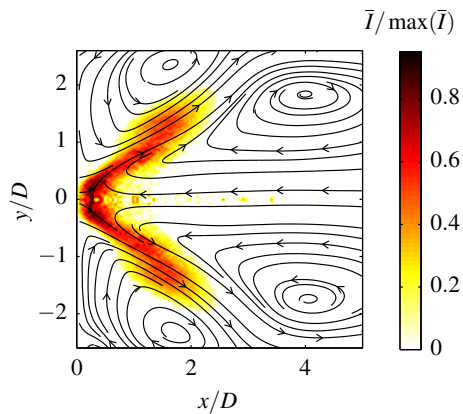


**FIGURE 3.** Natural mean OH\*-chemiluminescence field (de-Abeled) with superimposed streamlines

$N_f$ . In the SPOD scheme, the classic POD refers to a vanishing filter  $N_f = 0$ . For the SPOD shown here we choose a filter width of  $N_f = 24$ , which is equivalent to the period of the dominant oscillation with the lowest frequency ( $St=0.1$ ). It is calculated from the ratio of acquisition frequency  $f_a$  to mode frequency  $f_m$  as  $N_f = f_a/f_m$ . The decomposition is calculated only from the crosswise velocity (y-direction) since this has proven to give the best indication of coherent structures in this flow. The addition of the streamwise velocity puts the focus more towards large-scale variations of the base flow, which will be misleading in this context.

In conjunction with the crosswise velocity, the shape of symmetric and anti-symmetric structures in the rotational symmetric flow shall be clarified. The structures that are discussed in this article are the Precessing Vortex Core (PVC) [15] and the ac-

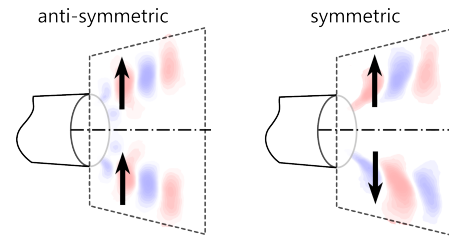


**FIGURE 4.** Relation between the sign of the crosswise velocities and the mode symmetries

tuated mode. The PVC is a helical mode, which appears as an anti-symmetric structure in the measured section. The actuated mode is rotationally symmetric and therefore also symmetric in the measured plane. However, the sign of the crosswise velocity shows an opposed symmetry as depicted in fig. 4.

The POD and SPOD of the natural flow are given in fig. 5 and fig. 6 respectively. For both decompositions, the first seven most energetic modes are drawn in descending order. They are represented by the power spectral density (PSD) of the mode coefficient  $a_i$  (left) and the contour plot of the spatial mode  $\Phi_i$  (right). The spatial modes are displayed together with the streamlines of the mean flow to allow for a better orientation.

The first pair of POD modes (fig. 5) show a similar structure that resembles the type I PVC identified in ref. [15] or the global mode reported in ref. [11]. The wavelength of this structure and the corresponding Strouhal number are very similar to those observed in other swirling flows. However, the mode coefficients spectrum shown here is considerably broader indicating low oscillation amplitudes, which is due to the specific design of this swirler [16]. The mode is located close to the combustor inlet and describes a periodic displacement of the conical jet, which is related to the precessing motion of the vortex core (PVC). Considering the remaining modes, we see what we call a “mode clutter”. The spatial modes reveal multiple wavelengths with no clear symmetries and the spectra reveal no distinct peaks. In the spectra of the modes 5 to 7, there is a peak at  $St \approx 0.1$ , which might indicate another dominant structure. However, it is not properly assigned to a single mode pair.

The SPOD decomposition gives a more ordered and clearer set of modes (fig. 6). Obviously, the applied filter restricts the spectral bandwidth of the individual modes, which results in well-defined spectral peaks of the mode coefficients. The PVC-I mode already found in the POD, is represented by mode 1 and 2, with a similar shape as for the POD, but with a well-defined peak in the spectrum. The 3rd and 4th SPOD modes also describe a single structure, which resembles the type II PCV identified in ref. [15]. The spectral peak at  $St=0.1$  as well as its spatial location inside the recirculation zone matches with the previous observations. However, the spatial structure of the PVC-II does

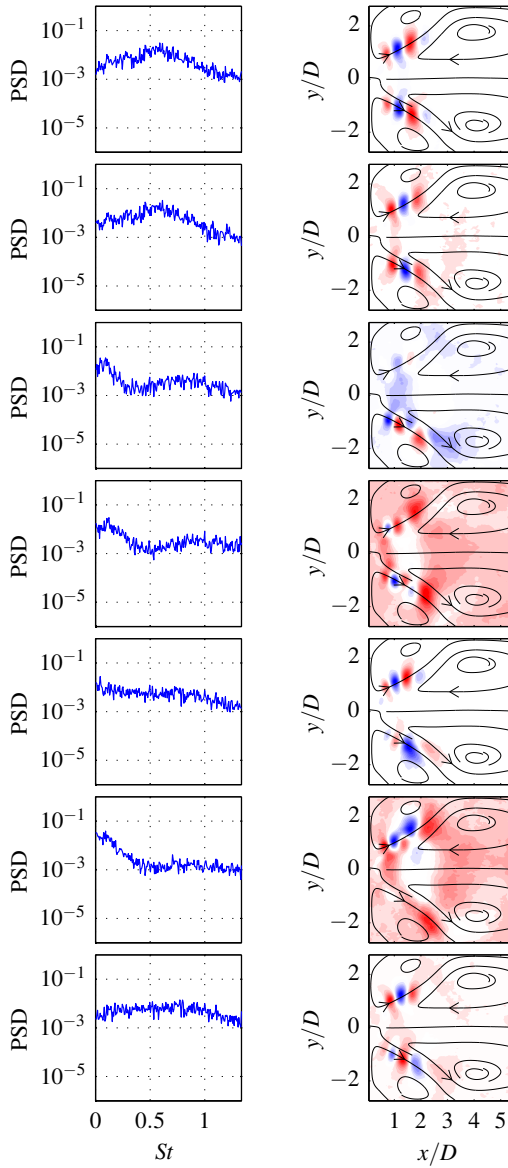


FIGURE 5. POD ( $N_f = 0$ ) modes of the natural flow.

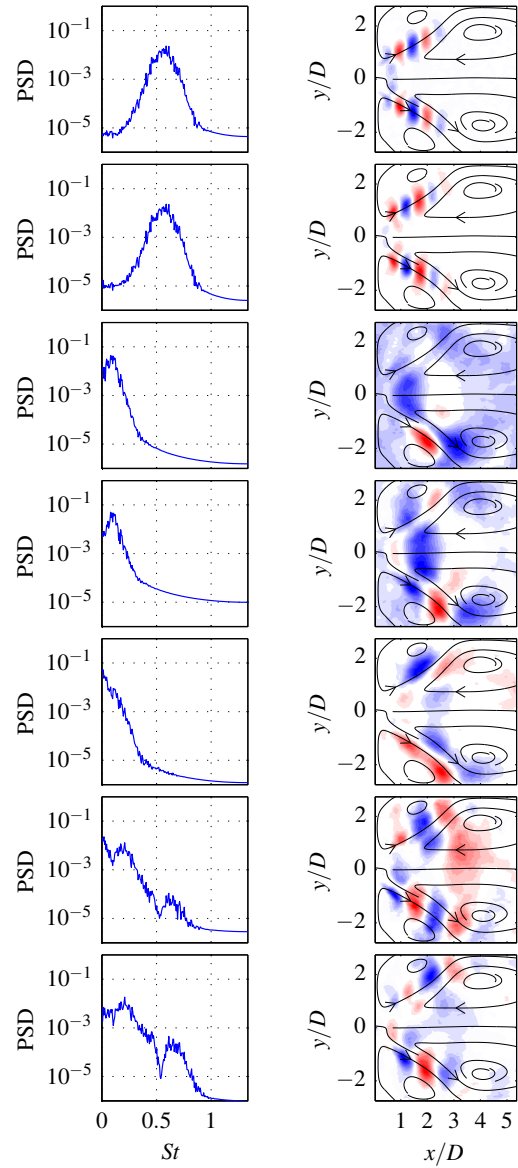


FIGURE 6. SPOD ( $N_f = 24$ ) modes of the natural flow.

not show such a proper anti-symmetry as the PVC-I. This is attributed to the very low frequencies, and hence, insufficient statistical convergence. In this context, it is also visible that the spatial development of this mode is limited by the confinement of the combustion chamber.

The SPOD modes 6 and 7 are also coupled, but their spec-

tra have two peaks close to the two other modes and their spatial wavelength lies in between the other two PVC modes. The 5th mode, however, has no counterpart. It shows low frequency temporal dynamics and the spatial mode tends towards a symmetric structure. It might be a so-called shift mode [12, 17] that describes slow changes of the mean velocity field.

This comparison of POD and SPOD shows that the additional spectral constraint of SPOD creates an interpretable set of modes, where individual phenomena are clearly assigned to single modes or mode pairs.

### Impact of Actuation on the Coherent Structures

The coherent structures are now identified from the measurements at increasing forcing amplitudes. The SPOD of the individual measurements are presented in fig. 7 using a compact presentation-scheme introduced in ref. [6]. A single configuration is represented by the so-called SPOD spectrum (see the scatter plot on the left), where each dot represents a pair of modes that is linked to the spectral coherence of each mode. The level of spectral coherence is indicated by the diameter and color of the dots. On the right-hand side, next to the SPOD spectrum, the spatial and temporal properties of selected modes are plotted. The selection is based on the SPOD spectrum and the modes are labeled by numbers (#1-4) in the SPOD spectrum as well as between the mode plots. The upper row displays the spatial structure of the modes ( $\Phi_i$ ) and the lower row the frequency spectrum (PSD) of the corresponding mode coefficients ( $a_i$ ).

The uppermost decomposition is the same as the one presented in the previous section (fig. 6). The SPOD spectrum clearly highlights the PVC-I (#1) and -II (#2) identified above. Moreover, mode #4 was also identified before and the additional mode #3 lies close to PVC-I. It shows two spectral peaks right above and below the Strouhal number of PVC-I and its spatial shape partially resembles the one of PVC-I.

The second configuration presented in the second row of fig. 7 corresponds to “weak” actuation, with a forcing amplitude of 10% of the mean flow. The two PVC modes (#1 and #2) stay nearly unaltered, but the SPOD spectrum indicates another mode that appears right at the forcing frequency of  $St = 0.35$  (#3). This mode exhibits a constant frequency and a symmetric spatial structure, corresponding to the symmetric forcing. The additional mode #4 may be related to mode #3 and #4 of the natural case. This mode is less energetic and shows weaker spectral coherence as can be seen from the SPOD spectrum.

In the configuration considered next, the forcing amplitude is increased considerably to 40% of the mean flow (see third row of fig. 7). This strongly alters the energy distribution among the observed modes. The forcing mode (#1) now clearly contributes most to the fluctuations in the flow, whereas the energy of the PVC-I mode (#4) is significantly reduced. The PVC-II mode (#2) stays at the same energy, but its spatial structure is altered. At the first harmonic of the forcing frequency, another mode appears (#3), with half the spatial wavelength and the same symmetry as the forcing mode.

For the last considered case, the forcing is increased to 70% of the mean flow (bottom row of fig. 7). The forcing mode (#1) together with its first (#4) and second harmonic broadly dominate

the SPOD spectrum. The only other modes that are distinct in the SPOD spectrum is the low frequency PVC-II and another mode (#3) that exhibits a somewhat higher frequency and spatial wavelengths than the PVC-II.

The SPOD allows for identifying the same coherent structures for every actuation case, and reveals the impact of the actuation on the entire mode spectrum. The three outstanding structures observed for the different measurements are the PVC-I, -II and the actuation mode. As expected, the energy of the actuation mode raises with increasing actuation amplitude. Moreover, the low frequency PVC-II mode seems little affected by the growing actuation. The energy only slightly reduces and the spatial structure changes a little. The PVC-I mode, however, does not take the actuation undisturbed. It is strongly reduced in energy until it entirely vanishes for the maximum actuation level. If the evolution of the entire mode spectrum is considered, it is visible that the actuation modes (fundamental together with the higher harmonics) dominate the high frequency part of the spectrum. All the modes with weaker energy are attenuated in the spectrum. Hence, the fluctuation energy in the flow is redistributed from the broad turbulent structures to the actuated structure and the higher harmonics. The modes with frequencies below the actuation are only weakly influenced by the actuation.

### Spatial OH\* Chemiluminescence Structures

The configuration with 10% actuation amplitude is selected for further investigations with respect to the OH\* chemiluminescence. This case is considered, because it features all three major structures identified so far, namely the PVC-I, -II and the actuated mode. Fig. 8 shows the corresponding OH\* modes as computed from an extended SPOD.

It is worth noting that for all three modes, the wavelengths of the extended SPOD OH\* modes do *not* match with those of the velocity modes. The OH\* modes show line integrated information that cannot directly be compared to the planar velocity data. A tomographic reconstruction of the OH\* mode field would be necessary to allow a direct comparison [3]. However, all the OH\* modes show clear structures that feature the same spatial symmetries as the velocity modes (recall fig. 4). Moreover, the velocity and OH\* modes both cover the same spatial areas. This shows that the extended SPOD is well suited to reveal the spatial heat release rate distribution corresponding to the coherent vortex structures in the flow field.

### Relation of Global Heat Release and Flow Structures

In order to quantify, which coherent structure contributes to the global heat release rate fluctuations in the combustor, the integrated chemiluminescence  $q'$  is correlated with the mode coefficients  $a_i$ , as expressed in eq. (12). For this purpose, the SPOD is computed from the symmetric part of the velocity field as described in [12]. The symmetric part is calculated from the sum

GTP-16-1246

Sieber

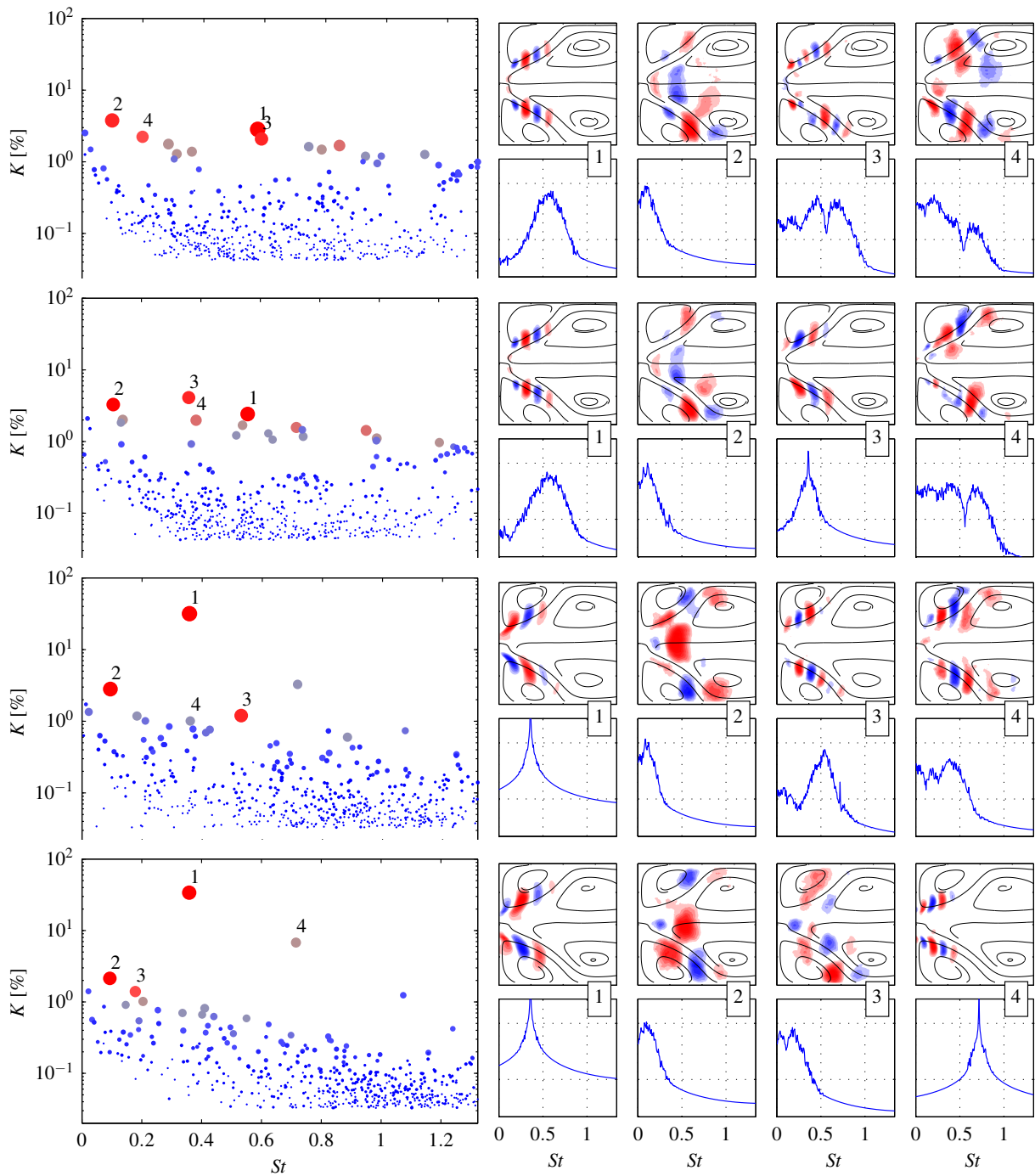


**FIGURE 7.** SPOD spectrum (left) and spatial modes with mode coefficient spectrum (right) for increasing forcing amplitudes (from top to bottom the forcing amplitudes are 0, 10, 40 and 70% of the bulk velocity)

GTP-16-1246

Sieber

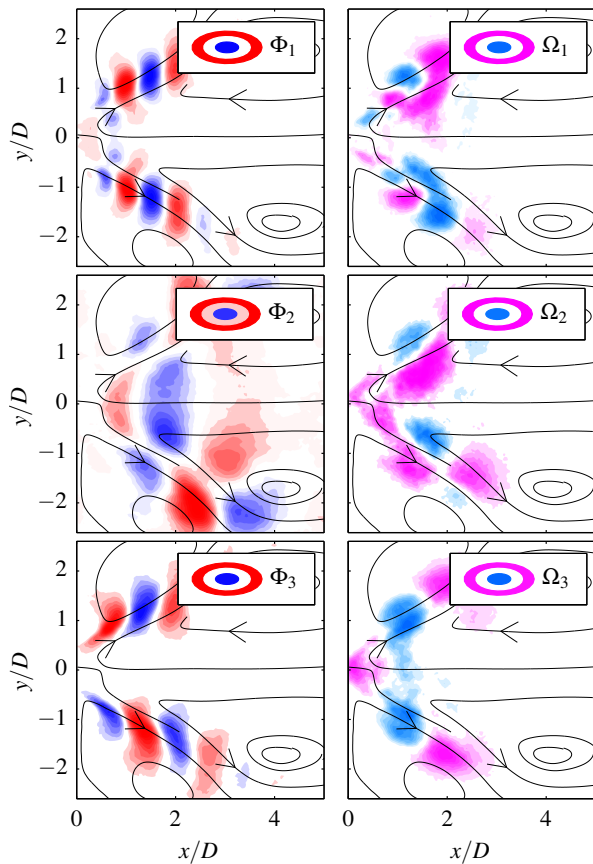


**FIGURE 8.** SPOD velocity modes  $\Phi_i$  and the corresponding SPOD OH\* modes  $\Omega_i$  for the dominant coherent structures

of the original field and the field mirrored at the  $x$ -axis. The reasoning behind this operation is that the anti-symmetric velocity fluctuations may only cause anti-symmetric heat release rate fluctuations that do not contribute to the integral heat release. Therefore, they are excluded from the analysis right from the beginning on.

Not surprisingly, the correlation reveals that the forced axis-symmetric mode contributes most to the global heat release rate fluctuations (not shown). The periodic vortex shedding deforms the flame and modulates the heat release rate. This interaction is also evident from fig. 8. Regardless of the actuation amplitude, the actuated mode is the only mode that shows significant correlation with the heat release rate.

The consideration of the natural case delivers more interesting results. We find one low frequency mode that shows significant correlation with  $q'$ . The coefficient of this mode together with the global heat release rate fluctuations is given in fig. 9. It

becomes visible that the low frequency variations of  $q'$  follows the same trend as the mode coefficient  $a_i$ . It is also evident that only a part of the global heat release rate fluctuations can be explained by this mode.

The spatial structure of this correlated mode together with the corresponding extended SPOD OH\* mode is given in fig. 10. The velocity mode is comparable to a mode found in the investigation of a generic unconfined swirling jet [12]. There, the mode corresponds to an axial shift of the recirculation region (upstream stagnation point), which is related to fluctuations of the swirl intensity. Here, this shift mode also describes very low frequency mean flow unsteadiness ( $0 < St < 0.01$ ) and shows a similar spatial structure. The corresponding OH\* mode shows an axis-symmetric shape and high amplitudes at the upstream end of the recirculation zone, which indicates axial fluctuations of the flame root.

Combining these findings, the analysis shows that the low frequency variations of the velocity field affect the flame root and thereby cause variations of the global heat release. This result indicates that the low frequency part of the flame describing function is governed by changes of the mean velocity field and not by hydrodynamic instabilities. In contrast, the actuation causes periodic vortex shedding, which strongly depends on the hydrodynamic stability of the base flow, as detailed by Oberleithner et al. [18].

## CONCLUSIONS

The newly introduced SPOD is demonstrated for measurement data of a swirl-stabilized combustor, where it precisely identifies all the dominant coherent structures in the flow. Two different PVC structures are identified in the same flow configuration, which were previously only separately observed in different configurations.

With the help of the SPOD, the coherent structures of four different sets could be compared in a consistent manner. The robust identification of the dominant coherent structures allows for tracking the evolution of these structures across the measurements. This allows for quantifying the effect of the actuation on all the coherent structures that are present in the flow and not only on the actuated structure alone. The analysis shows that the actuated mode suppresses the PVC-I mode, whereas the PVC-II mode stays remarkably unaffected.

Employing the extended SPOD, the OH\*-chemiluminescence measurements are related to the identified coherent structures. It appears that all the identified structures are relevant for spatial fluctuations of the heat release rate. A separate consideration of the integral OH\* data together with symmetric velocity fluctuations shows that low frequency variations of the recirculation region transfers to fluctuations of the global heat release. The results indicate that the pathway from velocity fluctuations to heat release fluctuations, which

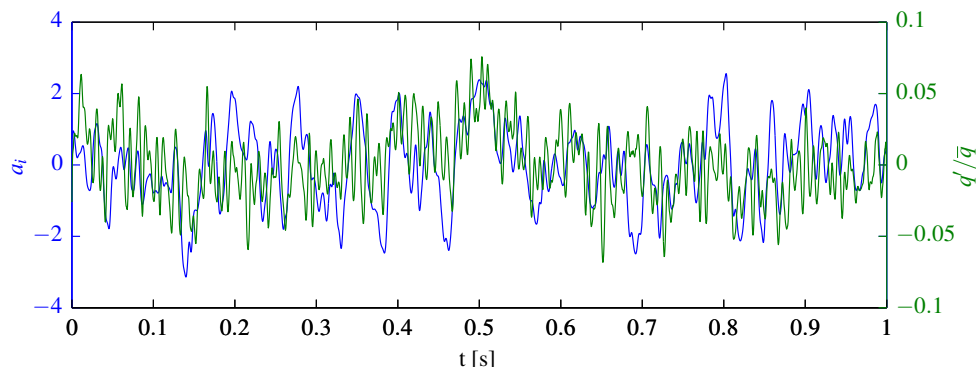


**FIGURE 9.** Time curve of the SPOD coefficient ( $a_i$ ) and the global heat release fluctuations ( $q'/\bar{q}$ )

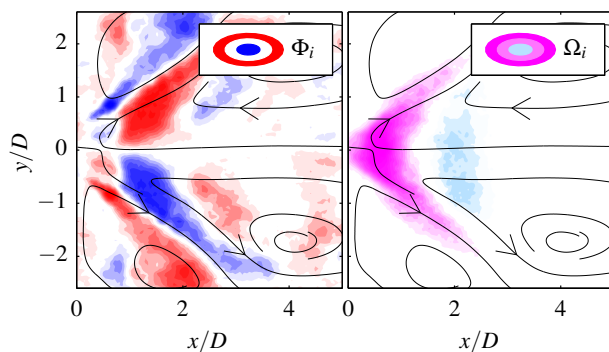


**FIGURE 10.** SPOD velocity modes  $\Phi_i$  and corresponding SPOD OH\* modes  $\Omega_i$  for the shift mode

is reflected by the flame describing function, is governed by different mechanisms, depending on the time scale of the fluctuations. The low frequency fluctuations can be interpreted as slow mean flow dynamics, which are presumably determined by slowly varying inflow conditions. The high frequency fluctuations, instead, correspond to coherent structures driven by the hydrodynamic instability of the underlying mean flow.

Although the application of SPOD is limited to a combustor flow in this presentation, it has high potential to ease the interpretation of data in most fluid dynamic research areas. It allows for the separation of multi-modal dynamics; it provides a very high noise rejection capability, which is very helpful when processing experimental data; it can reconstruct the dynamics of partially recorded phenomena and it provides clean dynamics that can be easily interpreted. These properties make it suited for many applications where the commonly used methods fail to provide insightful results.

#### ACKNOWLEDGMENT

Financial supports from the German Research Foundation (DFG) under project grants PA 920/30-1 and from the Research Association for Combustion Engines (FVV) are gratefully acknowledged.

#### REFERENCES

- [1] Holmes, P., Lumley, J., and Berkooz, G., 1998. *Turbulence, Coherent Structures, Dynamical Systems and Symmetry*. Cambridge Monographs on Mechanics. Cambridge University Press, Cambridge [England].
- [2] Poinso, T. J., Trounev, A. C., Veynante, D. P., Candel, S. M., and Esposito, E. J., 1987. "Vortex-driven acoustically coupled combustion instabilities". *Journal of Fluid Mechanics*, **177**, 4, pp. 265–292.
- [3] Moeck, J. P., Bourguin, J.-F., Durox, D., Schuller, T., and Candel, S., 2012. "Nonlinear interaction between a precessing vortex core and acoustic oscillations in a turbulent swirling flame". *Combustion and Flame*, **159**(8), pp. 2650–2668.
- [4] Rowley, C. W., Mezic, I., Bagheri, S., Schlatter, P., and Henningson, D. S., 2009. "Spectral analysis of nonlinear flows". *Journal of Fluid Mechanics*, **641**, pp. 115–127.
- [5] Schmid, P. J., 2010. "Dynamic mode decomposition of numerical and experimental data". *Journal of Fluid Mechanics*, **656**, pp. 5–28.
- [6] Sieber, M., Paschereit, C. O., and Oberleithner, K., 2015. "Spectral proper orthogonal decomposition". *Journal of Fluid Mechanics (accepted)*, preprint arXiv:1508.04642.
- [7] Paschereit, C. O., Schuermans, B., Polifke, W., and Mattson, O., 2002. "Measurement of transfer matrices and source terms of premixed flames". *Journal of Engineering for Gas Turbines and Power*, **124**(2), 3, pp. 239–247.
- [8] Willert, C., and Gharib, M., 1991. "Digital particle image

- velocimetry”. *Experiments in Fluids*, **10**(4), pp. 181–193.
- [9] Soria, J., 1996. “An investigation of the near wake of a circular cylinder using a video-based digital cross-correlation particle image velocimetry technique”. *Experimental Thermal and Fluid Science*, **12**(2), pp. 221 – 233.
- [10] Huang, H. T., Fiedler, H. E., and Wang, J. J., 1993. “Limitation and improvement of PIV: Part II: Particle image distortion, a novel technique”. *Experiments in Fluids*, **15**(4-5), pp. 263–273.
- [11] Oberleithner, K., Sieber, M., Nayeri, C. N., Paschereit, C. O., Petz, C., Hege, H.-C., Noack, B. R., and Wygnanski, I., 2011. “Three-dimensional coherent structures in a swirling jet undergoing vortex breakdown: stability analysis and empirical mode construction”. *Journal of Fluid Mechanics*, **679**, pp. 383–414.
- [12] Rukes, L., Sieber, M., Paschereit, C. O., and Oberleithner, K., 2015. “Effect of initial vortex core size on the coherent structures in the swirling jet near field”. *Experiments in Fluids*, **56**(10).
- [13] Rowley, C. W., Colonius, T., and Murray, R. M., 2004. “Model reduction for compressible flows using POD and galerkin projection”. *Physica D: Nonlinear Phenomena*, **189**(12), pp. 115 – 129.
- [14] Boree, J., 2003. “Extended proper orthogonal decomposition: a tool to analyse correlated events in turbulent flows”. *Experiments in Fluids*, **35**(2), pp. 188–192.
- [15] Terhaar, S., Reichel, T. G., Schrödinger, C., Rukes, L., Paschereit, C. O., and Oberleithner, K., 2014. “Vortex Breakdown Types and Global Modes in Swirling Combustor Flows with Axial Injection”. *Journal of Propulsion and Power*, **31**(1), pp. 219–229.
- [16] Reichel, T. G., Terhaar, S., and Paschereit, O., 2015. “Increasing Flashback Resistance in Lean Premixed Swirl-Stabilized Hydrogen Combustion by Axial Air Injection”. *Journal of Engineering for Gas Turbines and Power*, **137**(7), p. 071503.
- [17] Noack, B. R., Afanasiev, K., Morzynski, M., Tadmor, G., and Thiele, F., 2003. “A hierarchy of low-dimensional models for the transient and post-transient cylinder wake”. *Journal of Fluid Mechanics*, **497**, 12, pp. 335–363.
- [18] Oberleithner, K., Schimek, S., and Paschereit, C. O., 2015. “Shear flow instabilities in swirl-stabilized combustors and their impact on the amplitude dependent flame response: A linear stability analysis”. *Combustion and Flame*, **162**(1), pp. 86 – 99.

### 3.3 Experimental Study of Transient Mechanisms of Bi-Stable Flame Shape Transitions in a Swirl Combustor

This article is published in an edited form in the Journal of Engineering for Gas Turbines and Power under the following reference: M. Stöhr, K. Oberleithner, M. Sieber, Z. Yin, & W. Meier (2017). "Experimental Study Of Transient Mechanisms Of Bi-Stable Flame Shape Transitions In A Swirl Combustor". *Journal of Engineering for Gas Turbines and Power*, V04BT04A063. DOI: [10.1115/1.4037724](https://doi.org/10.1115/1.4037724). The following is the accepted manuscript of the article which is reprinted with permission of the American Society of Mechanical Engineers (ASME). This version is free to view and download for private research and study only. Not for re-distribution, re-sale or use in derivative works. ©2017 by ASME.

In this publication, experimental data from a transient switching between two flow states in a combustor are analysed with SPOD and linear stability analysis to reveal the physical mechanisms that lead to the switching.

**Methods:** No new methods are presented here. SPOD and linear stability analysis are utilised in common configurations.

**Results:** Data from the DLR Stuttgart are analysed that show a transition between an attached V-flame and a detached M-flame. The activity and interaction of the helical global mode and a thermoacoustic mode are revealed by an SPOD. The stability analysis further details the effect of density stratification on the amplification rate of the global mode.

**Physics:** In the basic flow configuration, the suppression of the helical global mode due to density stratification allows the formation of a stable V-flame. In a transient flame detachment event, the emergence of the global mode causes mixing in the flow that further increases the mode amplitude in a self-amplifying process. The resulting transition of the flow to the M-flame causes the emergence of a thermoacoustic instability that interferes with the global mode. The suppression of the global mode by the thermoacoustic oscillations allows the flow to return to the initial, stable state.



American Society of  
Mechanical Engineers

## ASME Accepted Manuscript Repository

### Institutional Repository Cover Sheet

66

*First*

76

*Last*

ASME Paper Title: Experimental Study of Transient Mechanisms of Bistable Flame Shape Transitions in a

Swirl Combustor

Authors: Michael Stöhr, Kilian Oberleithner, Moritz Sieber, Zhiyao Yin, Wolfgang Meier

ASME Journal Title: Journal of Engineering for Gas Turbines and Power

Volume/Issue 140(1): 011503 (8 pages) Date of Publication (VOR\* Online) September 19, 2017

ASME Digital Collection URL: https:// asmedigitalcollection.asme.org/gasturbinespower/  
article-abstract/140/1/011503/374503/

DOI: https://doi.org/10.1115/1.4037724

\*VOR (version of record)

Proceedings of Proceedings of ASME Turbo Expo 2017: Turbomachinery Technical  
Conference and Exposition  
GT2017

June 26-30, 2017, Charlotte, USA

**GT2017-65003**

**DRAFT: EXPERIMENTAL STUDY OF TRANSIENT MECHANISMS OF BI-STABLE  
FLAME SHAPE TRANSITIONS IN A SWIRL COMBUSTOR**

**Michael Stöhr \***

German Aerospace Center (DLR)  
Institute of Combustion Technology  
Pfaffenwaldring 38-40  
70569 Stuttgart, Germany

**Kilian Oberleithner, Moritz Sieber**

Chair of Fluid Dynamics  
Hermann-Föttinger-Institut  
Technische Universität Berlin  
Müller-Breslau-Str. 8  
10623 Berlin, Germany

**Zhiyao Yin, Wolfgang Meier**

German Aerospace Center (DLR)  
Institute of Combustion Technology  
Pfaffenwaldring 38-40  
70569 Stuttgart, Germany

**ABSTRACT**

*Sudden changes of flame shape are an undesired, yet poorly understood feature of swirl combustors used in gas turbines. The present work studies flame shape transition mechanisms of a bi-stable turbulent swirl flame in a gas turbine model combustor, which alternates intermittently between an attached V-form and a lifted M-form. Time-resolved velocity fields and 2D flame structures were measured simultaneously using high-speed stereo-PIV and OH-PLIF at 10 kHz. The data analysis is performed using two novel methods that are well adapted to the study of transient flame shape transitions: Firstly, the linear stability analysis (LSA) of a time-varying mean flow and secondly the recently proposed spectral proper orthogonal decomposition (SPOD). The results show that the transitions are governed by two types of instability, namely a hydrodynamic instability in the form of a precessing vortex core (PVC) and a thermoacoustic (TA) instability. The LSA shows that the V-M transition implies the transient formation of a PVC as the result of a self-amplification process. The V-M transition, on the other hand, is induced by the appearance of a TA instability that suppresses the PVC and thereby modifies the flow field such that the flame re-attaches at the nozzle. In summary these results provide novel insights into the complex interactions of TA and hydrodynamic instabilities that govern the shape of turbulent swirl-stabilized flames.*

\*Address all correspondence to this author: michael.stoehr@dlr.de

**INTRODUCTION**

Modern gas turbines are required to run at low NO<sub>x</sub> emissions and over a wide range of operating conditions. Rapid mixing of the reactants downstream of the fuel injection and robust flame stabilization mechanisms are strong requirements for the design of new combustors. Swirl-stabilized combustion is currently the most common approach. Strong swirl is imparted on the combustor flow to enhance turbulent mixing and to generate an internal recirculation zone (IRZ) which acts as an obstacle-free flame holder.

In an ideal case the turbulent swirl flame remains well anchored throughout a wide range of operating conditions and its shape changes only gradually within this range. In practice, however, swirl flames often exhibit abrupt changes of flame shape at certain operating conditions as reported, e.g., in Refs. [1–6]. This is highly undesired since it may lead to a sudden changes of emissions or thermoacoustic pulsations, or to thermal stresses of combustor walls due to abrupt changes of local temperature. When a flame is operated near the point of shape transition, it may further exhibit a so-called bi-stable behavior where the flame alternates intermittently between two shapes without external influence.

While a few studies of bi-stable flames have been reported [2, 5–7], the detailed mechanisms remain largely unclear since they take place on short time-scales and involve complex interactions of turbulent flow field and chemistry. Additional knowledge about the underlying mechanisms may help to design im-

proved combustors with an extended range of stable operation. The present work therefore aims at a detailed experimental investigation of flame shape transitions using time-resolved multi-parameter diagnostics and advanced methods of data analysis.

The work continues the previous study by Oberleithner et al. [6] focusing on the formation and suppression of a helical coherent flow structure, commonly known as the precessing vortex core (PVC), in a swirl combustor. The authors performed a linear stability analysis (LSA) of the time-averaged reacting flow fields. They investigated two different reacting operating conditions, one with an attached conical V-shaped flame with a strong density stratification at the combustor inlet and one with a detached M-shaped flame with mild density stratification at the inlet. Their analysis showed that the strong density stratification for the V-flame causes the suppression of the PVC instability. This explains the occasionally observed absence of the PVC under reacting conditions [8–10]. With the attempt to gain further insights into the interplay between the PVC, the density field and the flame, the authors investigated a bi-stable operating condition where the flame intermittently transitioned between the V- and M-shape. They tracked the flow field and flame shape during a V-M flame transition using high-speed PIV and OH-PLIF. They conjectured that the PVC plays a crucial role in the flame detachment process as it generates an unsteady stagnation point that destabilizes the flame root. Moreover it was found that the PVC induces additional mixing near the jet core that modifies the local density stratification in favor for the PVC, which potentially leads to a self-amplification process.

As an extension of the work of Oberleithner et al. [6], the present work now applies two novel methods of data analysis that are well adapted to the study of transient flame shape transitions: Firstly, the steady LSA is extended to the LSA of a time-varying mean flow. Secondly, the recently proposed spectral proper orthogonal decomposition (POD) is applied, which enables a better separation of different periodic instabilities than the conventional POD. Furthermore the present work now addresses the full bi-stable dynamics including both the V-M and M-V transitions.

## EXPERIMENTAL SETUP AND OPERATING CONDITION

### Gas turbine model combustor

Measurements were performed at atmospheric pressure with the GT-typical PRECCINSTA swirl combustor based on a design by Turbomeca, which is shown schematically in Fig. 1. Perfectly premixed methane and air enter the cylindrical plenum ( $d=78$  mm) and then pass through a swirl generator with 12 radial vanes. The swirling flow then reaches the combustion chamber through a burner nozzle ( $d=27.85$  mm) with a conical bluff body. The chamber has a square cross-section of  $85\times 85$  mm<sup>2</sup> and a height of 114 mm. Optical access to the chamber is provided by side walls made of quartz glass held by metal posts in the corners. The exit is composed of a conical part followed by

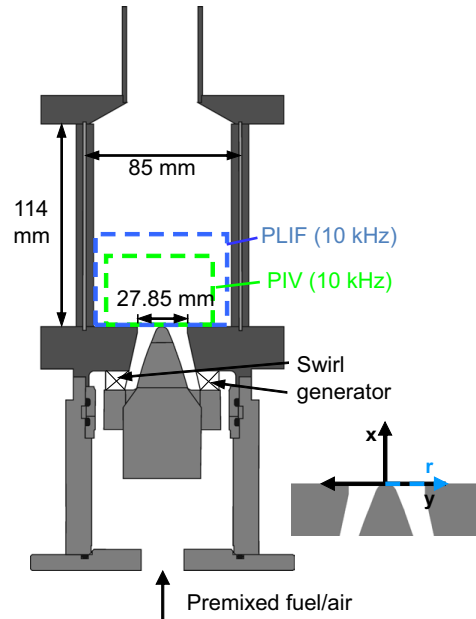


FIGURE 1. Schematics of gas turbine model combustor.

an exhaust duct ( $d=40$  mm).

### Operating condition

The previous work by Oberleithner et al. [6] showed that depending on the thermal power  $P_{th}$  and equivalence ratio  $\phi$ , the flame can either assume an attached V-shape, a detached M-shape, or a bi-stable behavior alternating intermittently between V- and M-shape. For a fixed value of  $P_{th}$ , V-flames appear for larger, M-flames for smaller and bi-stable flames for intermediate values of  $\phi$ . The work further showed that M-flames exhibit a PVC whereas V-flames do not. The present study was performed for a bi-stable flame at  $P_{th}=20$  kW and  $\phi=0.7$ . At this condition, the flame was alternating randomly about once per second between a V-shape without PVC and an M-shape with PVC.

### Measurement Techniques

Time-resolved simultaneous stereo-PIV and OH-PLIF measurements with a repetition rate of 10 kHz were performed using the experimental setup described in a recent publication [11]. The most important specifications are provided in the following. The stereo-PIV system employed a dual-cavity Nd:YAG laser (Edgewave IS-6IIDE, 2.6 mJ/pulse at 532 nm) and 2 CMOS cameras (LaVision HSS 8) equipped with Tokina lenses ( $f=100$  mm,  $f/2.8$ ) and bandpass filters ( $532\pm 1$  nm). OH-PLIF was excited at

283.2 nm by a dye laser (Sirah Credo, 80  $\mu\text{J}/\text{pulse}$  at 283.2 nm) pumped with a Nd:YAG laser (Edgewave IS-8III, 4 mJ/pulse at 523 nm). The OH-PLIF emission was recorded using an intensified CMOS camera (LaVision HSS 5 with HS-IRO) equipped with a Cerco UV lens ( $f=45$  mm,  $f/1.8$ ) and a bandpass filter (300-325 nm). The beams of the two laser systems were expanded into two coplanar vertical light sheets across the central section of the combustion chamber. About 4% of the UV light sheet was deflected into a cuvette filled with a fluorescent liquid for sheet profile imaging using an intensified CMOS camera (LaVision HSS 5 with HS-IRO) equipped with a Nikon lens ( $f=50$  mm, set to  $f/4$ ). The measurement domains of PIV and OH-PLIF are displayed in Fig. 1. For PIV the air flow was seeded with  $\text{TiO}_2$  particles with a diameter of about 1  $\mu\text{m}$ . The sustained recording time was 0.8 s corresponding to 8000 single measurements. The PIV images were processed using a cross-correlation algorithm (LaVision DaVis 8.2) with a final interrogation window size of  $16 \times 16$  pixel corresponding to  $1.3 \times 1.3$  mm<sup>2</sup>. The single-shot inhomogeneities and energy fluctuations of the PLIF laser sheet were corrected using the simultaneously recorded dye cuvette sheet profiles. The PIV particle images are further used to estimate the local gas density, which is required as an input of the LSA, according to the so-called quantitative light sheet (QLS) technique that derives the density from the Mie scattering signal of the PIV particles [6].

## DATA ANALYSIS METHODS

### Spectral Proper Orthogonal Decomposition

In order to survey the chronology of events during the measured transients, we employ a modal decomposition of the data reading

$$\mathbf{u}(\mathbf{x}, t) = \bar{\mathbf{u}}(\mathbf{x}) + \mathbf{u}'(\mathbf{x}, t) = \bar{\mathbf{u}}(\mathbf{x}) + \sum_{i=1}^N a_i(t) \Psi_i(\mathbf{x}), \quad (1)$$

which separates the fluctuating part of the velocity  $\mathbf{u}'$  into temporal coefficients  $a_i$  and spatial modes  $\Psi_i$ . The modal basis is constructed using the recently introduced Spectral Proper Orthogonal Decomposition (SPOD) [12], which is an extension of the classical Proper Orthogonal Decomposition (POD) [13]. Both methods were very successfully used to extract the dominant coherent structures from PIV measurements of swirling jets. Usually, the POD identifies the dominant coherent structures [14], but in case of multiple interacting and intermittent modes the single flow structures are not properly assigned to single modes. The SPOD includes an additional spectral constraint that provides much better separation in such cases [12, 15]. However, it should be noted that its application is limited to time-resolved measurements.

Here, a short overview of the SPOD approach is given. More detailed derivations can be found in [12]. To obtain the SPOD, the correlation matrix of the data set needs to be calculated between individual snapshots. The correlation matrix is computed as

$$R_{i,j} = \frac{1}{N} \int_V \mathbf{u}'(\mathbf{x}, t_i) \mathbf{u}'^T(\mathbf{x}, t_j) dV, \quad (2)$$

where  $N$  is the number of snapshots,  $V$  specifies the measured domain over which the correlation is integrated and  $()^T$  indicates the transpose. In addition to the classical POD algorithm, the correlation matrix is filtered along all diagonals with a low-pass filter, resulting in a filtered correlation matrix  $\mathbf{S}$ , with the elements given as

$$S_{i,j} = \sum_{k=-N_f}^{N_f} g_k R_{i+k, j+k}. \quad (3)$$

The low-pass filter is implemented as a symmetric finite impulse response filter with a filter coefficients vector  $\mathbf{g}$  of length  $2N_f + 1$ . A Gaussian filter is used to obtain a smooth response in time and frequency domain. The filter size  $N_f$  is the central adjusting parameter of the SPOD that controls the spectral constraint of the modes. In the current investigation this is set to two periods of the PVC oscillation ( $N_f = 50 \approx 2f_{PIV}/f_{PVC}$ ), which is in line with the previous applications. Generally, there are little changes of the results for small variations of the filter size. As a rule of thumb, the filter size should be at least as long as a single period of the lowest frequency mode but not too large to avoid splitting of flow structures into several modes. The latter is easily visible when the size is increased in moderate steps.

The temporal coefficients  $\mathbf{a}_i = [a_i(t_1), \dots, a_i(t_N)]^T$  and mode energies  $\lambda_i$  are obtained from the eigenvectors and eigenvalues of the filtered correlation matrix.

$$\mathbf{S} \mathbf{a}_i = \lambda_i \mathbf{a}_i; \quad \lambda_1 \geq \lambda_2 \geq \dots \geq \lambda_N \geq 0 \quad (4)$$

The subscript  $i$  refers to single eigenvalues, which are sorted in descending order. Naturally, the SPOD modes are sorted according to their kinetic energy content  $\lambda_i$ . This may sometimes hide less energetic modes among strong stochastic fluctuations. In the work of Sieber et al. [12] a ranking of the modes according to the spectral coherence of mode pairs is introduced. This is used to select relevant modes and graphically highlight periodic modes in the SPOD spectrum that will be shown later.

### Linear hydrodynamic stability analysis

Within the framework of linear stability theory, the PVC is interpreted as a global hydrodynamic instability [6, 14, 16–18].

The term *global* implies that the entire flow dynamics are dominated by a single oscillatory mode. The most prominent example of a global instability is the von Kármán vortex street. Global modes are self-excited and are driven by an internal feed-back mechanism. The place where this feed-back occurs is called the *wavemaker region*. The determination of the wavemaker is particularly important as it determines the growth rate (amplitude) and frequency of the global mode.

In this study we employ a local linear stability analysis (LSA) to find the wavemaker and to determine the growth rate and frequency of the PVC. The current approach is well in line with the previous investigations of the stable M- and V-flame configuration and the reader is referred to this article for further details [6]. However, in contrast to the previous study, the analysis is now applied to a mean flow that evolves in time, which requires some additional considerations regarding the involved time scales. The reader is referred to a recent analysis of a transient isothermal swirling jet for detailed discussion of this concept [19].

For the LSA, the transient mean flow data is decomposed into four parts: the mean, the shift, the periodic (coherent) and the turbulent part, reading

$$\mathbf{u}(\mathbf{x}, t) = \underbrace{\overline{\mathbf{u}}(\mathbf{x})}_{\text{mean}} + \underbrace{\tilde{\mathbf{u}}(\mathbf{x}, t)}_{\text{shift}} + \underbrace{\tilde{\mathbf{u}}(\mathbf{x}, t)}_{\text{periodic}} + \underbrace{\mathbf{u}''(\mathbf{x}, t)}_{\text{turbulent}}. \quad (5)$$

The governing equations are derived by substituting the decomposition  $\mathbf{u} = \overline{\mathbf{u}} + \tilde{\mathbf{u}}$  into the Navier-Stokes and continuity equations. Linearization around the transient mean state results in the stability equations

$$\frac{\partial \tilde{\mathbf{u}}}{\partial t} + (\tilde{\mathbf{u}} \cdot \nabla) \overline{\mathbf{u}} + (\overline{\mathbf{u}} \cdot \nabla) \tilde{\mathbf{u}} = -\frac{1}{\bar{\rho}} \nabla \tilde{p} + \frac{1}{\text{Re}} \Delta \tilde{\mathbf{u}} \quad (6)$$

$$\nabla \cdot \tilde{\mathbf{u}} = 0. \quad (7)$$

We assume that the transient mean state  $\overline{\mathbf{u}}$  is a quasi steady solution of the forced Navier-Stokes equations, as pursued by Mantič-Lugo et al. [20]. Therefore, the temporal changes of the mean flow are contributed to changes of the forcing by the Reynolds stresses. Hence, the timescale at which the mean flow changes is directly coupled to the timescale at which the coherent structure  $\tilde{\mathbf{u}}$  is amplified [19].

Assuming a quasi-parallel flow, the perturbation is decomposed into normal modes  $\tilde{\mathbf{u}} = \hat{\mathbf{u}} e^{i(\alpha x + m\theta - \omega t)}$  and  $\tilde{p} = \hat{p} e^{i(\alpha x + m\theta - \omega t)}$ , where  $\alpha$  denotes the axial wave number,  $m$  the azimuthal wave number and  $\omega$  the frequency. Eqs. (6) and (7) together with the disturbance ansatz and appropriate boundary conditions yield an eigenvalue problem that is discretized with

the Chebyshev pseudospectral collocation technique [21]. The resulting dispersion relation  $\mathcal{D}(\omega, \alpha, m) = 0$  is solved for complex  $\alpha$  and complex  $\omega$  and  $m = 1$ . We then search for a saddle-point in the mapping from  $\alpha$  to  $\omega$ , which corresponds to the wave with zero group velocity. The growth rate of this wave is called *absolute growth rate*  $\omega_0$  and it determines whether a flow profile is convectively or absolutely unstable [22]. The distinction between convective and absolute instability at every flow slice is an important information, because a finite region of absolute instability is necessary for the weakly non-parallel flow to sustain a global mode [23].

Once the absolute instability is determined, the wavemaker location is given by a frequency selection criterion [24]. For the M-flame configuration, the wavemaker is located at the combustor inlet [6] and the global mode growth rate  $\sigma$  is given by the imaginary part of the absolute frequency at this point, reading

$$\sigma = \Im \{ \omega_0(x=0) \}.$$

For  $\sigma > 0$  the flow is globally unstable and for  $\sigma < 0$  the flow is globally stable. The frequency of the PVC is given by the real part of the absolute frequency and has been shown to compare extremely well with the measurements [6].

Throughout this study, we assume that the wavemaker location does not change during the transient. This substantially simplifies the problem and we can track the PVC growth rate from a LSA at  $x = 0$ . Moreover, we use a constant eddy viscosity to model the turbulent-coherent interactions in contrast to previous studies [6, 18, 25]. The calibration of a spatially and temporally varying eddy viscosity from the transient data introduces more uncertainty than the potential benefit. The current eddy viscosity is calibrated against the M-flame case to achieve zero growth of the global mode. This results in an effective Reynolds number in Eq. (6) of  $\text{Re} = \frac{UD}{\nu + \nu_t} = 120$  with  $\nu$  as the molecular viscosity and  $\nu_t$  as the eddy viscosity.

As mentioned above, the LSA is based on a transient mean flow, which has to be properly estimated from the time-resolved fields of velocity and density. For this purpose the velocity and density fields are first smoothed temporally using a moving average filter with a span of 5 ms. Then the data is symmetrized in  $y$ -direction, i.e.,  $\mathbf{u}_{\text{symm}}(x, y, t) = (\mathbf{u}(x, y, t) + \mathbf{u}(x, -y, t))/2$ . The resulting fields of velocity and density that are used as input for the LSA are shown in Fig. 7.

## OVERALL CHARACTERISTICS OF THE FLOW AND FLAME TRANSIENT

In this work the dynamics of the bi-stable flame is analyzed using one sustained time-series of 8000 PIV and OH-PLIF measurements, corresponding to a duration of 800 ms. The series includes one transition from V- to M-shape and one sub-

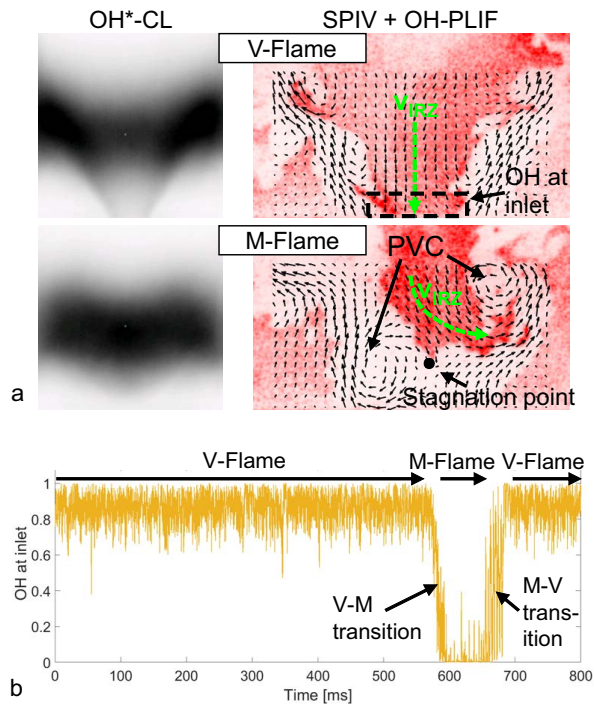


**FIGURE 2.** a) OH-chemiluminescence images and simultaneous PIV and OH-PLIF measurements during phases of V- and M-shape. b) Temporal dynamics of the OH signal at the inlet.

sequent transition back to V-shape. Figure 2a shows two OH-chemiluminescence images averaged during phases of V- and M-shape, respectively. It is seen that the V-flame is attached at the burner nozzle at the bottom, whereas the M-flame is lifted by about 10 mm. Further details of the V- and M-flame can be seen in the corresponding instantaneous PIV and OH-PLIF measurements on the right. While no major vortex structures appear for the V-flame, the flow field of the M-flame exhibits a distinct zig-zag vortex pattern that represents the PVC [6]. This implies the presence of the stagnation point in the inner recirculation zone (IRZ), which stabilizes the M-flame at  $x \approx 10$  mm. For the V-flame, by contrast, the flow in the IRZ goes straightly towards the nozzle at the bottom (green arrow).

The dynamics of the flame transitions is tracked using the OH-PLIF signal integrated over the zone near the chamber inlet (marked with the dashed rectangle). The resulting time-series is shown in Fig. 2b. The OH-signal is high until  $t \approx 570$  ms, which indicates an attached V-flame. The subsequent decrease of the OH-signal indicates a lift-off of the flame, and the formation of a detached M-flame at  $t \approx 600$  ms. Starting at  $t \approx 650$  ms, the OH-

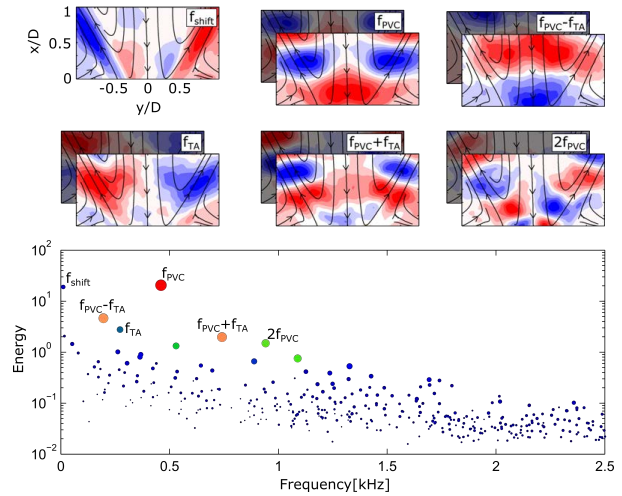


**FIGURE 3.** SPOD spectrum of the recorded transient. The dots represent the average frequency and energy of coupled SPOD modes and the size (and color) of the dots represents the spectral coherence. The most prominent modes are labeled and the corresponding mode shapes (transversal component) are shown in the images above. The mean flow direction is also indicated by streamlines.

signal increases again, indicating the transition back to a V-flame that remains until the end of the series.

The SPOD was applied to the snapshots recorded between  $t = 560$  and  $700$  ms, which covers the entire detachment and reattachment process of the flame. Figure 3 shows the corresponding SPOD spectrum, where the modes are plotted according to their average frequency and relative energy content. The size (or color) of the dots represent the spectral coherence of the modes. From the spectrum we identify a few discrete modes that clearly stick out due to their energy content or due to their spectral coherence. The shapes of these modes are displayed in the frames above the SPOD spectrum showing the fluctuating transversal velocity component with superimposed streamlines of the mean flow field.

The mode with the strongest temporal coherence and the highest energy with  $f_{PVC} = 460$  Hz can be identified as the PVC. The mode shape shows a clear axisymmetry of the transversal component which corresponds to a helical instability with azimuthal wavenumber  $m = 1$ . The SPOD also picks up the first higher harmonic of the PVC indicated by  $2f_{PVC}$ . The highly energetic mode at zero frequency is a shift mode. It represents the change of the mean flow field during the recorded sequence. At  $f_{TA} = 275$  Hz we find a relatively weak mode with poor temporal coherence. From the mode shape we can identify this mode as an axisymmetric flow oscillations. As the axisymmetric mode is not known to become self-excited in swirling jets, we conjecture that

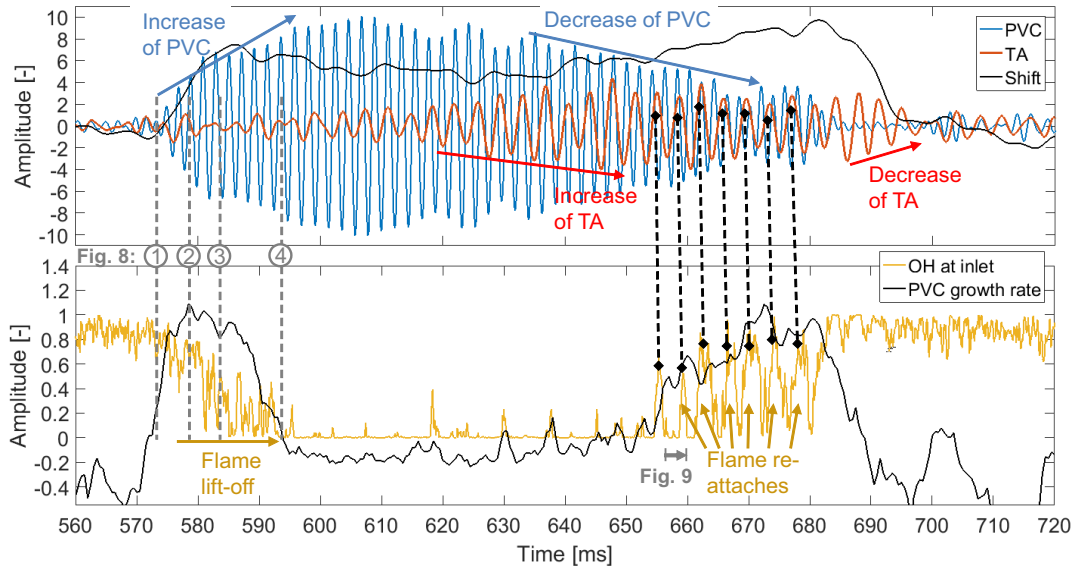


**FIGURE 4.** Dynamics of the V-M and M-V flame shape transition: The upper plot shows the SPOD coefficients of the PVC mode, the TA mode and the shift mode. The lower plot shows the OH signal at the inlet and the PVC growth rate  $\sigma$  obtained from the LSA.

this mode is forced by a thermoacoustic (TA) instability. There are two strong additional modes at the sum and difference of the PVC frequency  $f_{PVC}$  and the frequency  $f_{TA}$ . These modes show the same symmetry as the PVC and represent the interactions between the PVC and the mode at  $f_{TA}$ .

The main dynamical features identified from the SPOD spectrum are the shift mode, the PVC, an axisymmetric mode (TA instability) and two modes that represent the interaction between the PVC and the TA instability. As a next step we consider the temporal evolution of the modes and relate it to the flame shape transition process. In Fig. 4 the SPOD mode coefficients are shown together with the integrated OH at the inlet indicating the flame at-/detachment as described above. The PVC oscillation sets in at about 570 ms and saturates at 600 ms. Thereafter it continuously decays until it completely vanishes at about 680 ms. The flame detachment appears to occur somewhat after the onset of the PVC. The flame remains detached until 650 ms and then behaves intermittently for another 30 ms before it ultimately reattaches at about 680ms, which coincides with the total suppression of the PVC. The shift mode changes simultaneously with the PVC amplitude but it levels off much earlier and remains approximately constant until 690 ms. The TA mode starts to grow once the mean flow shift has terminated at about 590 ms and it continues growing until the mean flow shifts back to its initial shape at about 695 ms. As already seen from the SPOD

spectrum, the TA mode oscillates at a lower frequency than the PVC.

#### STEPS OF V-M and M-V FLAME TRANSITIONS

Based on the results from the SPOD, we postulate a sequence of events that describes the flame detachment and reattachment process. It will serve as a working hypothesis for the subsequent sections, where we investigate the mechanisms in more detail.

1. Slow drifts in the inflow conditions destabilize the PVC.
2. At the border of instability, a turbulent perturbation initiates the PVC.
3. Self-amplification sets in and the PVC evolves.
4. The PVC causes the flame to detach.
5. The PVC saturates at the limit-cycle and the flame stabilizes as an M-flame
6. The M-flame becomes TA unstable.
7. The TA oscillations suppresses the PVC.
8. The flame oscillates and reattaches to the inlet.
9. The attached V-flame is TA-stable and the oscillations die out.

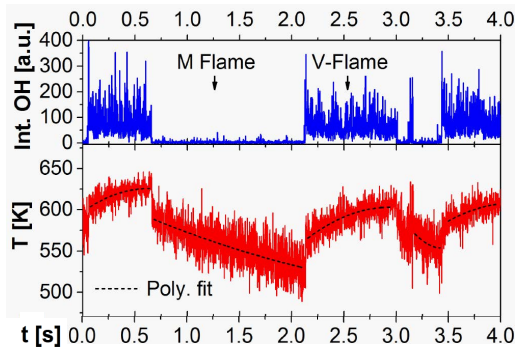


**FIGURE 5.** Temporal variation of bluff body temperature during bi-stable flame shape transitions, reprinted from Ref. [26]

### Step 1: Slow temperature and flow field changes

When the flame changes its shape from V to M or vice versa, the heat load at different parts of the combustion chamber also changes. A recent experimental study for the present bi-stable flame using thermographic phosphors showed that this in turn leads to local changes of the temperature at the bluff body and base plate of the chamber [26]. An exemplary time-series from this study is plotted in Fig. 5. It is seen that the bluff body heats up by more than 50 K when the flame is attached, and cools down when the flame is detached.

The observed drifts of temperature may in turn induce slow drifts of the flow and density fields in the chamber. These drifts were quantified using linear fits of the local time-series of velocities  $v_x$  and  $v_z$  and density  $\rho$  during the long time interval from  $t = 0$  ms until the onset of the flame detachment at  $t = 568$  ms. The resulting drift of the axial velocity field is shown in Fig. 6 for  $t = 0, 300$  and  $568$  ms. It can be seen that the axial velocity field changes indeed, with the main difference being the increase of backflow in the IRZ (marked red). The corresponding drifts of  $v_z$  and  $\rho$  (not shown), on the other hand, were found to be much smaller.

To infer the possible effects on the stability of the PVC, we conduct a LSA of the drifting velocity and density fields at  $t = 0, 100, \dots, 500$  and  $568$  ms. The resulting PVC growth rate at these times is plotted in Fig. 6. It is negative throughout indicating the global stability of the flow field prior to the V-M-transition, but it increases continuously in time and approaches the border of instability ( $\sigma \approx 0$ ) as we get closer to the start of the transition at  $t=570$  ms. Since the main temporal changes were observed for the backflow velocity in the IRZ, this increase of growth rate is largely attributed to the drift of the backflow velocity. This agrees well with the study of Terhaar et al., who found that the PVC growth rate is largely determined by the backflow velocity [27].

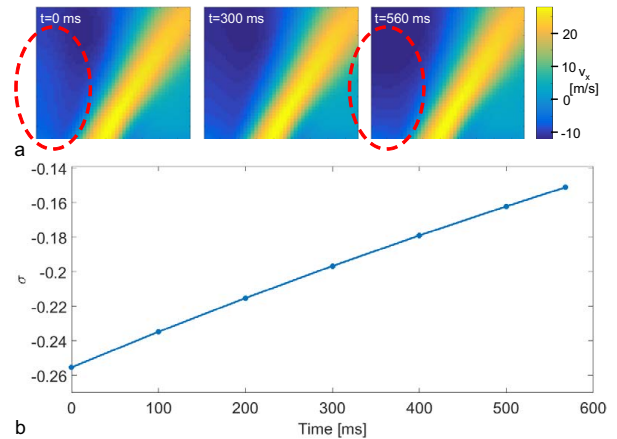


**FIGURE 6.** a) Variation of axial velocity field during the V-flame period  $t = 0 - 568$  ms before the onset of transition. b) Corresponding variation of the PVC growth rate  $\sigma$ .

### Steps 2-3: Onset of the PVC

Once the flow is at the border of instability (PVC growth rate  $\sigma \approx 0$ ), a small variation of the inflow velocities may lead to a short-time destabilization of the PVC. In the previous investigation, a short-time appearance of the PVC was observed that was found to be correlated with a turbulent short-time increase of the inflow velocity and a lift-off of the flame [6]. It was conjectured in that study that the PVC is only sustained once it is strong enough to activate a self-amplifying process. In order to validate this hypothesis, we apply the LSA to the transient mean flow and track the PVC growth rate throughout the flame detachment process.

The role of the PVC in the V-M flame transition starting at  $t \approx 570$  ms is studied in the following using the time series plotted in Fig. 4 and the sequence of PIV and OH-PLIF images shown in Fig. 8. The times of the images in Fig. 8 are marked with dashed lines in Fig. 4. At  $t = 572.8$  ms, the V-shaped flame is well attached and no PVC is present as inferred from the low value of the SPOD PVC mode coefficient in Fig. 4. At  $t = 578.7$  ms, the flame is still attached, but now a distinct PVC-like vortex pattern appears in the flow field, and the PVC mode coefficient has increased significantly. It is difficult to identify the specific event that caused the formation of the PVC since the flow is at the border of instability and thus even minor turbulent fluctuations of velocity or density, possibly out of the plane of measurement, may initiate the formation.

Comparing the PVC amplitude with the PVC growth rate shown in Fig. 4 within the time interval  $t=570-580$  ms, we note that the amplitude of the PVC increases synchronously with the predicted growth rate. This is striking, as one would expect from

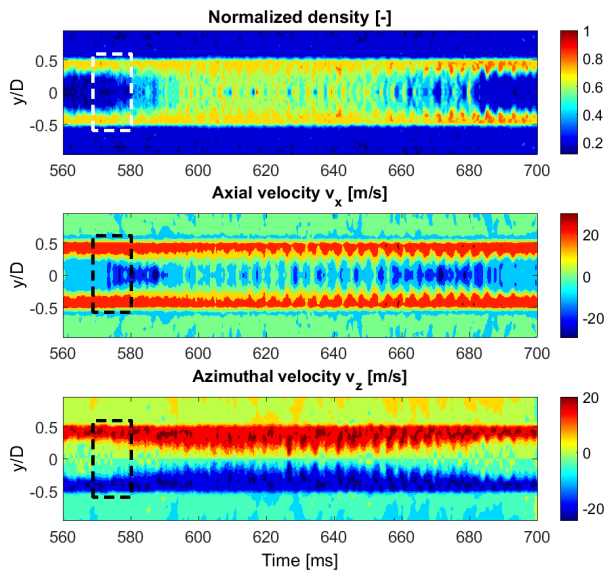


**FIGURE 7.** Temporally smoothed and radially symmetrized flow and density field at the inlet versus time.

mean field theory [28, 29] that the growth rate is positive and maximum prior to the onset of the PVC and it should decrease with increasing PVC amplitude. The increase of the growth rate with an increase of the PVC amplitude is strongly indicative for a self-amplification mechanism. To further study this mechanism, the temporal dynamics of profiles of density and velocity at the inlet ( $x = 0$  mm) that were used for the LSA is shown in Fig. 7. It is seen that during the phase  $t=570-580$  ms, the axial velocity decreases and the stratification of density increases in the region around the centerline ( $y = 0$  mm). Computations based on a constant density field (not shown) indicate that both the modification of the density field and the velocity field contribute to the increase of the growth rate. The results from the transient LSA give credibility to the idea that the interaction between the PVC and the flow/density field induces a self-amplification process that helps to sustain the growth of the PVC. This allows the PVC to arise at subcritical or near critical conditions. The question whether additional mixing or flame lift-off is causing this favorable change of the mean flow and density field cannot be answered at this point.

**Steps 4-5: Flame detachment and saturation of the PVC limit-cycle**

After the PVC has reached a high amplitude at  $t \approx 580$  ms, the attached V-flame starts to detach from the nozzle, as indicated by the decrease of OH signal plotted in Fig. 4. The image for

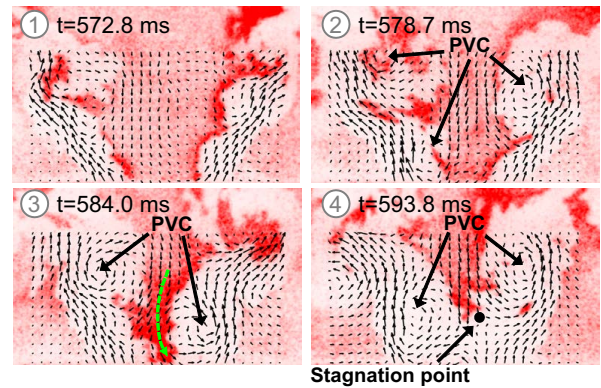


**FIGURE 8.** Sequence of PIV and OH-PLIF measurements showing the formation of the PVC and the subsequent detachment of the flame.

$t = 584.0$  ms in Fig. 8 shows that a strong PVC is present and the size of the IRZ has decreased significantly compared to  $t = 572.8$  ms. There is, however, still a continuous backflow in the IRZ (green arrow) and therefore the flame is still attached. At  $t = 593.8$  ms, the strength of the PVC has further increased and now a stagnation point appears in the IRZ. This blocks the backflow of hot burned gas towards the nozzle and thus stabilizes the flame base near this point.

The flame detachment process is completed at approximately  $t = 600$  ms and the PVC reaches its maximum amplitude. The flow and flame dynamics have converged to a new stable condition, which is characterized by an M-shaped flame with a PVC. The saturation of the PVC occurs through a mean flow modification induced by coherent Reynolds stresses, which is reflected by the decrease of the global mode growth rate  $\sigma$  to zero. The results from the LSA at the limit-cycle ( $t = 600 - 640$  ms) are perfectly in line with our study of the stable M-flame [6] and confirm the saturation mechanism of this type of instability according to mean field theory [28, 29].

**Steps 6-7: Onset of TA instability and suppression of the PVC**

The plots of the SPOD coefficients in Fig. 4 reveal that once the flame has transitioned to a stable M-flame, a TA instability arises after  $t = 620$  ms that goes along with the decay of the PVC oscillations. The dynamics of flow field and flame during one cycle of the TA instability is shown in Fig. 9. At  $t = 657.1$  ms the typical configuration of the M-flame with PVC and lifted flame base is present. At  $t = 658.2$  ms the formation of a symmetric vortex pair above the inlet is observed that is likely caused by the pumping motion of the TA instability. The formation of the symmetric vortices goes along with the formation of a contin-

uous backflow in the IRZ (green arrow). This enables the flame to propagate upstream as seen in the images at  $t = 658.6$ ,  $659.1$  and  $659.6$  ms. At  $t = 660.1$  ms the symmetric vortex pair has decayed and the PVC vortex pattern is re-established, and the flame is lifted again. The comparison of TA mode coefficients and OH signal in Fig. 4 during the phase  $t = 655 - 675$  ms (marked with dashed lines) shows that a similar dynamics of transient flame re-attachment and detachment takes place repeatedly, and that this dynamics is directly coupled to the oscillation of the TA instability.

From the viewpoint of stability theory, the TA instability and the PVC may interact in two different ways according to Terhaar et al. [30]: They may either interact through a *mean flow modification* or through a *mean flow modulation*. The first mechanism implies that the perturbations induced by the TA instability are amplified in the shear layers to large-scale coherent structures that modify the mean flow as such that the PVC becomes linearly stable. This requires a strong convective shear layer instability (Kelvin-Helmholtz instability) at the frequency of the TA instability. The LSA can model this type of interaction, as it is based on the modified mean flow itself. Hence, the suppression of the PVC via this mechanism would be indicated by a *reduction* of the growth rate  $\sigma$ . This is not observed in the present case (see Fig. 4).

The *mean flow modulation* represents a direct nonlinear interaction between the PVC and the TA instability. It can be understood as a modulation of the PVC growth rate and frequency at the TA instability frequency. In other words, the pressure fluctuations induced by the TA instability effectively modulate the massflow into the combustor and thereby the PVC dynamics. Peaks in the frequency spectrum with the sum and difference of the frequencies of the PVC and the TA instability as seen in the SPOD spectrum (Fig. 3) is a clear indicator of this mechanism [30, 31].

Due to the negligence of the nonlinear terms, the LSA cannot account for the nonlinear interactions between the PVC and the TA instability. However, the PVC growth rates derived from the LSA give some indication that the suppression mechanism does indeed not occur via a mean flow modification. As seen in Fig. 4, the global mode growth rate  $\sigma$  gets larger than zero at  $t = 650$  ms and increases as the PVC amplitude decreases. This appears counter-intuitive at the first glance, but it can be explained by mean field theory. When the PVC grows to a finite amplitude (see Fig. 4;  $t = 570 - 600$  ms), it induces Reynolds stresses that act as a forcing on the mean flow. This forcing causes the saturation of the PVC as it modifies the mean flow as such that the PVC growth rate reduces to zero ( $t = 600 - 650$  ms). Once the PVC gets suppressed by the TA instability, the Reynolds stress forcing and corresponding mean flow correction are suppressed as well. This is reflected by a positive PVC growth rate ( $t = 670$  ms). If one would, theoretically, switch off the TA instability at this point, the PVC would immediately grow

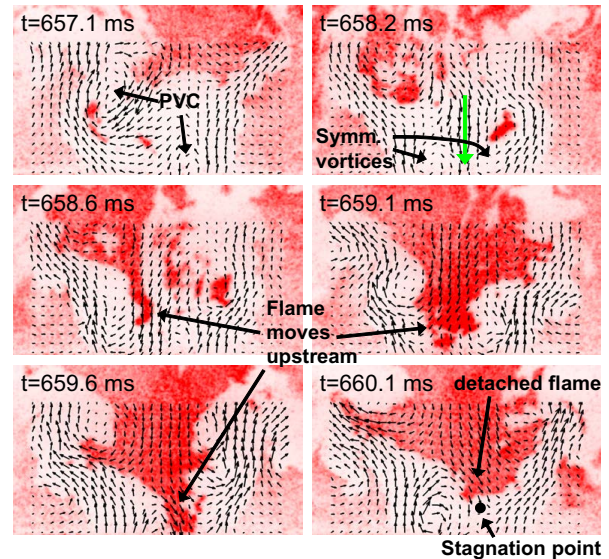


**FIGURE 9.** Sequence of PIV and OH-PLIF measurements showing the transient attachment and detachment of the flame during one cycle of the TA instability.

again at the growth rate that is given by the LSA.

### Steps 8-9: The reattachment process

As described above, the increased amplitude of the TA instability after  $t = 655$  ms leads to periodic flame re-attachment and detachment. At the same time, the PVC amplitude further decreases and reaches a near zero value at  $t = 685$  ms. Therefore, the process of detachment, which is induced by the PVC, is no longer sustained and the flame remains attached after  $t = 685$  ms. It is further seen that after the attached V-flame has stabilized, the TA instability dies out after  $t = 700$  ms, which is most likely attributed to the change of the convective time-delays.

## SUMMARY AND CONCLUSIONS

The flame shape transition mechanisms of a turbulent swirling bi-stable flame have been studied using time-resolved simultaneous stereo-PIV and OH-PLIF measurements, spectral proper orthogonal decomposition (SPOD) and linear stability analysis (LSA). The flame alternates intermittently between an M-shape featuring a precessing vortex core (PVC) and a V-shape without PVC, which implies that the PVC is repeatedly formed and suppressed. It was further observed that a thermoacoustic (TA) instability arises and decays temporarily.

The starting point of the V-M-transition is a slow drift of ve-

locity and density fields during the phase with V-flame that are likely caused by slow variations of temperature within the combustor. The LSA showed that these drifts lead to an increase of the (negative) growth rate of the PVC. When the growth rate is close to zero, a random turbulent event can trigger the formation of the PVC, which then undergoes a self-amplification and reaches a limit-cycle. The PVC in turn leads to the formation of an unsteady stagnation point in the IRZ that causes the lift-off of the flame, which then assumes an M-shape.

The M-V-transition is governed by completely different mechanisms: After the flame has assumed the M-shape, a TA instability develops. The pumping motion of the TA instability leads to a periodic formation of symmetric ring vortices at the nozzle exit, and to a decay of the PVC. The symmetric vortices temporarily suppress the stagnation point in the IRZ and thus lead to periodic short-time re-attachment and subsequent lift-off of the flame. When the PVC has decreased sufficiently, the flame remains attached and assumes a V-shape. When the formation of the V-flame is completed the TA instability decays again.

The results show that the dynamics of turbulent bi-stable swirl flames is governed by complex interactions of TA and hydrodynamic instabilities, and slow temperature-induced drifts of velocity and density. The better understanding of these interactions obtained in this work may support the design of improved swirl combustors with enlarged ranges of stable operation.

#### ACKNOWLEDGMENT

The authors from DLR gratefully acknowledge funding from the DLR project IVTAS. Authors from TU Berlin would like to thank for financial support from the Research Association for Combustion Engines (FVV) and funding from the German Research Foundation (DFG) under project grants PA 920/30-1.

#### REFERENCES

- [1] Fritsche, D., Füre, M., and Boulouchos, K., 2007. "An experimental investigation of thermoacoustic instabilities in a premixed swirl-stabilized flame". *Combustion and Flame*, **151**, pp. 29–36.
- [2] Biagioli, F., Güthe, F., and Schuermans, B., 2008. "Combustion dynamics linked to flame behaviour in a partially premixed swirled industrial burner". *Experimental Thermal and Fluid Science*, **32**, pp. 1344–1353.
- [3] Tummers, M.J., Hbner, A., van Veen, E.H., H. K., and van der Meer, T., 2009. "Hysteresis and transition in swirling nonpremixed flames". *Combustion and Flame*, **156**, pp. 447–459.
- [4] Renaud, A., Ducruix, S., Scoufflaire, P., and Zimmer, L., 2015. "Flame shape transition in a swirl stabilised liquid fueled burner". *Proceedings of the Combustion Institute*, **35**, p. 33653372.
- [5] Guiberti, T., Durox, D., Scoufflaire, P., and Schuller, T., 2015. "Impact of heat loss and hydrogen enrichment on the shape of confined swirling flames". *Proceedings of the Combustion Institute*, **35**, pp. 1385–1392.
- [6] Oberleithner, K., Stöhr, M., Seong, H. I., and Arndt, Christoph M. and Steinberg, A. M., 2015. "Formation and flame-induced suppression of the precessing vortex core in a swirl combustor: Experiments and linear stability analysis". *Combustion and Flame*, **162**(8), pp. 3100–3114.
- [7] Hermeth, S., Staffebach, G., Gicquel, L. Y., Anisimov, V., Cirigliano, C., and Poinso, T., 2014. "Bistable swirled flames and influence on flame transfer functions". *Combustion and Flame*, **161**(1), pp. 184 – 196.
- [8] Selle, L., Lartigue, G., Poinso, T., Koch, R., Schildmacher, K.-U., Krebs, W., Prade, B., Kaufmann, P., and Veynante, D., 2004. "Compressible large eddy simulation of turbulent combustion in complex geometry on unstructured meshes". *Combustion and Flame*, **137**, pp. 489–505.
- [9] Freitag, M., and Janicka, J., 2007. "Investigation of a strongly swirled unconfined premixed flame using les". *Proceedings of the Combustion Institute*, **31**, pp. 1477–1485.
- [10] De, A., Zhu, S., and Acharya, S., 2010. "An experimental and computational study of a swirl-stabilized premixed flame". *Journal of Engineering for Gas Turbines and Power*, **132**, p. 071503.
- [11] Stöhr, M., Yin, Z., and Meier, W., 2016. "Interaction between velocity fluctuations and equivalence ratio fluctuations during thermoacoustic oscillations in a partially premixed swirl combustor". *Proceedings of the Combustion Institute*, **36**, in press, doi: 10.1016/j.proci.2016.06.084.
- [12] Sieber, M., Paschereit, C. O., and Oberleithner, K., 2016. "Spectral proper orthogonal decomposition". *Journal of Fluid Mechanics*, **792**, 4, pp. 798–828.
- [13] Holmes, P., Lumley, J., and Berkooz, G., 1998. *Turbulence, Coherent Structures, Dynamical Systems and Symmetry*. Cambridge Monographs on Mechanics. Cambridge University Press, Cambridge [England].
- [14] Oberleithner, K., Sieber, M., Nayeri, C. N., Paschereit, C. O., Petz, C., Hege, H.-C., Noack, B. R., and Wygnanski, I., 2011. "Three-dimensional coherent structures in a swirling jet undergoing vortex breakdown: stability analysis and empirical mode construction". *Journal of Fluid Mechanics*, **679**, pp. 383–414.
- [15] Sieber, M., Paschereit, C. O., and Oberleithner, K., 2016. "Advanced Identification of Coherent Structures in Swirl-Stabilized Combustors". *Journal of Engineering for Gas Turbines and Power*, **139**(2), p. 021503.
- [16] Gallaire, F., Ruith, M., Meiburg, E., Chomaz, J.-M., and Huerre, P., 2006. "Spiral vortex breakdown as a global mode". *Journal of Fluid Mechanics*, **549**, pp. 71–80.
- [17] Juniper, M. P., 2012. "Absolute and convective instability in

- gas turbine fuel injectors”. In Proceedings of ASME Turbo Expo, GT2012-68253, pp. 189–198.
- [18] Tammisola, O., and Juniper, M. P., 2016. “Coherent structures in a swirl injector at  $re = 4800$  by nonlinear simulations and linear global modes”. *Journal of Fluid Mechanics*, **792**, 003, pp. 620–657.
- [19] Rukes, L., Sieber, M., Paschereit Oliver, C., and Oberleithner, K., 2015. “Transient evolution of the global mode in turbulent swirling jets: experiments and modal stability analysis”. *European Journal of Mechanics - B-Fluids*. (under review).
- [20] Mantič-Lugo, V., Arratia, C., and Gallaire, F., 2015. “A self-consistent model for the saturation dynamics of the vortex shedding around the mean flow in the unstable cylinder wake”. *Physics of Fluids*, **27**(7), p. 074103.
- [21] Khorrami, M. R., Malik, M. R., and Ash, R. L., 1989. “Application of spectral collocation techniques to the stability of swirling flows”. *J. Comput. Phys.*, **81**(1), pp. 206–229.
- [22] Huerre, P., and Monkewitz, P. A., 1990. “Local and global instabilities in spatially developing flows”. *Annual Review of Fluid Mechanics*, **22**, pp. 473–537.
- [23] Chomaz, J. M., Huerre, P., and Redekopp, L. G., 1988. “Bifurcations to local and global modes in spatially developing flows”. *Physical Review Letters*, **60**, pp. 25–28.
- [24] Chomaz, J.-M., Huerre, P., and Redekopp, L. G., 1991. “A frequency selection criterion in spatially developing flows”. *Stud. Appl. Math.*, **84**, pp. 119–144.
- [25] Rukes, L., Paschereit Oliver, C., and Oberleithner, K., 2016. “An assessment of turbulence models for linear hydrodynamic stability analysis of strongly swirling jets”. *European Journal of Mechanics - B/Fluids*, **59**, pp. 205–218.
- [26] Yin, Z., Nau, P., and Meier, W., 2016. “Responses of combustor surface temperature to flame shape transitions in a turbulent bi-stable swirl flame”. *Experimental Thermal and Fluid Science*, in press, doi: 10.1016/j.expthermflusci.2016.11.004.
- [27] Terhaar, S., Oberleithner, K., and Paschereit, C., 2015. “Key parameters governing the precessing vortex core in reacting flows: An experimental and analytical study”. *Proceedings of the Combustion Institute*, **35**(3), pp. 3347 – 3354.
- [28] Noack, B. R., Afanasiev, K., Morzyński, M., Tadmor, G., and Thiele, F., 2003. “A hierarchy of low-dimensional models for the transient and post-transient cylinder wake”. *Journal of Fluid Mechanics*, **497**, pp. 335–363.
- [29] Barkley, D., 2006. “Linear analysis of the cylinder wake mean flow”. *Europhysics Letters*, **75**, pp. 750–756.
- [30] Terhaar, S., Ćosić, B., Paschereit, C., and Oberleithner, K., 2016. “Suppression and excitation of the precessing vortex core by acoustic velocity fluctuations: An experimental and analytical study”. *Combustion and Flame*, **172**, pp. 234–251.
- [31] Moeck, J. P., Bourgooin, J.-F., Durox, D., Schuller, T., and Candel, S., 2012. “Nonlinear interaction between a precessing vortex core and acoustic oscillations in a turbulent swirling flame”. *Combustion and Flame*, **159**(8), pp. 2650–2668.

### 3.4 Stochastic modelling of a noise-driven global instability in a turbulent swirling jet

This article is published in a revised form in the Journal of Fluid Mechanics under the following reference: M. Sieber, C. O. Paschereit, & K. Oberleithner (2021a). “Stochastic modelling of a noise-driven global instability in a turbulent swirling jet”. *Journal of Fluid Mechanics* 916, A7. DOI: [10.1017/jfm.2021.133](https://doi.org/10.1017/jfm.2021.133). The following is a pre-peer-review version of the article. Reprinted with permission. This version is free to view and download for private research and study only. Not for re-distribution, re-sale or use in derivative works. ©Cambridge University Press.

The bifurcation of the helical global mode in a turbulent swirling jet is investigated experimentally. Since the common reduced order flow models do not fit the measured dynamics, stochastic methods are employed to describe the flow.

**Methods:** Existing reduced-order models for the description of hydrodynamic instabilities are extended by a stochastic forcing to describe the dynamics of a turbulent flow. Landau’s amplitude equation and the mean-field model are considered to replicate the flow dynamics. The calibration procedure of the model from stationary measurements is further described in detail.

**Results:** The generic swirling jet setup is used for the investigation, where the bifurcation of the global mode with increasing swirl is considered. The SPOD of high-speed PIV data shows that the emergence of the global mode is the dominant dynamics in this flow at the investigated conditions. The different stochastic models are calibrated by long-time pressure measurements.

**Physics:** The dynamics of the global mode under turbulent conditions is very well captured by the proposed models. The stochastic model clarifies why the global mode is observed at stable flow conditions and how stable and unstable flow conditions are classified from stationary statistics. The different models further detail how the delay in the mean-flow correction can interfere with the estimation of the flow state. The accurate representation of the nonlinear saturation mechanism is essential for the description of the flow physics.

*Under consideration for publication in J. Fluid Mech.*

1

# Stochastic modelling of a noise driven global instability in a turbulent swirling jet

Moritz Sieber<sup>1 2†</sup>, C. Oliver Paschereit<sup>1</sup> and Kilian Oberleithner<sup>2</sup>

<sup>1</sup>Chair of Fluid Dynamics, Institut für Strömungsmechanik und Technische Akustik,  
Technische Universität Berlin, Berlin, Germany

<sup>2</sup>Laboratory for Flow Instabilities and Dynamics, Institut für Strömungsmechanik und  
Technische Akustik, Technische Universität Berlin, Berlin, Germany

(Received xx; revised xx; accepted xx)

A method is developed to estimate the properties of a global hydrodynamic instability in turbulent flows from measurement data of the limit-cycle oscillations. For this purpose, the flow dynamics are separated in deterministic contributions representing the global mode and a stochastic contribution representing the intrinsic turbulent forcing. Stochastic models are developed that account for the interaction between the two and that allow determining the dynamic properties of the flow from stationary data. The deterministic contributions are modelled by an amplitude equation, which describes the oscillatory dynamics of the instability, and in a second approach by a mean-field model, which additionally captures the interaction between the instability and the mean-flow corrections. The stochastic contributions are considered as coloured noise forcing, representing the spectral characteristics of the stochastic turbulent perturbations. The methodology is applied to a turbulent swirling jet with a dominant global mode. PIV measurements are conducted to ensure that the mode is the most dominant coherent structure and further pressure measurements provide long time series for the model calibration. The supercritical Hopf bifurcation is identified from the linear growthrate of the global mode and the excellent agreement between measured and estimated statistics suggest that the model captures the relevant dynamics. This work demonstrates that the sole observation of limit-cycle oscillations is not sufficient to determine the stability of turbulent flows since the stochastic perturbations obscure the actual bifurcation point. However, the proposed separation of deterministic and stochastic contributions in the dynamical model allows identifying the flow state from stationary measurements.

## 1. Introduction

### 1.1. General research approach

Considering a turbulent flow that is dominated by a strong coherent oscillatory motion, the dynamics observed from measurements are twofold. There are the deterministic oscillatory motions potentially stemming from an intrinsic global hydrodynamic instability and the broad-band stochastic motion of the background turbulence. The differentiation of these deterministic and stochastic dynamics is key for accurately interpreting and modelling the dominant flow dynamics. While this separation can be achieved from a Fourier decomposition, a POD or phase averaging of time-resolved data (Holmes *et al.* 2012), it does not reveal the origin of the oscillatory motion independently from the stochastic turbulent forcing. Analogously, if oscillations in turbulent flows are modelled by approaches formerly used to describe instabilities in laminar flows, an appropriate closure

† Email address for correspondence: moritz.sieber@fd.tu-berlin.de

2

for the neglected turbulent fluctuations must be included. In this spirit, the dynamical models developed here built on models that were derived to describe dominant instabilities of laminar flows in the vicinity of the bifurcation point (Stuart 1958). However, these models are extended to account for perturbation from background turbulence by adding a stochastic forcing term with the goal of determining the global stability of turbulent flows based only on observational data.

### 1.2. Linear instabilities in turbulent flows

To predict the bifurcation of laminar flows, linear stability analysis has been applied successfully in many cases (Landau & Lifshitz 1987). The consideration of small perturbations on the base flow and their effect on the eigenmode response of the linearised Navier-Stokes equations provides the decisive exponential growth rate of the coherent structures. Even for unstable flows, where the instability has already grown considerably, the mode shapes and frequencies of the coherent structures can still be derived from a stability analysis based on the mean-flow field (Barkley 2006). This mean-flow stability analysis furthermore allows to assess the sensitivity of the coherent structures to perturbations or forcing of the velocity field (Meliga *et al.* 2012*b*; Carini *et al.* 2017). In the case of turbulent flows, the coherent fluctuations can be interpreted as linear perturbations of the mean flow, while the remaining fluctuations act as an increased viscosity. The accurate modelling of the turbulent viscosity is essential to predict the observed coherent structures in highly turbulent flows (Oberleithner *et al.* 2014; Viola *et al.* 2014; Tammisola & Juniper 2016; Rukes *et al.* 2016).

The mean-flow stability analysis has a general trait resulting from the fact that the mean flow is also formed by the Reynolds stresses induced by the investigated coherent structures. Namely, the predicted amplification rates indicate only neutral stability, no matter how large the original linear instability was that caused the coherent structures to grow. The investigation of Mantič-Lugo *et al.* (2015) demonstrates this property from a coupled simulation using mean-field stability analysis and the steady Navier-Stokes equation to describe the transition of the cylinder wake flow from an unstable stationary state to saturated limit-cycle oscillations of the Kármán vortex street. There, it is shown that the Reynolds stresses of the coherent structures change the mean flow such that the instability becomes neutrally stable when the flow reaches the limit-cycle.

The concept of this nonlinearity describing the saturation mechanism of hydrodynamic instabilities is referred to as mean-field theory. The idea of a weakly nonlinear saturation was first given by Landau's amplitude equation (Landau 1944) derived from analytical reasoning. In the context of nonlinear stability theory, the mean-field theory explains the observation of supercritical and subcritical Hopf bifurcations via hydrodynamic instabilities (Stuart 1958). The work of Noack *et al.* (2003) further shows that also the transient dynamics from a steady state to the limit-cycle can be covered by a simple mean-field model including an oscillatory mode for the dynamics of the instability and a shift-mode capturing the slow mean-flow corrections. In this work, the model structure and naming are adopted and extended by the consideration of stochastic disturbances induced by background turbulence.

An open aspect of describing transient dynamics by the amplitude equation and the mean-field model is the time-delay between a change of the oscillation amplitude and the resulting correction of the mean flow that leads to a change of the amplification rate. Stuart (1958) assumed this to be an instant feedback which justifies the use of only the amplitude equation without considering the shift-mode. However, experimental investigations showed that there are flows that exhibit a delay in this feedback, which motivates the delay-saturation model suggested by Villermaux & Hopfinger (1994). In

the present work, this delay-saturation model cannot be used because the involved delay operation constitutes a memory of the system that conflicts with the requirements of the stochastic method. Alternatively, the mean-field model allows considering this delay through the inclusion of the shift-mode as an additional state variable. Accordingly, we adjust the mean-field model to the dynamics observed in the flow.

### 1.3. Stochastic methods for system identification

The identification of the fundamental properties of a physical system from observation data is essential for retaining physical parameters of the flow from the calibrated models. From the many aspects of this field, we focus on the output-only calibration of grey-box models (Ljung 2012). The term output-only refers to the utilisation of observation data of a system. This approach is in contrast to input-output data that refers to an active forcing of the system and recording of the corresponding response. The term grey-box model refers to the use of empirical models that are motivated by physics or the observed dynamics. This is in contrast to white-box models which are derived directly from the governing equations and also in contrast to black-box models that only reproduce dynamics and are not related to the physics of the system.

The models employed in this work for the system identification are the amplitude equation and the mean-field model. Having two and three state variables, respectively, these are low-order models that represent only the dominant dynamics of a turbulent flow. The remaining dynamics are considered as stochastic turbulent fluctuations that may enter the model as a stochastic forcing. From the experimental perspective, an output-only calibration is performed that uses only stationary measurements of the flow. However, the intrinsic forcing of the flow by its background turbulence is also considered for the system identification. This requires to estimate the properties of the stochastic forcing in line with the deterministic dynamics of the flow.

The accurate treatment of such stochastic equations requires a systematic introduction of the model. An overview of the topic can be found in the review of Friedrich *et al.* (2011) about stochastic methods for data-driven identification of physical systems. The general concept of the approach is a strict separation of deterministic and stochastic contributions in the model. This is obtained by requiring the model to have the form of a Langevine equation. Therefore, the model must account for all the deterministic dynamics contained in the data. It is not possible to oversimplify the model and lump secondary dynamics to the stochastic forcing. The stochastic part must be uncorrelated from the deterministic part to handle the data in this framework.

The requirement of the stochastic differential equation having the form of a Langevine equation implies that the future evolution of the system depends only on the current state of the system. Therefore, there should be no memory of the system or hidden variables that interfere with the resolved state variables. Moreover, the stochastic component of the equation must be uncorrelated such that the evolution of the system behaves like a Markov process. All deterministic dynamics present in the observed system must be described by the model since they cannot be lumped together with the unresolved stochastic turbulence. However, a sufficient separation of time-scales allows treating some of the dynamics as stochastic contributions. The assumption of a Markov process allows describing the temporal evolution of the probability density function (PDF) by the corresponding Fokker-Planck equation. This eliminates the stochastic variable and gives a probabilistic description of the system that can be compared to statistical moments obtained from measured data.

The basic principle of stochastic methods proposed by Friedrich *et al.* (2000) utilises the direct computation of the drift and diffusion terms from the first and second statistical

4

moments of the data. This requires to conduct a limiting process that may conflict with the non-vanishing correlation time of the stochastic process (Lehle & Peinke 2018). An alternative is the evaluation of finite time propagation of the PDF with the Fokker-Planck equation and comparison with the PDF of the data (Kleinhans & Friedrich 2007) or the direct estimation of the parameters from the adjoined Fokker-Planck equation (Boujo & Noiray 2017). Furthermore, the stationary PDF of the data can be compared to the stationary solution of the Fokker-Planck equation as pursued by Noiray & Schuermans (2013), Bonciolini *et al.* (2017) and Lee *et al.* (2019).

Stochastic methods were applied to identify universal features of the turbulent cascade (Friedrich & Peinke 1997; Reinke *et al.* 2018), leading to very simple models that correctly capture the spectral properties of the cascade. Concerning the thermoacoustic system of a combustor, Noiray & Schuermans (2013) proposed various approaches to derive the parameters of a Van der Pol oscillator from different measures of the data. This was further extended to handle also systems with non-white noise (Bonciolini *et al.* 2017). The existence of coherence resonance in a thermoacoustic system was also shown by Kabiraj *et al.* (2015), where the external stochastic forcing allowed to further classify the associated Hopf bifurcation before the onset of the instability (Saurabh *et al.* 2017).

The stochastic dynamics of turbulent axisymmetric and bluff-body wakes were studied by Rigas *et al.* (2015) and Brackston *et al.* (2016), respectively, showing that the symmetry-breaking modes are governed by simple stochastic models. The dynamics of a freely rotating disc in uniform flow was shown by Boujo & Cadot (2019) to be governed by a stochastic low-order model that captures the main features. The self-excited oscillations in the fluid acoustic system of bottle whistling were furthermore shown to be governed by a randomly forced Van der Pol oscillator (Boujo *et al.* 2020). The investigations of Zhu *et al.* (2019) and Lee *et al.* (2019) revealed that the bifurcation, leading to the global instability of a low-density jet, can be characterised from the evaluation of stochastic forcing in the stable regime of the flow.

Beyond these very recent investigations, there were previous approaches to model the dynamics of turbulent flows by stochastic equations. For example, the description of the *bursts* in boundary layers as noisy heteroclinic cycles by Stone & Holmes (1989) and the control of such dynamics by Coller *et al.* (1994). The occurrence of noise-induced dynamics of marginally stable modes is often also referred to as coherence resonance referring to the work of Gang *et al.* (1993). Another probabilistic description of fluid dynamics was recently proposed by Kaiser *et al.* (2014), who used data-driven state-space segmentation to identify the related transition probability that allows inferring the dynamics of the flow. In the work of Brunton *et al.* (2016), the residuals of the model are interpreted as intermittent forcing of a deterministic system, this is in contrast to the present approach, where Markov properties of the stochastic forcing are expected.

Besides the work of Zhu *et al.* (2019) and Lee *et al.* (2019), there are no applications of stochastic methods to describe the characteristics of a global hydrodynamic instability. In contrast to their work, the current investigation does not rely on external forcing of the flow but utilises the background turbulence as intrinsic stochastic forcing.

#### 1.4. Detailed research approach

In the present work, we consider the dominant coherent structure occurring in turbulent jets at high swirl. Swirling jets are commonly used in combustors to provide anchoring of the flame (Syred & Beér 1974). This is due to the unique feature of the flow which is known as vortex breakdown. If the swirl intensity in the jet exceeds a certain threshold, the jet breaks down and forms a recirculation region in the centre (Billant *et al.* 1998). In combustion applications, this provides recirculation of hot exhausts that

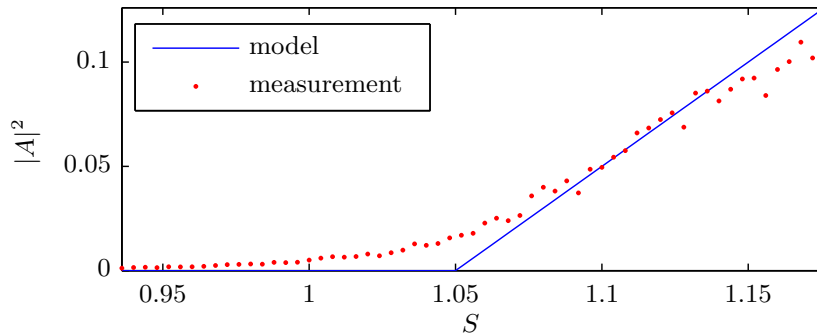


FIGURE 1. Bifurcation diagram for a supercritical Hopf Bifurcation as described by the Landau equation. The solid line gives the limit-cycle of the model and the dots indicate measurements from a turbulent flow.

stabilises the flame. The swirl intensity that governs the onset of vortex breakdown is quantified by the swirl number, given by the ratio of azimuthal to axial momentum flux (Chigier & Chervinsky 1967) (see also appendix A for the definition).

Beyond the onset of vortex breakdown, the swirl number remains the major control parameter for a global hydrodynamic instability. With increasing swirl number, the flow passes through a supercritical Hopf bifurcation that gives rise to a global mode (Gallaire & Chomaz 2003; Liang & Maxworthy 2005; Oberleithner *et al.* 2011). It takes the form of a single helical structure that precesses around the centre axis of the jet. In the following, this specific global mode is referred to as a *helical mode*. In combustion-related applications, the helical mode is also known as a *precessing vortex core* (Syred & Beér 1974; Terhaar *et al.* 2014; Vanierschot & Ogun 2019).

The supercritical Hopf bifurcation of global modes are commonly described by the Landau equation (Landau 1944). Accordingly, the limit-cycle amplitude of the helical mode  $|A_{LC}|$  should be proportional to the swirl number  $S$  as

$$|A_{LC}|^2 \propto S - S_c, \quad (1.1)$$

with the swirl number being the control parameter that governs the instability of the global mode. The critical swirl number  $S_c$  marks the bifurcation point, where the flow transitions from a stable to an unstable state.

However, in turbulent flows, the helical mode dynamics are subjected to stochastic turbulent forcing, which leads to a deviation from the Landau model in the vicinity of the bifurcation point. This is shown in figure 1, where measurements in a turbulent swirling flow reveal a continuous increase of the helical mode amplitude at potentially subcritical conditions. This observation calls for stochastic methods to develop a dynamical system that explains the diffusion of the observed dynamics. Such a model differentiates between helical mode activity due to an intrinsic flow instability or due to turbulent forcing, providing a clear description of the dynamical flow state that enables the identification of the bifurcation point.

The immediate approach to handle these stochastic contributions is the investigation of the amplitude equation with additive noise, and the estimation of equation parameters by inspection of the stationary probability density function (PDF) of measured amplitudes. This is also pursued in the present investigations as the first attempt. Therefore, an analytical expression for the stationary PDF is derived from the amplitude equation and calibrated from measured PDFs as done in the investigations of Noiray & Schuermans (2013), Bonciolini *et al.* (2017) and Lee *et al.* (2019).

For reasons of simplicity, the noise in the stochastic equation is usually assumed to be

6

white, which is not the case for turbulent perturbations. This property is addressed in this work by the use of coloured noise created by an Ornstein–Uhlenbeck (OU) process (Hänggi & Jung 1994). The effect of the noise properties on the accuracy of the system identification is assessed from a numerical model study, as done by Bonciolini *et al.* (2017). Similar to their study, a sufficient separation of noise and model time-scales is found to be decisive for the reliability of the approach.

Furthermore, a mean-field model is incorporated in the dynamical system to capture the mean-field corrections related to the saturation of the instability on the limit-cycle. This provides a deeper insight into the interaction between deterministic and stochastic dynamics. However, the system identification is adapted since no analytical expression for the stationary PDF was obtained. Therefore, it is calibrated and adapted to fit directly the estimated dynamics derived from the data. This is in contrast to the amplitude equation, which can be solved analytically and compared to well-converged PDFs, allowing an application to a large class of problems.

The remainder of this work is organised in the following way. In section 2 we outline the main experimental methods and the identification of coherent structures from the data and the dynamic content of the flow is presented from a decomposition of PIV and pressure measurements. In section 3, the stochastic amplitude equation and the corresponding system identification are described, followed by the validation of the approach based on a numerical study and the calibration of the model from the experimental data. Section 4 shows the stochastic mean-field model and its calibration from measurement data. Finally, the main findings are summarised in section 5.

## 2. Experimental details and observations of swirling jet dynamics

### 2.1. Experimental setup and data acquisition

Experiments are conducted using a generic swirling jet setup, shown schematically in figure 2 together with the measurement devices used. It consists of an adjustable radial swirl generator that is supplied at four azimuthal positions by regulated air from a pressure reservoir. Several grids ensure a homogeneous distribution of the supplied air. The swirling air is guided normally to the swirler plane in a circular duct of 150 mm diameter followed by a contoured contraction reducing the diameter to  $D = 51$  mm. The jet is emanating into a large space (4 m wide, 3 m high) that constitute unconfined boundary conditions in radial and streamwise direction. Further details of the experimental setup can be found in Rukes *et al.* (2015); Müller *et al.* (2020).

The jet is investigated at a fixed mass flow of  $50 \text{ kg h}^{-1}$  that results in a nozzle bulk velocity of  $u_{\text{bulk}} = 5.7 \text{ m s}^{-1}$  and a respective Reynolds number of 20.000 based on the nozzle diameter  $D$ . The swirl intensity is adjusted by an automated stepper motor that controls the angle of the swirler vanes. Swirl numbers in the range of 0.8 to 1.35 were tested. The current swirl number definition is based on the linear fit of the integral swirl number against the angle of the swirler vanes. The reason for this approach is due to difficulties with a consistent formulation of the integral swirl number across the investigated swirl range, which is further detailed in appendix A.

The velocity field of the swirling jet is captured by high-speed particle image velocimetry (PIV) as indicated in figure 2. A meridional section of the jet is illuminated by the laser and recorded by a high-speed camera. The flow is seeded by silicon-oil droplets (DEHS:Bis(2-ethylhexyl) sebacate) of a nominal diameter smaller than  $5 \mu\text{m}$  which are added to the air between mass flow controller and swirler. For each configuration, a set of 2000 images was recorded at a rate of 1 kHz. The images were processed with PIVview

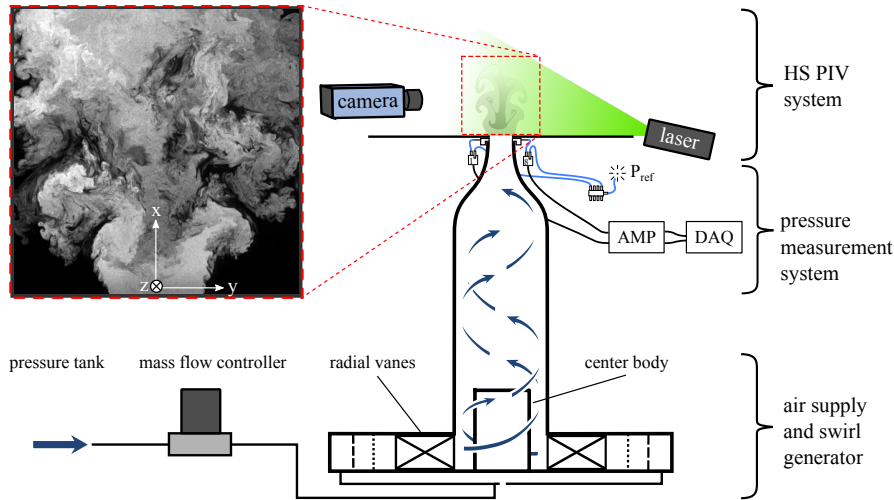


FIGURE 2. Schematic of the experimental setup and the utilised measurement systems. The magnified picture of the flow field is an experimental dye visualisation of the jet.

(PIVTEC GmbH) using standard PIV processing (Willert & Gharib 1991) enhanced by iterative multigrid interrogation (Soria 1996) and image deformation (Huang *et al.* 1993).

The high-speed PIV captured only the axial and radial velocity component, which is sufficient for the determination of coherent structures. The time resolution of the measurement, however, is essential for the later analysis. The computation of the swirl number, however, requires also the mean azimuthal velocity component. It was determined from non-time-resolved stereoscopic PIV measurements conducted in a previous investigation (Rukes *et al.* 2015).

Together with the PIV acquisition, pressure measurements were conducted. The probes are located at eight positions around the circumference of the nozzle lip, which are referred to in the following as  $p_k$   $k = 1 \dots 8$ . The piezoresistive sensors with a range of 1 kPa were amplified with an in-house bridge amplifier and recorded with a 24bit AD converter at a rate of 2 kHz. The resonance frequency of the sensor-tubing-system was at 400 Hz, which is acceptable for the conducted investigations, where the oscillations of the dominant mode were in the range of 50 Hz to 80 Hz. The resonance of the sensor caused an amplification of the signal by 2% at 50 Hz and 4% at 80 Hz. Other than the PIV, the pressure was recorded for 60 sec to achieve converged statistics. Pressure measurements were conducted in an automated procedure, where the swirler angle was increased in steps of  $0.1^\circ$  corresponding to  $\Delta S$  of  $4 \times 10^{-3}$ .

## 2.2. Identification of coherent structures from measurement data

This section details how the helical mode is identified from the PIV and pressure data. The first part covers the extraction of the dominant coherent structures from the PIV data using the spectral proper orthogonal decomposition (SPOD) as described by Sieber *et al.* (2016a). The method allows for a modal decomposition of the velocity snapshots, reading

$$\mathbf{v}(\mathbf{x}, t) = \bar{\mathbf{v}}(\mathbf{x}) + \mathbf{v}'(\mathbf{x}, t) = \bar{\mathbf{v}}(\mathbf{x}) + \sum_{i=1}^N a_i(t) \Phi_i(\mathbf{x}), \quad (2.1)$$

where the fluctuating part of the velocity field  $\mathbf{v}'$  is expressed as a sum of spatial modes  $\Phi$  and time coefficients  $a$ . The used variant of the SPOD provides a time-domain representation of the decomposition, which is essential for the present analysis of flow

8

dynamics. This is in contrast to a related frequency domain representation (Towne *et al.* 2018), which is not applicable here.

The SPOD has promising potential for the analysis of time-domain phenomena in turbulent flows (Noack *et al.* 2016). This has been shown for the identification of dynamics in the flow of a separated airfoil (Ribeiro & Wolf 2017), the transient interaction and switching between different dynamics in a combustor (Stöhr *et al.* 2017), or the provision of proper dynamics for the autonomous modelling of flow dynamics (Lui & Wolf 2019). The principal advantage of the SPOD in these applications is that the dynamics are separated according to their space-time coherence while the time information is maintained, allowing the time-domain analysis of the individual dynamics.

The SPOD is based on the snapshot POD proposed by Sirovich (1987), with the extensions that the snapshot correlation matrix

$$R_{i,j} = \frac{1}{N} \langle \mathbf{v}'(\mathbf{x}, t_i), \mathbf{v}'(\mathbf{x}, t_j) \rangle \quad (2.2)$$

is filtered, which constrains the spectral bandwidth of the coefficients. The advantage of this approach against spectral filtering of data before or after performing the POD is that the filtering is implicitly handled by the decomposition. Hence, there is no need to specify central frequencies of individual phenomena within the data or to apply digital filters. Instead, only the filter width  $N_f$  must be chosen, as it sets the bandwidth of the coefficients. The filter is implemented as a simple convolution filter of the snapshot correlation matrix

$$S_{i,j} = \sum_{k=-N_f}^{N_f} g_k R_{i+k,j+k}. \quad (2.3)$$

where  $g_k$  is a Gaussian filter kernel. Other than snapshot POD, the SPOD needs time-resolved data to allow time-domain filtering of the data. Further details on the selection of the filter size and handling of boundary conditions can be found in Sieber *et al.* (2016a, 2017). Beyond the application of the filter to the correlation matrix, the procedure is the same as for the snapshot POD. In the present investigation, a filter width  $N_f$  of two times the oscillation period is used.

For further analysis, the link of mode pairs in the decomposition is identified from a cross-spectral correlation among all possible pairs of coefficients (harmonic correlation as in Sieber *et al.* (2016a)). The appearance of coherent structures as pairs is commonly observed in the POD of real-valued input data. It can be understood as the real and imaginary part of a mode that is obtained from a spectral analysis. In the following, mode pairs (e.g. SPOD mode 1 and 2) are treated as one mode and they are coupled for the time domain analysis as the real and imaginary part of a complex coefficient  $A(t) = a_1(t) + ia_2(t)$ .

In the present application, the pressure measurements are used for the dynamic modelling since they allow much longer time series resulting in better-converged statistics than the PIV snapshots. The agreement of mode amplitudes determined from PIV and pressure measurements is detailed in appendix B. To obtain the mode amplitude, the pressure measurements from the eight positions around the nozzle lip are decomposed azimuthally into Fourier modes, according to

$$\hat{p}_m(t) = \frac{1}{8} \sum_{k=1}^8 p_k(t) e^{-imk\pi/4}, \quad (2.4)$$

where  $m$  indicates the azimuthal mode number. The instantaneous amplitude of the

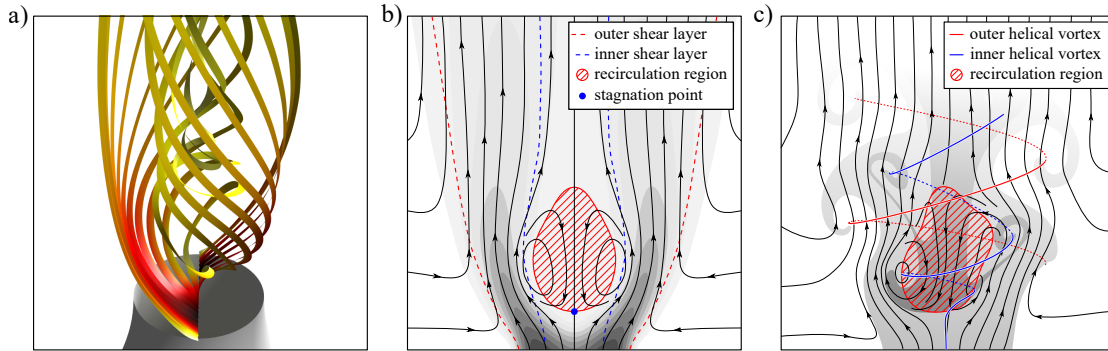


FIGURE 3. Schematics of the flow field of a swirling jet: a) stream lines of the mean velocity field coloured by velocity magnitude, b) slice through the symmetry axis of the mean velocity field represented by sectional streamlines and velocity magnitude as gray contour levels, c) instantaneous velocity field indicated by sectional streamlines and coherent structure as gray background. Specific features of the flow fields are marked and indicated in the legends. The breakdown bubble is indicated by the recirculating flow in the centre.

helical mode with azimuthal wavenumber  $m = 1$  is then given as  $A(t) = \hat{p}_1(t)$ , accounting for the single-helical shape of this coherent structure. The signal was filtered around the average oscillation frequency of the helical mode  $f_o$  in the band  $[\frac{2}{3}f_o, \frac{3}{2}f_o]$ . To set the centre of the filter band, the frequency of the mode was identified from the peak in the unfiltered spectrum and also compared to the frequency of the SPOD coefficients from the PIV measurements. In the low swirl regime where no peak was visible, the frequency was extrapolated from larger swirl numbers.

In addition to the oscillatory mode, the dynamics of the slow-varying contributions to the flow are obtained from the pressure measurements. They are represented by the shift-mode that is determined from the  $m = 0$  pressure mode:  $B(t) = \hat{p}_0(t)$ . Thereby, a relation of the mean flow and the mean pressure is assumed which is supported by the data shown in appendices A and B. The  $\hat{p}_0$  signal is low pass filtered at  $4f_o$  to remove acoustic perturbations from the upstream duct. All pressure signals are normalised by the maximum amplitude of the helical mode, being 6 Pa, to ease the numerical procedures and improve the readability of graphs. The normalisation is not related to the dynamic pressure which would be around 20 Pa in the present case.

### 2.3. Flow field and dominant coherent structures

The mean flow field and the structure of the global mode in the swirling jet are sketched in figure 3. Due to vortex breakdown, the flow forms an annular jet with inner and outer shear layers. The global mode manifests in the central vortex of the jet that meanders and wraps around the breakdown bubble in a helical shape. The roll-up of the outer shear layer is synchronised with this motion resulting in a secondary helical vortex. These counter winding helical vortices cause a spiralling, flapping motion of the annular jet. With respect to the mean flow, the helical vortices are co-rotating and counter winding. In the current section, the global mode is referred to as helical mode, in contrast to secondary dynamics that are also observed in the data. The helical mode is considered as the oscillatory mode in the amplitude equation.

The velocity field and pressure spectra across the investigated swirl range are collectively presented in figure 4. The velocity is normalised with the bulk velocity and the frequency is normalised with the bulk velocity and nozzle diameter to obtain Stouhal numbers as  $St = \frac{f_o D}{u_{\text{bulk}}}$ .

The mean velocity fields (figure 4 top row) show typical features of a swirling jet

10

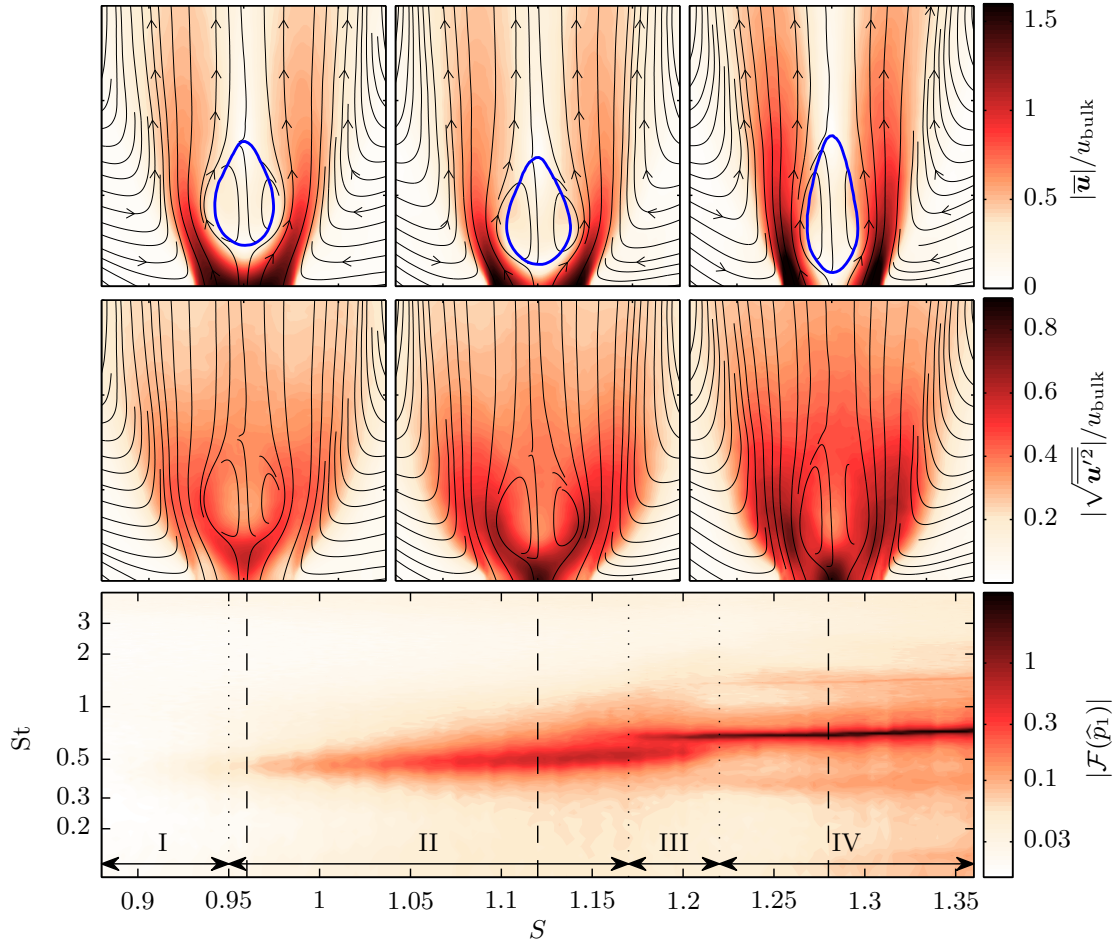


FIGURE 4. Mean flow and spectrum of the dominant oscillatory mode at different swirl numbers. The top row shows contours of relative velocity magnitude together with streamlines and a thick blue line indicating zero axial velocity. The mid-row shows the relative turbulence intensity as contours together with streamlines. The bottom plot shows the magnitude of the spectrum of the pressure Fourier mode  $\hat{p}_1$  with a log scaled colour-map for all investigated swirl numbers across the relevant Strouhal number range. The dashed vertical lines indicate the respective swirl number ( $S = [0.96, 1.12, 1.28]$ ) of the mean flow plots above. The arrows and vertical dotted lines indicate different regimes in the swirl number range.

undergoing vortex breakdown as sketched in figure 3. From the low to the medium swirl number case there is only little change of the velocity field. The breakdown bubble mainly moves upstream closer to the nozzle in connection with an increased jet spreading. At large swirl number, the breakdown bubble becomes narrower and longer, while the jet spreading decreases.

The turbulence intensity (figure 4 mid row) constantly increases with the swirl strength. The peak intensity is concentrated in the shear layers, while the value at the upstream stagnation point is always the largest. With increasing swirl the shear layers become thicker and the fluctuations become spread over a larger area.

Several different regimes are visible from the spectrum of the helical mode (figure 4 bottom). Starting from low swirl, there is a range where no oscillations are observed. At swirl numbers of approximately 0.95 there is a slight peak in the spectrum at Strouhal numbers around 0.5. With increasing swirl, the intensity of the peak increases as well as the frequency. Throughout the range, the spectral peak is rather broad. At swirl number

of 1.17, a second, narrow peak at slightly higher frequency appears which continues to grow while the previous one fades out. After the first peak disappeared at a swirl number of 1.22, the second peak further grows and the frequency increases slightly. At the upper end of the range, the Strouhal number is at 0.73.

Based on the characteristics of the pressure spectra, the investigated swirl range can be divided into four regimes as indicated in the bottom plot of figure 4. Regime I corresponds to the swirl range where no helical mode dynamics are observable. In regime II, the helical mode appears with a broad spectral peak and the mean flow shows a continuous change. Regime III corresponds to a bi-stable condition. It is characterised by intermittent switching between the states in regimes II and IV, which is visible from time-series data not shown here. Regime IV shows a similar trend as regime II, but with a sharper spectral peak and a longer breakdown bubble.

To provide an overview of the range of dynamics observed in the flow, SPOD is conducted based on flow snapshots acquired at three selected swirl numbers. The cases correspond to the mean velocity fields given in figure 4. The SPOD spectrum presented in figure 5 shows all modes contained in the flow. The detailed picture of spatial structures and coefficient spectra are given for some modes, which are selected such that a consistent ordering is obtained for the different swirl numbers.

Figure 5 (top-row) shows the SPOD results for the low swirl case  $S = 0.96$ , which corresponds to the onset of the helical mode. The first SPOD mode (#1) shows a clear peak at  $St = 0.4$  and the corresponding spatial structure shows typical characteristics of the helical mode (Rukes *et al.* 2015). Another dominant structure (mode #4) with low frequency ( $St = 0.05$ ) is also prominent. It corresponds to an axial movement of the breakdown bubble as also observed previously by Rukes *et al.* (2015). The other inspected modes (#2 and #3) do not indicate clear structures but might be precursors of the dynamics that become more pronounced at higher swirl numbers.

The medium swirl case  $S = 1.12$  (figure 5, mid-row) shows the helical mode again as the most dominant structure (mode #1). There is little change in the mode shape compared to the low swirl case, but its relative energy increased significantly and it oscillates at a higher frequency of  $St = 0.5$ . There exists another prominent coherent structure at  $St = 0.3$  (mode #2) that resembles a helical mode in the wake of the breakdown bubble, which has already been observed in combustor flows (Sieber *et al.* 2016b; Terhaar *et al.* 2014). The location in the wake and the single helical mode structure indicates a strong relation to the global mode that is observed in laminar swirling flows, known as spiral vortex breakdown (Ruith *et al.* 2003; Gallaire *et al.* 2006; Qadri *et al.* 2013). In the following, this structure is called the wake mode. At  $St = 0.8$  there is another mode that slightly sticks out from the continuous spectrum (mode #3). The spatial structure does not exhibit clear symmetries and the coefficient spectrum shows two peaks at  $St = 0.8$  and  $St = 1.0$ . This mode supposedly represents the helical modes second harmonic together with an interaction between the wake mode and the helical mode. The mode at very low frequency (mode #4) corresponds to the slow-varying changes of the flow, which is still considerable.

For the high swirl case  $S = 1.28$  (figure 5, bottom row), the mode dynamic is very clear and the low-frequency modes are reduced. The helical mode (#1) at  $St = 0.69$  has further gained in energy and now clearly exhibits higher harmonics at  $St = 1.38$  (mode #3) and  $St = 2.1$ . The wake mode (#2) has consolidated at  $St = 0.36$  and also exhibits a higher harmonic at  $St = 0.77$  (mode #4). At the frequency of  $St = 1.05$ , where interactions between helical mode and wake mode are expected, there is an agglomeration of less dominant modes. This indicates an interaction between both structures, which, however, is not captured by a single mode.

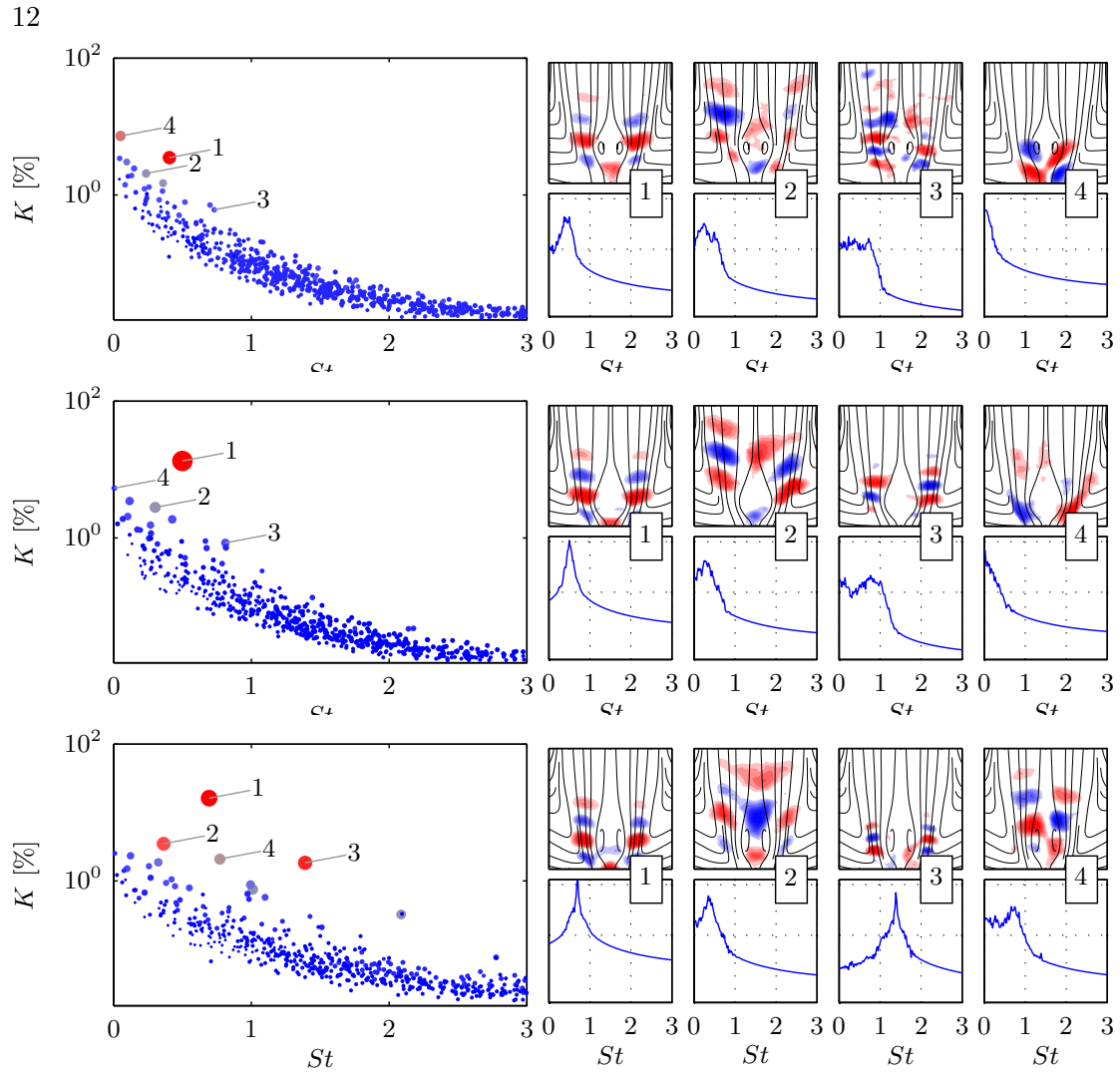


FIGURE 5. SPOD spectrum (left) and spatial modes with mode coefficient spectrum (right) for  $S = [0.96, 1.12, 1.28]$  (from top to bottom). The spectrum shows mode energy against Strouhal number, where each dot corresponds to a mode pair and the colour/size indicated the spectral coherence. For selected modes the spatial and spectral content is detailed as indicated by the numbers. The spatial modes are shown by the transverse velocity together with streamlines of the mean flow. The mode coefficients are given as power spectral density.

Overall, the SPOD of the flow shows only little change of the helical mode shape with increasing swirl number. The observed increase in energy and the shift of the oscillation frequency is consistent with the pressure spectra (figure 4). The variations of the mean flow decrease with increasing swirl, which is probably due to the proximity of the breakdown bubble to the nozzle lip at high swirl, which constraints its movement. The SPOD reveals other modes such as the wake mode and higher harmonics, but the helical mode is most dominant for the entire swirl range. The identified interaction modes remain weak with energies of at least one order of magnitude less than the helical mode. Therefore, the interaction between the helical mode and subdominant modes can be neglected in the following analysis.

### 3. Modelling and system identification by the amplitude equation

The dynamics of the helical mode are modelled by a stochastic amplitude equation. The corresponding model is derived at the beginning of the following section. This is followed by the consideration of coloured noise forcing and the derivation of the calibration procedure from data. Thereafter, the reliability of the model is investigated from a numerical study and the model is calibrated from experimental data.

#### 3.1. Model design for the stochastic amplitude equation

The form of the presented model is based on the stochastic methods described by Friedrich *et al.* (2011). Accordingly, the stochastic differential equation that describes the temporal evolution of a system has the form of a Langevine equation

$$\dot{X} = f(X) + g(X)\xi, \quad (3.1)$$

where the dot indicates the time derivative of the state  $X$ . The deterministic contributions are collected in the drift  $f$  and stochastic contributions are covered by the diffusion  $g$ . The stochastic forcing  $\xi$  is Gaussian white noise with vanishing correlation time  $\langle \xi(t)\xi(s) \rangle = \delta(t-s)$  ( $\delta$  being the Dirac delta function). The vanishing correlation, which was initially referred to as a Markov process, is essential for the later analysis of the equation.

The amplitude equation serves here as the most simple model to describe the dynamics of the helical mode and the leading-order nonlinearity that governs the saturation at the limit-cycle (Stuart 1958; Landau & Lifshitz 1987). It is given as

$$\dot{A} = (\sigma + i\omega)A - \alpha |A|^2 A + \dots, \quad (3.2)$$

where  $A$  is a complex variable that describes the modal coefficient of a periodic perturbation of the flow field. The model parameters are the oscillation frequency  $\omega$ , amplification rate  $\sigma$  and the Landau constant  $\alpha$ . Here, no change of frequency due to saturation and no higher-order contributions are considered. Higher-order terms are neglected since we expect a supercritical Hopf bifurcation as previously observed by Oberleithner *et al.* (2011) rather than a sub-critical bifurcation that would require a higher-order model (Meliga *et al.* 2012a).

For the stochastic flow model, noise is added to the amplitude equation (3.2), reading

$$\dot{A} = (\sigma + i\omega)A - \alpha |A|^2 A + \xi, \quad (3.3)$$

where the noise is complex  $\xi = \xi_r + i\xi_i$  with uncorrelated real and imaginary part  $\langle \xi_r \xi_i \rangle = 0$ . The noise has zero mean and the variance  $\Gamma = \overline{\xi \xi^*}$  (\* indicates the complex conjugate). A complex-valued noise is necessary to maintain the symmetry of the equation.

The representation of the mode coefficient as amplitude and phase  $A = |A|e^{i\phi}$  allows to separate the unperturbed amplitude equation (3.2) into two simple real valued equations reading

$$|\dot{A}| = \sigma|A| - \alpha|A|^3; \quad \dot{\phi} = \omega. \quad (3.4)$$

The amplitude and phase are regarded as slow and fast variables meaning that  $\sigma \ll \omega$ . In combination with the amplitude and phase representation, this allows stochastic averaging over the fast variables of the stochastic equation (3.3) (Roberts & Spanos 1986) that gives

$$|\dot{A}| = \sigma|A| - \alpha|A|^3 + \frac{\Gamma}{|A|} + \xi_A \quad (3.5)$$

$$\dot{\phi} = \omega + \frac{\xi_\phi}{|A|}. \quad (3.6)$$

14

The conversion results in different contributions of the noise to the amplitude and phase ( $\xi_A$  and  $\xi_\phi$ ) as indicated by the subscripts. These noise contributions are real valued, uncorrelated  $\langle \xi_A \xi_\phi \rangle = 0$  and have halve the variance of the complex perturbation  $\langle \xi_A, \xi_A \rangle = \langle \xi_\phi, \xi_\phi \rangle = \Gamma/2$ .

The stochastic averaging of the equation refers to a short-term integration of the stochastic contributions that is analogue to previous approaches (Noiray 2017; Lee *et al.* 2019), where the Van der Pol oscillator instead of the amplitude equation was considered. The Van der Pol oscillator has an equivalent amplitude and phase representation as (3.5)-(3.6) which makes the approaches comparable. The only difference in the present approach is the use of complex noise that maintains the symmetry of the equation even for large amplitudes and strong noise.

The change of variables separates the model into two equations. The amplitude equation (3.5) is independent of the phase, describing the exponential amplification and saturation mechanism of the oscillatory mode. In the unperturbed case (3.4), the sign of the amplification rate  $\sigma$  determines whether the oscillations occur or not. However, the additional deterministic contribution  $\frac{\Gamma}{|A|}$  in the stochastic amplitude equation (3.5) prevents the oscillator from decaying to zero amplitude even for negative amplification rates. In addition to the new deterministic contribution, the additive stochastic perturbation remains in the amplitude equation. Considering the phase equation (3.6), the stochastic forcing causes the phase to be dependent not only on the frequency but also on parametric perturbations that scale inversely with the the amplitude. Therefore, the stochastic forcing couples the phase to the amplitude equation.

To estimate the noise intensity from experimental data, the phase equation (3.6) is rearranged to

$$\xi_{\phi, \text{est}} = |A| \left( \dot{\phi} - \omega \right), \quad (3.7)$$

which can be used to estimate the noise intensity using

$$\frac{\Gamma_{\text{est}}}{2} = \langle \xi_{\phi, \text{est}}, \xi_{\phi, \text{est}} \rangle. \quad (3.8)$$

The extraction of the remaining parameters from the amplitude equation is detailed in the subsequent section.

### 3.2. Stochastic perturbations with coloured noise

The application of stochastic methods requires the noise to be white (uncorrelated) to obtain a Langevine equation. However, the noise may have a short correlation time, which makes the stochastic forcing coloured instead of white noise. This is reasonable as long as the time scales of the deterministic and stochastic dynamics are well separated (Hänggi & Jung 1994). A simple type of coloured noise is obtained from an Ornstein–Uhlenbeck (OU) process which has the autocorrelation

$$\langle \xi(t), \xi(s) \rangle = \frac{D}{\tau} e^{-|t-s|/\tau} \quad (3.9)$$

and is created from a basic stochastic process as

$$\dot{\xi} = -\frac{1}{\tau} \xi + \frac{\sqrt{D}}{\tau} \xi_w. \quad (3.10)$$

In the above equations  $\xi$  denotes the noise created from the OU process with time scale  $\tau$  and intensity  $D$ . The variable  $\xi_w$  denotes a white noise process with a variance of one that drives the OU process. To incorporate the coloured noise into the stochastic

flow model, the specific correlation (3.9) is included in the stochastic averaging of the amplitude equation (Noiray 2017; Bonciolini *et al.* 2017). Accordingly, it is sufficient to replace the noise intensity in 3.5 by an effective noise intensity

$$\Gamma_\tau = \frac{2D}{\tau^2\omega^2 + 1} = \frac{2\tau \langle \xi, \xi \rangle}{\tau^2\omega^2 + 1}, \quad (3.11)$$

which is equivalent to the power spectrum of the OU noise at the oscillator frequency  $\omega$ . Note that the factor two in the equation results from the two noise components in the complex-valued forcing.

The time scale and intensity of the stochastic forcing were estimated from the following empirical relation

$$\langle \xi_\phi(t), \xi_\phi(s) \rangle \approx \frac{D}{2\tau} e^{|t-s|/\tau} \cos(\omega(t-s)). \quad (3.12)$$

There, the phase distortion according to (3.7) is compared to the analytical correlation of an OU process (3.9). The additional cosine term accounts for the different coordinates the noise is represented in. The noise adds to the amplitude equation as uncorrelated real and imaginary parts, whereas the phase distortion is considered in the rotating coordinates of the oscillator.

The procedure outlined here, using an effective noise and the estimation of the noise properties from the phase distortion, is only strictly valid for noise time scales that are smaller than the oscillator time scale and for small noise amplitudes. This limit of applicability is further investigated in section 3.4.

### 3.3. System identification from stationary probability density functions

The method presented here is used to estimate the parameters of the amplitude equation by inspecting the stationary probability density function (PDF) of measured amplitudes. An analytical expression for the stationary PDF is derived from the amplitude equation (3.5) through the corresponding Fokker-Planck equation. Therefore, the amplitude equation is brought in the form of the Langevine equation (3.1), where the corresponding drift and diffusion terms are

$$f(|A|) = |A| (\sigma - \alpha|A|^2) + \frac{\Gamma}{|A|} \quad (3.13)$$

$$g(|A|) = \sqrt{\Gamma/2}, \quad (3.14)$$

respectively. The assumption of a Markov process allows to describe the temporal evolution of the PDF of the magnitude  $|A|$  by the the Fokker-Planck equation (Friedrich *et al.* 2011)

$$\frac{\partial}{\partial t} P(|A|, t) = -\frac{\partial}{\partial |A|} (f(|A|)P(|A|, t)) + \frac{1}{2} \frac{\partial^2}{\partial |A|^2} (g^2(|A|)P(|A|, t)), \quad (3.15)$$

where  $P$  refers to the PDF. This eliminates the stochastic variable and gives a probabilistic description of the system, which can be compared to statistical moments obtained from measured data.

In order to identify the model parameters, a stationary solution of the Fokker-Planck equation  $\frac{\partial}{\partial t} P(|A|, t) = 0$  has to be found. Following the derivations of Noiray (2017), the stationary Fokker-Planck equation with vanishing PDF at infinite amplitudes and constant diffusion  $g$  simplifies to

$$\frac{d}{d|A|} P(|A|) - \frac{2}{g^2} f(|A|)P(|A|) = 0. \quad (3.16)$$

16

The corresponding solution is obtained by writing the drift equation in a potential form, reading

$$f(|A|) = -\frac{\partial \mathcal{V}(|A|)}{\partial |A|} \quad \text{with} \quad \mathcal{V}(|A|) = -\frac{\sigma}{2}|A|^2 + \frac{\alpha}{4}|A|^4 - \Gamma \ln |A|, \quad (3.17)$$

which gives

$$P(|A|) = \mathcal{N} \exp\left(-\frac{4}{\Gamma} \mathcal{V}(|A|)\right). \quad (3.18)$$

The scale parameter  $\mathcal{N}$  is chosen to normalise the PDF such that  $\int_0^\infty P(|A|)d|A| = 1$ . The expression contains a mixture of stochastic and deterministic parameters that are identified from different measures.

The strategy for the presented analysis is the following. We use a generic model of the PDF

$$P_{mod}(|A|) = \mathcal{N}|A| \exp(c_1|A|^2 + c_2|A|^4) \quad (3.19)$$

with the parameters  $c_1$  and  $c_2$ . It is fit to the experimental PDF  $P_{exp}$  using the Kulback-Leibler divergence

$$D_{KL} = \int_0^\infty P_{exp}(|A|) \log\left(\frac{P_{exp}(|A|)}{P_{mod}(|A|)}\right) d|A| \quad (3.20)$$

as similarity measure. The divergence  $D_{KL}$  is minimised using common numerical procedures. The effective noise intensity  $\Gamma_\tau$  is obtained from the procedure described in section 3.2. Together with the fit parameters of the model PDF, this provides the physical model parameters

$$\sigma = \frac{c_1 \Gamma_\tau}{2} \quad \text{and} \quad \alpha = -c_2 \Gamma_\tau, \quad (3.21)$$

where the estimation of the amplification rate  $\sigma$  is most important for the interpretation of the flow state.

For illustrative purposes, figure 6 shows a characteristic time series of an unstable system ( $\sigma > 0$ ) and a stable system ( $\sigma < 0$ ) that are both subjected to stochastic forcing. The signal was generated by numeric integration of the forced amplitude equation (3.3). The unstable system is initialised at  $A = 0$  and quickly approaches the limit-cycle. Due to the stochastic forcing, it never settles at the limit-cycle. The stationary PDF of the amplitude has the expected value at the limit-cycle and a Gaussian-like distribution. The distribution reflects the balance between the stabilising drift that pushes the system to the limit-cycle and the destabilising stochastic forcing. This is the same for the stable system, with the difference that the deterministic dynamics of the system tends to zero amplitude but gets continuously excited by the stochastic forcing. The estimation of the model parameters from the stationary PDF and the phase distortion allows to quantify the balance between these forces and provides estimates of physical amplification rates.

#### 3.4. Numerical study of the amplitude equation with coloured noise

The numerical study aims to validate the assumptions made during the derivation of the analytical procedure in sections 3.1 to 3.3. Especially the stochastic averaging (3.5) and the estimation of the noise properties (3.12) need to be validated for coloured noise. Therefore, the original complex-valued equation (3.3) is numerically integrated in time with coloured noise from an OU process (3.10). The OU process is integrated with a second-order Runge-Kutta scheme for stochastic equations (Tocino & Ardanuy 2002).

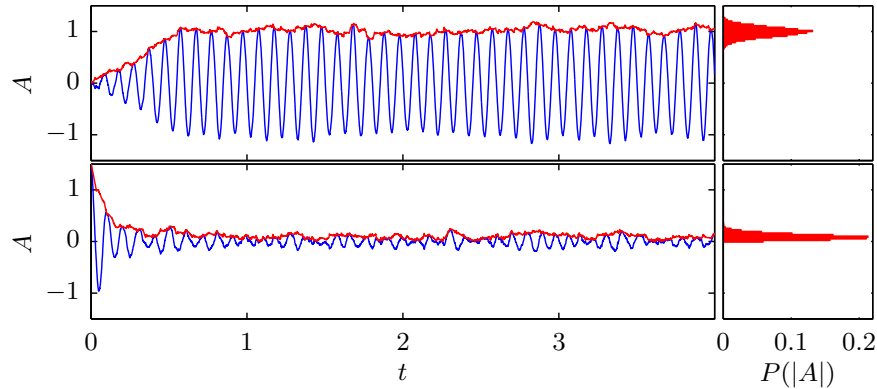


FIGURE 6. Exemplary time series of the simulated stochastic amplitude equation (3.3) for an unstable system (upper plot) and a stable system (lower plot). The blue lines show the real part of  $A$  and the red line gives the corresponding magnitude  $|A|$ . The bar blots on the right show the stationary probability density function of the magnitude. The models are simulated with white noise and the ratio  $\omega/\sigma$  is 10 for the unstable and -10 for the stable case.

The amplitude equation is integrated with a fourth-order Runge-Kutta scheme with fixed time steps corresponding to 100 steps per oscillation period. The coloured noise is simulated with twice the temporal resolution to allow the Runge-Kutta scheme to be evaluated for intermediate time steps. In the cases with white noise forcing, the amplitude equation is simulated like the OU process. The amplitude equation is simulated for a range of amplification rates  $\sigma = -1 \dots 1 \text{ s}^{-1}$ , noise time scales  $\tau = 0 \dots 1 \text{ s}$  and effective noise intensities  $\Gamma_\tau = 0.01 \dots 1$ . The frequency is kept constant at  $f_o = 10 \text{ Hz}$  as well as the Landau constant  $\alpha = 1$ . The parameters of the amplitude equation are identified according to equation (3.21) and the effective noise intensity according to equation (3.11) and (3.12).

The fit of the model to the simulation data is exemplified in figure 7 for selected cases. The selection shows an unstable system for different noise time scales but the same effective noise intensity. In the top row of figure 7 the autocorrelation of the phase distortion is shown. Accordingly, the estimation of the noise parameters from the decay of the correlation envelope works well for small and intermediate noise time scales but deviates for the large noise time scale. The bottom row of figure 7 shows the simulated, estimated and analytically derived amplitude PDFs. Since all presented simulations have the same effective noise intensity and model parameters, the analytic PDF must be the same for all cases (see equation (3.12)). For the small noise time scale ( $\tau = 0.01$ ) all shown PDFs agree very well. For the moderate noise time scale ( $\tau = 0.1$ ) the analytic and simulated PDFs deviate slightly. Note that the noise time scale here is of the same order as the oscillation frequency. Therefore, the assumed separation of time scales is no longer met, but nevertheless, the deviations stay small. The long noise time scale ( $\tau = 1$ ) causes significant deviations of the expected and simulated PDFs. Furthermore, the shape of the PDF is not correctly captured by the analytical model, indicating the need for higher-order approximations.

The estimated amplification rates and effective noise intensities for all simulated cases are presented in figure 8. The estimated amplification rate is displayed against the one used in the simulation. For a perfect estimation, the graph displays a straight diagonal, which is the case for the simulation with white noise ( $\tau = 0$ ). For  $\tau = 0.01$  and  $\tau = 0.1$  the relative deviations stay below 10%, while for  $\tau = 1$  the deviations exceed this limit. The source for the error are either an inaccurate fit of the PDF with the model equation (3.19) or an inaccurate estimation of the noise properties from the empirical correlation

18

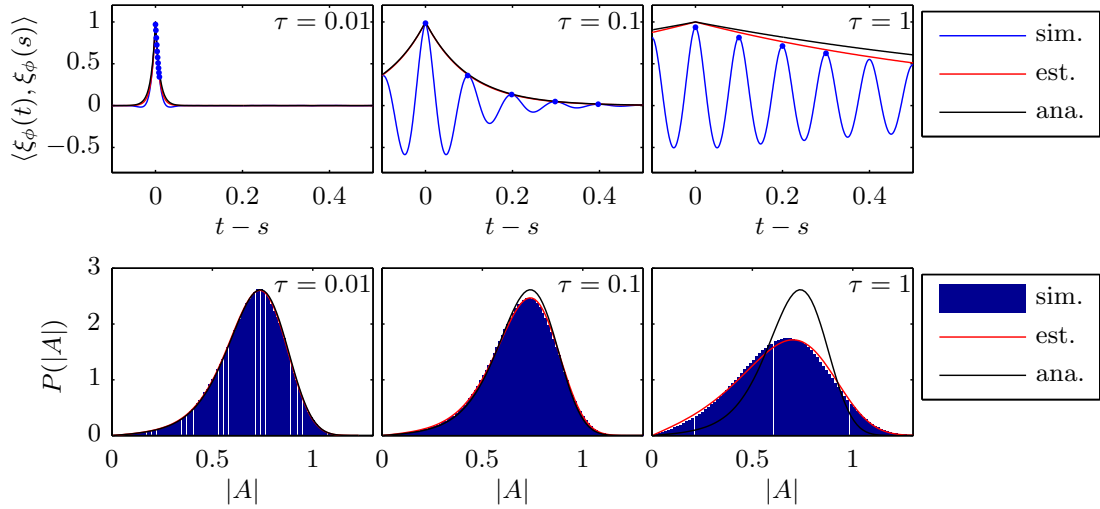


FIGURE 7. Selected simulation results of the numerical study at  $\sigma = 0.5$ ,  $\Gamma_\tau = 0.1$  and  $\tau = [0.01, 0.1, 1]$ , as indicated in the up-right corner. The top row shows noise correlation from the simulation, as well as the estimated and analytical decay (plots are normalised by the value at zero shift  $t = s$ ). The blue dots indicate the local maxima which are used to estimate the decay. The bottom row shows the PDF of the envelope calculated from the simulation, the estimated fit to the simulation results and the expected analytical PDF.

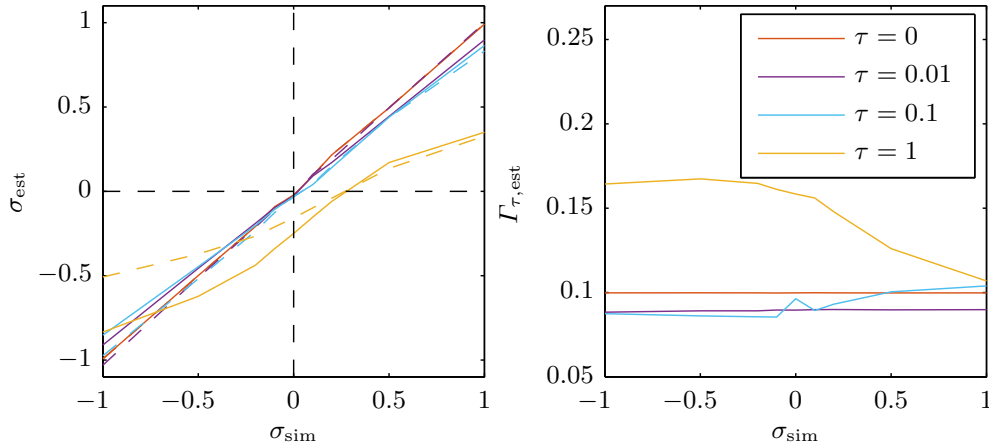


FIGURE 8. Estimates of the model coefficients from the simulation data at  $\Gamma_\tau = 0.1$  and different noise time scales indicated in the legend. The left plot shows the estimated against the true amplification rate. The solid curves show results with estimated  $\Gamma_\tau$  and the dashed lines with true  $\Gamma_\tau = 0.1$ . The plot on the right shows the corresponding estimation of the effective noise intensity from data.

function (3.12). To differentiate between these two error sources, the estimates are also shown based on the true noise intensity. Accordingly, the errors from both sources are of the same order of magnitude. For the cases with  $\tau \leq 0.1$ , the error generally only changes the slope of the amplification curve and the bifurcation point (zero crossing) is accurately captured. With increasing noise time scales, the absolute rate becomes increasingly underpredicted, as seen from the decreasing slope. The estimation for  $\tau = 1$  strongly deviates for the PDF fit as well as for the noise estimation. Hence, the model is not able to cover cases with noise time scales larger than the oscillation period  $\tau > 1/f_o$ .

The numerical study shows that the model and the simplifications made in the deviations are valid as long as the noise time scale stays below the oscillatory time scale.

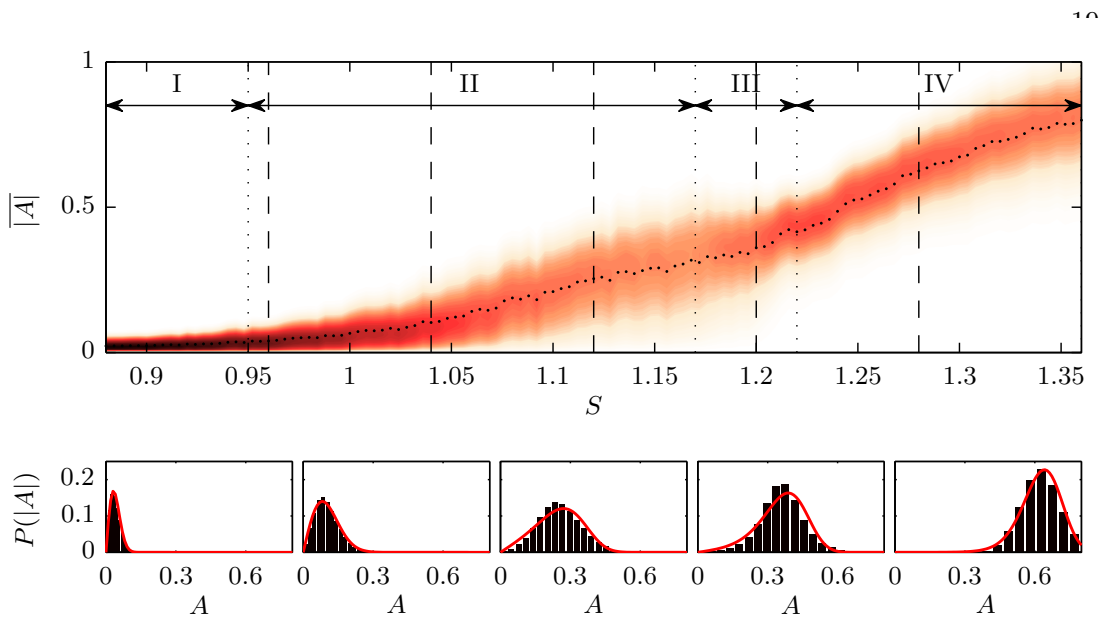


FIGURE 9. Analysis of the amplitude statistics derived from pressure measurement. The top plot shows the PDF of the envelope  $P(|A|)$  as contours for different swirl numbers. The second row shows bar plots of the measurement data together with the best fit of the theoretical PDF as a red line. These plots correspond to sections of the contour plot above, where the corresponding positions are marked as dashed lines. The arrows and vertical dotted lines indicate different regimes in the swirl number range.

Surprisingly, there is no need for a large separation of time scales if small deviations are acceptable. A perfect agreement, however, is only possible for purely white noise.

### 3.5. Parameter estimation of the amplitude equation from experiments

This section shows the results from the application of the procedure outlined in sections 3.1 to 3.3 to the oscillatory mode measured from the pressure Fourier modes (2.4). An overview of the measured PDFs is given in figure 9 and the estimated model parameters are presented in figure 10.

The amplitude PDFs presented in figure 9 show a continuous transition from narrow to wider distributions. A qualitative change can be observed in regime III, where the bi-stability of the mean flow occurs. The analytical model fits the observed PDF adequately and larger deviations are only visible in the bi-stable regime. The gradual change of the PDF and the mean amplitude does not indicate a bifurcation point from this representation.

Figure 10 displays the estimated amplification rate (top), the estimated noise time scale (mid) and the deviation of the PDF fit (bottom) quantified with the Kulback-Leibler divergence. Going through the graphs from low to high swirl, the amplification rate shows first a strong increase from largely negative values up to zero. After the bifurcation at  $S = 1.1$ , the estimated rates stay positive but the curve flattens and stays close to zero before there is a sudden increase in regime III. The noise time scale is always smaller than the oscillation time scale except for regime III. Similarly, a high divergence is observed in this regime, indicating a poor fit quality, whereas the divergence is low for all other swirl intensities. The overall divergence level is lowest in the stable regime and increases a little at  $S = 1.05$ . Overall, the presented model parameters give a clear indication of the bifurcation point and also provide a quantification of the reliability of the estimation.

The estimation results in the bi-stable regime of the flow appear not to be reliable.

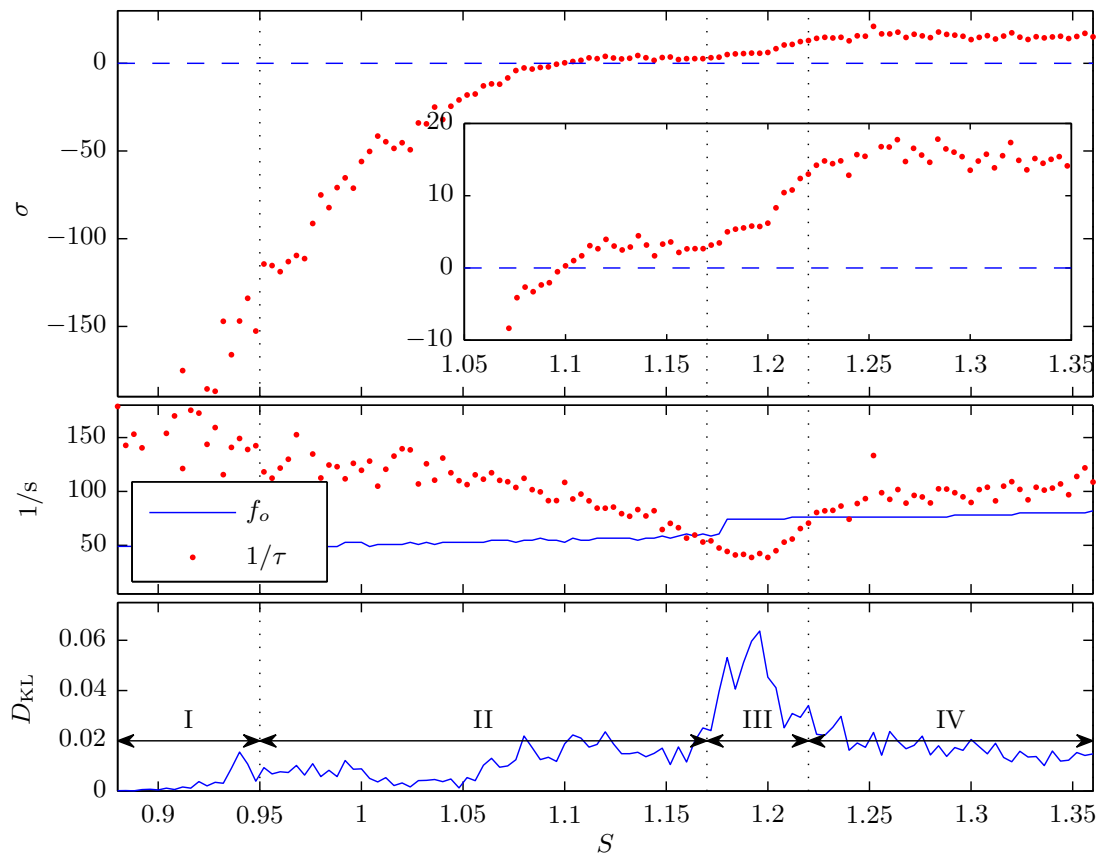


FIGURE 10. Estimated model parameters against the swirl number obtained from pressure measurements. The top plot gives the amplification rate and the small insert is a vertical zoom into the region around zero. The mid plot shows the oscillation frequency  $f_o$  together with the noise time scale  $\tau$ . The lower plot shows the divergence (3.20) between the measured and the theoretical PDF (see fig. 9). The arrows and vertical dotted lines indicate different regimes in the swirl number range.

This is primarily due to the stochastic switching between the two flow states that creates low-frequency perturbations of the oscillatory mode which are outside of the model's valid parameter range. This is distinctly indicated by the noise time scale that becomes larger than the oscillation time scale (figure 10, mid). The divergence consistently shows the failure of the model in that range. However, the estimated amplification rate does not show large outliers in that region but rather a continuous trend between the two neighbouring regions.

The unexpected plateau of the amplification rate at swirl levels slightly above the bifurcation point may be due to the following reasons: Either the decreasing noise time scale causes an under-prediction of the estimation in confirmation with the model study (section 3.4) or the one-dimensional dynamical model oversimplifies the underlying system dynamics at this flow regime. The latter will be addressed in the following section.

## 4. Modelling and system identification by the mean-field model

### 4.1. Model design and calibration procedure

In the model described in the previous section, the dynamics of the oscillatory mode are assumed to be independent of other state variable of the flow. However, the interaction of

the oscillatory mode with the mean flow might take some time such that there is a delayed saturation of the amplitude equation. This is further evaluated from an inspection of the mean-flow changes given by the shift-mode, which is referred by the mode coefficient  $B$ . The coupled dynamics of the oscillatory mode  $A$  and the shift-mode  $B$  is described by the mean-field model (Noack *et al.* 2003; Luchtenburg *et al.* 2009), which is given as

$$\dot{A} = (\sigma + i\omega) A - \beta(B - B_0)A \quad (4.1)$$

$$\dot{B} = -\frac{1}{\tau_B} (B - B_0 - \gamma|A|^2) \quad (4.2)$$

in the present nomenclature. The dynamics of the oscillatory mode  $A$  is very similar to the amplitude equation (3.2), but the saturation  $\alpha|A|^2$  is exchanged by the feedback from the shift-mode  $\beta(B - B_0)$ . The change of the shift-mode  $B$  is driven by the Reynolds stresses induced by the oscillatory mode  $\gamma|A|^2$ . If there is no oscillatory mode, the mean flow restores to the fixed point  $B_0$ , commonly called base flow. The rate of return to the fixed point is given by the time constant  $\tau_B$ . At the limit of an infinitely short time constant, the shift-mode is slaved to the oscillatory mode as  $(B - B_0) = \gamma|A|^2$  and the amplitude equation (3.2) is obtained again with the Landau constant being  $\alpha = \beta\gamma$ .

In the present investigation, the mean-field model is adapted to capture the dynamics observed in the experimental data. This results in the following model, where the dimension is reduced similar to the amplitude equation (3.4) by changing variables to the phase-magnitude-representation and retaining only the magnitude, yielding

$$|\dot{A}| = (\sigma - \alpha|A|^2 - \beta(B - B_0)) |A| + \frac{\Gamma}{|A|} \quad (4.3)$$

$$\dot{B} = -\frac{1}{\tau_B} (B - B_0 - \gamma|A|^2), \quad (4.4)$$

which describes the evolution of the oscillation magnitude  $|A|$  and the shift-mode  $B$ .

The amplitude equation in the adapted mean-field model (4.3) covers two saturation mechanisms. The first is called *direct saturation* and is represented by the quadratic term  $\alpha|A|^2$ , which is equivalent to the representation in the amplitude equation (3.2). The second is called *delayed saturation* and it is represented by the shift-mode-term  $\beta(B - B_0)$  introduced in the basic mean-field model (4.1). The inclusion of both mechanisms is necessary to capture the dynamics observed in the data, which are discussed in the following section.

The parameters  $\alpha$ ,  $\beta$  and  $\gamma$  in equation (4.3) and (4.4) are positive, which implies only negative feedback. In other words, an increasing amplitude shifts the mean flow to a state that causes less amplitude growth and vice versa. The fixed points of the system of equations lie on an inertial manifold called mean-field paraboloid, given by  $\gamma|A|^2 = B - B_0$  (Noack *et al.* 2003). This is an attracting manifold where the mean flow state corresponds to the Reynolds stresses induced by the limit-cycle oscillations of the system.

The current mean-field model (4.3) is further adapted by the inclusion of the drift term from the amplitude equation (3.5) that results from the additive noise, reading  $\Gamma/|A|$ . This empirical adaption considers the effect of an additive noise which is not explicitly modelled for the mean-field model. The actual addition of a stochastic forcing would need another independent noise term for the shift-mode and an extensive stochastic averaging to reduce the system to the two slow variables, the magnitude of the oscillatory mode and the shift-mode. Furthermore, there is most probably no simple analytical form for this two-dimensional system, which would require a numerical solution of the Fokker-Planck equation (Friedrich *et al.* 2011).

22

To overcome these difficulties, a different approach is pursued that extracts the deterministic drift directly from the statistical moments of the measured data. Therefore, the mean-field model needs to cover only the deterministic dynamics and no stochastic forcing. The drift is identified from a conditional average of the observed state  $X$  of the stochastic process (Friedrich *et al.* 2000), reading

$$\tilde{f}(X_k) = \lim_{\Delta t \rightarrow 0} \frac{1}{\Delta t} \langle X(t + \Delta t) - X(t) \rangle |_{X(t)=X_k}, \quad (4.5)$$

where  $\langle \rangle$  indicates the averaging operation. The function  $\tilde{f}(X)$  is an estimate of the drift function that drives the process as given by the Langevine equation (3.1). In the present case, the system state is  $X = [|A|, B]^T$  and the drift function  $\dot{X} = f(X)$  is equations (4.3) and (4.4). The conditional average in equation (4.5) considers the mean drift of all trajectories that passed through a certain point in state space  $X_k$ , where the drift is approximated by a forward-time finite-difference. The limit in equation (4.5) is only valid for strictly white noise, which is often not given for experimental data (Lehle & Peinke 2018) and generally not for turbulent perturbations. Therefore, a fixed interval of one oscillation period was chosen to estimate the drift of the slow variables. Neglecting the limit causes an inaccurate prediction of the drift, but relative differences and trends are still captured.

The evaluation of the conditional average in (4.5) requires the subdivision of the state space  $X = [|A|, B]^T$  in bins. For this purpose, data-based k-means clustering of the state space is pursued. This approach has shown to be very effective for a statistical description of fluid dynamics (Kaiser *et al.* 2014). The drift, determined for each cluster centre  $X_k$ , is fit to the model (4.3) and (4.4) by tuning the parameters to minimise  $\sum_i (\tilde{f}(X_k) - f(X_k))^2$ . To make the estimation of the noise-induced drift more robust, the parameter  $\Gamma$  in (4.3) is not estimated from the drift function. Instead, it is determined from the phase distortion (3.8) and scaled with a constant factor to adapt it to the drift function.

#### 4.2. Parameter estimation of the mean-field model from experimental data

The parameters of the stochastic mean-field model (4.3)-(4.4) are determined from the drift coefficients estimated from the pressure measurements of the flow, according to the procedure outlined in section 4.1. The pressure data are processed as described in section 2.2 to obtain the magnitude of the oscillatory mode  $|A|$  and the shift-mode  $B$ . The data are scaled to equal variance to obtain clusters from k-means clustering with 100 centres. Throughout the processing, the clusters have an average of 1500 elements and an absolute minimum of 24 elements.

The drift coefficients estimated for each cluster centre and the fitted mean-field model are displayed in figure 11. The model shows some deviations from the measurement data, especially at states far away from the fixed point. However, the general trend is very accurately captured. The model shows the attraction of the flow to the fixed point and also the mean-field paraboloid that appears as a bent region with low drift magnitudes. The three displayed cases correspond to the stable and the two unstable regimes, respectively. Despite their different dynamic states, the models show very similar dynamics in state space. The main change in the drift field is due to the increase of the limit-cycle amplitude and the corresponding movement of the fixed point in state space to larger amplitudes  $|A|$ . A specific characteristic of the present model is visible from the horizontal approach towards the fixed point. Especially for the intermediate case (figure 11 mid), there is an upward trend on the left side and a downward trend on the right side. This indicates the dependence of the oscillatory mode dynamics on the

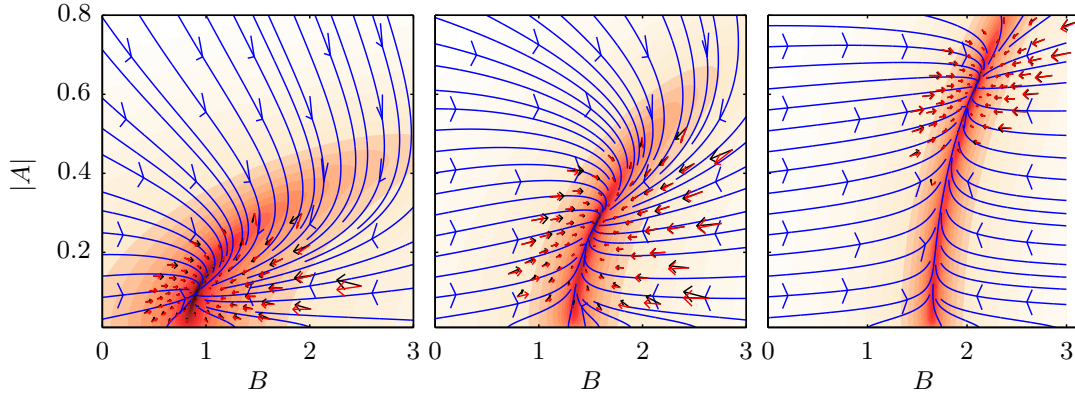


FIGURE 11. Fit of the stochastic mean-field model (4.3)-(4.4) to the estimated drift coefficients (4.5). Black arrows indicate the estimated coefficients and red arrows show the model coefficient at the same point. The streamlines and the contour in the background show the global picture of the model drift direction and magnitude, respectively (drift:  $f(X) = \dot{X}$  with  $X = [|A|, B]^T$ ). Fields for  $S = [0.96, 1.12, 1.28]$  are depicted from left to right.

shift-mode, otherwise, there must be horizontal drift lines at the limit-cycle amplitude. The general agreement of the observed and modelled dynamics is also a validation of the empirical mean-field model. The model is designed such that it covers the shown dynamics by combining elements from the stochastic amplitude equation and a basic mean-field model. Therefore, it indicates the dynamics which are relevant for the observed flow.

Figure 12 shows the estimated amplification rate obtained from the calibration of the mean-field model. The graph gives the linear amplification rate similar to figure 9 and further details which mechanism in the model leads to the saturation at the limit-cycle. The coloured areas indicate different contributions to the saturation of the amplification rate at the limit-cycle as given in equation (4.3). Accordingly, the effective amplification rate at the limit-cycle is given by

$$\sigma_{LC} = \sigma - \alpha|A_{LC}|^2 - \beta(B_{LC} - B_0), \quad (4.6)$$

where the subscript LC refers to a specific amplitude at the limit-cycle. The two contributions that lead to the reduction of the initial linear amplification rate  $\sigma$  to the amplification rate at the limit-cycle  $\sigma_{LC}$  are shown. The difference due to the direct saturation  $\alpha|A_{LC}|^2$  and the delayed saturation  $\beta(B_{LC} - B_0)$  are indicated in the graph. In contrast to the estimates from the amplitude equation (figure 10), which showed a bifurcation at  $S = 1.1$ , the mean-field model shows a bifurcation of the flow at  $S = 1.05$ . The graph further shows that the delayed saturation is much more relevant in regime II. In regime IV, the main contribution comes from the direct saturation term in the model. For the larger swirl numbers, the two saturation mechanism always add up to neutral stability at the limit-cycle ( $\sigma_{LC} \approx 0$ ). Furthermore, the magnitude of the linear amplification rate  $\sigma$  in regime II goes clearly above the zero line in contrast to the previous estimation from the amplitude equation (figure 10). This is more consistent with the continuous increase of the limit-cycle amplitude observed in figure 9.

The agreement of the observed and modelled drift coefficients, as well as the consistent description of the flow physics, suggest a more reliable description of the bifurcation by the mean-field model than the amplitude equation. Especially at the bifurcation point, the secondary dynamics from the shift-mode contribute significantly to the dynamics of the oscillatory mode, which causes the deviation of the more simple approach based on the amplitude equation.

24

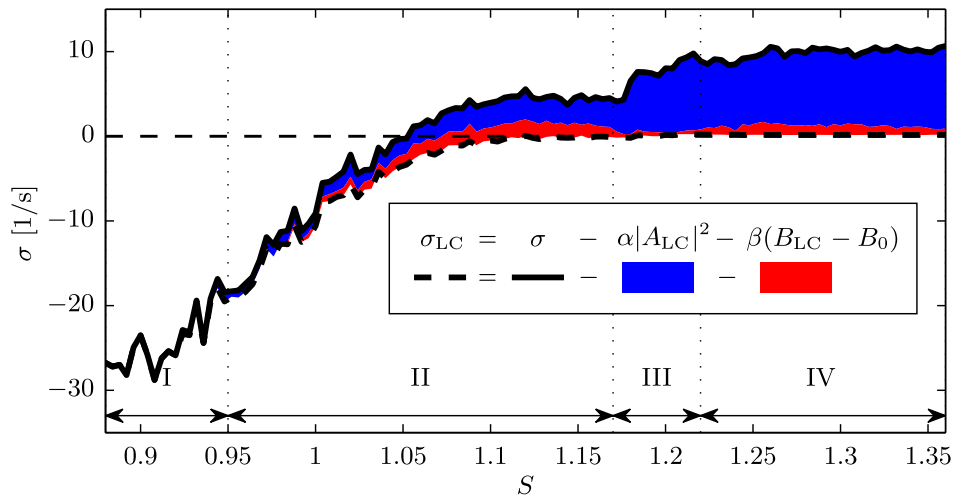


FIGURE 12. Estimated model parameters from pressure measurements using the mean-field model. The coloured areas indicate different contributions to the saturation of the amplification rate in (4.6). The arrows and vertical dotted lines indicate different regimes in the swirl number range.

#### 4.3. Insights from the description of the flow by the mean-field model

The parameters estimated from the 2D mean-field model (4.3)-(4.4) allow an accurate description of the dominant flow dynamics in consistency with the 1D amplitude equation (3.5). The 2D model, however, differs in two main points: (i) The identified bifurcation point and (ii) the growth rates for swirl numbers closely beyond the bifurcation point. The 2D model reveals that the interaction of the shift-mode and the oscillatory mode in this regime is of large importance, which is not covered by the 1D model. Hence, neglecting the shift-mode and describing the system solely based on the amplitude makes it a non-Markovian process, which can not be covered by the proposed Langevine equation. The unresolved dynamics between the shift-mode and oscillatory mode cause the additive noise to be correlated with the dynamics, which violates the basic assumptions.

The results from the calibration of the mean-field model provide a deeper understanding of the dynamics governing the swirling flow. The corresponding properties of the flow model are summarised in figure 13 a. Two distinct flow states can be derived from the model: (i) The base flow, which constitutes the quasi-stationary state of the flow before the onset of the instability; and (ii) the mean flow, which is the mean velocity field corresponding to the instability oscillating at the limit-cycle. The base flow is a state that is rarely reached in unstable conditions due to the unavoidable external perturbations from turbulence and instabilities. It can only be obtained artificially through active flow control or from transient investigations of the flow. The unique feature of the current approach is that one can make statements about the stationary base flow state, although one considers only fluctuations around the mean flow state.

More generally, the better understanding of the interaction between hydrodynamic instabilities and the mean flow helps to link the experimental observations and numerical results from mean-flow stability analysis beyond the comparison of mode shapes. The quantitative assessment of amplification rates and mean-flow corrections from measurements makes the results from both approaches directly comparable. Moreover, the distinction between deterministic and stochastic parts and their contribution to the flow dynamics enriches the picture of hydrodynamic instabilities in turbulent flows and helps to interpret the amplification rates obtained from mean-flow stability analysis.

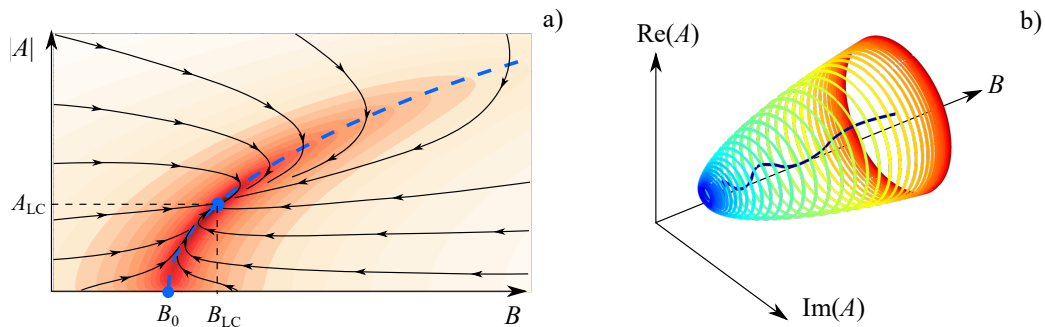


FIGURE 13. a) Reduced schematic of one of the plots from figure 11, where the mean-field paraboloid is indicated as dashed line. The base flow is indicated by  $B_0$  and the mean flow (limit-cycle) by  $B_{LC}$ . b) Simulated time series of the mean-field model for  $S = 1.12$ , where the line is coloured by the simulation time (from blue to red). The time series is starting at  $B = B_{LC}$  and  $A = 0$ , the unperturbed mean-flow.

The effective limit-cycle amplification rate (see figure 12) are directly comparable to the amplification rate of a corresponding mean-flow stability analysis.

The simulation of a time series shown in figure 13 b, starting from the mean flow with no oscillations, further illustrates the essence of the mean-field model. Before the oscillations grow significantly, the flow rapidly shifts towards the base flow and then grows in amplitude along the mean-field paraboloid. This behaviour is consistently observed for simulations of the cylinder wake (Noack *et al.* 2003; Brunton *et al.* 2016), where the mean-field paraboloid is also identified as an inertial/slow manifold. The drift in state space (figure 13 a) clearly shows that the mean-field paraboloid constitutes an attracting, slow manifold for the swirling jet. This knowledge of the mean-field model helps to understand the transient and intermittent dynamics of the swirling jet.

## 5. Conclusions

In this work, a method was developed to estimate the properties of a global hydrodynamic instability from measurement data of turbulent flows. The approach makes use of the stochastic perturbations that are present in the flow due to background turbulence. Background turbulence pushes the flow away from stable fixed-points or limit-cycles and, thus, forces the dynamics into other parts of the state space. From the deterministic return to the fixed-point or limit-cycle, the dynamic properties of the flow can be extracted.

The dynamical system is modelled by a stochastic amplitude equation describing the oscillatory dynamics of the instability (1D model) and, in a second approach, by a stochastic mean-field model that captures additionally the interaction between the instability and the mean-flow corrections (2D model). The stochastic perturbations are incorporated as additive forcing.

To capture the spectral properties of the turbulent perturbations, coloured noise was used for the stochastic forcing in the dynamical system. The validity of the derived amplitude equation for coloured noise was investigated by a numerical study. It is shown that the approach is feasible as long as the noise time-scale is smaller than the oscillation period of the instability.

The methodology was applied to experimental data of a turbulent swirling jet undergoing vortex breakdown. This flow is dominated by a helical global mode commonly termed the precessing vortex core. Thereby, the swirl number is the major control parameter

26

that governs the supercritical Hopf bifurcation of the global mode. PIV measurements were conducted to ensure that this mode is the most dominant coherent structure in the flow for the investigated swirl number range. For the system identification, pressure measurements around the nozzle lip were used providing longer time series than PIV.

The application of the 1D model showed very good capabilities to fit the observed dynamics of the flow. The bifurcation point of the global mode was identified and the good agreement between measured and estimated statistics showed that the model captures the relevant dynamics. The approach also identifies regions of a potential mismatch between the modelled and observed dynamics. The occurrence of an intermediate bistable switching between two flow states was correctly identified as a regime that is not accurately captured by the model. Moreover, the 1D model predicts a plateauing of the growth rate of the instability shortly beyond the bifurcation point, which contradicts the continuous increase of the limit-cycle amplitude. This discrepancy is addressed in the 2D mean-field model. Nevertheless, the 1D approach is fairly robust with regard to increased noise magnitude and noise time-scales.

The description of the flow from a stochastic mean-field model was introduced as an alternative estimate of the flow properties. The calibration of the 2D model provides a coarse estimate since no reduced analytical solution was derived. In contrast to the analytical approach pursued for the 1D amplitude equation, the drift coefficients were determined from statistical moments of the measurement data. Other than the development of the equation for the amplitude PDF in the first approach, the estimate of the drift coefficients need no prior knowledge of the flow model. The 2D model was constructed a posteriori to correspond to the observed dynamics. This will serve as a point of departure for future developments of a stochastic mean-field model that also incorporates accurate stochastic forcing and consequent development of 2D analytical models from stochastic averaging.

The main difference in the description of the flow by the 2D instead of 1D model, is a bifurcation of the flow at slightly lower swirl numbers and an increased growth rate right after the bifurcation. These differences most probably arise from not accounting for the interaction between the oscillatory mode and the slow mean-flow corrections by the shift-mode. In the 1D model, these are lumped into the stochastic forcing which violates the assumption of purely additive forcing. The consideration of the of the mean-flow corrections by the 2D model clarifies this transient dynamic of the flow. This gives a more detailed picture of the flow dynamics and allows an estimation of the unperturbed base-flow state.

The work demonstrates that the observation of limit-cycle oscillations is not sufficient to determine the flow state as the influence of the stochastic turbulent forcing is significant and masks the actual bifurcation point. However, the proposed separation of deterministic and stochastic contributions in the dynamical model allows identifying the flow state solely based on stationary measurement data. The inclusion of the shift-mode gives further capabilities to handle flows with a pronounced mean-flow correction. The methodology is expected to apply to a wide range of turbulent flows subjected to global flow instabilities.

## Appendix A. Swirl number determination

The swirl number for the present investigations is obtained from PIV and LVD measurements as presented in figure 14. The integral swirl number is computed as in

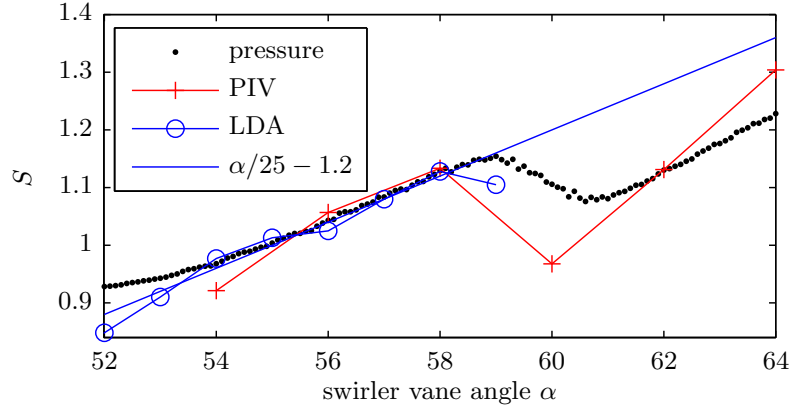


FIGURE 14. Different swirl number definitions against the swirler vane angle of the experimental apparatus. The integral swirl numbers are obtained from PIV and Laser Doppler Anemometer (LDA) measurements. Approximations of the integral swirl number based on the pressure measurements and the swirler angle are given as well.

Oberleithner *et al.* (2012) from the ratio of axial flux of azimuthal to axial momentum

$$S = \frac{2\dot{G}_\theta}{D\dot{G}_x} = \frac{2\pi \int_0^\infty \rho \bar{v}_x \bar{v}_\theta r^2 dr}{D\pi \int_0^\infty \rho \left( \bar{v}_x^2 - \frac{\bar{v}_\theta^2}{2} \right) r dr}. \quad (\text{A1})$$

The general perception is that the integral swirl number is very sensitive to the axial position utilised for the calculations, although it should be constant along the jet axis. This is due to difficulties of an accurate representation of the pressure-related momentum transport in a turbulent flow. Especially the presence of stagnant or reversed flow at the axial position of evaluation causes complications.

Since the current investigations span a large range of swirl numbers, there are cases where the recirculation region reaches up to the nozzle and different breakdown shapes occur. The graphs in figure 14 reflect these properties, where different measures of the swirl number are plotted against the swirl generator vane angle. Due to the transition between the two mean flow states, there is a jump in the representation of swirl number against the swirler vane angle. As the integral swirl number is not unique for the investigated range, a swirl number based on the swirl angle is calibrated to the integral swirl number resulting in  $S_\alpha = \alpha/25^\circ - 1.2$ . This geometry based swirl number is used throughout the current investigation.

The black dots in figure 14 represent a swirl measure based on the time mean  $m = 0$  pressure Fourier mode  $\langle \hat{p}_0 \rangle$  as  $S_p = \langle \hat{p}_0 \rangle / 28\text{Pa} + 0.9$ . It becomes clear that the pressure is a good indicator for the mean flow state, which justifies the description of the shift-mode being proportional to the mean pressure. The relation is only violated in the bi-stable region where the model predictions fail anyway.

## Appendix B. Relation between PIV and pressure measurements

In this work, the dynamics of the helical mode and the shift-mode are quantified based on velocity and pressure data. To confirm the correlation between these two quantities, the data from simultaneous PIV and pressure measurements of the flow are analysed and presented in figure 15. The presented data are from a 5.5 s measurement series, where synchronised measurements are recorded at a swirl number of  $S = 1.12$ . The plot

28

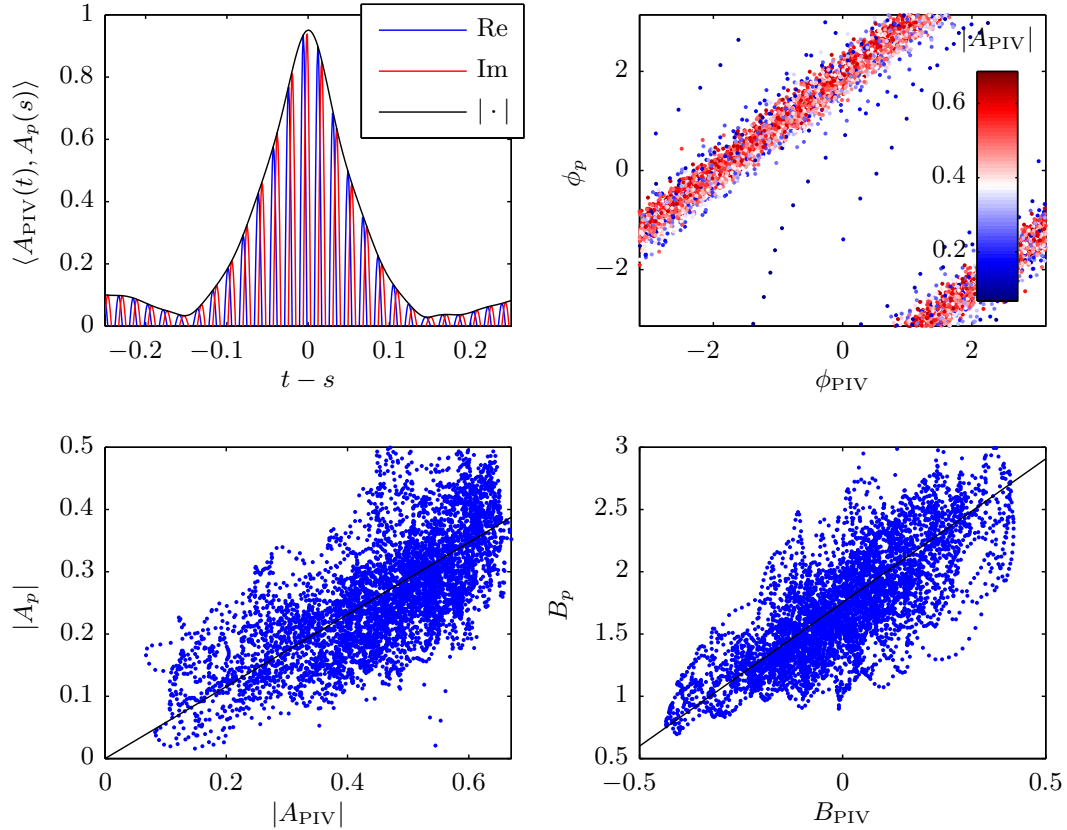


FIGURE 15. Comparison of the helical mode coefficient obtained from simultaneous PIV and pressure measurements as indicated by the subscripts PIV and  $p$ , respectively. (top left) The correlation coefficient between the complex coefficient from both measurements. (top right) Relation of the phases (argument of the complex amplitude), the colour indicates  $|A_{\text{PIV}}|$ . (bottom left) Relation of the helical magnitudes and (bottom right) relation of the shift-modes, where the linear trend is indicated by black lines.

compares the oscillatory mode  $A$  and the shift-mode  $B$  obtained (i) from the pressure measurements as Fourier decomposition of the pressure signals as  $A_p = \hat{p}_1$  and  $B_p = \hat{p}_0$  and (ii) from the SPOD coefficients of the PIV measurements as  $A_{\text{PIV}} = a_1 + ia_2$  and  $B_{\text{PIV}} = a_3$ . The phase and magnitude of the oscillatory mode are obtained from the polar representation of the complex coefficient, reading  $A = |A| \exp(i\phi)$ .

The cross-correlation (figure 15 top left) indicate a good overall agreement of the helical mode obtained from both approaches, where the maximum correlation coefficient is 0.95. Since both measurements are taken at different locations, there is a 5 ms shift in time between PIV and pressure data, corresponding to a quarter oscillation period of the flow oscillation. The maximum of the correlation is used to align both measurement series in time.

The direct comparison of the phase (figure 15 top right) and the magnitude (figure 15 bottom left) allows a more detailed investigation of this relation. The phases show limited jitter with a standard deviation of less than 5% of a period and a very good agreement. Relatively larger deviations are mainly observed at times with low oscillation magnitude.

The magnitude comparison (figure 15 bottom left) indicates larger deviations between the two measures, especially the pressure shows stronger fluctuation around the limit-cycle. This is because the SPOD coefficient of the PIV data represents the average

magnitude over a large measurement domain, whereas the pressure measurement only senses the local dynamics near the nozzle lip. Thus, any local perturbations of the helical mode is spatially averaged in the SPOD coefficient but directly visible in the pressure signal. Moreover, the large difference in the number of spatial measurement points causes a larger pickup of measurement noise in the pressure estimation of the mode coefficient.

Figure 15 (bottom right) shows the corresponding comparison of the shift-mode from both measurements. Similar to the magnitudes, the pressure estimation shows larger fluctuations, but the average dynamics agree very well.

## Acknowledgment

The authors kindly acknowledge the funding from the German Research Foundation under DFG Project PA 920/30-1 and DFG Project PA 920/37-1.

## Declaration of interests

The authors report no conflict of interest.

## REFERENCES

- BARKLEY, D. 2006 Linear analysis of the cylinder wake mean flow. *Europhysics Letters (EPL)* **75** (5), 750–756.
- BILLANT, PAUL, CHOMAZ, JEAN-MARC & HUERRE, PATRICK 1998 Experimental study of vortex breakdown in swirling jets. *Journal of Fluid Mechanics* **376**, 183–219.
- BONCIOLINI, GIACOMO, BOUJO, EDOUARD & NOIRAY, NICOLAS 2017 Output-only parameter identification of a colored-noise-driven van-der-pol oscillator: Thermoacoustic instabilities as an example. *Physical review. E* **95** (6-1), 062217.
- BOUJO, E., BOURQUARD, C., XIONG, Y. & NOIRAY, N. 2020 Processing time-series of randomly forced self-oscillators: The example of beer bottle whistling. *Journal of Sound and Vibration* **464**, 114981.
- BOUJO, EDOUARD & CADOT, OLIVIER 2019 Stochastic modeling of a freely rotating disk facing a uniform flow. *Journal of Fluids and Structures* **86**, 34–43.
- BOUJO, E. & NOIRAY, N. 2017 Robust identification of harmonic oscillator parameters using the adjoint fokker-planck equation. *Proceedings. Mathematical, physical, and engineering sciences* **473** (2200), 20160894.
- BRACKSTON, R. D., GARCÍA DE LA CRUZ, J. M., WYNN, A., RIGAS, G. & MORRISON, J. F. 2016 Stochastic modelling and feedback control of bistability in a turbulent bluff body wake. *Journal of Fluid Mechanics* **802**, 726–749.
- BRUNTON, STEVEN L., PROCTOR, JOSHUA L. & KUTZ, J. NATHAN 2016 Discovering governing equations from data by sparse identification of nonlinear dynamical systems. *Proceedings of the National Academy of Sciences of the United States of America* **113** (15), 3932–3937.
- CARINI, M., AIRIAU, C., DEBIEN, A., LÉON, O. & PRALITS, J. O. 2017 Global stability and control of the confined turbulent flow past a thick flat plate. *Physics of Fluids* **29** (2), 024102.
- CHIGIER, N. A. & CHERVINSKY, A. 1967 Experimental investigation of swirling vortex motion in jets. *Journal of Applied Mechanics* **34** (2), 443–451.
- COLLER, B. D., HOLMES, PHILIP & LUMLEY, JOHN L. 1994 Control of noisy heteroclinic cycles. *Physica D: Nonlinear Phenomena* **72** (1-2), 135–160.
- FRIEDRICH, R. & PEINKE, J. 1997 Description of a turbulent cascade by a fokker-planck equation. *Physical review letters* **78** (5), 863–866.
- FRIEDRICH, RUDOLF, PEINKE, JOACHIM, SAHIMI, MUHAMMAD & REZA RAHIMI TABAR, M. 2011 Approaching complexity by stochastic methods: From biological systems to turbulence. *Physics Reports* **506** (5), 87–162.
- FRIEDRICH, R., SIEGERT, S., PEINKE, J., ST. LÜCK, SIEFERT, M., LINDEMANN, M., RAETHJEN,

30

- J., DEUSCHL, G. & PFISTER, G. 2000 Extracting model equations from experimental data. *Physics Letters A* **271** (3), 217–222.
- GALLAIRE, FRANÇOIS & CHOMAZ, JEAN-MARC 2003 Mode selection in swirling jet experiments: a linear stability analysis. *Journal of Fluid Mechanics* **494**, 223–253.
- GALLAIRE, FRANÇOIS, RUIITH, M. R., MEIBURG, E., CHOMAZ, JEAN-MARC & HUERRE, PATRICK 2006 Spiral vortex breakdown as a global mode. *Journal of Fluid Mechanics* **549**, 71–80.
- GANG, DITZINGER, NING & HAKEN 1993 Stochastic resonance without external periodic force. *Physical review letters* **71** (6), 807–810.
- HÄNGGI, PETER & JUNG, PETER 1994 Colored noise in dynamical systems. In *Advances in Chemical Physics* (ed. I. Prigogine & Stuart A. Rice), , vol. 18, pp. 239–326. Hoboken, NJ, USA: John Wiley & Sons, Inc.
- HOLMES, PHILIP, LUMLEY, JOHN L., BERKOOZ, GAL & ROWLEY, CLARENCE W. 2012 *Turbulence, Coherent Structures, Dynamical Systems and Symmetry*, 2nd edn. *Cambridge monographs on mechanics* ". Cambridge, UK and New York: Cambridge University Press.
- HUANG, H. T., FIEDLER, H. E. & WANG, J. J. 1993 Limitation and improvement of piv: Part ii: Particle image distortion, a novel technique. *Experiments in Fluids* **15** (4-5), 263–273.
- KABIRAJ, LIPIKA, STEINERT, RICHARD, SAURABH, ADITYA & PASCHEREIT, CHRISTIAN OLIVER 2015 Coherence resonance in a thermoacoustic system. *Physical review. E, Statistical, nonlinear, and soft matter physics* **92** (4), 042909.
- KAISER, EURIKA, NOACK, BERND R., CORDIER, LAURENT, SPOHN, ANDREAS, SEGOND, MARC, ABEL, MARKUS, DAVILLER, GUILLAUME, ÖSTH, JAN, KRAJNOVIĆ, SINIŠA & NIVEN, ROBERT K. 2014 Cluster-based reduced-order modelling of a mixing layer. *Journal of Fluid Mechanics* **754**, 365–414.
- KLEINHANS, DAVID & FRIEDRICH, RUDOLF 2007 Maximum likelihood estimation of drift and diffusion functions. *Physics Letters A* **368** (3-4), 194–198.
- LANDAU, L. D. 1944 On the problem of turbulence. *C. R. Acad. Sci. URSS* **44** (311).
- LANDAU, L. D. & LIFSHITZ, E. M. 1987 *Fluid Mechanics*, 2nd edn., *Course of theoretical physics*, vol. v. 6. Oxford: Pergamon.
- LEE, MINWOO, ZHU, YUANHANG, LI, LARRY K. B. & GUPTA, VIKRANT 2019 System identification of a low-density jet via its noise-induced dynamics. *Journal of Fluid Mechanics* **862**, 200–215.
- LEHLE, B. & PEINKE, J. 2018 Analyzing a stochastic process driven by ornstein-uhlenbeck noise. *Physical review. E* **97** (1-1), 012113.
- LIANG, HANZHUANG & MAXWORTHY, T. 2005 An experimental investigation of swirling jets. *Journal of Fluid Mechanics* **525**, 115–159.
- LJUNG, LENNART 2012 *System identification: Theory for the user*, 2nd edn. *Prentice Hall information and system sciences series* ". Upper Saddle River, NJ: Prentice Hall PTR.
- LUCHTENBURG, DIRK MARC, GÜNTHER, BERT, NOACK, BERND R., KING, RUDIBERT & TADMOR, GILEAD 2009 A generalized mean-field model of the natural and high-frequency actuated flow around a high-lift configuration. *Journal of Fluid Mechanics* **623**, 283–316.
- LUI, HUGO F. S. & WOLF, WILLIAM R. 2019 Construction of reduced-order models for fluid flows using deep feedforward neural networks. *Journal of Fluid Mechanics* **872**, 963–994.
- MANTIČ-LUGO, VLADISLAV, ARRATIA, CRISTÓBAL & GALLAIRE, FRANÇOIS 2015 A self-consistent model for the saturation dynamics of the vortex shedding around the mean flow in the unstable cylinder wake. *Physics of Fluids* **27** (7), 074103.
- MELIGA, PHILIPPE, GALLAIRE, FRANÇOIS & CHOMAZ, JEAN-MARC 2012a A weakly nonlinear mechanism for mode selection in swirling jets. *Journal of Fluid Mechanics* **699**, 216–262.
- MELIGA, PHILIPPE, PUJALS, GREGORY & SERRE, ÉRIC 2012b Sensitivity of 2-d turbulent flow past a d-shaped cylinder using global stability. *Physics of Fluids* **24** (6), 061701.
- MÜLLER, J. S., LÜCKOFF, F., PAREDES, P., THEOFILIS, V. & OBERLEITHNER, K. 2020 Receptivity of the turbulent precessing vortex core: synchronization experiments and global adjoint linear stability analysis. *Journal of Fluid Mechanics* **888**.
- NOACK, BERND R., AFANASIEV, KONSTANTIN, MORZYŃSKI, MAREK, TADMOR, GILEAD & THIELE, FRANK 2003 A hierarchy of low-dimensional models for the transient and post-transient cylinder wake. *Journal of Fluid Mechanics* **497**, 335–363.
- NOACK, BERND R., STANKIEWICZ, WITOLD, MORZYŃSKI, MAREK & SCHMID, PETER J.

- 2016 Recursive dynamic mode decomposition of transient and post-transient wake flows. *Journal of Fluid Mechanics* **809**, 843–872.
- NOIRAY, NICOLAS 2017 Linear growth rate estimation from dynamics and statistics of acoustic signal envelope in turbulent combustors. *Journal of Engineering for Gas Turbines and Power* **139** (4), 041503.
- NOIRAY, NICOLAS & SCHUERMANS, BRUNO 2013 Deterministic quantities characterizing noise driven hopf bifurcations in gas turbine combustors. *International Journal of Non-Linear Mechanics* **50**, 152–163.
- OBERLEITHNER, KILIAN, PASCHEREIT, CHRISTIAN OLIVER, SEELE, R. & WYGNANSKI, I. 2012 Formation of turbulent vortex breakdown: Intermittency, criticality, and global instability. *AIAA Journal* **50** (7), 1437–1452.
- OBERLEITHNER, K., PASCHEREIT, C. O. & WYGNANSKI, I. 2014 On the impact of swirl on the growth of coherent structures. *Journal of Fluid Mechanics* **741**, 156–199.
- OBERLEITHNER, K., SIEBER, MORITZ, NAYERI, C. N., PASCHEREIT, CHRISTIAN OLIVER, PETZ, C., HEGE, HANS-CHRISTIAN, NOACK, BERND R. & WYGNANSKI, I. 2011 Three-dimensional coherent structures in a swirling jet undergoing vortex breakdown: stability analysis and empirical mode construction. *Journal of Fluid Mechanics* **679**, 383–414.
- QADRI, UBAID ALI, MISTRY, DHIREN & JUNIPER, MATTHEW P. 2013 Structural sensitivity of spiral vortex breakdown. *Journal of Fluid Mechanics* **720**, 558–581.
- REINKE, NICO, FUCHS, ANDRÉ, NICKELSEN, DANIEL & PEINKE, JOACHIM 2018 On universal features of the turbulent cascade in terms of non-equilibrium thermodynamics. *Journal of Fluid Mechanics* **848**, 117–153.
- RIBEIRO, JEAN HÉLDER MARQUES & WOLF, WILLIAM ROBERTO 2017 Identification of coherent structures in the flow past a naca0012 airfoil via proper orthogonal decomposition. *Physics of Fluids* **29** (8), 085104.
- RIGAS, G., MORGANS, A. S., BRACKSTON, R. D. & MORRISON, J. F. 2015 Diffusive dynamics and stochastic models of turbulent axisymmetric wakes. *Journal of Fluid Mechanics* **778**.
- ROBERTS, J. B. & SPANOS, P. D. 1986 Stochastic averaging: An approximate method of solving random vibration problems. *International Journal of Non-Linear Mechanics* **21** (2), 111–134.
- RUITH, M. R., CHEN, P., MEIBURG, E. & MAXWORTHY, T. 2003 Three-dimensional vortex breakdown in swirling jets and wakes: direct numerical simulation. *Journal of Fluid Mechanics* **486**, 331–378.
- RUKES, LOTHAR, PASCHEREIT, CHRISTIAN OLIVER & OBERLEITHNER, KILIAN 2016 An assessment of turbulence models for linear hydrodynamic stability analysis of strongly swirling jets. *European Journal of Mechanics - B/Fluids* **59**, 205–218.
- RUKES, LOTHAR, SIEBER, MORITZ, PASCHEREIT, C. OLIVER & OBERLEITHNER, KILIAN 2015 Effect of initial vortex core size on the coherent structures in the swirling jet near field. *Experiments in Fluids* **56** (10), 183.
- SAURABH, ADITYA, KABIRAJ, LIPIKA, STEINERT, RICHARD & OLIVER PASCHEREIT, CHRISTIAN 2017 Noise-induced dynamics in the subthreshold region in thermoacoustic systems. *Journal of Engineering for Gas Turbines and Power* **139** (3), 1.
- SIEBER, MORITZ, PASCHEREIT, CHRISTIAN OLIVER & OBERLEITHNER, KILIAN 2016a Advanced identification of coherent structures in swirl-stabilized combustors. *Journal of Engineering for Gas Turbines and Power* **139** (2), 021503.
- SIEBER, MORITZ, PASCHEREIT, CHRISTIAN OLIVER & OBERLEITHNER, KILIAN 2016b Spectral proper orthogonal decomposition. *Journal of Fluid Mechanics* **792**, 798–828.
- SIEBER, MORITZ, PASCHEREIT, C. OLIVER & OBERLEITHNER, KILIAN 2017 On the nature of spectral proper orthogonal decomposition and related modal decompositions. *arXiv preprint arXiv:1712.08054* .
- SIROVICH, L. 1987 Turbulence and the dynamics of coherent structures: Part i: Coherent structures. *Quarterly of Applied Mathematics* **45** (3), 561–571.
- SORIA, J. 1996 An investigation of the near wake of a circular cylinder using a video-based digital cross-correlation particle image velocimetry technique. *Experimental Thermal and Fluid Science* **12** (2), 221–233.
- STÖHR, MICHAEL, OBERLEITHNER, KILIAN, SIEBER, MORITZ, YIN, ZHIYAO & MEIER, WOLFGANG 2017 Experimental study of transient mechanisms of bi-stable flame shape

32

- transitions in a swirl combustor. *Journal of Engineering for Gas Turbines and Power* p. V04BT04A063.
- STONE, EMILY & HOLMES, PHILIP 1989 Noise induced intermittency in a model of a turbulent boundary layer. *Physica D: Nonlinear Phenomena* **37** (1-3), 20–32.
- STUART, J. T. 1958 On the non-linear mechanics of hydrodynamic stability. *Journal of Fluid Mechanics* **4** (1), 1–21.
- SYRED, N. & BEÉR, J. M. 1974 Combustion in swirling flows: A review. *Combustion and Flame* **23** (2), 143–201.
- TAMMISOLA, O. & JUNIPER, M. P. 2016 Coherent structures in a swirl injector at  $re = 4800$  by nonlinear simulations and linear global modes. *Journal of Fluid Mechanics* **792**, 620–657.
- TERHAAR, STEFFEN, REICHEL, THORALF G., SCHRÖDINGER, CHRISTINA, RUKES, LOTHAR, PASCHEREIT, CHRISTIAN OLIVER & OBERLEITHNER, KILIAN 2014 Vortex breakdown types and global modes in swirling combustor flows with axial injection. *Journal of Propulsion and Power* **31** (1), 219–229.
- TOCINO, A. & ARDANUY, R. 2002 Runge–kutta methods for numerical solution of stochastic differential equations. *Journal of Computational and Applied Mathematics* **138** (2), 219–241.
- TOWNE, AARON, SCHMIDT, OLIVER T. & COLONIUS, TIM 2018 Spectral proper orthogonal decomposition and its relationship to dynamic mode decomposition and resolvent analysis. *Journal of Fluid Mechanics* **847**, 821–867.
- VANIERSCROT, MAARTEN & OGUS, GUVEN 2019 Experimental investigation of the precessing vortex core in annular swirling jet flows in the transitional regime. *Experimental Thermal and Fluid Science* **106**, 148–158.
- VILLERMAUX, E. & HOPFINGER, E. J. 1994 Periodically arranged co-flowing jets. *Journal of Fluid Mechanics* **263**, 63–92.
- VIOLA, F., IUNGO, G. V., CAMARRI, S., PORTÉ-AGEL, F. & GALLAIRE, F. 2014 Prediction of the hub vortex instability in a wind turbine wake: stability analysis with eddy-viscosity models calibrated on wind tunnel data. *Journal of Fluid Mechanics* **750**.
- WILLERT, C. E. & GHARIB, M. 1991 Digital particle image velocimetry. *Experiments in Fluids* **10** (4).
- ZHU, YUANHANG, GUPTA, VIKRANT & LI, LARRY K. B. 2019 Coherence resonance in low-density jets. *Journal of Fluid Mechanics* **881**, 55.

### 3.5 Impact of density stratification on the global mode in a swirling jet: Stochastic modelling and Lagrangian coherent structures

This article is published in a revised form in the International Journal of Heat and Fluid Flow under the following reference: M. Sieber, C. O. Paschereit, & K. Oberleithner (2021b). "Impact of density stratification on the global mode in a swirling jet: Stochastic modelling and Lagrangian coherent structures". *International Journal of Heat and Fluid Flow* 90, p. 108820. DOI: <https://doi.org/10.1016/j.ijheatfluidflow.2021.108820>. The following is a pre-peer-review version of the article. Reprinted with permission. This version is free to view and download for private research and study only. Not for re-distribution, re-sale or use in derivative works. ©Elsevier.

The suppression of the global mode due to density stratification is investigated in a generic experiment. The bifurcation of the flow is examined depending on the swirl intensity, the density difference and the Reynolds number. Spatial structures from PIV based flow models and experimental schlieren visualisations are considered to detail the mixing and the influence of the Reynolds number.

**Methods:** The stochastic amplitude equation as presented in the previous publication is used to characterise the bifurcation. The computation of Lagrangian coherent structures from planar PIV measurements is presented. Phase averaging and physics-based filtering of the data is used to obtain a 3D time-resolved representation of the flow. This allows the computation of finite-time Lyapunov exponents that represent the spatial structure of the global mode.

**Results:** The generic swirling jet setup is used and density stratifications are generated by local, electric heating. The stochastic model is calibrated from pressure measurements at various operation conditions. A pronounced effect of the density stratification of the global mode is only observed for low Reynolds numbers. The effect of the Reynolds number is further investigated using Schlieren visualisations. Images of finite-time Lyapunov exponents and schlieren are considered to investigate the spatial structure of the global mode.

**Physics:** The suppression of the global mode due to density stratification is replicated in a generic setup. The Reynolds dependency of the effect is explained from the emergence of small-scale mixing and the resulting diffusion of the density gradients.

## Impact of density stratification on the global mode in a swirling jet: Stochastic modelling and Lagrangian coherent structures

Moritz Sieber<sup>a,b,\*</sup>, Cristian Oliver Paschereit<sup>b</sup>, Kilian Oberleithner<sup>a</sup>

<sup>a</sup> *Laboratory for Flow Instabilities and Dynamics, ISTA, Technische Universität Berlin*

<sup>b</sup> *Chair of Fluid Dynamics, ISTA, Technische Universität Berlin*

---

### Abstract

In an experimental investigation, the stochastic dynamics of the global mode in a turbulent swirling jet are considered. From the application of the swirling jet in gas turbine combustors, it was observed that a specific density gradient in the flow leads to a suppression of the global mode. This phenomenon was replicated in a generic swirling jet using an electrical heating coil placed inside the breakdown bubble. In the present investigation, the dynamics of the global mode obtained from PIV and pressure measurements are analysed using a stochastic reduced-order model to describe the instability. The stochastic model is necessary to explain the interaction between the deterministic dynamics of the global mode and the perturbations by the background turbulence. The calibration of the stochastic model provides the amplification rate of the global mode that defines the transition of the flow, dependent on the swirling strength and the density difference. The spatial structure of the global mode is further investigated from Lagrangian coherent structures of the flow field which are computed from the 3D time-resolved velocity field reconstruction based on planar PIV measurements. The Lagrangian visualisations and schlieren visualisations are used to explain the absence of the density effects on the global mode at larger Reynolds numbers. The analysis gives a detailed view of the stochastic dynamics of a hydrodynamic instability in a turbulent flow that might be valuable for other investigations.

*Keywords:* swirling jet, global mode, hydrodynamic instability, stochastic model, Lagrangian coherent structures, finite time Lyapunov exponent, flow visualisation

---

### 1. Introduction

A swirling jet denotes a class of circular jets that have a circular motion in addition to the axial motion of the fluid. It is widely used in gas turbine combustors due to a unique fluid dynamic feature called vortex breakdown [1]. The vortex breakdown manifests as a region of reversed flow in the centre of the jet [2]. In a swirl-stabilised combustor, the vortex breakdown stabilises the flame due to the recirculation of hot products and provides low velocities, which facilitates aerodynamic anchoring of the flame.

The swirling jet gives also rise to a global hydrodynamic instability that is controlled by the swirl intensity of the flow [3, 4, 5]. In combustion-related investigations, this instability is referred to as the precessing vortex core (PVC). The PVC is known to interact with the flame due to the mixing of reactants and stretching of the flame front [1, 6]. In reverse, the flame also influences the PVC which may lead to suppression or emergence of the PVC at certain operating conditions of a combustor [1, 7]. It has been shown that the combustion-induced density stratification

in the shear layers leads to a suppression of the hydrodynamic instability [8]. Detailed experiments with a generic swirling jet were able to reproduce the phenomenon by mimicking the heat release of the flame by an electric heater [9, 10]. The combined experimental and numerical study showed that the amplitude of the PVC is strongly reduced, however, no complete suppression was attained experimentally. However, the appearance of the global mode in the data appeared to be in contradiction to the global instability of the mean flow as it was determined from a spatio-temporal stability analysis. As will be shown in this work, this contradiction can be resolved by considering the stochastic forcing of the global modes by turbulence.

In the present study, the dynamics of the global mode in the turbulent flow is modelled by a stochastic dynamical system. The model consists of a deterministic part that describes the oscillatory motion of the global mode and the leading nonlinearities that cause saturation at the limit-cycle. Secondly, the model includes the perturbations by the background turbulence as a stochastic forcing. At stationary operation conditions, the flow tends to settle at a stable state or limit-cycle. However, the turbulent perturbations continuously disturb the flow about that stable state. From the deterministic return to the stable state, the model can be calibrated. Therefore, the deterministic and stochastic dynamics are identified from the data and

---

\*Corresponding author

*Email addresses:* [moritz.sieber@fd.tu-berlin.de](mailto:moritz.sieber@fd.tu-berlin.de) (Moritz Sieber), [www.fd.tu-berlin.de](http://www.fd.tu-berlin.de) (Cristian Oliver Paschereit), [www.flow.tu-berlin.de](http://www.flow.tu-berlin.de) (Kilian Oberleithner)

the model is adjusted to replicate thous. This requires only stationary, but time-resolved measurements of the flow.

The modelling approach adopted here was previously used to determine the deterministic characteristics of thermoacoustic oscillations in combustors [11, 12]. Furthermore, it was used to determine the bifurcation point of a hydrodynamic instability in a low-density jet from randomly forced measurements in the stable regime [13]. Moreover, the experimental observations of the PVC in an isothermal swirling jet were described in detail in a very recent investigation using the same stochastic approach [14]. In the present study, this work is extended to clarify the impact of heating on the global stability that causes the formation of the PVC.

The general difference of a stochastic model to a purely deterministic model is the possibility to capture dynamics in the flow that arise from linearly stable modes. Due to the stochastic forcing, stable modes of the flow get excited and require some time to decay again, which allows them to be observed in measurements. In the field of dynamical systems, this phenomenon is commonly denoted as coherence resonances [15].

An essential aspect for the understanding of fluid dynamics is not only the analysis of the temporal dynamics but also the investigation of the spatial structures. Therefore, schlieren images are recorded in this study making use of the density differences in this flow. The visual representation of a flow structure allows drawing an intuitive connection to the interaction between the stochastic turbulent fluctuations and the coherent structure. In the present investigation, the schlieren images are further compared to Lagrangian coherent structures computed from the measured velocity fields [16]. For this purpose, a regularisation procedure is applied in combination with a reconstruction scheme to obtain a smooth 3D time-dependent representation of the flow field. The determined Lagrangian coherent structures allow a good comparison to the schlieren-based flow visualisations and help to understand mixing phenomena [17, 18, 19]. Furthermore, the relation to instabilities of variable-density Kelvin-Helmholtz instabilities is discussed [20, 21].

The paper is organised as follows. In section 2, the experimental and analytical methods are detailed. This comprises the description of measurement techniques, the identification of flow structure and the computation of Lagrangian coherent structures as well as the description of the stochastic model and the related calibration from measurement data. The corresponding results for the mean flow field, different flow visualisations and calibration of the stochastic model are given in section 3. In section 5, the results are discussed in light of previous related studies and swirl combustion applications.

## 2. Experimental and numerical methods

### 2.1. Experimental setup and measurement techniques

The flow of a generic swirling jet was investigated experimentally. The utilised setup is depicted schematically in figure 1. It consists of a radial swirl generator that is connected to a settling chamber followed by a contoured contraction. The flow emanates into the unconfined ambient, where the swirling jet evolves. The airflow into the swirler was adjusted with a mass flow controller and the radial vanes in the swirler were adjusted with an automated stepper motor. The setup was utilised in previous investigations for the dynamics of the PVC under isothermal conditions [22, 23, 14] as well as with a heated breakdown bubble [9, 10, 18].

The breakdown region of the flow was heated by a loose wire coil that was directly exposed to the flow. It was made of a spirally wound 0.5 mm Nickel-Chromium wire (NiCr6015) and held in place by two thicker metal rods that also provided the electrical connection. The heating coil had a diameter of 20 mm and height of 43 mm. The coil was mounted such that the laser can pass between the two metal rods that hold the coil. A part of the laser light was reflected by a mirror to illuminate the part of the flow that was shadowed by the coil (figure 1). For the PIV measurements, a card mask with the shape of the coil was put between the coil and the camera to protect the chip from strong reflections. The coil was connected to an adjustable power supplied that was operated in constant current mode. The maximum operation current for the presented measurements was 4.6 A which corresponds to 165 W electrical power.

The coordinate orientation is indicated in the experimental setup in figure 1. The velocities in  $x$ -,  $y$ - and  $z$ -direction are given by  $v_x$ ,  $v_y$  and  $v_z$ , which are commonly represented as vector  $\mathbf{v} = [v_x, v_y, v_z]^T$ . The origin of the coordinate system is located in the centre of the nozzle exit plane. The  $x$ -direction is aligned with the direction of gravity to avoid symmetry breaking. Furthermore, cylindrical coordinates are used given as  $[x, r, \theta]$  that correspond to the Cartesian as  $r = \sqrt{y^2 + z^2}$  and  $\theta = \angle(y + iz)$ .

The flow velocity was measured using stereoscopic particle image velocimetry (PIV) as sketched in figure 1. The three velocity components were measured in the  $x$ - $y$ -plane right after the nozzle. Two 4 megapixel cameras with 50 mm lenses and a 150 mJ dual laser were used for the measurement. The flow was seeded with Titanium oxide powder that was introduced into the flow between the mass flow controller and the swirler. For each configuration, a set of 1000 snapshots were recorded at a rate of 6 Hz. The images were processed with PIVview (PIVTEC GmbH) using standard digital PIV processing [24]. Further details about the PIV measurement procedure can be found in Rukes et al. [22, 9].

Schlieren images of the flow were recorded with a Toepler Z-type setup with a knife-edge in  $x$ -direction [25]. Therefore, two identical mirrors with a focal length of

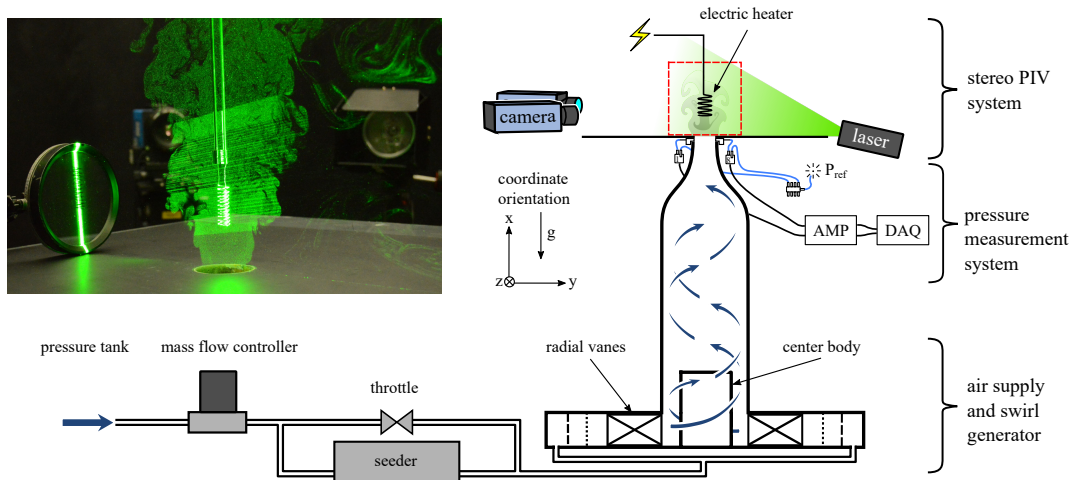


Figure 1: Schematic of the experimental setup together with the utilised measurement equipment. The red square marks the PIV measurement domain. The coordinate system is given next to the setup, the actual origin is in the centre of the nozzle exit plane. The photo shows the seeded jet and the heating coil, illuminated by the laser.

2.5 m were placed with an opening angle of approximately  $15^\circ$ . The light, emanated from a white LED (10 mm diameter), was guided through the flow and recorded with a Nikon-3200 DSLR camera placed in the setup without a lens.

Around the circumference of the nozzle, eight pressure sensors were mounted to sense the PVC dynamics. Differential pressure sensors with a measurement range of 1000 Pa were used. The signals were amplified by in house bridge amplifiers and recorded with 24 bit AD converters. Further details are given in Lang et al. [18] and Sieber et al. [14]. For each configuration, 180 s were recorded at a rate of 2 kHz. The data was digitally down-sampled to a rate of 100 Hz with an appropriate aliasing filter. At the investigated conditions, the measured pressure differences were of the order of 1 Pa. Therefore, the bridge amplifiers were set to high gain and high-resolution AD converters were used. Special care was taken to avoid electromagnetic interference by additional shielding of cables, mounting of ferrite cores and proper grounding of all components. The power supply of the data acquisition and the amplifiers were isolated from the main grid by a coil transformer.

The temperature in the breakdown region was measured by a type-K thermocouple with 0.25 mm shaft diameter. It was traversed through the domain to record the mean temperature distribution in the flow. These measurements are further detailed in Rukes et al. [9] and Lang et al. [18].

## 2.2. Operation conditions

The heated swirling jet is characterised by the Reynolds number, swirl number and the density ratio. The Reynolds number is given as

$$\text{Re} = \frac{v_{\text{bulk}} D}{\nu} \quad \text{with} \quad v_{\text{bulk}} = \frac{\dot{m}}{\rho_j \pi (D/2)^2}, \quad (1)$$

where  $\dot{m}$  denotes the mass flow and  $D = 51$  mm is the nozzle diameter. The density inside the breakdown bubble  $\rho_b$  relative to the jet density  $\rho_j$  defines the density ratio as

$$\rho^* = \frac{\rho_b}{\rho_j}. \quad (2)$$

Temperature measurements at an intermediate swirl number are used to calibrate a polynomial relation between the heating current and the density in the breakdown bubble,  $\rho_b$ . The reference density of the jet,  $\rho_j$ , is calculated from ambient conditions.

The swirl number  $S$  is assumed to be proportional to the swirler vane angle. This was confirmed in previous studies [22, 9, 14], where offset and proportionality are adjusted from the integral swirl number at some conditions. Compressibility effects and the influence of buoyancy are neglected due to the small Mach and Richardson numbers for the investigated conditions. With the definitions according to Rukes et al. [9], the Mach numbers are below 0.01 and Richardson numbers are below 0.05.

The PIV measurement were conducted for  $\text{Re} = 4000$  and  $S = 0.98$  whereas  $\rho^*$  was varied in the range between 0.32 and 1. Measurements were conducted on three consecutive days whereby the entire range of density ratios was measured repeatedly. For the pressure measurements, two sets were recorded at different Reynolds numbers. The measurements were conducted by an automated procedure, where the swirler vanes and heating current was changed. The corresponding parameter ranges are summarised in table 1. For both configurations, the swirl was increased in 9 steps and the density ratio was decreased in 21 steps. Each pressure measurement set has been acquired during continuous operation of the facility for approximately 12 h. Schlieren visualisations were conducted for various Reynolds numbers but only with mild heating

and at a fixed swirl number.

### 2.3. Measurement data preprocessing

The PVC is identified from the PIV measurement using snapshot proper orthogonal decomposition (POD) [26]. Accordingly, the fluctuation part of the velocity field  $\mathbf{v}' = \mathbf{v} - \bar{\mathbf{v}}$  is conceived as modal decomposition

$$\mathbf{v}(x, t) = \bar{\mathbf{v}}(x) + \sum_{i=1}^N a_i(t) \boldsymbol{\Phi}_i(x), \quad (3)$$

where  $a$  denotes the mode coefficients and  $\boldsymbol{\Phi}$  the mode shape. Note that the bold symbols stand for vector quantities. The coefficients are obtained from the eigenvectors  $\mathbf{a}_i = [a_i(t_1) \dots a_i(t_N)]^T$  of the snapshot correlation matrix  $\mathbf{R}$  as follows

$$\mathbf{R}\mathbf{a}_i = \lambda_i \mathbf{a}_i, \quad \text{with } R_{j,k} = \int \mathbf{v}(x, t_j) \mathbf{v}^T(x, t_k) dx. \quad (4)$$

Further detail on the application of POD to PIV data from swirling jets can be found in Oberleithner et al. [5] and Rukes et al. [22].

The PVC is commonly represented by the first two POD modes which can be combined to a complex mode coefficient  $A = a_1 + ia_2$ . The PVC energy, in turn, results from the average squared magnitude  $E = |A|^2$ .

For the stochastic modelling of the flow, long, time-resolved recordings of the PVC amplitude are necessary. These were obtained from the pressure measurements of the flow. From previous investigations, it is well established that the PVC mode can be deduced from circumferential pressure measurements [18, 23, 14, 27]. The pressure signals  $p_k$  recorded at eight azimuthal measurement positions were decomposed into azimuthal Fourier modes, reading

$$\hat{p}_m(t) = \frac{1}{8} \sum_{k=1}^8 p_k(t) e^{-imk\pi/4}, \quad (5)$$

where  $m$  stands for the azimuthal wavenumber. The PVC was directly obtained as the first azimuthal mode  $A = \hat{p}_1$ . The quality of the signal  $\hat{p}_1$  was furthermore improved by using a bandpass filter with the band  $[\frac{2}{3}f_{\text{PVC}}, \frac{3}{2}f_{\text{PVC}}]$  centred around the average PVC frequency  $f_{\text{PVC}}$ , which was identified from the peak in the unfiltered spectrum. A second-order polynomial was fit to the region around the peak to estimate the frequency  $f_{\text{PVC}}$ . This was necessary for certain operation conditions, where the signal level was very low. The pressure data were normalised by a factor of 0.1 Pa to have PVC amplitudes in the range 0 to 1.

### 2.4. 3D flow field reconstruction

This section describes the reconstruction of the 3D velocity field from PIV measurements, which is a preliminary stage for calculating the Lagrangian coherent structures. There are two essential steps, the estimation of the mode

structure from phase averaging and the filtering of the data to retain the symmetries in the data and reduce measurement artefacts. The phase of the PVC is obtained from the argument of the complex amplitude,  $\phi = \angle(a_1 + ia_2)$ , where  $a_1$  and  $a_2$  are the coefficients of the two leading POD modes. This allows assigning a phase  $\phi_k$  to each of the  $N$  PIV snapshot  $\mathbf{v}_k$ . Phase averaging is conducted according to the Fourier-averaging procedure described by [28]. Accordingly, the phase averaged flow is represented as a Fourier series

$$\tilde{\mathbf{v}}(\phi) = \sum_{n=-M}^M \hat{\mathbf{v}}_n e^{in\phi}, \quad (6)$$

where the Fourier coefficients are given as

$$\hat{\mathbf{v}}_n = \sum_{k=1}^N \mathbf{v}_k e^{-in\phi_k}. \quad (7)$$

The Fourier series is truncated after  $M$  modes to reject measurement noise. For real valued input data, the positive and negative Fourier coefficients are the same  $\hat{\mathbf{v}}_n = \hat{\mathbf{v}}_{-n}$ . In contrast to common bin-based phase averaging, the Fourier-averaging allows the evaluation at arbitrary phases which is relevant for the following reconstruction. Furthermore, the cut-off of the averaging in the frequency domain (fixed number of harmonics  $M$ ) is more accurate than the selection of bin sizes and bin overlap [28]. In the current investigation, the mean ( $n = 0$ ) and the first two harmonics are used as depicted in figure 2. The least number of Fourier modes  $M$  that contribute to the phase averaged flow are found by inspecting the spatial structure of  $\hat{\mathbf{v}}_n$  and the decay of the L2-norm  $\|\hat{\mathbf{v}}_n\|$  with  $n$ .

In the present case, the oscillation in time is equivalent to a rotation about the symmetry axis of the jet. This is due to the swirling motion of the flow that couples axial and azimuthal phase velocity of the flow. Therefore, the azimuthal mode number  $m$  is equivalent to the temporal Fourier mode  $n$ . The coupling allows the reconstruction of the phase averaged 3D velocity field from a meridional measurement section [5]. Accordingly,

$$\tilde{\mathbf{v}}(x, r, \theta, t) = \sum_{n=-M}^M \hat{\mathbf{v}}_n(x, r) e^{in(\theta - \omega t)}, \quad (8)$$

where  $[x, r, \theta]$  are the cylindrical coordinates.

For the reconstruction procedure, care has to be taken that the symmetry conditions are fulfilled at the jet axis. This is crucial as slight deviations are to be expected due to unavoidable misalignment of the measurement plane or imperfections in the experimental setup (see figure 2). Especially on the centre line, the symmetries between left and right half, and also between the  $\pi/2$  phase-shifted  $v_y$  and  $v_z$  component must match. The symmetries are restored by a subsequent filtering procedure that solves a constrained minimization problem which fits a velocity

configuration	Re	$S$	$\rho^*$
PIV	4000	0.98	1 to 0.32
pressure 1	4000	0.81 to 1.15	1 to 0.40
pressure 2	6000	0.94 to 1.11	1 to 0.53
schlieren	1000 to 20 000	0.98	0.9

Table 1: Operation conditions for different measurement configurations.

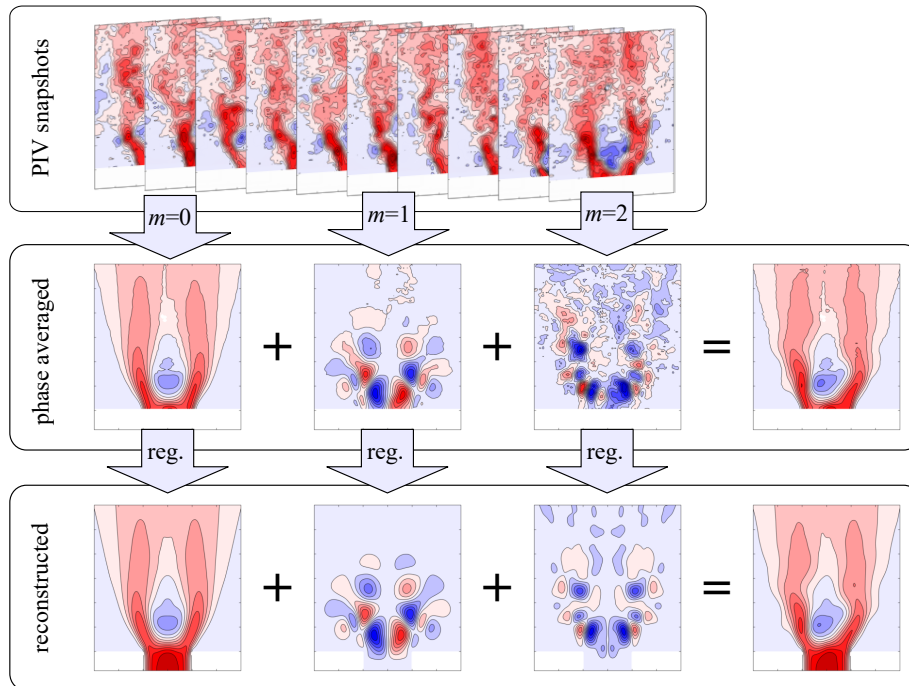


Figure 2: Schematics of the flow field reconstruction exemplified by the real part of the streamwise velocity component  $\Re(v_x)$ . The harmonic components  $\hat{v}_n$  as well as their sum  $\tilde{v}$  are presented ( $\text{Re} = 4000$ ,  $S = 0.98$ ,  $\rho^* = 1$ ). The process involves phase averaging from the PIV snapshots and a regularisation (reg.) of the different Fourier components indicated by the azimuthal wavenumber  $m$ . The azimuthal mode number  $m$  is equivalent to the temporal harmonic  $n$  for the swirling jet.

field to the data. The numerical procedure is adopted from a surface fitting algorithm proposed by D’Errico [29], where a surface is fitted to elevation data with a regularization penalty that controls the smoothness of the surface. The same approach is implemented for velocity data here, where additional constraints are included to satisfy the boundary conditions of the velocity field at the symmetry axis and the walls. Furthermore, constraints are included to fulfil the continuity equation. The thermal expansion in the vicinity of the coil is neglected since this region is not covered by the PIV and the reconstruction is only a coarse interpolation.

The velocity field reconstruction is carried out with the following steps. The velocity on the meridional plane of a regular polar grid  $X = [v_x, v_r, v_\theta]$  is estimated from the measurements  $Y = [v_x, v_y, v_z]$  on the  $x$ - $y$ -plane. Misalignments and the match of the velocity component are han-

dled by an interpolation operation  $I(X) = Y$  that is implemented as a bi-linear interpolation. The interpolation is implemented as an implicit operation, which means that the data does not have to be available in a regular grid. The smoothness of the solution is controlled by a regularisation operator  $R(X)$  that is the sum of the second derivatives of the individual fields. The boundary conditions are adopted as Dirichlet or Neumann conditions with the operator  $B(X) = Y_b$  and the continuity equation is represented as  $C(X) = 0$ . All operators are approximated as first-order finite differences. The velocity field is finally obtained by the minimisation of the combined problem

$$\|I(X) - Y\|^2 + \lambda_R \|R(X)\|^2 + \quad (9)$$

$$\lambda_B \|B(X) - Y_b\|^2 + \lambda_C \|C(X)\|^2, \quad (10)$$

where the parameters  $\lambda_R$ ,  $\lambda_B$  and  $\lambda_C$  control the relative weighting of the individual constraints. The parameters

are balanced by visual inspection of the solution. For the implementation of the continuity equation  $C(X)$  in the polar coordinate system, the azimuthal mode number is considered, reading

$$\frac{\partial v_x}{\partial x} + \frac{\partial v_r}{\partial r} + \frac{1}{r}v_r + \frac{im}{r}v_\theta = 0. \quad (11)$$

The regularisation  $R(X)$  is applied separately for each velocity and has the form (exemplified for  $v_x$ )

$$\frac{\partial^2 v_x}{\partial x^2} + \frac{\partial^2 v_x}{\partial r^2} = 0. \quad (12)$$

The approach provides smooth and reasonable velocity fields for each of the harmonics as presented in figure 2. The velocity field is also extrapolated into the nozzle, where no measurements were possible. This is helpful to allow reasonable computation of Lagrangian coherent structures near the nozzle. Moreover, the data are restored in the region of the heating element, where no measurement data were recorded. The removal of measurement uncertainties and the restoration of the symmetry of the flow provides a much better foundation for the computation of Lagrangian coherent structures than taking a simple phase average. Especially the uncertainties at the jet axis would otherwise create unphysical artefacts.

### 2.5. Lagrangian coherent structures

The Lagrangian coherent structures are computed from the finite-time Lyapunov exponents (FTLE) [16]. The FTLE is a measure for the divergence of path lines in a fixed time interval, which can be calculate forward or backwards in time. Forward time FTLE highlights repelling structures whereas backward time FTLE pronounces attracting structures. In the present study, the interfaces between the jet and the breakdown bubble are investigated. These correspond to interfaces where the flow from different regions meets, which is highlighted by backward time FTLE.

The different steps towards the FTLE representation of the flow are graphically summarised in figure 3. The basis for the computation of the FTLE is a 3D time-resolved representation of the flow field as it was determined from the procedure described in the previous section. To compute the FTLE, the flow is homogeneously seeded with virtual particles  $\mathbf{x}_p$ . The pathlines of these particles are computed backward in time from the velocity, reading

$$\mathbf{x}_p(t_0 - \Delta t) = \mathbf{x}_p(t_0) - \int_{t_0}^{t_0 - \Delta t} \tilde{\mathbf{v}}(\mathbf{x}_p(t), t) dt. \quad (13)$$

The integral is calculated with a 4th order Runge-Kutta solver and the integration time is chosen to be 1.5 periods of the PVC oscillation. The actual FTLE is calculated from the distance of particles after the integration relative to their initial distance. This is given by

$$\sigma_{\text{FTLE}} = \frac{\log(d_0/d_1)}{\Delta t}, \quad (14)$$

where  $d_0$  is the initial distance and  $d_1$  the final distance after the integration time  $\Delta t$ . The divergence for one point is computed from a group of four particles, separated by a very small initial distance  $d_0$  in all three coordinate directions. Since the divergence of pathlines is not homogeneous in all spatial direction, the maximal separation of the initial quadruplet of points is determined from the leading eigenvalue of the space spanned by the final distances between the points.

### 2.6. Stochastic modelling

To describe the observed dynamics of the PVC, Landau's amplitude equation is used [30]. The stochastic perturbations induced by turbulence are included as additive coloured noise. Accordingly, the dynamics are described by the stochastic amplitude equation as

$$\dot{A} = (\sigma + i\omega)A - \alpha|A|^2 A + \xi. \quad (15)$$

The first term on the right hand side contains the frequency  $\omega = 2\pi f_{\text{PVC}}$  and the growthrate  $\sigma$  of the PVC mode. The second term reflects the nonlinear saturation of the PVC at the limit-cycle that is governed by the Landau constant  $\alpha$ . The third term contains the stochastic forcing with the coloured noise  $\xi$ . It is characterised by the autocorrelation

$$\langle \xi(t), \xi(s) \rangle = \frac{D_\xi}{\tau} e^{-|t-s|/\tau}. \quad (16)$$

The added noise depends on the noise intensity  $D_\xi$  and the noise time scale  $\tau$ .

By changing the variables to phase and magnitude, with  $A = |A|e^{i\phi}$ , and by subsequent stochastic averaging [31], a separation of equation 15 into magnitude and phase is achieved, reading

$$|\dot{A}| = \sigma|A| - \alpha|A|^3 + \frac{\Gamma}{|A|} + \xi_A \quad \text{and} \quad \dot{\phi} = \omega + \frac{\xi_\phi}{|A|}, \quad (17)$$

respectively. This allows the dynamics of the magnitude  $|A|$  to be described independently from the phase.

However, due to the stochastic forcing, another deterministic contribution is added to the equation that is governed by the effective noise intensity  $\Gamma$ . This corresponds to the power spectral density of the noise at the oscillation frequency which is given by

$$\Gamma = \frac{2D_\xi}{\tau^2\omega^2 + 1}. \quad (18)$$

From equation (17), the stationary solution for the probability density function (PDF) of the magnitude  $P(|A|)$  is derived, which has the following form

$$P(|A|) = \mathcal{N}|A| \exp(c_1|A|^2 + c_2|A|^4) \quad (19)$$

with the unknown parameters  $c_1$  and  $c_2$ . The parameter  $\mathcal{N}$  is chosen such that the integral PDF is normalised as  $\int_0^\infty P(|A|) = 1$ . The analytical solution (19) is fit to the

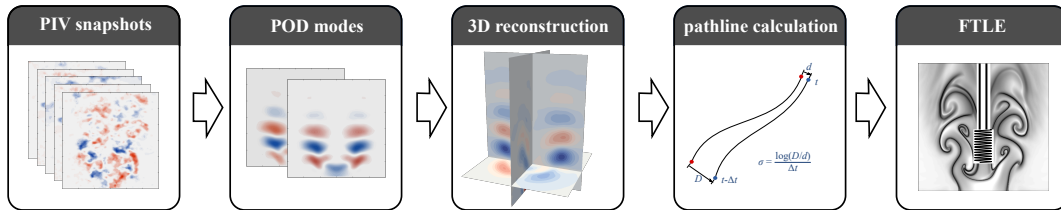


Figure 3: Flowmap depicting the steps from PIV measurements to the finite time Lyapunov exponents (FTLE).

measured PDF to estimate the unknown model parameters. The physical parameters of the amplitude equation (15) depend on these model parameters as

$$\sigma = \frac{c_1 \Gamma}{2} \quad \text{and} \quad \alpha = -c_2 \Gamma, \quad (20)$$

which includes an additional dependence on the added noise. To estimate the noise intensity from experimental data, the phase equation (17) is rearranged to

$$\xi_{\text{est}} = |A| \left( \dot{\phi} - 2\pi f \right), \quad (21)$$

which provides an estimate of the stochastic forcing. The comparison of the autocorrelation of the estimated forcing  $\langle \xi_{\text{est}}(t), \xi_{\text{est}}(s) \rangle$  to the theoretical function (16) allows the noise parameters  $D_\xi$  and  $\tau$  to be determined, which in turn determine the effective noise intensity  $\Gamma$  (18).

Further details about the stochastic model and the related derivations can also be found in the investigation by Sieber et al. [14].

### 3. Results

The results are divided into two groups according to the experimental parameters. The PIV and flow visualisations are all conducted for a fixed swirl number of  $S = 0.98$  and Reynolds number of  $\text{Re} = 4000$ , whereas the pressure measurements span a larger range of swirl numbers. Therefore, the mean flow field and the mode structure obtained from POD, FTLE and schlieren images are presented first. This is followed by the presentation of the stochastic model calibration based on pressure measurements.

#### 3.1. Mean flow and temperature field

The basic characteristics of the flow field of a swirling jet undergoing vortex breakdown are illustrated in the sketch in figure 4 a. It shows the breakdown bubble that forms the annular jet with inner and outer shear layers. The shape of the dominant coherent structure, sketched in figure 4 b, is indicating that the vortex centre of the swirling jet precesses and wraps around the recirculating region. Due to this phenomenon, this coherent structure is termed the preprocessing vortex core (PCV). The roll-up of the vortices in the inner and outer shear layer due to Kelvin-Helmholtz-instability is synchronised with the motion of

the vortex core. As indicated in the figure, the PVC motion causes a strong deformation of the breakdown bubble.

The shape of the mean flow field is further quantified in figure 5 based on the PIV data. The displayed axial velocity contours allow the backflow in the recirculation bubble to be compared to the velocity in the annular jet. In figure 5 a, it is visible that the magnitude of the backflow is approximately a third of the bulk velocity. Furthermore, the comparison of the velocity field without a coil (figure 5 a) and the field with unheated coil inserted in the flow (figure 5 b) allows to quantify the influence of the coil on the mean flow. It shows that the velocity field outside of the coil is barely altered. Mainly, the breakdown bubble has become a little wider with the coil. However, a large part of the recirculating flow is guided through the coil which was the reason to place it there. Hence, the coil heats the backflow in the bubble and creates a density jump at the interface between the jet and the breakdown bubble.

The flow field with a heated coil is shown in figure 5 c. It shows that the heating does not change the overall characteristics of the flow. However, the considerable amount of heating applied in this case causes a decrease in the width of the breakdown bubble. The backflow has still a similar magnitude as observed for the cold case. This underlines the neglect of buoyancy effects due to the small Richardson numbers [9].

The mean temperature field is exemplified in figure 6 as a horizontal and vertical profile for the same case as shown in 5 c. Accordingly, the applied heating causes a strong temperature gradient in the inner shear layer. The slope of the temperature gradient in  $y$ -direction is opposite to the radial gradient of the axial velocity, which is decisive for the suppression of the PVC considered here. The maximum temperature at  $x/D = 0.6$  and  $y/D = z/D = 0$  is taken as reference for the density ratio introduced in equation (2). A more detailed discussion of the mean and phase averaged temperature field can be found in a related study, where the temperature field was reconstructed using tomographic background oriented schlieren [18].

#### 3.2. POD mode shapes and energy

The POD was applied as the first measure to quantify the impact of the heating on the PVC. The display of the energy in figure 7 a shows that the heating strongly reduces the PVC energy as determined from the POD. However, a reduction is only prevailing until a density ratio of

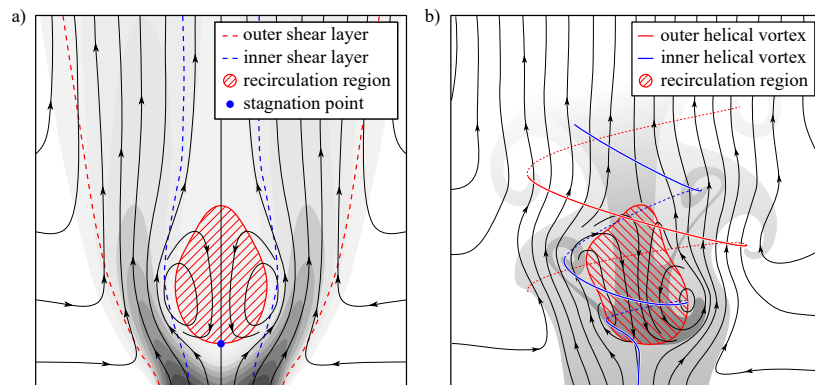


Figure 4: Schematics of the flow field: a) mean velocity field indicated by streamlines and velocity magnitude as grey contour levels, b) instantaneous velocity field indicated by streamlines and coherent structure as grey background. Specific features of the flow fields are marked and indicated in the legends. The breakdown bubble is indicated by the recirculating flow in the centre of the jet.

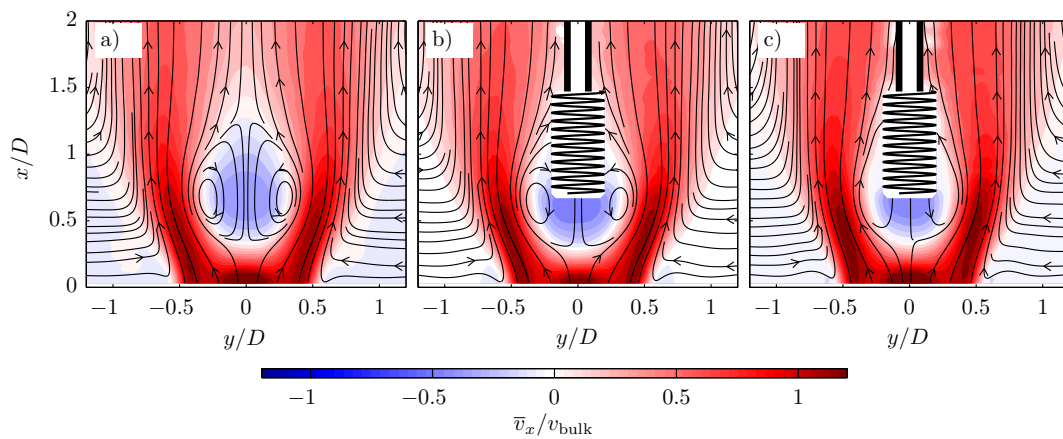


Figure 5: Mean velocity field for the baseline case a), flow with unheated coil  $\rho^* = 1$  b) and heated flow  $\rho^* = 0.5$  c) ( $Re = 4000$ ,  $S = 0.98$ ).

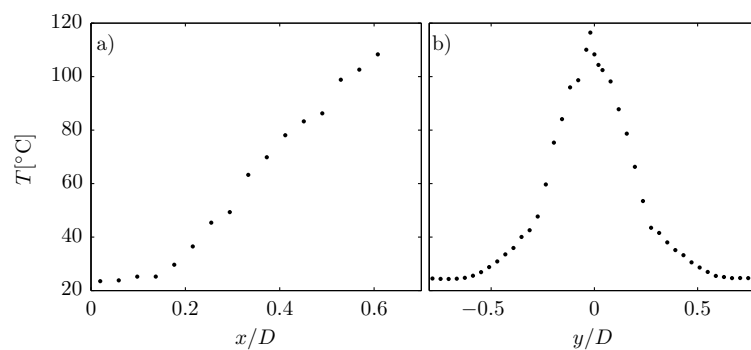


Figure 6: Measured mean temperature profiles a) along the centerline ( $y = z = 0$ ) and b) along a crosswise profile below the heating coil ( $x/D = 0.6$ ,  $z = 0$ ) ( $\rho^* = 0.8$ ,  $Re = 4000$ ,  $S = 0.98$ ).

$\rho^* = 0.65$ . Below that, there is only a marginal decay. Moreover, it is only reduced at maximum to 40% of the energy in the cold case. With one exception, these observations are consistent with the earlier studies presented in Rukes et al. [9]. Previously, a slight increase in energy at low heating was observed. This was not reproduced in the present case although many repeated PIV measurements were undertaken in the present investigation (58 measurements). The variance of the results indicates that there is an intrinsic variance in the slow time scales in the order of minutes (PIV measurements are averages from approximately 3 min). This was also discussed in the context of the temperate field tomography in Lang et al. [18]. Therefore, the previously observed increase in energy at slight heating was most probably due to a variance of the experimental boundary conditions.

Figure 7 b shows the PDF of the PVC amplitude. Accordingly, the variance of individual snapshots is larger than the relative change of the mean value due to the changing density ratio. This explains the large variance of individual PIV as indicated by the grey surface in figure 7 a.

The POD mode shape of the PVC is presented in figure 8, again showing cases without the coil, with unheated coil and with the heated coil. The display of different cases shows again that the insertion of the unheated coil does not alter the flow significantly. The presented spatial structures for both cases agree nearly perfectly, except for a slight change in magnitude directly below the coil. Moreover, the heating of the flow (figure 8 c) does also not have a visible impact on the mode shape.

The combined information from mode energy and mode shape indicates that the heating of the breakdown bubble roughly halves the PVC energy but does not change the spatial structure. This is important, as a systematic study of the influence of heating on PVC and the modelling does not work if the heating alters the mean flow or the PVC mode shape.

### 3.3. Visualisation of the spatial structures

The spatial structure of the PVC is visualised from FTLE and schlieren images. The different approaches are compared to validate the extensive processing of the measurement data during the calculation of the FTLE. Furthermore, the schlieren images, which are instantaneous and not phase-averaged, provide insight into the small scale turbulent mixing in the presented case.

The FTLE images for the baseline case, as well as one with an unheated and heated coil, are presented in figure 9. The spatial structure of the FTLE is also shown in the sketch in figure 4, which allows a direct assignment to the vortex structures presented there. The deformed interfaces of the inner and outer shear layer are well visible from the FTLE. Furthermore, the synchronised roll-up of both shear layers in counter-rotating pairs becomes precisely visible. Whereby the vortex in the inner shear layer leads in streamwise position and magnitude. The general

perception from the comparison of the three visualisations (figure 9 a-c) is that the insertion of the coil does not affect the structure and that the heating reduces the strength of the shear layer roll-up. This agrees well with the observations from the mode energy and mode shape in the previous section.

In figure 10 different experimental flow visualisations are presented. These show remarkable similarities with the FTLE visualisations in figure 9. The roll-up intensity and staggering of vortices at the two interfaces agree very well. The experimental visualisations represent a snapshot of a flow instance that is deliberately selected due to the good agreement with the other visualisations. Note that there is typically a phase-jitter in the experiment that disrupts the spatial arrangement of structures, which is also visible from the downstream dispersion of the structures. The experimental flow visualisations are carried out at halve the Reynolds number to reduce the present distortions as far as possible. The FTLE images, instead, constitute idealised representations of the flow structures, where phase jitter is eliminated due to the phase averaging involved in the data processing. The qualitative agreement with experimental flow visualisations shows that the FTLE based on a low order reconstruction of the flow is a good approach to capture the essential features of the dominant coherent structure.

The schlieren visualisations are further used to investigate the influence of an increased Reynolds number on the density stratification between jet and breakdown bubble. Figure 11 shows schlieren images of the flow around the heating coil for increasing Reynolds numbers. The selected snapshots show qualitative changes that are visible in all images for a specific Reynolds number. At  $Re = 4000$  (Figure 11 a), there is a very sharp interface between jet and breakdown bubble around the stagnation point (see figure 4 a). With an increase to  $Re = 10000$  and  $Re = 20000$  (Figure 11 b and c), this interface becomes more and more dispersed due to turbulent diffusion of the small scale structures. The flow still exhibits the same large scale structures concerning the convective transport of heated air, however, the density gradient at the interface becomes blurred. The large scale structures are governed by the mean flow that is relatively unaffected by the Reynolds number changes, while the small scale structures scale with the Reynolds number due to a reduction of the viscous effects. This observation will be important for understanding the mixing process involved in the current experiments.

### 3.4. Calibration of the stochastic model from pressure measurements

In the following, the calibration of the stochastic model using pressure measurement data are explained and the estimated model parameters for different operating conditions are presented.

To ease the understanding of the basic approach, we first consider a measured time series and the correspond-

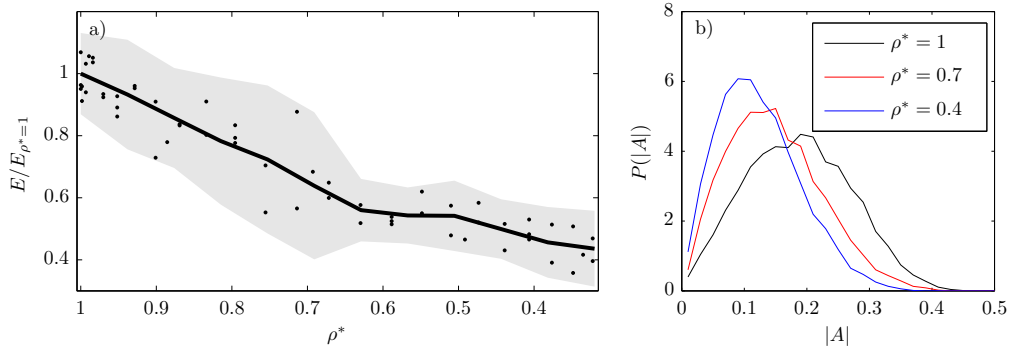


Figure 7: Energy of the PVC for decreasing density ratios a) and PDF of the oscillation magnitude b). a): The dots correspond to the mean energy from single PIV measurement with 1000 images each. The line and the gray surface mark estimates for the mean value and the 95% percentile respectively. b): The PDF constitutes the ensemble of PIV measurements in the range of  $\Delta\rho^* = 0.06$  around the value indicated in the legend. ( $Re = 4000$ ,  $S = 0.98$ ).

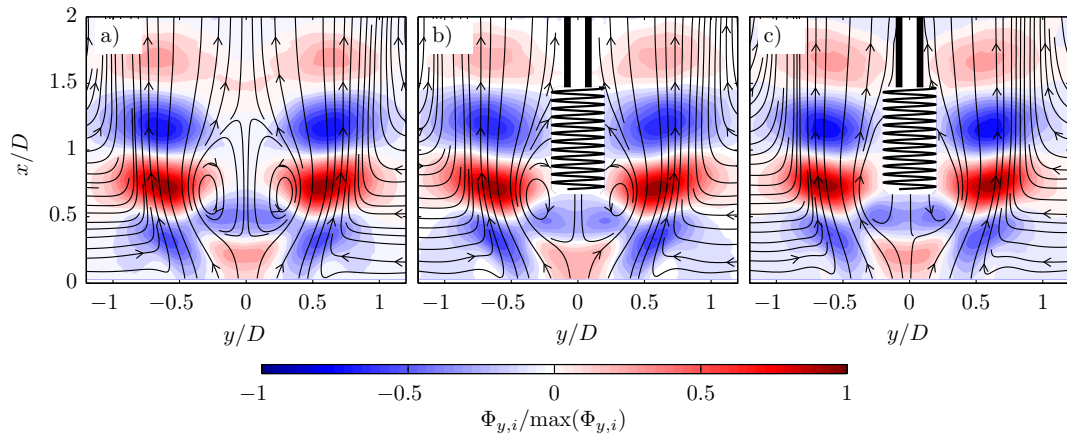


Figure 8: Leading POD mode for the baseline case a), flow with unheated coil  $\rho^* = 1$  b) and heated flow  $\rho^* = 0.5$  c). The phases of the modes are aligned to facilitate a comparison of the structure ( $Re = 4000$ ,  $S = 0.98$ ).

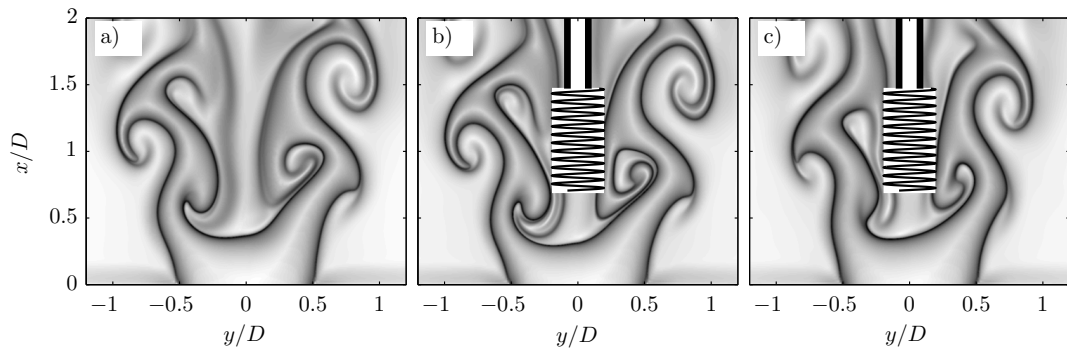


Figure 9: FTLE of the phase averaged flow for the baseline case a), flow with unheated coil  $\rho^* = 1$  b) and heated flow  $\rho^* = 0.5$  c) ( $Re = 4000$ ,  $S = 0.98$ ).

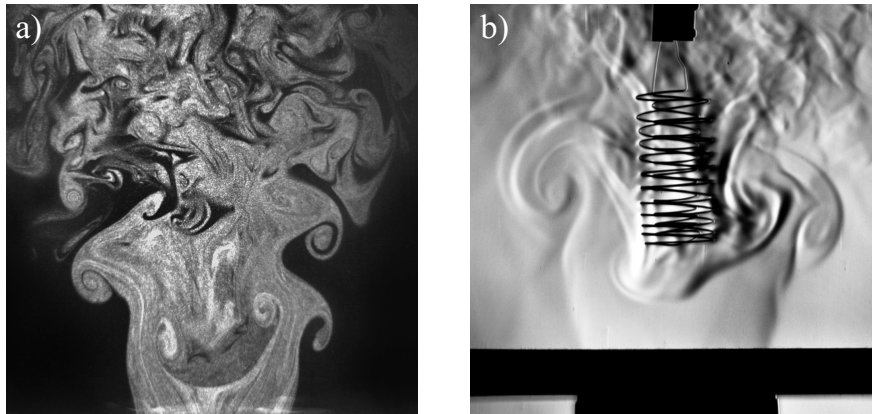


Figure 10: Smoke a) and Schlieren b) visualisation of the swirling jet at  $Re = 2000$ . For the smoke visualisation, the jet is seeded with oil particles and illuminated by a laser sheet. For the schlieren visualisation, the jet is heated slightly above the ambient temperature and the breakdown bubble is heated additionally by the coil ( $S = 0.98$ ).

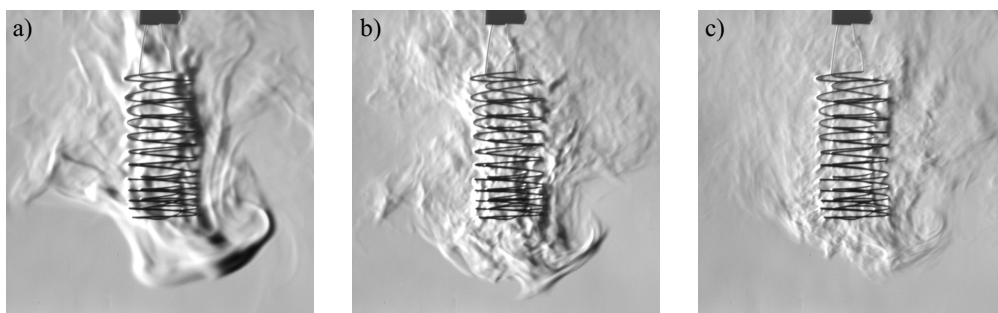


Figure 11: Schlieren visualisation of the heated breakdown bubble for increasing Reynolds numbers: a)  $Re = 4000$ , b)  $Re = 10000$ , c)  $Re = 20000$ . Similar phases of the global mode for different  $Re$  are selected according to visual similarity. Images are taken at slightly heated conditions  $\rho^* \approx 0.9$  ( $S = 0.98$ ).

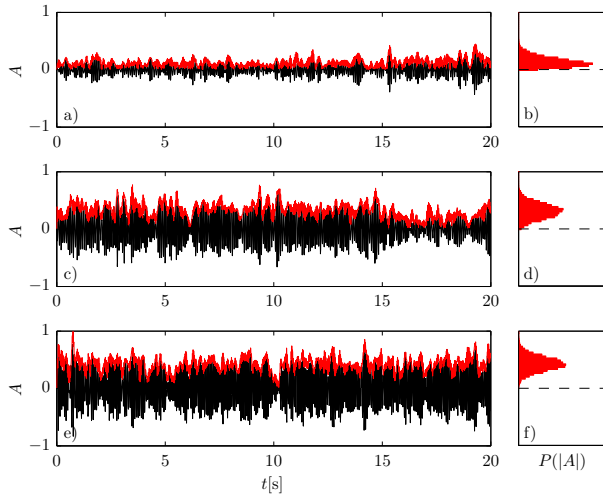


Figure 12: Timeseries of the PVC amplitude determined from the pressure Fourier coefficient  $A = \hat{p}_1$  (a,c,e) and probability density of the envelope  $|A|$  (b,d,f) for increasing swirl numbers at  $S = 0.98$  (a,b),  $S = 1.06$  (c,d) and  $S = 1.15$  (e,f). The black lines show the real part of the signal  $\Re(A)$  and red lines and bars indicate the magnitude  $|A|$  ( $Re = 4000$ ,  $\rho^* = 1$ ).

ing stationary PDF of the oscillation magnitude. In figure 12, the PVC amplitudes determined from the pressure signal according to equation 5 are presented for different swirl numbers. Strong modulation of the oscillation amplitude is evident for all conditions. The envelope of the oscillation further shows that the magnitude of the oscillation increases with swirl and the variance changes substantially. This can be even better inspected from the amplitude PDF shown next to the time series. At the lowest swirl number (figure 12 b), the PDF is similar to a Rayleigh distribution, while at the highest swirl number (figure 12 f) it is similar to a Gaussian distribution. For the intermediate swirl (figure 12 d) the PDF resembles a mixture of both distribution types.

To calibrate the model the analytical function (19) must be fitted to the measured PDF. This is done for different  $S$  and  $\rho^*$  to investigate the stability of the PVC depending on the operation conditions. Figure 12 a) shows that this approximation is in good agreement. The changes in the PDF for different swirl numbers are further detailed in figure 13 b). It shows a continuous change of the PDF starting with narrow, low amplitude distributions, which increase in width and amplitude for increasing swirl intensity. The change from a Rayleigh to a Gaussian distribution, which was already observed in figure 12, is also visible. The fit to the experimental data is further conducted for all the investigated operation conditions to obtain the growth rate of the PVC according to equation (20) as a function of swirl number and density ratio.

In figure 14 d, the amplification rate determined from the model is shown for all investigated Swirl numbers and density ratios for  $Re = 4000$ . The stability margin, where

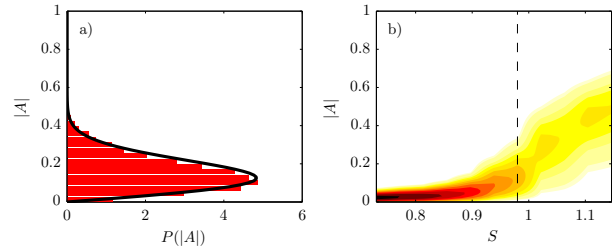


Figure 13: Probability density of the envelope  $|A|$  at  $S = 0.98$  together with the analytical fit (a) and fit of the probability density for increasing swirl numbers as contour plot (b). The dashed line indicates the position of the curve in plot a) ( $Re = 4000$ ,  $\rho^* = 1$ ).

the flow changes from negative to positive amplification rate is highlighted by a thick contour line. Furthermore, the mean magnitude, frequency and noise intensity are represented together with the stability margin (figure 14 a-c). In this representation, the frequency and amplification rate are normalised by the bulk velocity and nozzle diameter given by  $St = fu_{\text{bulk}}/D$  and  $\sigma^* = \sigma_{\text{bulk}}/D$ . The data for the contour graphs are filtered in the  $S$ - $\rho^*$ -plane by a  $3 \times 3$  Gaussian filter to facilitate the visibility of contour lines and the perception of trends in the data. The same procedure applies for the analogue representation of the data at higher Reynolds numbers given in figure 15.

Figure 14 shows that the stability margin of the PVC mainly depends on the swirl number. At the lower Reynolds number (figure 14), the stability margin is inclined towards lower swirl numbers at isothermal conditions. This confirms a dependency of the flow instability on the density ration. There is a PVC magnitude level that coarsely coincides with the stability margin, which indicates that the amplitude of the instability is linked to the instability growth rate. However, the contours show that even at stable conditions there is still a substantial PVC amplitude, which clearly shows the influence of the stochastic forcing. Furthermore, no indication of a bifurcation is visible from the magnitude.

The PVC frequency (figure 14 b) increases with swirl number and with decreasing density ratio. The increase at low swirl numbers and low-density ratios must be evaluated carefully since the signal level in this range are very low ( $|A| < 0.1$ ). The effective noise, shown in figure 14 c, which is perturbing the PVC dynamics, scales mainly with the swirl number. Similar to the magnitude, it shows a continuous increase in the investigated range. The amplification rate (figure 14 d), however, shows a clear dependency on the density ration. Besides the inclination of the stability margin, the increase of the amplification rate with the swirl number becomes much steeper for reduced density ratios.

Figure 15 shows the identified model parameters for the higher Reynolds number. Accordingly, the dependency of the model parameters on the swirl stays very similar to the low Reynolds case, whereas the density ratio dependency

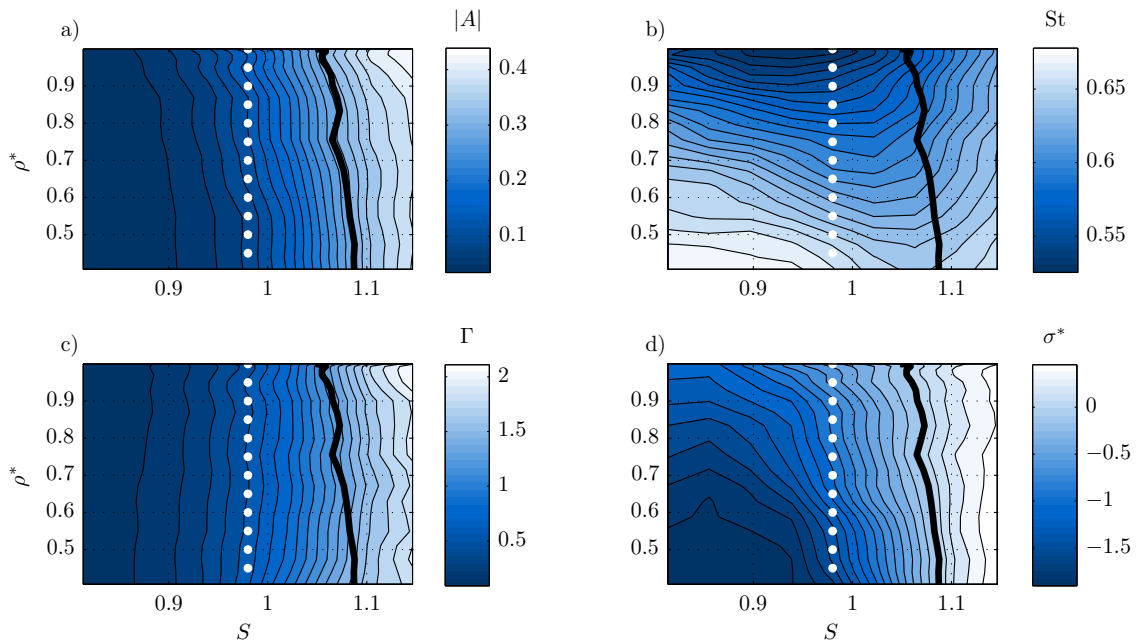


Figure 14: Calibration of the low dimensional model for changing swirl numbers  $S$  and density ratios  $\rho^*$  for  $Re = 4000$ . The contour plots show levels of the PVC amplitude  $|A|$  a), normalised frequency  $St$  b), noise level  $\Gamma$  c) and normalised amplification rate  $\sigma^*$  d). The black line indicates the stability margin that separates the stable (left) and unstable (right) region in the parameter space. The white dots indicate the parameters of the PIV measurements in figure 7.

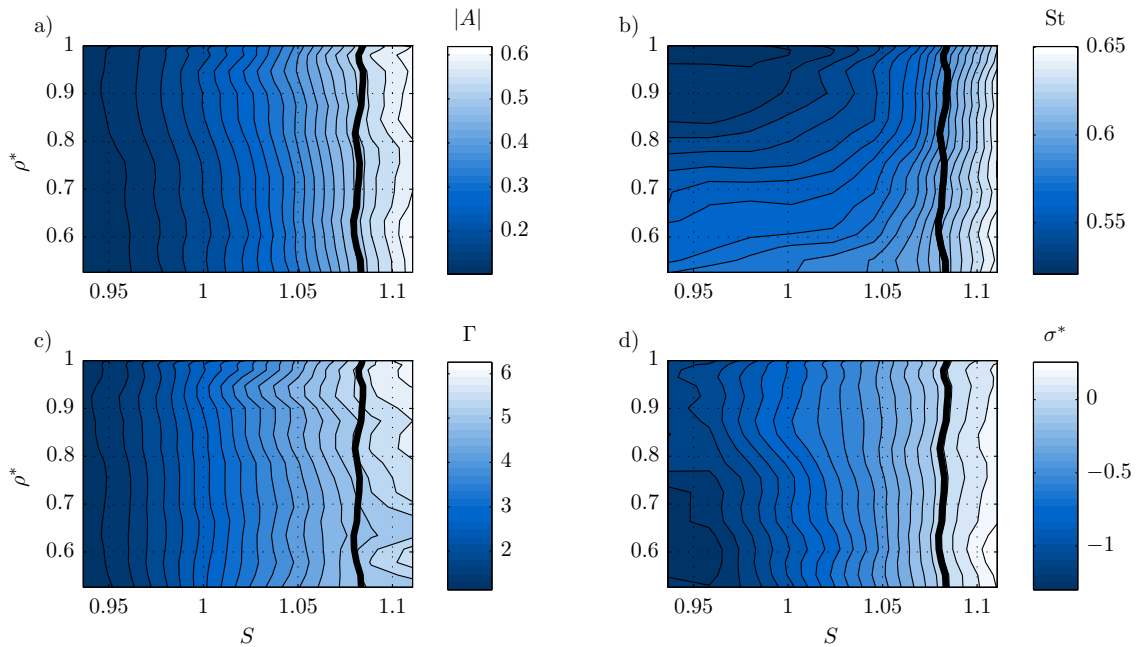


Figure 15: Same as fig. 14 but for  $Re = 6000$ .

has weakened or disappeared. The amplification rate (figure 15 d) still shows a steeper increase with the swirl number for lower density ratios, however, the stability margin does not depend on the density ratio. The frequency (figure 15 b) is also increasing slightly with decreasing density ratio. The amplitude (figure 15 a) and the effective noise (figure 15 c), however, depend only on the swirl number. It can be seen that by increasing the Reynolds number, the critical swirl number has not changed, but the influence of density ratio becomes very small.

#### 4. Discussion

Different aspects the reveal from the combined consideration of the presented results are discussed in the following. This primarily concerns the influence of the Reynolds number on the stability margin of the PVC. Second, the relevance of FTLE images and the related low order representation of the flow for mixing is discussed. Finally, the impact of stochastic dynamics in a turbulent flow on experimental observations is explained.

##### 4.1. Influence of the Reynolds number on the PVC suppression

The investigation at higher Reynolds numbers does not reveal a significant influence of the heating on the PVC. This is in line with previous observations by Rukes et al. [9], where experimental observations and linear stability analysis on the mean flow were confronted. There, it was shown that the change of the Reynolds number does not substantially change the amplification of the related instability. However, the position of the density gradient relative to the velocity gradient was demonstrated to be as relevant as the (global) density ratio for the stability of the flow. This is in agreement with the more general investigation of density stratification on Kelvin-Helmholtz instabilities conducted by Fontane and Joly [21]. There, it was similarly shown that the density ratio, as well as the collocation of density and velocity gradients, are the governing parameters for a change of the growth rates.

The present investigation of schlieren images at increasing Reynolds numbers shows that the emerging small-scale turbulence affects the density contrast at the interfaces between the heated breakdown bubble and the jet. The increasing turbulent diffusion flattens the density gradient and shifts it towards the low-density side. This is not visible from the mean temperature profiles since they are governed by the large scale perturbations in the flow. The difference between averaged and instantaneous temperature gradients of the investigated flow is further discussed in the course of a related BOS tomography [18].

##### 4.2. Spatial structures from FTLE and schlieren

The observation of the temporal PVC dynamics reveals that there is no constant amplitude that changes according to the operating conditions. It is a perturbed intermittent

dynamic that only reveals a change of the dynamics from a statistical analysis of the observations. In this context, the FTLE structures constitute prototype coherent structures that represent only the phase averaged flow state.

The experimental smoke and schlieren visualisations contain all sorts of temporal and spatial variations of the structures. The agreement of some instantaneous experimental observations with the FTLE visualisations indicates the phase averaged shape is characteristic for the underlying coherent structure. However, the turbulent dispersion and diffusion must be kept in mind when comparing it to instantaneous realisations of the flow.

The comparison of the experimental visualisations and the FTLE images shows that simplified perception of the flow as mean flow and the dominant oscillatory motion is sufficient to describe the large scale mixing in the flow. The FTLE computations are based on this basic flow model and they accurately reproduce the instantaneous interfaces between the jet and the breakdown bubble as well as between the jet and the ambient. The undisturbed structure in the FTLE images gives a clear picture of the flow dynamics and allows a better understanding of the mixing processes.

##### 4.3. Observation of stable modes in a turbulent flow

The description of the dynamics by the stochastic amplitude equation explains why the PVC is always observed in measurement data, no matter if the related global mode is stable or unstable. The essential feature of the stochastic model is that it never settles to a stable state. Due to the stochastic forcing, it is always perturbed but it seeks to return to the stable states due to the deterministic dynamics. Therefore, the model responds with an oscillatory dynamics to the broadband excitation, which is also known as coherence resonance Gang et al. [15]. For experimental investigations, this implies that the observation of a dominant mode in the data does not mean that the extracted structure belongs to an unstable mode of the flow. There can be slightly damped modes that become excited by the turbulent perturbations.

The operation parameters for the PIV measurements were selected according to the observation of a low amplitude PVC in the measurements. The subsequent reductions of the PVC due to the heating showed a dependence but no clear transition from stable to unstable conditions was attained. The broad scan of operation conditions by pressure measurements revealed that the PIV investigations were conducted only at stable conditions.

This work suggests that the stationary PDF of the oscillation magnitude from (non-time-resolved) PIV measurements can be used as an indicator for the flow state. The PDFs from stable and unstable modes differ mainly in the range near zero. Stable modes show a Rayleigh distribution with nearly linear decay of the function towards zero, while unstable modes have an exponential decay towards zero. The determination of the actual amplification rate needs the knowledge of the noise properties as well, but the

sign of the amplification rate depends only on the shape of the PDF.

## 5. Summary and Conclusions

In the present study, the effect of local heating inside the breakdown bubble on the global mode of the swirling jet was investigated. Motivated by the observations in swirl-stabilised burners, the suppression of the global mode by density stratification was examined. Concerning the combustion studies, the global mode is referred to as precessing vortex core (PVC). The application of electric heating allowed to replicate the suppression of the PVC in a generic swirling jet, as already shown in a previous study. Further effects, such as the observation of a weak PVC at stable conditions and the disappearance of the density dependence at higher Reynolds numbers remained unclear. The present study employs a stochastic model to describe the experimental observations which further allows characterising the stability margin that marks the transition from a stable to an unstable flow state. The investigation of visualisations from finite-time Lyapunov exponents (FTLE) and experimental schlieren visualisations further detailed the mixing due to the PVC and the dependency on the Reynolds number.

The calibration of the stochastic model using pressure measurements over a wide range of operating conditions allowed to describe the stability margin as a function of the swirl number, the density ratio and the Reynolds number. The applied heating of the breakdown bubble shifts the bifurcation point towards larger swirl numbers, showing that the density ratio, is a second control parameter for the PVC. This dependency vanishes at larger Reynolds numbers, where the stability margin depends only on the swirl number.

The strong influence of the Reynolds number on the stability of the heated flow is attributed to the occurrence of small scale mixing that smears the sharp density interface. The global density ratio, which is considered as a sole control parameter in the current study, is not sufficient to characterise the influence of density stratification on the PVC. The collocation of density and velocity gradients and the instantaneous density gradient must be considered as well.

The present investigations provide a detailed view of the dynamics of a hydrodynamic instability in a turbulent flow. The stability margin of the flow is identified although the flow is strongly perturbed by turbulent fluctuations at all scales. The proposed procedure needs only measurements from the stationary flow state, no transient or forced experiments are required. This may serve as an example for the investigation on instabilities in other flows. Furthermore, the extraction of FTLE images from non-time-resolved PIV measurements outlines a way for the computation of valuable flow visualisations from limited experimental data.

## Acknowledgment

The authors kindly acknowledge the funding from the German Research Foundation under DFG Project PA 920/30-1 and DFG Project PA 920/37-1.

## References

- [1] N. Syred, J. M. Beér, Combustion in swirling flows: A review, *Combustion and Flame* 23 (1974) 143–201. doi:10.1016/0010-2180(74)90057-1.
- [2] P. Billant, J.-M. Chomaz, P. Huerre, Experimental study of vortex breakdown in swirling jets, *Journal of Fluid Mechanics* 376 (1998) 183–219. doi:10.1017/S0022112098002870.
- [3] F. Gallaire, J.-M. Chomaz, Mode selection in swirling jet experiments: a linear stability analysis, *Journal of Fluid Mechanics* 494 (2003) 223–253. doi:10.1017/S0022112003006104.
- [4] H. Liang, T. Maxworthy, An experimental investigation of swirling jets, *Journal of Fluid Mechanics* 525 (2005) 115–159. doi:10.1017/S0022112004002629.
- [5] K. Oberleithner, M. Sieber, C. N. Nayeri, C. O. Paschereit, C. Petz, H.-C. Hege, B. R. Noack, I. Wygnanski, Three-dimensional coherent structures in a swirling jet undergoing vortex breakdown: stability analysis and empirical mode construction, *Journal of Fluid Mechanics* 679 (2011) 383–414. doi:10.1017/jfm.2011.141.
- [6] M. Stöhr, I. Boxx, C. D. Carter, W. Meier, Experimental study of vortex-flame interaction in a gas turbine model combustor, *Combustion and Flame* 159 (2012) 2636–2649. doi:10.1016/j.combustflame.2012.03.020.
- [7] S. Terhaar, T. G. Reichel, C. Schrödinger, L. Rukes, C. O. Paschereit, K. Oberleithner, Vortex breakdown types and global modes in swirling combustor flows with axial injection, *Journal of Propulsion and Power* 31 (2014) 219–229. doi:10.2514/1.B35217.
- [8] K. Oberleithner, S. Terhaar, L. Rukes, C. Oliver Paschereit, Why nonuniform density suppresses the precessing vortex core, *Journal of Engineering for Gas Turbines and Power* 135 (2013). doi:10.1115/1.4025130.
- [9] L. Rukes, M. Sieber, C. O. Paschereit, K. Oberleithner, The impact of heating the breakdown bubble on the global mode of a swirling jet: Experiments and linear stability analysis, *Physics of Fluids* 28 (2016). doi:10.1063/1.4963274.
- [10] L. Rukes, M. Sieber, C. O. Paschereit, K. Oberleithner, Methods for the extraction and analysis of the global mode in swirling jets undergoing vortex breakdown, *Journal of Engineering for Gas Turbines and Power* 139 (2016) 022604. doi:10.1115/1.4034315.
- [11] N. Noiray, B. Schuermans, Deterministic quantities characterizing noise driven hopf bifurcations in gas turbine combustors, *International Journal of Non-Linear Mechanics* 50 (2013) 152–163. doi:10.1016/j.ijnonlinmec.2012.11.008.
- [12] N. Noiray, Linear growth rate estimation from dynamics and statistics of acoustic signal envelope in turbulent combustors, *Journal of Engineering for Gas Turbines and Power* 139 (2017) 041503. doi:10.1115/1.4034601.
- [13] M. Lee, Y. Zhu, L. K. B. Li, V. Gupta, System identification of a low-density jet via its noise-induced dynamics, *Journal of Fluid Mechanics* 862 (2019) 200–215. doi:10.1017/jfm.2018.961.
- [14] M. Sieber, C. O. Paschereit, K. Oberleithner, Stochastic modelling of a noise driven global instability in a turbulent swirling jet, arXiv:2007.07555 (2020).
- [15] Gang, Ditzinger, Ning, Haken, Stochastic resonance without external periodic force, *Physical review letters* 71 (1993) 807–810. doi:10.1103/PhysRevLett.71.807.
- [16] G. Haller, Lagrangian coherent structures, *Annual Review of Fluid Mechanics* 47 (2015) 137–162. doi:10.1146/annurev-fluid-010313-141322.
- [17] M. Sieber, F. Ostermann, R. Woszidlo, K. Oberleithner, C. O. Paschereit, Lagrangian coherent structures in the flow field

- of a fluidic oscillator, *Phys. Rev. Fluids* 1 (2016) 050509. doi:10.1103/PhysRevFluids.1.050509.
- [18] H. M. Lang, K. Oberleithner, C. O. Paschereit, M. Sieber, Measurement of the fluctuating temperature field in a heated swirling jet with bos tomography, *Experiments in Fluids* 58 (2017) 88. doi:10.1007/s00348-017-2367-1.
- [19] F. Lückoff, M. Sieber, C. O. Paschereit, K. Oberleithner, Impact of the precessing vortex core on nox emissions in premixed swirl-stabilized flames - an experimental study, *Proceedings of ASME Turbo Expo 2020* (2020).
- [20] J. Reinaud, L. Joly, P. Chassaing, The baroclinic secondary instability of the two-dimensional shear layer, *Physics of Fluids* 12 (2000) 2489. doi:10.1063/1.1289503.
- [21] J. Fontane, L. Joly, The stability of the variable-density kelvin-helmholtz billow, *Journal of Fluid Mechanics* 612 (2008) 237–260. doi:10.1017/S0022112008002966.
- [22] L. Rukes, M. Sieber, C. O. Paschereit, K. Oberleithner, Effect of initial vortex core size on the coherent structures in the swirling jet near field, *Experiments in Fluids* 56 (2015) 183. doi:10.1007/s00348-015-2066-8.
- [23] J. S. Müller, F. Lückoff, P. Paredes, V. Theofilis, K. Oberleithner, Receptivity of the turbulent precessing vortex core: synchronization experiments and global adjoint linear stability analysis, *Journal of Fluid Mechanics* 888 (2020).
- [24] C. E. Willert, M. Gharib, Digital particle image velocimetry, *Experiments in Fluids* 10 (1991). doi:10.1007/BF00190388.
- [25] G. S. Settles, *Schlieren and shadowgraph techniques: Visualizing phenomena in transparent media*, Experimental Fluid Mechanics, Springer, Berlin and Heidelberg and New York, 2001. doi:10.1007/978-3-642-56640-0.
- [26] L. Sirovich, Turbulence and the dynamics of coherent structures: Part i: Coherent structures, *Quarterly of Applied Mathematics* 45 (1987) 561–571.
- [27] F. Lückoff, M. Sieber, C. O. Paschereit, K. Oberleithner, Phase-opposition control of the precessing vortex core in turbulent swirl flames for investigation of mixing and flame stability, *Journal of Engineering for Gas Turbines and Power* 141 (2019). doi:10.1115/1.4044469.
- [28] R. Sonnenberger, K. Graichen, P. Erk, Fourier averaging: a phase-averaging method for periodic flow, *Experiments in Fluids* 28 (2000) 217–224. doi:10.1007/s003480050381.
- [29] J. D’Errico, *Surface fitting using gridfit, matlab central file exchange*, 2006.
- [30] L. D. Landau, On the problem of turbulence, *C. R. Acad. Sci. URSS* 44 (1944).
- [31] J. B. Roberts, P. D. Spanos, Stochastic averaging: An approximate method of solving random vibration problems, *International Journal of Non-Linear Mechanics* 21 (1986) 111–134. doi:10.1016/0020-7462(86)90025-9.

## Chapter 4

# Discussion

### 4.1 SPOD for the analysis of flow dynamics

This section discusses the collective findings from the application of the SPOD to various flows presented in the different publications in chapter 3. Furthermore, the supplementary material in the appendix shows specific features of the SPOD for generic and experimental data. There, the equivalence of time and frequency domain SPOD is demonstrated for experimental data of a turbulent jet (appendix A.1). The application of boundary conditions and the capability of the SPOD to identify periodic dynamics in noisy environments are demonstrated using generic data (appendix A.2 and A.3). Finally, the dependency of the decomposition on the extend of the SPOD filter is clarified (appendix A.4).

#### 4.1.1 Relation between different SPOD variants

The initial naming of the time domain SPOD proposed in publication 3.1 has led to some confusion having overseen the similar naming of the frequency domain SPOD (Towne et al., 2018). However, this unfortunate choice of names has focused our investigations on this topic with the perspective that similar names may be attributed to common features. The derivation presented in chapter 2 showed that both SPOD approaches can be converted into each other and that they rely on similar principles, which affirms this assumption. The two variants are distinguished by the treatment of the temporal dimension and therefore we have chosen to call it either a time-domain SPOD (tdSPOD) or a frequency-domain SPOD (fdSPOD). As the differentiation between tdSPOD and fdSPOD is only needed in this subsection, SPOD refers to the tdSPOD in the remainder of the discussion. The analogy of both approaches is further approved by the decomposition of experimental data from a turbulent jet (appendix A.1). It showed that the dominant modes of time- and frequency-domain SPOD have comparable mode shapes. A general difference, however, is the representation of the mode coefficient. The strict separation of the modes according to frequencies in the fdSPOD does not allow further analysis of temporal flow dynamics. This is the general difference to the tdSPOD which is used in various forms for the identification of flow dynamics in the current work.

The close similarity between delay embedding and tdSPOD explains the previously reported ability of tdSPOD to reconstruct dynamics of partially recorded phenomena (Sieber et al., 2016c), which is the main feature of delay embedding. Moreover, it explains why delay embedding in combination with POD (the same as tdSPOD) by Brunton et al.

(2017) tends to yield coefficients that can be described by linear models. This is evident if the tdSPOD is considered as an operation that locally linearises the flow dynamics by restricting the change of frequency and amplitude of the modes (Sieber et al., 2016c). Similarly, the HAVOK models (Brunton et al., 2017) tend to exhibit linear dynamics and the nonlinearities contribute as intermittent forcing. In the more recent work by Kamb et al., 2020, the time-delay embedding is described more systematically as convolutional coordinates. Where it is also shown that the time-delay snapshot POD (or SVD) constitutes a local linearisation of the dynamics obtained by the decomposition.

The capabilities of the HAVOK approach to identify system dynamics motivated an evaluation of the ability of tdSPOD to identify dynamics in generic noisy data. This short study is presented in detail in appendix A.3. The application of the method requires a more detailed specification of the treatment of signal boundaries, which is provided in appendix A.2. Within the analysis, different boundary conditions are evaluated to assess their characteristics. The analysis shows that tdSPOD, similar to delay embedding, provides a more robust identification of system dynamics than the utilisation of the raw data alone. A reduction of prediction errors by two orders of magnitude is possible for some cases when the boundary conditions are selected appropriately.

#### 4.1.2 Coping with nonlinear interactions and stochastic disturbances

As described in the previous section, the SPOD (abbr. for tdSPOD in the following) constitutes a short-time linearisation of the dynamics contained in the analysed data. Therefore, the application of SPOD for the identification of coherent structures constitutes specific dynamic properties of these structures. The SPOD seeks a modal decomposition, where the coefficients separate between slow variations of amplitude and frequency and the fast variation of the phase. From a physical point of view, this reflects the separation of slow variations governed by the mean flow and the fast oscillations of a hydrodynamic instability.

The SPOD decomposes according to spatial coherence and short-time temporal coherence (see section 2.1). The spatial coherence requires fixed spatial modes and results in the separation of temporal dynamics and spatial mode shapes. The short-time temporal coherence is equivalent to a short-time linearisation of the dynamics. The SPOD gives the freedom to fade between an energetically optimal POD and a spectrally pure Fourier decomposition. The stronger the filter of the SPOD is set, the more the coefficients converge to constant amplitude oscillations. This property is decisive to separate nonlinear interactions in the flow into interpretable modal contributions.

As demonstrated in publication 3.2 and 3.3, the SPOD assigns a mode pair to each fundamental contribution and to the modal interactions at different frequencies. This allows a proper quantification of different contributions and allows a simple interpretation of the transient development. The separation into modal contributions with limited spectral bandwidth is most natural for the interpretation of the temporal dynamics. In contrast, the common POD tends to mix fundamental contributions and interactions in single modes, which causes the interpretation of time dynamics to be cumbersome and confusing.

However, the linearisation introduced with the SPOD can also interfere with the non-linear flow dynamics. If the SPOD filters too strictly, the linearisation does not match the nonlinear dynamics in the data and the dynamics are spread across several modes. This becomes clear by the consideration of the limiting case of a Fourier decomposition in publication 3.1. Furthermore, the dispersion of dynamics is demonstrated from a series of decompositions with a continuous increase of the filter size presented in appendix A.4.

The effect of the SPOD filter becomes even more pronounced when investigating stochastic perturbations of the dynamics. The stochastic modelling procedure introduced in publication 3.4 makes use of the phase-jitter present in the dynamics. It is used to estimate the intensity of the stochastic perturbations that act on a specific mode. If the SPOD filter attenuates the phase jitter, this can lead to an underestimation of the stochastic perturbations. This is similar to the effect of a bandpass filter in the data preprocessing discussed by Bonciolini et al. (2017). Therefore, when using the SPOD coefficients for stochastic modelling, special care must be taken to adjust the filter size.

### 4.1.3 Principal disadvantage of modal decompositions

The interpretation of flow data in a modal decomposition is very convenient from a mathematical point of view. The separation of spatial modes and temporal coefficients allows a very reduced representation of the flow dynamics by the mode coefficients. However, the representation of spatial structures by static modes misses a fundamental transport phenomenon in fluid dynamics, the convection.

Generally, an arbitrary vortex structure in the flow can be composed of many fundamental frequencies. The superposition of those frequencies at the correct phases constitutes a wave package that replicates the vortex. The convective motion can be described by a constant group velocity of the fundamental contributions of the wave package. Nevertheless, this is not the most intuitive way to describe convective motion.

A simpler approach to describe convective motion is the detachment from a fixed Eulerian view of the dynamics and the transition to a Lagrangian view. There are approaches to describe a modal decomposition in a moving reference frame (Reiss et al., 2018), however, this transfers the difficulty to the determination of the convection velocity. There are further promising approaches from flow visualisation that distinguish between features (vortices) and feature flow field (convection) (Günther et al., 2017). This might also serve as an approach to define moving reference frames for a modal decomposition.

Another approach to handle convection in a decomposition can be inspired by the handling of the time-domain in the SPOD (see section 2.1). In analogy to the definition of a local time-scale, the spatial coherence can also be considered only locally. This would mean to consult a correlation function of the form

$$R(r, r', \tau, \tau') = \iint u(x + r, t + \tau)w(r + c\tau)u^*(x + r', t + \tau')w^*(r' + c\tau')dxdt, \quad (4.1)$$

where the convective velocity scale  $c$  accounts for the relative scaling of local time  $\tau$  and local distance  $r$ . The integral is considered in analogy to equation (2.8), where the Gaussian weighting function  $w$  determines the extent of the local scales. The solution of the

corresponding *Lumley integral equation*

$$\iint R(r, r', \tau, \tau') \Phi_i(r', \tau') dr' d\tau' = \lambda_i \Phi_i(r, \tau) \quad (4.2)$$

will give modes that only depend on relative distances and are therefore translation invariant in space and time. They might be interpreted similarly to spatio-temporal wavelets with the difference that their construction is data-driven, which may result in a basis that is much more compact. This decomposition might provide fundamental building blocks of turbulent flows that remain valid beyond a specific flow configuration. In principal, this decomposition does not constitute a reduction of the dimensionality, since the mode coefficients still depend on space and time. However, it could provide a useful alternative to the rapidly developing use of convolutional neural networks for the abstraction of flow data in machine learning algorithms (Ye et al., 2020).

In the current work, the investigations are focused on the analysis of global modes, where the influence of convection is not very pronounced. Due to the global instability, the entire velocity field oscillates at the same frequency and with a fixed mode shape. This perfectly fits the representation by a modal decomposition. However, the ideas presented here may inspire other researchers to probe these approaches where needed.

## 4.2 Coherent structures in turbulent flows

This section comprises the overall findings from the application of stochastic methods for the description of hydrodynamic instabilities in turbulent flows. They originate largely from the publications 3.4 and 3.5, but also from general findings from the entire dissertation.

### 4.2.1 Observation of hydrodynamic instabilities in a turbulent flow

The observation of a hydrodynamic instability evolving in a turbulent flow must be interpreted taking into account the background turbulence. The turbulence does not constitute a secondary dynamic that exists on top of large-scale structures, but it interacts with larger scales. This was shown in detail in the investigations in publication 3.4 and publication 3.5, where the proposed stochastic model captures the dynamics.

The essential feature of the employed stochastic model is that it never settles to a fixed point or limit cycle. The model is always perturbed by the stochastic forcing but it exhibits deterministic dynamics when returning to the fixed point or limit cycle. Therefore, it responds with an oscillatory dynamic to the broadband excitation. Since the turbulent flow was seen to behave similarly, this led to the insight that the observation of a dominant mode in the measurement data does not mean that the extracted structure belongs to an unstable mode of the flow.

The further investigation of the interaction between the instability and the slow mean-flow corrections (section 3.4) has shown that secondary dynamics play an important role. The deterministic and stochastic dynamics must be strictly separated for the description of the dynamics in a turbulent flow by the proposed stochastic method. Therefore, all remaining flow dynamics that interact with the investigated instability must be covered

in the model. They cannot be lumped with the stochastic perturbations, as this would violate the basic assumptions of the method.

The accurate modelling of secondary dynamics provided a better understanding of the investigated swirling jet. However, the basic approach still identifies the underlying bifurcation very accurately. There were slight changes in the bifurcation point and the magnitude of the linear growth rate. Nevertheless, the requirement of a profound model for the flow dynamics should not discourage from applying the proposed stochastic methods. The insights gained from the most simple models are already a big improvement compared to the consideration of basic statistical moments (e.g., mean and variance).

#### 4.2.2 Discrepancies between modal, phase averaged and instantaneous flow structures

Although modal decompositions offer valuable opportunities to analyse flow dynamics, the representation of the corresponding spatial structures is often unintuitive and cumbersome. The spatial velocity distribution of one mode does not explain a lot about the associated coherent structure. The picture only emerges from the reconstruction of the flow from the mean flow and the investigated mode. The reconstruction of the velocity field and the further computation of finite-time Lyapunov exponents (FTLE) in publication 3.5 showed this very clearly.

The phase averaged flow constitutes the mean representation of the velocity that corresponds to a certain coherent structure. From the derivations of Sonnenberger et al. (2000) it is clear that the phase averaged flow constitutes the sum of the mean flow, the fundamental oscillation, and all higher harmonics. Therefore, a single (S)POD mode does not constitute a coherent structure but only a part of it. The coherent flow field associated with an (S)POD mode is obtained from the sum of the specific mode, the mean flow, and the higher harmonics that are in phase with the mode. Usually, these higher harmonics appear as additional modes with a fixed phase relation to the fundamental mode. In practice, however, it is much more convenient to phase average based on the phase of the fundamental mode.

In publication 3.5 the phase averaged flow is further used to compute FTLE fields. This has been shown to be in remarkable agreement with experimental schlieren and smoke visualisations. The resemblance of the instantaneous experimental observations and FTLE visualisations indicate that the phase-averaged flow is characteristic for the underlying coherent structure. Accordingly, the FTLE structures are prototype coherent structures that represent the phase-averaged flow state. The undisturbed structure in the FTLE images gives a clear picture of the coherent structure that facilitates the interpretation of flow dynamics. This has been further demonstrated in a video awarded at the APS Gallery of Fluid Motion (Sieber et al., 2016a).

#### 4.2.3 Difference between measurement noise and turbulent perturbations

The modal decomposition of measurement data from turbulent flows usually gives a small set of energetic large scale modes and a continuous range of smaller scales that fade

into measurement noise at some point. For the representation of coherent structures, only the few energetic modes are relevant. Since the smaller scales cannot be distinguished from the measurement noise, the conclusion is close considering they are similar to measurement noise. The representation of the flow as a sum of modes further confirms the assumption that higher-order modes are only additive contributions. However, this led to many false interpretations of low-order dynamics from modal coefficients in the current work.

The actual difference between measurement noise and turbulent perturbations is that the turbulent perturbations cause a response of the flow. The accurate incorporation of turbulent perturbations into the dynamical models was the key element for the correct interpretation of measurement data. Therefore, this short section shall remind that turbulence can't just be cut-off or filtered out like measurement noise. It constitutes an essential part of the flow that must be modelled appropriately when it is not represented by the considered state variables.

At the moment the flow is disturbed, the perturbation can be assumed to be just a superposition. But the disturbance does not disappear immediately - it is dispersed according to the prevailing fluid dynamics. Like a stone thrown into a lake, which is just a random disturbance when it hits the surface, but the waves that spread on the water are completely deterministic.

### 4.3 The dominant modes in a turbulent swirling jet

The general knowledge gained about the dynamics of the global (helical) mode is summarised here. In contrast to previous studies focusing on one single configuration, the variety of swirling jet flows analysed in the framework of this manuscript allows to draw more general conclusions. For the sake of brevity, the term precessing vortex core (PVC) is used in the following, which is commonly used in the gas turbine community for a hydrodynamic global mode of helical shape. The following discussion gives a summary of the different modes observed in swirling jets, the identified control parameters for the PVC, and an alternative explanation for the observed bifurcation scenarios.

#### 4.3.1 Observed modes and mode interactions in a swirling jet

Throughout the investigations, the single helical PVC was always the most dominant oscillatory mode that appeared solely due to fluid dynamics. In combustion-related investigations (publication 3.2 and 3.3), a dominant axis symmetric mode appears due to the thermo-acoustic (TA) oscillations, which is referred here as TA mode. Often, a second helical mode in the wake of the breakdown bubble is observed (publication 3.1, 3.2, and 3.4), which is referred here as wake mode.

It was shown that the presence of a TA mode of low amplitude modulates the PVC frequency. However, at large TA mode amplitudes, the PVC dynamic is suppressed. The wake mode, instead, is not affected by the TA mode in the presented investigations. This is most likely because the TA mode and wake modes have only little spatial overlap. The PVC and the wake mode, however, overlap in the breakdown bubble and they show modal interaction. In the high swirl case analysed with the SPOD in publication 3.4,

modes at interaction frequencies occur. The relevant SPOD spectrum is replicated in figure 4.1 to discuss further aspects in the next section.

Beyond the oscillatory modes, there appear two relevant shift-modes that are not distinguished up to this point. First, there is one shift-mode that corresponds to the stream-wise movement of the breakdown bubble (shift-mode 1), which is referred to in the presented publications. Second, another shift-mode can be identified from the SPOD modes corresponding to a change of the breakdown bubble width (shift-mode 2). Both modes and their effect on the flow are discussed in more detail in the investigation of Rukes et al. (2015).

The two shift-modes are brought up to provide a tentative physical explanation of the existence of the two saturation mechanisms in the stochastic mean-field model (see publication 3.4). The pressure measurements used in the investigations indicate only shift-mode 1, which is assumed to be strongly driven by random swirl fluctuation in the setup. On the other hand, shift-mode 2 is mainly driven by Reynolds stresses induced by the PVC. Accordingly, the *delayed saturation* in the mean-field model is governed by shift-mode 1 and the *direct saturation* is governed by shift-mode 2. Since the *direct saturation* can be implicitly handled by the model through the cubic saturation term, the corresponding shift-mode does not need to be explicitly represented in the model.

The comprehensive studies of the swirling jet provided a very clear picture of the participating modes and underlying dynamics. This helped to identify the source of dynamic phenomena in a swirl stabilised combustors (see section 3.3). Furthermore, this can give a guideline to interpret the dynamics in future investigations of swirling flows. The rediscovery of modes in various studies has reinforced the evidence that the phenomena described here are general properties of swirling jets.

#### 4.3.2 Stochastic modelling for the entire SPOD spectrum

The development of a stochastic model has provided a simple procedure to assign a growth rate to the dominant mode in a flow. This raises the question: Why shouldn't a growth rate be assigned to each SPOD mode of the flow? The stochastic modelling, as applied to the PVC, is not suited for this task because low-energy modes are not resolved correctly, which hinders the determination of the effective noise intensity disturbing each mode. However, the shape of the magnitude probability density function (PDF) can be determined to give a ranking of the instability. Therefore, the magnitude PDF of each mode pair is fit to the analytical function (3.19) in publication 3.4 and the fit parameter  $c_1$  is used to indicate the mode stability. The SPOD coefficient magnitudes are normalised by the mean value prior to the fit, such that the value of  $c_1$  converges to  $-\pi/4$  for a Rayleigh distribution, which indicates the limit of purely random dynamics.

The representation of the SPOD spectrum with the common display of mode coherence and the new display of mode growth rate is given in figure 4.1. The principal difference to the previous representation is that it is possible to distinguish between stable and unstable modes. The new representation with the growth rate (figure 4.1 bottom), indicates the PVC (1) and its first two harmonics (2 and 3) as unstable modes. These are followed by the marginally stable wake mode (4), the higher harmonic of the wake mode (6), and a meandering mode in the far wake (5). The old representation (figure 4.1 top),

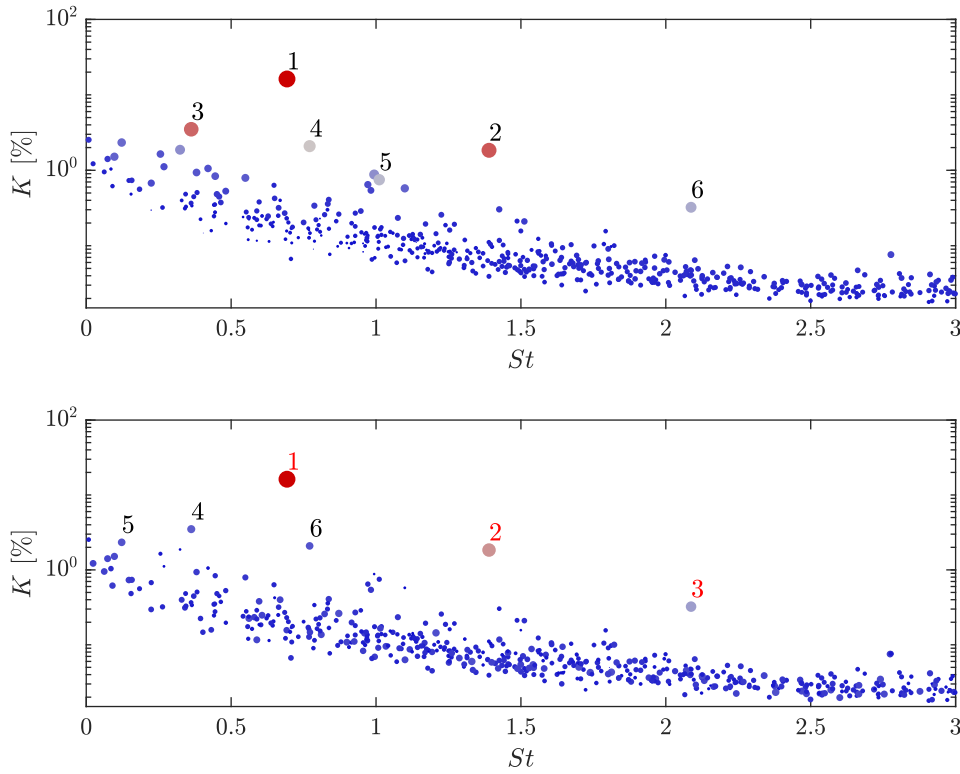


FIGURE 4.1: (top) SPOD mode spectrum reproduced from figure 5 of publication 3.4 showing mode energy  $K$  across the Strouhal number  $St$ , where marker size and colour represent the spectral coherence of mode pairs (equation (2.21) of publication 3.1). (bottom) An adaption of the SPOD spectrum, where marker size and colour represent the growth rate of the mode according to the magnitude PDF. The numbering in both representations is in decreasing order according to the marker size. Red numbers indicate unstable modes in the growth-rate representation (bottom).

assigns also the PVC to be the most dominant mode (1). However, the wake mode (3) is found to be similarly important as the second harmonic of the PVC (2), according to the mode coherence. This is followed by the harmonic of the wake mode (4), an interaction mode (5), and the second harmonic of the PVC (6).

Generally, the ranking of the modes by growth rate clearly distinguishes between the primary instability and secondary dynamics. It similarly assigns the fundamental and higher harmonics of the PVC to one category. This is plausible since they add up to one coherent structure as disused in the previous section. The growth rate representation looks very promising for the analysis of flows with potentially unclear dynamics and can complement or replace the representation with the mode coherence.

The PDF of the mode pair magnitude can be linked to the phase portrait of a mode pair (e.g., figure 2 in publication 3.1). An unstable mode exhibits a clear limit cycle that appears as a "doughnut" shape due to the turbulent perturbations. If these doughnuts become filled, the modes belong to more stable flow structures. Entirely random mode pairs exhibit a 2D Gaussian distribution that converts to a Rayleigh distribution in the magnitude representation. Therefore, the ranking of modes by growth rate from the PDF gives a measure for the phase portrait characteristics that also relates to the hydrodynamic stability of modes.

### 4.3.3 Control parameters of the PVC bifurcation

In agreement with previous studies, the presented stochastic models showed that the swirl number controls a supercritical Hopf bifurcation of the swirling jet that leads to the PVC. The fundamental scientific addition is that the change of the oscillation magnitude with the swirl number is not a good indicator to identify the stability margin. Due to the turbulent perturbations, different characteristics are observed that are also referred to as stochastic Hopf bifurcation in related studies (Noiray & Schuermans, 2013; Noiray, 2017).

The density ratio between the jet and the breakdown bubble was further studied as a possible control parameter for the bifurcation. This was motivated by the findings from swirl-stabilized combustors, where the suppression of the PVC is observed for specific flame shapes. The current studies confirmed the relevance of the density ratio to some extent. It was shown that the Reynolds number of the flow plays an important role in this context, due to the introduction of small scale mixing. This mixing changes the density profiles and position which is of similar importance for the stability properties as the density ratio. The Reynolds dependency in the stratified investigations contrasts with the isothermal case, where the bifurcation is largely independent from the Reynolds number.

The following section will provide a further explanation for the role of the Reynolds number for the density ratio as PVC control parameter. There, the influence of turbulent perturbations on the stochastic Hopf bifurcation is investigated, assuming that the perturbations scale with the Reynolds number.

### 4.3.4 Explanation of experimental observations by a subcritical bifurcation

There are two observations in the investigation of stratified swirling jets for which the explanations given in the respective investigations are not entirely satisfactory. First, there is the sudden occurrence of a PVC in the investigation of the transient flame shape transition (section 3.3). Second, the absence of the density influence on the bifurcation at higher Reynolds numbers in the parametric swirling jet study (section 3.5). The following statements are intended to provide an alternative explanation, whereby the saturation mechanism in the amplitude equation is reconsidered.

In the transient investigations (section 3.3), the sudden occurrence of the PVC initiates the transient procedure that leads to the detachment and subsequent reattachment of the flame. However, the base state from which the procedure starts is actually stable and all perturbations must decay. In the investigations, it is argued that the PVC induced mixing decreases the density difference which in turn increases the growth rate of the PVC that might lead to a self-amplifying process. However, such a mechanism is inconsistent with the emergence of PVC from a supercritical Hopf bifurcation. Accordingly, an increase of the PVC amplitude is expected to decrease the growth rate due to the induced Reynolds stresses. The positive feedback, such as the proposed increase due to mixing, would rather call for the description of the dynamics by subcritical Hopf bifurcation.

In the parametric swirling jet study (publication 3.5), the absence of density ratio effects at higher Reynolds numbers was only explained qualitatively by an increase in mixing. With regard to a subcritical bifurcation, parts of the results of the investigation

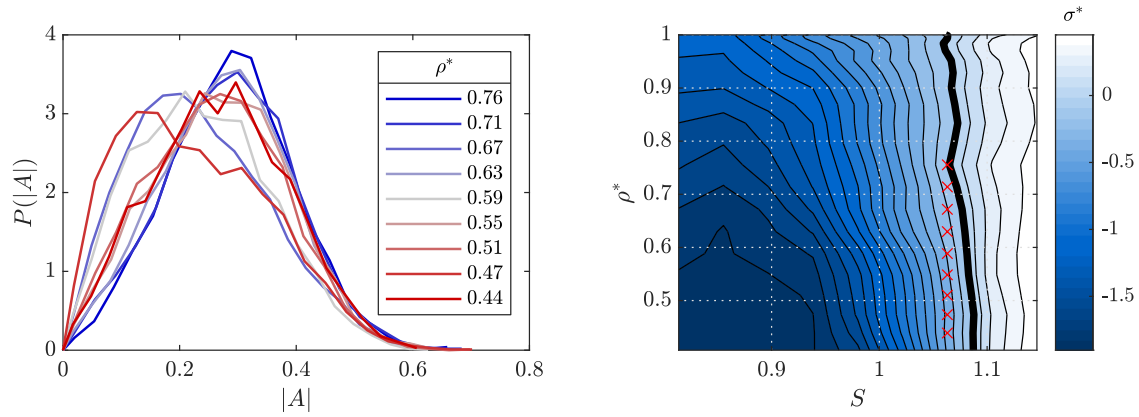


FIGURE 4.2: Probability density functions of the PVC oscillation magnitude a) at specific operation conditions as marked by the red x in the stability map b). The stability map is a reproduction of figure 14 from publication 3.5.

should be examined more closely. A more detailed view on the change of amplitude probability density functions (PDF) at different density ratios is given in figure 4.2. The focus on this specific part of the data is due to the bimodality visible in the PDF. Although the density ratio is changed in very small steps, there is no continuous transition of the PDF. Furthermore, the PDF switches between the two preferred locations as the density ratio gradually decrease. This characteristic is indicative for a bistable regime which also calls for the presence of subcritical bifurcation rather than a supercritical bifurcation.

The form of the amplitude equation (3.5) in publication 3.4 was selected explicitly to handle supercritical bifurcations. However, the addition of the next higher-order term allows to furthermore describe subcritical bifurcations (Noiray, 2017; Lee et al., 2019; Zhu et al., 2019). Accordingly, the slow dynamics of the magnitude of the oscillatory amplitude read

$$\dot{|A|} = \sigma|A| - \alpha|A|^3 - \gamma|A|^5 + \frac{\Gamma}{|A|} + \xi_A, \quad (4.3)$$

with the additional quintic term  $\gamma|A|^5$ . The linear growth rate is still represented by  $\sigma$  which may take positive and negative values governing the bifurcation of the flow. The parameter  $\alpha$  now is allowed to take also negative values that correspond to an increase of the growth rate for moderate amplitudes, which was discussed above in the context of PVC induced mixing. The saturation in the limit-cycle is then governed by the constant  $\gamma$  which is required to have positive values only. Otherwise, the amplitude may grow infinitely. The remaining terms are governed by the stochastic perturbation in analogy to the original implementation in publication 3.4.

From the amplitude equation (4.3) the potential and the corresponding probability distribution according to equations (3.17) and (3.18) in publication 3.4 is derived. To discuss different aspects of the equation, several prototype bifurcations are presented in figure 4.2. There, the linear growth rate  $\sigma$  is assumed to be proportional to the hypothetical number  $S$  ranging from  $-2$  to  $2$ . Three different scenarios concerning the noise intensity are given: a laminar flow with  $\Gamma = 0$ , a weakly turbulent flow with  $\Gamma = 0.01$ , and a strongly turbulent flow with  $\Gamma = 0.1$ . This shows the effects of turbulence on a

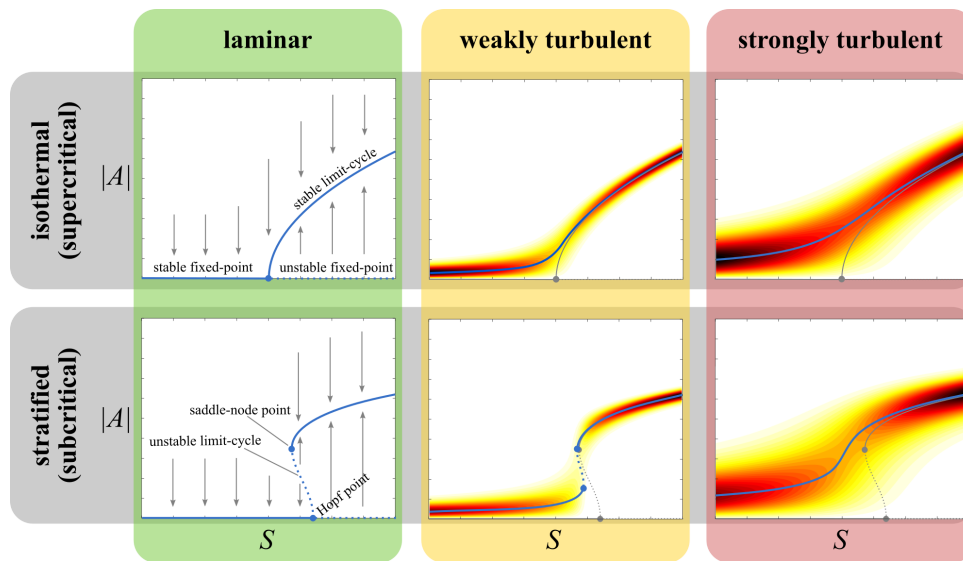


FIGURE 4.3: Schematic representation of possible bifurcation scenarios in isothermal and stratified swirling jets at different turbulence levels. The plots indicate the oscillation magnitude  $|A|$  at different swirl numbers  $S$ . The contours represent the probability density function of the oscillation magnitude. The lines indicate fixed points and limit-cycles as annotated in the graph.

supercritical bifurcation with  $\alpha = 1$  and  $\gamma = 0$  as well as a subcritical bifurcation with  $\alpha = -2$  and  $\gamma = 3$ .

The representation of these prototype bifurcations in figure 4.2 show known characteristics for the laminar case, where the additional term in the subcritical bifurcation leads to a bistable regime between saddle node and Hopf point. There, the flow state can either converge to the stable fixed point or to the stable limit-cycle. The weak turbulent perturbations cause the emergence of oscillations in the entire subcritical regime for both scenarios. Furthermore, the bistable region in the subcritical bifurcation shrinks since the turbulent perturbations push the amplitude across the unstable limit-cycle at some point. For strong turbulent perturbations, this can lead to the complete elimination of the bistable regime. In consequence, there is no longer a pronounced difference between the subcritical and the supercritical scenario.

Concerning the presented scenarios, the experimental observations can be explained as follows. In the case of the transient change of the flame shape publication 3.3), a subcritical bifurcation with weak turbulence is considered. In that case, the flow is assumed to be in the bistable regime between saddle node and Hopf point. The initial condition of the flow is the stable fixed point with damped PVC oscillations. However, at some time the stochastic perturbations are strong enough to push the amplitude across the unstable limit-cycle. Therefore, the PVC becomes unstable and starts to converge to stable limit-cycle oscillations. Due to the changing flame shape, the TA mode arises, which has a destructive interference with the PVC oscillations. This pushes the PVC amplitude below the unstable limit-cycle and reinitialises the flow state.

For the heating induced bifurcation of the flow (section 3.5) the situation is slightly different. In consistency with the previous explanation, a subcritical bifurcation with weak turbulence is considered for the low Reynolds number case, where an effect of the density ration on the bifurcation is observed. However, it is assumed that mainly

the Hopf point moves to higher swirl numbers due to the reduced density ratio. The saddle node is assumed to stay approximately at the swirl number, where the isothermal supercritical bifurcation occurs. Moreover, in the bistable regime, the flow is assumed to have a preference for the stable fixed point. This would explain the movement of the bifurcation to larger swirl numbers as observed in the experiment.

In the investigation with a larger Reynolds number, no change of the bifurcation point was observed with density stratification (reduced density ratios). Concerning the subcritical bifurcation scenario, a change of the stochastic forcing leads to a reduced preference for the stable fixed point in the bistable regime. The extreme case with strong disturbances shown in figure 4.2 illustrates that stochastic disturbances can eliminate the probability of observing the system in the stable branch of the bistable regime. Therefore, the increase of the stochastic perturbations due to a larger Reynolds number shifts the transition point to smaller swirl numbers, at which the flow is no longer observable on the stable branch. This may eliminate the change of the bifurcation point due to a reduced density ratio. In practice, the change of the Reynolds number furthermore influences the location of the Hopf or saddle-node point, as argued in publication 3.5. The combined influence of the stochastic forcing and the change in parameters may be relevant for the phenomenology observed in the experiments.

Considering the given experimental evidence, the explanations given here are rather speculative. Nevertheless, they show an approach to be probed in future research. The explanation of some of the experimental observations from a subcritical bifurcation provides a more consistent picture of the flow. However, the effect of stochastic disturbances on subcritical bifurcation needs further investigation.

## 4.4 Concluding Remarks

The development and refinement of the methods in this thesis were driven by the curiosity to understand how things relate by probing their behaviour with experiments, data analysis, and models. This led to valuable insights into the swirling jet and the dynamics of the helical mode. The presented path provided a fundamental understanding of the flow and has left behind several useful methods waiting to be tested on other fluid dynamics problems. The key enabler provided by the different methods is summarised here.

The separation of flow data in a modal decomposition gives the possibility to grasp the flow dynamics from a few modes, which are obstructed in the original data. The further assignment of individual coherent dynamics to separate modes by the SPOD allows building simple models that capture the mode dynamics. In this context, the SPOD provides a weakly nonlinear representation of the flow dynamics that is very well suited to approximate the dynamics by linear models supplemented with few leading nonlinear terms. In doing so, the SPOD filter allows to adjust the extent of nonlinear effects, represented by the mode coefficients, in such a way that it fits the analysis and modelling approach.

The representation of the fluid dynamics by a stochastic model allows a consistent description of the observed dynamics and enables a better understanding of the physics

of a turbulent flow. The inclusion of the stochastic forcing was an essential step to close the gap between the experimental observations of turbulent flows and the low-order flow models. Beyond the description of flow physics, a stochastic model will also be helpful for predictive control and monitoring of the flow. Furthermore, the approach is not limited to the swirling jet, but can be applied to any flow that exhibits a global instability. However, the swirling jet served well to investigate the onset of the global instability at different turbulence levels since the bifurcation is largely independent of the Reynolds number (at isothermal conditions).

The computation of FTLE visualisations of the flow relates the modal decomposition to the spatial structures of experimental flow visualisations. Therefore, it provides an intuitive representation of flow structures that facilitates access to the related fluid dynamics. The FTLE of the phase-averaged flow gives a prototype coherent structure without the turbulent perturbations. In doing so, it visually relates back to the laminar coherent structures which were the starting point for modelling the dynamics.

The presented methods may inspire others to tackle their observations with new approaches. These methods can easily be transferred to other configurations, as some studies have already shown. For those who seek to take these methods further, the previous sections in this chapter highlight some open topics that are worth being revisited.



## Appendix A

# SPOD related supplements

### A.1 Decomposition of experimental data from a turbulent jet

This section exemplifies the relation between time- and frequency-domain SPOD by the decomposition of experimental data from a turbulent jet. The considered data are PIV snapshots of the velocity vectors on a plane oriented along the symmetry axis of a round jet. The experiments were conducted in a water tunnel with nozzle diameter ( $D$ ) of 10mm at a Reynolds number of 5000. The corresponding experimental setup can be found in a previous publication Oberleithner et al., 2014 and will not be further detailed. The data was acquired with a high-speed PIV system operated at 500 Hz, which corresponds to a Strouhal number of 9.4, given as  $St = fu_\infty/D$  ( $f$ : frequency,  $u_\infty$ : jet bulk velocity). A continuously acquired series of 3000 samples is investigated here.

To perform the frequency-domain SPOD, the time series is segmented into pieces of 120 samples that are weighted with a Gaussian window function. This corresponds to a filter size of  $N_f = 60$  (2.12) or an observation horizon  $T$  that is equivalent to two periods of the most dominant frequency at  $St=0.3$ . From the entire series, 49 segments  $u_k(x, \tau)$  with 50% overlap are created. These are Fourier transformed and the decomposition is calculated from the eigenvalues of the spectral snapshot correlation (2.23) (compare also Towne et al., 2018).

The time-domain SPOD is analogously computed from the snapshot correlation (2.10), where the same segmentation as above is used. This approach provides only very coarsely sampled coefficients  $\hat{a}(t_k)$  according to the utilised segment length and overlap. However, the temporal extension of the spatial modes can be easily obtained from this approach. Additionally, the decomposition is computed from the filtered correlation matrix (2.11) where all 3000 samples are included (corresponds to 99% segment overlap). The equivalence of the time-domain SPOD from 50% overlap with spatial correlation and 99% overlap with snapshot correlation was verified by comparing the spatial modes at  $\tau = 0$  of both approaches.

The mode spectrum of time and frequency-domain SPOD is presented in figure A.1. The frequency-domain SPOD is depicted by a line for each eigenvalue at all frequencies  $\lambda_i(\omega)$ . A significant gap between the energy of the leading mode and the following modes is indicative for a low-rank dynamic Schmidt et al., 2018. The spectrum of the time-domain SPOD is given as a scatter plot, where each dot corresponds to one mode pair that describes the real and imaginary part of a periodic oscillation Sieber et al., 2016c. The modes are paired according to their spectral coherence (also called cross-spectral density or harmonic correlation). This measure is indicated by the size and colour of the dots. It is interesting to note that both representations indicate dominant coherent structures in the Strouhal number range from 0.2 to 0.6. Apart from this, also the distribution of stochastic fluctuations is comparable. These are represented by the continuous decrease of mode

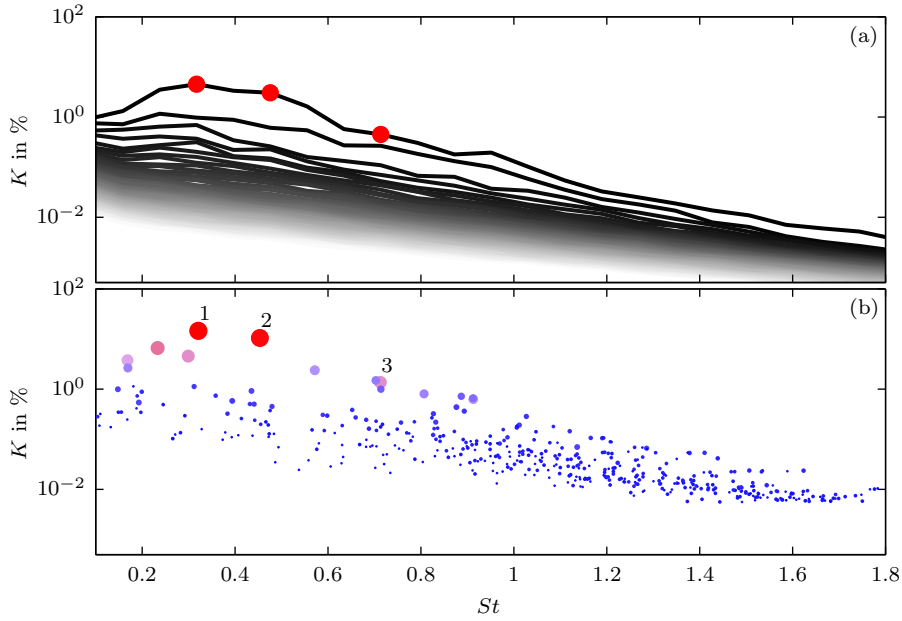


FIGURE A.1: SPOD spectrum for the frequency- (a) and time-domain (b) decomposition indicated in percent of the total turbulent kinetic energy. The frequency-domain SPOD spectrum (a) is given as a plot of each mode over  $St$  where the shades from black to white correspond to the mode ordering ( $\lambda_1 > \lambda_2 > \dots > \lambda_N$ ) Schmidt et al., 2018. In the time-domain SPOD spectrum (b), each dot corresponds to one mode pair and the size and color of the dot indicate the spectral coherence of the mode pair Sieber et al., 2016c. The red dots in (a) and numbers in (b) indicate the modes that are shown in figure A.2.

energies in the frequency-domain representation (fig. A.1 a) and an even distribution of modes with weak spectral coherence in the time-domain plot (fig. A.1 b).

The mode shapes for the different approaches are displayed in figure A.2 for three selected frequencies. The figure shows the frequency-domain mode  $\hat{\Phi}(x, \omega)$ , the time-domain mode  $\hat{\Phi}(x, \tau = 0)$ , and its Fourier transform  $\int \hat{\Phi}_k(x, \tau) e^{-i\omega\tau} d\tau$ , where  $\omega$  matches the frequency-domain mode. The frequency-domain mode is displayed at the frequencies that correspond to dominant time-domain modes (see fig. A.1). Note that the frequencies cannot be matched precisely since (for the frequency-domain SPOD) the frequencies are determined by the acquisition rate and segment length.

Although the frequency-domain mode and the Fourier transform of the time-domain modes should theoretically agree (see section A.5.1), we observe some differences in figure A.2. These deviations might be caused by the short time segment analysed, which contrasts with the statistically stationary flow assumed for the derivations. The investigated segment should ideally cover all observed time scales, which often cannot be achieved in experiments. Nevertheless, the dominant coherent oscillations are covered and they show good agreement.

The comparison of the time-domain modes (fig. A.2 a-c) and the frequency-domain modes (fig. A.2 g-i) further shows some clear differences for all frequencies. The dominant wavelength agrees with the frequency-domain mode, but there are also other wavelengths contained and the wave train does not show a smooth evolution in the streamwise direction. These phenomena can be attributed to the growth of vortices in the jet and vortex merging, which are both phenomena that are not captured by a frequency-domain approach. For illustrative reasons, the entire space-time evolution of the most dominant time-domain mode is given in figure A.3. The graph shows that this mode covers the

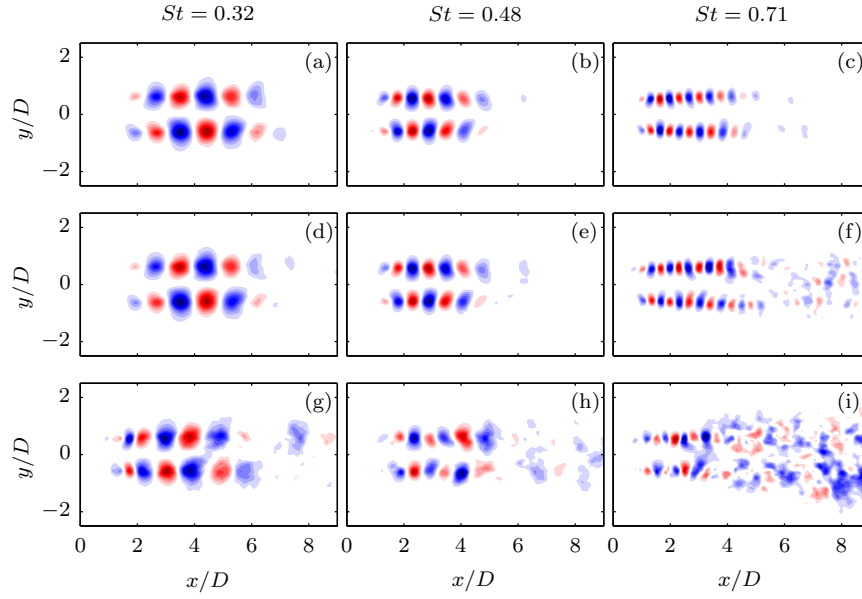


FIGURE A.2: Spatial mode shapes for the frequency- and time-domain SPOD for three frequencies indicated at the top of each column and in figure A.1, given as contours of the velocity in  $y$ -direction. The top row (a-c) corresponds to the frequency-domain modes  $\tilde{\Phi}(x, \omega)$ , the bottom row (g-i) to the time-domain modes at zero time lag  $\hat{\Phi}(x, \tau = 0)$  and the mid row (d-f) shows the Fourier decomposition of the time-domain mode at the corresponding frequency.

spatio-temporal evolution of a periodic structure. The apparent tilting angle corresponds to the convective speed or phase velocity of the structure.

The presentation of this example shows that the frequency- and time-domain SPOD are directly related through a Fourier transform. However, for the analysis of wave dispersion, the frequency-domain approach is preferable, while for the investigation of interactions between different wavelengths and/or vortex merging, the time-domain approach is more suitable. Therefore, the different decomposition strategies account for different aspects of coherent structure dynamics.

## A.2 Boundary conditions for the SPOD filter

The preceding derivations have not specified the treatment of domain boundaries for finite data sets. They were omitted deliberately to allow a seamless description of the derivations and different methods without introducing complicated notations. In this section, we present four variants of possible boundary conditions and discuss their impact on decomposition accuracy.

Generally, for convolutions like  $\hat{u}(t) = \int w(\tau)u(t + \tau)d\tau$ , where the function  $w$  is given and  $u$  is a finite measurement series, appropriate boundary conditions (BC) must be defined. Since they are required in discrete numerical implementations, we present them as discrete formulas. Therefore, a discrete series  $u_k$  of length  $N$  is considered together with a filter  $g_l$  of length  $2N_f + 1$  and the convolution  $\hat{u}_k = \sum g_l u_{k+l}$ . The use of Gaussian filter coefficients  $g_l = \exp(-\frac{3|l|}{N_f})$  has shown to provide good results. The first two BC were already proposed in Sieber et al. (2016c) and two new BCs are added here. For each BC variant, the short description and the recommended applications for the convolution of the time series  $u_k$  with the filter  $g_l$  are given in the following subsections. The effect of

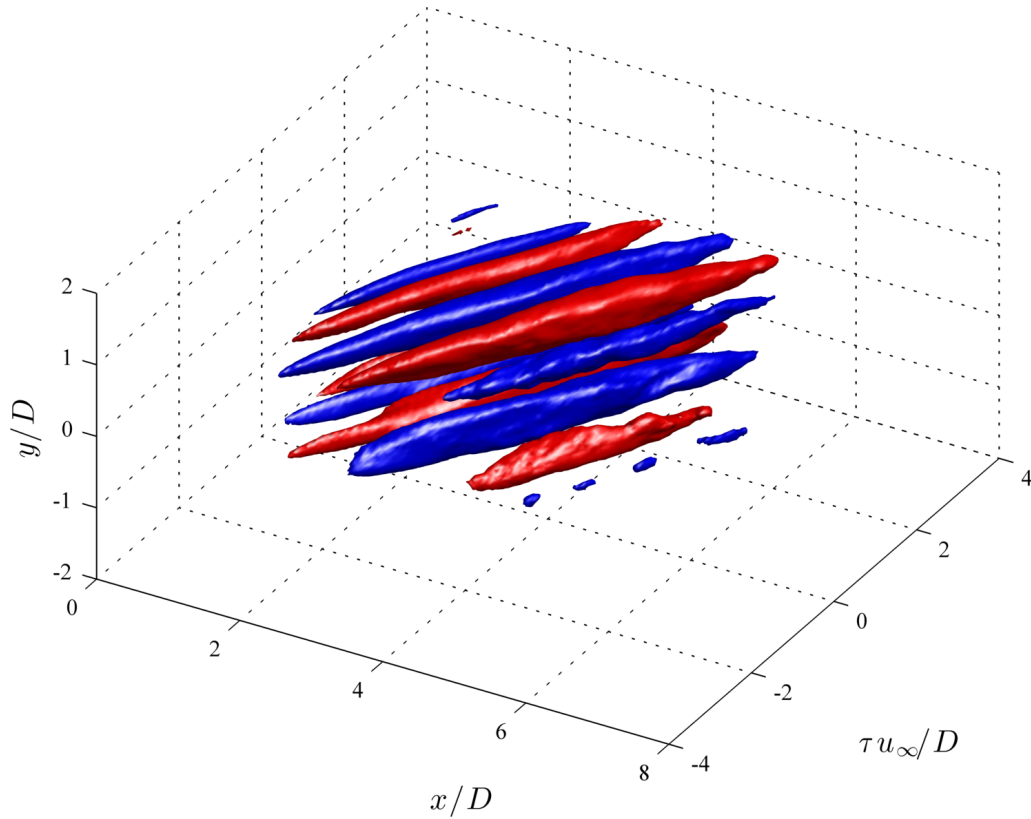


FIGURE A.3: Surface plot of the entire time-domain SPOD mode  $\widehat{\Phi}(x, \tau = 0)$  given in figure A.2 (g).

different BC on the SPOD will briefly be discussed in appendix A.3. Furthermore, the effect of the different BC on A.4 is shown.

### Periodic BC

With periodic BC a periodic continuation of the time series is assumed. For a numerical implementation, this is best described using the modulus function (mod)

$$\widehat{u}_k = \sum_{l=-N_f}^{N_f} g_l u_{\text{mod}(k+l, N)}. \quad (\text{A.1})$$

For periodic BC the time-domain SPOD converges to a Fourier decomposition for increasing filter size. However, the approach is only advisable for statistically stationary time series.

### Zero padded BC

For zero padded BC, the signal is padded with zeros for values outside of the measured sequence. This can be equivalently described by limiting the summation to the existing data

$$\widehat{u}_k = \sum_{l=\max(-k, -N_f)}^{\min(N-k, N_f)} g_l u_{k+l}, \quad (\text{A.2})$$

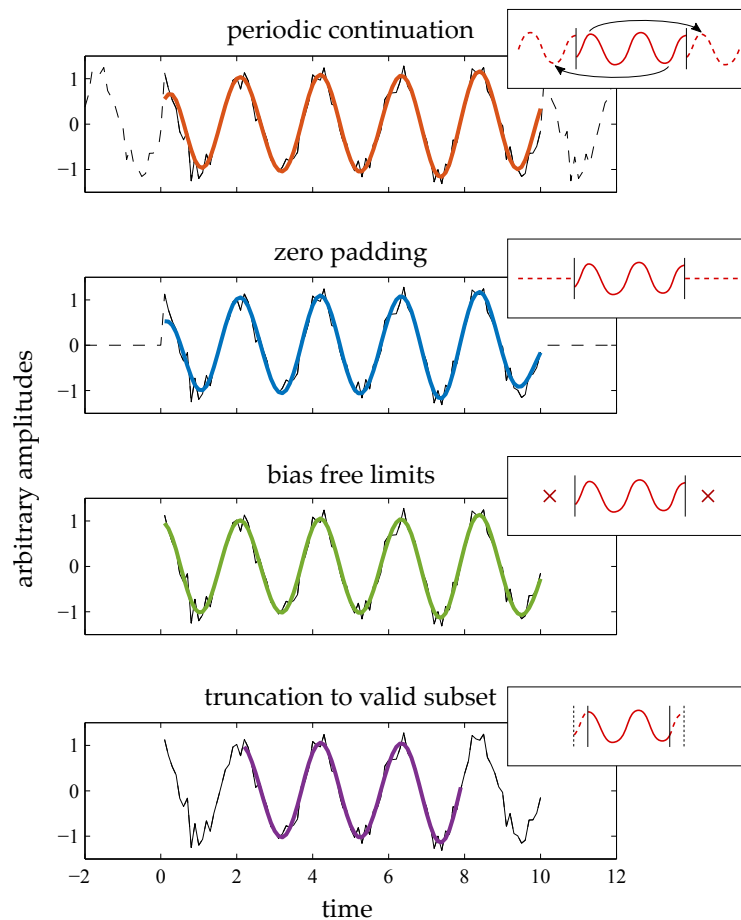


FIGURE A.4: Comparison of different boundary conditions for the separation of a periodic signal from noise. The time series show a generic noisy signal as dashed line and the filtered signal as thick solid lines. The pictogram indicate the signal treatment and are reconsidered in figure A.7.

where min and max describe the minimum and maximum function, respectively. This BC might be an option for transient measurements, where periodic conditions do not apply. The mean of the data should be removed to avoid step jumps at the boundaries, but data with drifts may still be prone to BC artefacts.

### Unbiased BC

The unbiased BC is intended to eliminate the degradation of the zero-padded BC by weighting it with the actually summed data. It was previously proposed by Protas et al. (2015) to avoid degradation of the autocorrelation. For this BC, the summation is conducted only over the existing data, analogously to the zero padded BC and divided by the sum of the corresponding filtered coefficients, reading

$$\hat{u}_k = \frac{\sum_{l=\max(-k, -N_f)}^{\min(N-k, N_f)} g_l u_{k+l}}{\sum_{l=\max(-k, -N_f)}^{\min(N-k, N_f)} g_l}. \quad (\text{A.3})$$

The approach may work for transient series with drift, but the influence of the first and last snapshot is stronger compared to the rest of the sequence. Therefore, the unbiased BC may lead to divergence for larger filter sizes.

### Truncated BC

For this BC, the filtered sequence is truncated to a valid subset for which the convolution can be applied without restrictions

$$\hat{u}_k = \sum_{l=-N_f}^{N_f} g_l u_{k+l}, \quad N_f < k < (N - N_f). \quad (\text{A.4})$$

This procedure does not restrict the SPOD to special kinds of time series, but it reduces the possible information obtained from the sequence. The length of the filtered time series reduces by twice the size of the filter. Therefore, this BC is limited to filter sizes shorter than the analyzed series, as the length of the valid sequence reduces with increasing  $N_f$ . For this kind of BCs, the time-domain SPOD is equivalent to delay embedding as described in section 2.4.

### A.3 Decomposition of generic noisy data

The possibility to judge the quality of the decomposition from real flow data is always strongly limited because the true decomposition is rarely known. Therefore, we investigate generic data with additive noise to show the effect of the filter size and BC on the time-domain SPOD.

This short evaluation is also meant to highlight some aspects of the close relation between the HAVOK approach (Brunton et al., 2017) and the time-domain SPOD. The HAVOK approach comprises the use of time-delay embedding in connection with a POD (SVD) based reduction of system complexity. The time coefficients of the leading POD modes are used to develop reduced-order models of the underlying dynamic system. One of the key findings was that this approach tends to favour linear systems and non-linear effects appear as intermittent forcing.

To mimic the signal of a coherent structure in a turbulent flow, we generate a time series of an amplified periodic signal and add normally distributed white noise to the series. The same approach was adopted by Dawson et al. (2016) to evaluate the accuracy of DMD under noisy conditions. Moreover, the dynamics are chosen to be linear, which favours the properties of the SPOD (Sieber et al., 2016c). The task of the decomposition in this scenario is to separate the coherent dynamics from the stochastic noise. This is quantified by how accurately the dynamics of the linear system might be recovered after the decomposition.

The investigated signal is an amplified periodic oscillation that is observed at different phase angles. This can either be represented by a spatial function that is temporally modulated (like in the modal decomposition)

$$u(x, t) = e^{\sigma t} \begin{bmatrix} \sin(\omega t) \\ \cos(\omega t) \end{bmatrix} \begin{bmatrix} \sin(kx) & \cos(kx) \end{bmatrix} + n(x, t) \quad (\text{A.5})$$

or alternatively as a travelling wave in space and time

$$u(x, t) = e^{\sigma t} \cos(kx - \omega t) + n(x, t). \quad (\text{A.6})$$

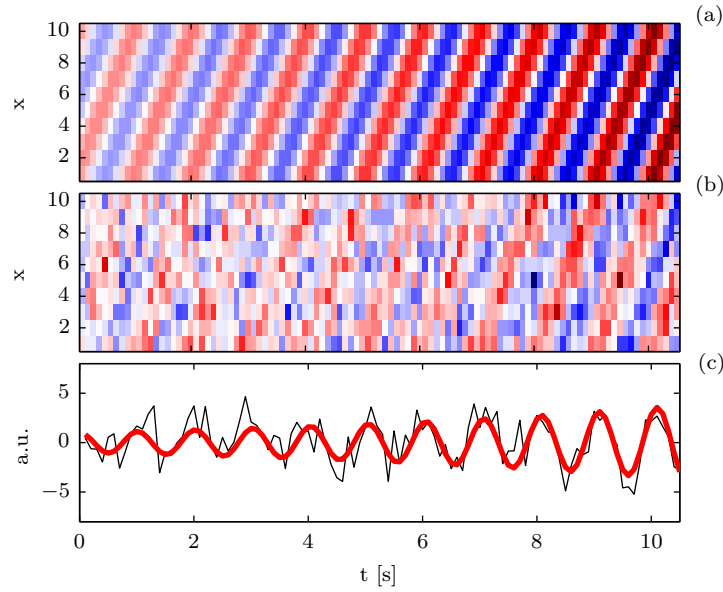


FIGURE A.5: Generic data sequence representing an amplified travelling wave. a) pure signal, b) signal with additive noise of SNR = 1 and c) time series at  $x = 1$  for pure (red) and noisy (black) signal.

The additional term  $n$  represents the noise which is modelled as normally distributed random numbers and scaled to match a specific signal-to-noise ratio (SNR), given as

$$\text{SNR} = \frac{\iint s^2(x, t) dx dt}{\iint n^2(x, t) dx dt}, \quad (\text{A.7})$$

where  $s = u - n$  indicates the periodic part of the signal. The dynamics can be represented by a linear system as

$$[u(t + \Delta t, x_1), \dots, u(t + \Delta t, x_N)]^T = \mathbf{A}[u(t, x_1), \dots, u(t, x_N)]^T, \quad (\text{A.8})$$

where the matrix  $\mathbf{A}$  contains all system dynamics Taira et al., 2017. The frequency  $\omega$  and temporal growth rate  $\sigma$  shall be recovered from the later decomposition of the noisy data. The actual test signal is presented in figure A.5 for a SNR = 1. The time-domain parameters of the test signal are chosen to be  $\omega = 6.22\text{s}^{-1}$  and  $\sigma = 0.126\text{s}^{-1}$  with a sampling rate of 10Hz and a length of 105 samples. The odd numbers of the generic signal are chosen to avoid matching phases at the beginning and the end of the signal as well as common multipliers of sampling rate and frequency.

The evaluation procedure of the test signal is as follows:

1. Compute snapshot correlation and filter with a Gaussian filter of size  $N_f$  (2.12).
2. Perform eigenvalue decomposition of the correlation matrix to obtain temporal coefficients  $a$ .
3. Create coefficient state matrices that are truncated to the  $r$  leading modes

$$\mathbf{Y}_0 = \begin{bmatrix} a_1(t_1) & \cdots & a_1(t_{N-1}) \\ \vdots & \ddots & \vdots \\ a_r(t_1) & \cdots & a_r(t_{N-1}) \end{bmatrix}; \quad \mathbf{Y}_1 = \begin{bmatrix} a_1(t_2) & \cdots & a_1(t_N) \\ \vdots & \ddots & \vdots \\ a_r(t_2) & \cdots & a_r(t_N) \end{bmatrix} \quad (\text{A.9})$$

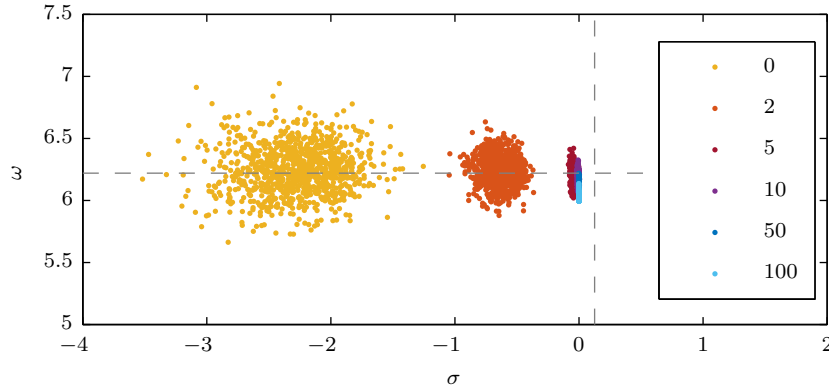


FIGURE A.6: Scatter plot of estimated system dynamics for 1000 repeated runs with SNR = 1, periodic boundary conditions and six different filter lengths  $N_f$ , as indicated by the legend. The dashed lines indicate the true value for frequency  $\omega$  and amplification rate  $\sigma$ .

4. Compute eigenvalues  $\mu_i$  of matrix  $\mathbf{A} = \mathbf{Y}_1 \mathbf{Y}_0^{-1}$  (the inverse might be a pseudoinverse or the matrix can be inferred from a regression like  $\mathbf{A} = \mathbf{Y}_1 / \mathbf{Y}_0'$  in Matlab)
5. The estimated frequency and amplification rate of the signal are given by

$$\hat{\sigma}_i + i\hat{\omega}_i = \frac{\log(\mu_i)}{t_2 - t_1}. \quad (\text{A.10})$$

The estimate of the dynamic parameters is essentially a dynamic mode decomposition (DMD) as described by Dawson Dawson et al., 2016. The main difference compared to a DMD is that the coefficients are taken from an SPOD instead of a POD.

The procedure is repeated 1000 times with different noise distributions, for six different filter sizes  $N_f$ , and the four different BCs proposed above. The decomposition is always truncated to the two leading SPOD modes according to the dynamic content of the generic signal. Therefore, the estimate of the dynamics results in a pair of complex conjugate eigenvalues  $\mu_i$ .

Figure A.6 shows the estimated dynamics for a fixed SNR and BC. The graph indicates that the error of the amplification rate is generally more pronounced than the frequency error. Moreover, the estimates become less scattered as the filter size is increased. Figure A.6 further indicates that two different errors occur: First, there is an average offset of the estimated values and second, there is variance due to random noise. To incorporate both error sources in a common measure, the RMS error of the estimates from  $N_k = 1000$  trials with different added noise is considered. The normalised RMS frequency error reads

$$E_\omega = \frac{1}{\omega} \sqrt{\frac{1}{N_k} \sum_{k=1}^{N_t} (\omega - |\Im\{\hat{\mu}_k\}|)^2} \quad (\text{A.11})$$

and the normalised RMS amplification error reads

$$E_\sigma = \frac{1}{\sigma} \sqrt{\frac{1}{N_k} \sum_{k=1}^{N_t} (\sigma - \Re\{\hat{\mu}_k\})^2}. \quad (\text{A.12})$$

Figure A.7 shows both error measures for all the tested parameters. In these graphs, the case for  $N_f = 0$  corresponds to a POD decomposition and therefore, the estimation of the dynamics is equivalent to a DMD of the time series. There seems to be a general lower bound of the SNR for which no reasonable estimation is possible. For the presented data this boundary is slightly above an SNR of 0.1. All presented errors decrease with increasing filter size for SNR close to this boundary. However, at larger SNR this trend changes depending on the utilized BC.

For the periodic BC (figure A.7 a) the frequency error rises for large  $N_f$ . This is due to the fixed frequency resolution that is introduced by the length of the signal and the sampling rate. A period that matches the signal length would give zero error for large  $N_f$ . The corresponding amplification error (figure A.7 b) converges to 1 for large  $N_f$ . This is because the periodic BC results in a signal with zero amplification.

The zero-padded BC (figure A.7 c-d) is not affected by the frequency quantisation and therefore does not show increasing errors at high SNR. However, there is a growth of errors with increasing  $N_f$  at large SNR that cannot be explained so far. The amplification error of a zero-padded signal, similar to the periodic BC, corresponds to a signal with zero amplification.

The frequency error for the bias-free BC (figure A.7 e) is similar to the zero padded BC, whereas the amplification error (figure A.7 f) provides smaller values at large SNR. This is possible because the bias-free BC intent to retain the transient development of the time series. Nevertheless, the performance does strongly depend on the first and last samples of the signal.

The truncation BC (figure A.7 g-h) shows the best overall performance. However, the error increases for  $N_f = 50$  and calculations are impossible for  $N_f = 100$ , as increasing the filter size reduces the possible signal length of the resulting SPOD coefficients. Therefore, truncation BC performs good and robust for intermediate  $N_f$ , but deviates stronger for large  $N_f$ .

The reconstruction of the dynamics from a time-domain SPOD with delay embedding BC is principally equivalent to the HAVOK approach presented by Brunton et al. (Brunton et al., 2017). The implementation with other BCs gives possible variants that might be favourable for specific types of signals. Principally, the time-domain SPOD provides coefficients that correspond to a local linearization of the dynamics Sieber et al., 2016c. The linearization horizon corresponds to the filter size  $N_f$  and therefore allows to adjust the dynamic properties of the decomposition. For the above task, the goal is the identification of linear dynamics, which favours large  $N_f$  given that the right BCs are utilized. If there are strong nonlinearities present in the data, a large filter size might disperse the dynamics among several modes (see appendix A.4). However, this might be intended to model nonlinear interactions with a large but linear and therefore more simple system. The smart idea by Brunton et al. (Brunton et al., 2017) was to reintroduce the nonlinear effects as external forcing of the system. Although this measure does not allow for the prediction of states beyond a nonlinear event, a deviation between the predicted and the real state provides an indicator for an imminent nonlinear event.

## A.4 Effect of filter variation on the SPOD

The influence of the selected observation horizon  $T$  on the decomposition is only shortly regarded in appendix A.3. The observation horizon is synonymous with the filter size  $N_f$  that is presented in that section. However, the generic linear dynamics, which are identified in that section, do perfectly match the restrictions of the SPOD to such dynamics.

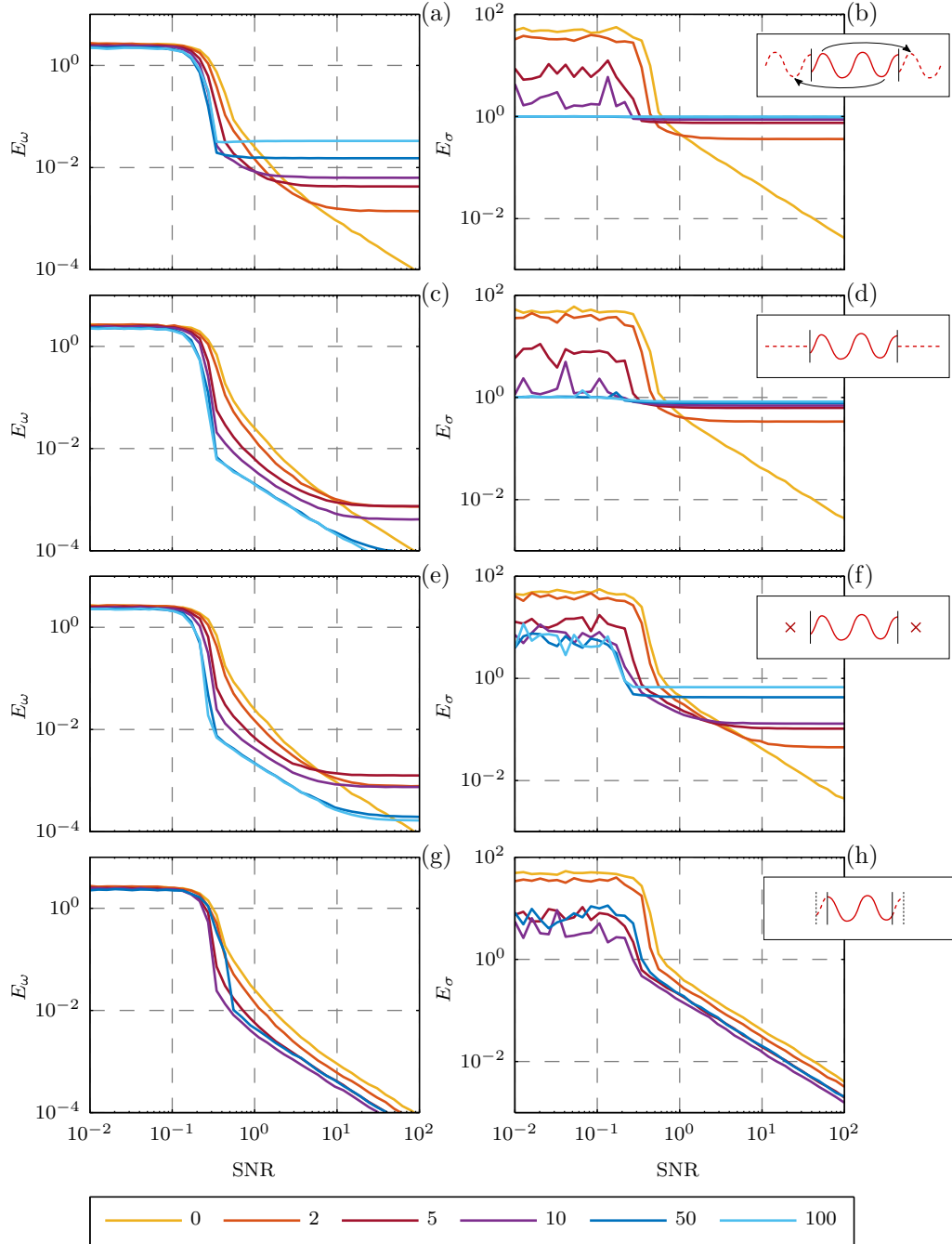


FIGURE A.7: Frequency error (A.11) (a,c,e,g) and amplification error (A.12) (b,d,f,h) over SNR for different filter sizes  $N_f$  as indicated by the legend. The error measures are presented for periodic BC (a,b), zero padded BC (c,d), bias free BC (e,f) and truncation BC (g,h). The pictograms also refer to the different BC as introduced in figure A.4.

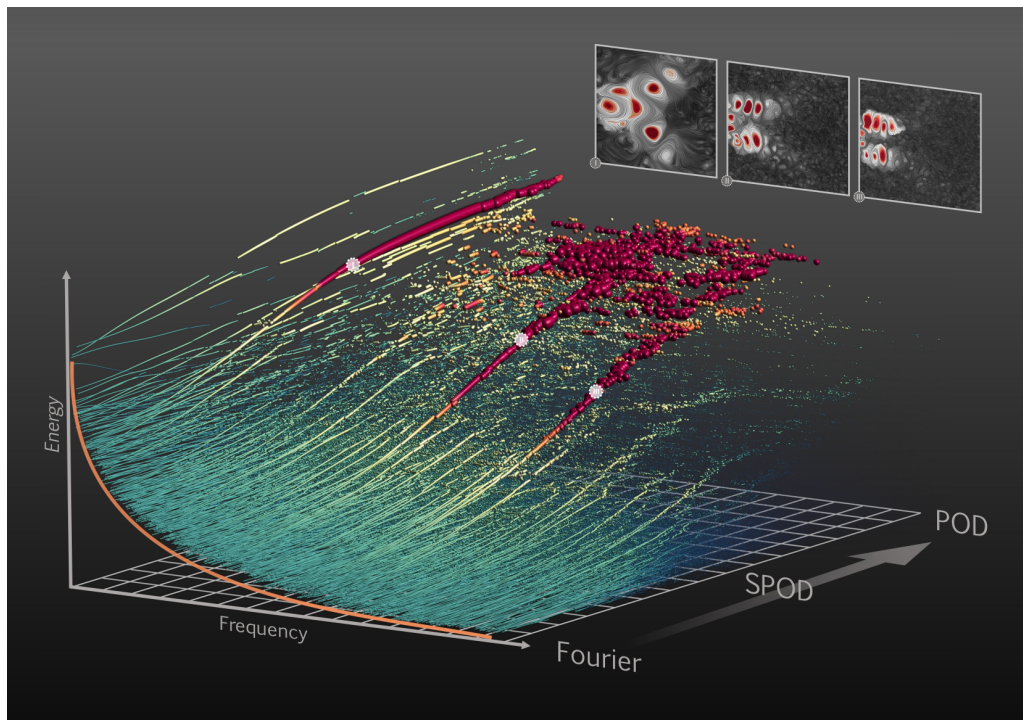


FIGURE A.8: Reproduction of a visualisation of the time-domain SPOD spectrum that was presented at the APS gallery of fluid motion Sieber et al., 2015. The image shows repeated spectra like the one in figure A.1 (b) for changes of the filter size. The flow that is decomposed is the turbulent swirling jet that was also presented in Sieber et al., 2016c. Note that the energy axis and filter size axis (Fourier to SPOD to POD) are scaled logarithmically.

Therefore, no degradation of the decomposition for large filter sizes is observed. In contrast, measurement data from real flows can also contain coherent structures that feature nonlinear phenomena. The usage of large filter sizes can pose to severe restrictions on the SPOD, which hinders the identification of such coherent structures.

The phenomenology was visualised in a poster that is reproduced in figure A.8. It shows several SPOD mode spectra like the one given in figure A.1 (b), with the filter size  $N_f$  gradually changing from the length of the time series (Fourier) to zero (POD). Therefore, every energy-frequency-plane represents one version of the decomposition of the data set. The visualisation highlights that three coherent modes are present, which are only isolated for intermediate filter settings. They are marked with numbers and the corresponding spatial structure is given at the side. For the intermediate filter sizes, a slight variation of the filter does not change the general decomposition, it only changes the relative energy distribution among modes.

It is visible that there is an optimal range for the filter setting to identify the coherent structures in the SPOD spectrum. It should be large enough to get distinct coherent structures and small enough to avoid the dispersion of coherent structures among several modes. The choice depends on the investigated flow, but a good rule of thumb is the selection of one or two periods of the coherent structure of interest.

## A.5 Mathematical derivations

This section gives some detailed mathematical derivations of the equalities presented in the paper.

### A.5.1 Conversion of the modes from time- to frequency-domain

We start with the time-domain integral equation (2.9)

$$\iint \widehat{R}(x, x', \tau, \tau') \widehat{\Phi}_k(x', \tau') d\tau' dx' = \lambda_k \widehat{\Phi}_k(x, \tau), \quad (\text{A.13})$$

which is multiplied with  $e^{-i\omega\tau}$  and integrated across  $\tau$  ( $\int d\tau$ ), giving

$$\iiint \widehat{R}(x, x', \tau, \tau') \widehat{\Phi}_k(x', \tau') e^{-i\omega\tau} d\tau d\tau' dx' = \lambda_k \int \widehat{\Phi}_k(x, \tau) e^{-i\omega\tau} d\tau. \quad (\text{A.14})$$

This equation is simplified assuming a statistically stationary time series, which results in a correlation function that only depends on time differences, giving  $\widehat{R}(x, x', \tau, \tau') = \widehat{R}(x, x', \tau' - \tau)$  (George, 1988). Rearranging (A.14) and inserting  $e^{i\omega(\tau' - \tau)} = 1$  leads to

$$\iiint \widehat{R}(x, x', \tau - \tau') e^{i\omega(\tau' - \tau)} \widehat{\Phi}_k(x', \tau') e^{-i\omega\tau'} d\tau d\tau' dx' = \lambda_k \int \widehat{\Phi}_k(x, \tau) e^{-i\omega\tau} d\tau, \quad (\text{A.15})$$

where the integrals can be separated using Fubini's theorem

$$\int \int \widehat{R}(x, x', \tau) e^{-i\omega\tau} d\tau \int \widehat{\Phi}_k(x', \tau) e^{-i\omega\tau} d\tau dx' = \lambda_k \int \widehat{\Phi}_k(x, \tau) e^{-i\omega\tau} d\tau \quad (\text{A.16})$$

and the insertion of equation (2.20) ultimately leads to

$$\int \widetilde{R}(x, x', \omega) \int \widehat{\Phi}_k(x', \tau') e^{-i\omega\tau'} d\tau' dx' = \lambda_k \int \widehat{\Phi}_k(x, \tau) e^{-i\omega\tau} d\tau. \quad (\text{A.17})$$

The comparison of (A.17) with (2.21) leads to the conclusion that the modes that result from the frequency-domain SPOD are identical with the Fourier transform of the time-domain modes that reads as

$$\widetilde{\Phi}_k(x, \omega) = \int \widehat{\Phi}_k(x, \tau) e^{-i\omega\tau} d\tau. \quad (\text{A.18})$$

### A.5.2 Conversion of the SPOD snapshot correlation

The derivation starts with equation (2.23), and a Gaussian weighting function  $w(\tau) = \exp(-(\tau/T)^2)$  is assumed:

$$\widetilde{S}(t, t', \omega) = \int \int u(x, t + \tau) w(\tau) e^{-i\omega\tau} d\tau \int u^*(x, t' + \tau') w(\tau') e^{i\omega\tau'} d\tau' dx \quad (\text{A.19})$$

$$= \int \int \int u(x, t + \tau) u^*(x, t' + \tau') dx w(\tau) w(\tau') e^{i\omega(\tau' - \tau)} d\tau d\tau' \quad (\text{A.20})$$

$$= \int \int C(t + \tau, t' + \tau') w(\tau) w(\tau') e^{i\omega(\tau' - \tau)} d\tau d\tau' \quad (\text{A.21})$$

The change of variables with  $\tau = \alpha + \beta$  and  $\tau' = \alpha - \beta$  gives

$$\widetilde{S}(t, t', \omega) = \iint C(t + \alpha + \beta, t' + \alpha - \beta) w(\alpha + \beta) w(\alpha - \beta) e^{-i\omega 2\beta} 2d\alpha d\beta, \quad (\text{A.22})$$

where the weighting can be simplified to  $w(\alpha + \beta)w(\alpha - \beta) = w^2(\alpha)w^2(\beta)$ , which allows to insert the time-domain correlation (2.11) giving

$$\tilde{S}(t, t', \omega) = \int \int C(t + \alpha + \beta, t' + \alpha - \beta) w^2(\alpha) d\alpha w^2(\beta) e^{-i\omega 2\beta} 2d\beta \quad (\text{A.23})$$

$$= \int \hat{S}(t + \beta, t' - \beta) w^2(\beta) e^{-i\omega 2\beta} 2d\beta. \quad (\text{A.24})$$

Replacing  $\tau$  again with  $\tau = 2\beta$  and using  $w^2(\beta) = w(2\beta)$  gives

$$\tilde{S}(t, t', \omega) = \int \hat{S}(t + \tau/2, t' - \tau/2) w(\tau) e^{-i\omega\tau} d\tau. \quad (\text{A.25})$$

The transformation from frequency- to time-domain of the snapshot correlation is given by integrating all frequencies (or by the inverse Fourier transform at  $\tau = 0$ )

$$\hat{S}(t, t') = \int \tilde{S}(t, t', \omega) d\omega \quad (\text{A.26})$$

$$= \int \int \tilde{S}(t + \tau/2, t' - \tau/2) w(\tau) e^{-i\omega\tau} d\tau d\omega \quad (\text{A.27})$$

$$= \int \tilde{S}(t + \tau/2, t' - \tau/2) w(\tau) \delta(\tau) d\tau \quad (\text{A.28})$$

$$= \hat{S}(t, t') \quad (\text{A.29})$$



# Bibliography

- AUBRY, N. (1991). "On the hidden beauty of the proper orthogonal decomposition". *Theoretical and Computational Fluid Dynamics* 2.5-6, pp. 339–352. DOI: [10.1007/BF00271473](https://doi.org/10.1007/BF00271473).
- BERKOOZ, G., P. HOLMES, & J. L. LUMLEY (1993). "The Proper Orthogonal Decomposition in the Analysis of Turbulent Flows". *Annual Review of Fluid Mechanics* 25, pp. 539–575. DOI: [10.1146/annurev.fl.25.010193.002543](https://doi.org/10.1146/annurev.fl.25.010193.002543).
- BONCIOLINI, G., E. BOUJO, & N. NOIRAY (2017). "Output-only parameter identification of a colored-noise-driven Van-der-Pol oscillator: Thermoacoustic instabilities as an example". *Physical review. E* 95.6-1, p. 062217. DOI: [10.1103/PhysRevE.95.062217](https://doi.org/10.1103/PhysRevE.95.062217).
- BRUNTON, S. L., B. W. BRUNTON, J. L. PROCTOR, E. KAISER, & J. N. KUTZ (2017). "Chaos as an intermittently forced linear system". *Nature Communications* 8.1, A3. DOI: [10.1038/s41467-017-00030-8](https://doi.org/10.1038/s41467-017-00030-8).
- BRUNTON, S. L. & B. R. NOACK (2015). "Closed-Loop Turbulence Control: Progress and Challenges". *Applied Mechanics Reviews* 67.5, p. 050801. DOI: [10.1115/1.4031175](https://doi.org/10.1115/1.4031175).
- CHEN, J.-M. & P. A. HARR (1993). "Interpretation of Extended Empirical Orthogonal Function (EEOF) Analysis". *Monthly Weather Review* 121.9, pp. 2631–2636. DOI: [10.1175/1520-0493\(1993\)121<2631:IOEEOF>2.0.CO;2](https://doi.org/10.1175/1520-0493(1993)121<2631:IOEEOF>2.0.CO;2).
- CITRINITI, J. H. & W. K. GEORGE (2000). "Reconstruction of the global velocity field in the axisymmetric mixing layer utilizing the proper orthogonal decomposition". *Journal of Fluid Mechanics* 418, pp. 137–166. DOI: [10.1017/S0022112000001087](https://doi.org/10.1017/S0022112000001087).
- DAWSON, S. T. M., M. S. HEMATI, M. O. WILLIAMS, & C. W. ROWLEY (2016). "Characterizing and correcting for the effect of sensor noise in the dynamic mode decomposition". *Experiments in Fluids* 57.3, p. 596. DOI: [10.1007/s00348-016-2127-7](https://doi.org/10.1007/s00348-016-2127-7).
- GEORGE, W. K. (1988). "Insight into the dynamics of coherent structures from a proper orthogonal decomposition". In: *Near Wall Turbulence*. Ed. by S. KLINE & N. AFGHAN. New York: Hemisphere.
- (2017). "A 50-Year Retrospective and the Future". In: *Whither Turbulence and Big Data in the 21st Century?* Ed. by A. POLLARD, L. CASTILLO, L. DANAILA, M. GLAUSER, & W. K. GEORGE. Springer, pp. 13–43.
- GLAUSER, M. N., S. J. LEIB, & W. K. GEORGE (1987). "Coherent Structures in the Axisymmetric Turbulent Jet Mixing Layer". In: *Turbulent Shear Flows 5: Selected Papers from the Fifth International Symposium on Turbulent Shear Flows, Cornell University, Ithaca, New York, USA, August 7–9, 1985*. Ed. by F. DURST, B. E. LAUNDER, J. L. LUMLEY,

- F. W. SCHMIDT, & J. H. WHITEHEAD. Berlin and Heidelberg: Springer Berlin Heidelberg, pp. 134–145. DOI: [10.1007/978-3-642-71435-1\\_textunderscore13](https://doi.org/10.1007/978-3-642-71435-1_textunderscore13).
- GORDEYEV, S. V. & F. O. THOMAS (2013). “A temporal proper decomposition (TPOD) for closed-loop flow control”. *Experiments in Fluids* 54.3, p. 115. DOI: [10.1007/s00348-013-1477-7](https://doi.org/10.1007/s00348-013-1477-7).
- GUDMUNDSSON, K. & T. COLONIUS (2011). “Instability wave models for the near-field fluctuations of turbulent jets”. *Journal of Fluid Mechanics* 689, pp. 97–128. DOI: [10.1017/jfm.2011.401](https://doi.org/10.1017/jfm.2011.401).
- GÜNTHER, T., M. GROSS, & H. THEISEL (2017). “Generic objective vortices for flow visualization”. *ACM Transactions on Graphics* 36.4, pp. 1–11. DOI: [10.1145/3072959.3073684](https://doi.org/10.1145/3072959.3073684).
- HALLER, G. (2015). “Lagrangian Coherent Structures”. *Annual Review of Fluid Mechanics* 47.1, pp. 137–162. DOI: [10.1146/annurev-fluid-010313-141322](https://doi.org/10.1146/annurev-fluid-010313-141322).
- HOLMES, P., J. L. LUMLEY, G. BERKOOZ, & C. W. ROWLEY (2012). *Turbulence, Coherent Structures, Dynamical Systems and Symmetry*. 2nd ed. Cambridge monographs on mechanics. Cambridge, UK and New York: Cambridge University Press.
- KAMB, M., E. KAISER, S. L. BRUNTON, & J. N. KUTZ (2020). “Time-Delay Observables for Koopman: Theory and Applications”. *SIAM Journal on Applied Dynamical Systems* 19.2, pp. 886–917. DOI: [10.1137/18M1216572](https://doi.org/10.1137/18M1216572).
- KEMP, M. (2019). “Leonardo da Vinci’s laboratory: studies in flow”. *Nature* 571.7765, pp. 322–323. DOI: [10.1038/d41586-019-02144-z](https://doi.org/10.1038/d41586-019-02144-z).
- LANDAU, L. D. & E. M. LIFSHITZ (1987). *Fluid Mechanics*. 2nd ed. rev. Vol. v. 6. Course of theoretical physics. Oxford: Pergamon.
- LANG, H. M., K. OBERLEITHNER, C. O. PASCHEREIT, & M. SIEBER (2017). “Measurement of the fluctuating temperature field in a heated swirling jet with BOS tomography”. *Experiments in Fluids* 58.7, p. 88. DOI: [10.1007/s00348-017-2367-1](https://doi.org/10.1007/s00348-017-2367-1).
- LASAGNA, D., M. ORAZI, & G. IUSO (2013). “Multi-time delay, multi-point linear stochastic estimation of a cavity shear layer velocity from wall-pressure measurements”. *Physics of Fluids* 25.1, p. 017101. DOI: [10.1063/1.4774337](https://doi.org/10.1063/1.4774337).
- LEE, M., Y. ZHU, L. K. B. LI, & V. GUPTA (2019). “System identification of a low-density jet via its noise-induced dynamics”. *Journal of Fluid Mechanics* 862, pp. 200–215. DOI: [10.1017/jfm.2018.961](https://doi.org/10.1017/jfm.2018.961).
- LIANG, H. & T. MAXWORTHY (2005). “An experimental investigation of swirling jets”. *Journal of Fluid Mechanics* 525, pp. 115–159. DOI: [10.1017/S0022112004002629](https://doi.org/10.1017/S0022112004002629).
- LÜCKOFF, F., M. SIEBER, C. O. PASCHEREIT, & K. OBERLEITHNER (2018). “Characterization of Different Actuator Designs for the Control of the Precessing Vortex Core in a Swirl-Stabilized Combustor”. *Journal of Engineering for Gas Turbines and Power* 140.4, p. 041503. DOI: [10.1115/1.4038039](https://doi.org/10.1115/1.4038039).

- (2019). “Phase-Opposition Control of the Precessing Vortex Core in Turbulent Swirl Flames for Investigation of Mixing and Flame Stability”. *Journal of Engineering for Gas Turbines and Power* 141.11. DOI: [10.1115/1.4044469](https://doi.org/10.1115/1.4044469).
- LUMLEY, J. L. (1967). “The structure of inhomogeneous turbulent flows”. In: *Atmospheric Turbulence and Radio Wave Propagation*. Moscow: Publishing House Nauka, pp. 166–176.
- (1970). *Stochastic Tools in Turbulence*. New York and London: Academic Press.
- LÜCKOFF, F., M. SIEBER, C. O. PASCHEREIT, & K. OBERLEITHNER (2020). “Impact of the Precessing Vortex Core on NO<sub>x</sub> Emissions in Premixed Swirl-Stabilized Flames—An Experimental Study”. *Journal of Engineering for Gas Turbines and Power* 142.11. 111010. DOI: [10.1115/1.4048603](https://doi.org/10.1115/1.4048603).
- MÜLLER, J. S., M. SIEBER, I. LITVINOV, S. SHTORK, S. ALEKSEENKO, & K. OBERLEITHNER (2020). “Prediction of vortex precession in the draft tube of a model hydro turbine using mean field stability theory and stochastic modelling”. In: *30th Symposium on Hydraulic Machinery and Systems 2020*. Lausanne, Switzerland.
- NOACK, B. R., K. AFANASIEV, M. MORZYŃSKI, G. TADMOR, & F. THIELE (2003). “A hierarchy of low-dimensional models for the transient and post-transient cylinder wake”. *Journal of Fluid Mechanics* 497, pp. 335–363. DOI: [10.1017/S0022112003006694](https://doi.org/10.1017/S0022112003006694).
- NOIRAY, N. (2017). “Linear Growth Rate Estimation From Dynamics and Statistics of Acoustic Signal Envelope in Turbulent Combustors”. *Journal of Engineering for Gas Turbines and Power* 139.4, p. 041503. DOI: [10.1115/1.4034601](https://doi.org/10.1115/1.4034601).
- NOIRAY, N. & B. SCHUERMANS (2013). “Deterministic quantities characterizing noise driven Hopf bifurcations in gas turbine combustors”. *International Journal of Non-Linear Mechanics* 50, pp. 152–163. DOI: [10.1016/j.ijnonlinmec.2012.11.008](https://doi.org/10.1016/j.ijnonlinmec.2012.11.008).
- OBERLEITHNER, K., C. O. PASCHEREIT, & I. WYGNANSKI (2014). “On the impact of swirl on the growth of coherent structures”. *Journal of Fluid Mechanics* 741, pp. 156–199. DOI: [10.1017/jfm.2013.669](https://doi.org/10.1017/jfm.2013.669).
- OERTEL, H. & J. DELFS (1996). *Strömungsmechanische Instabilitäten*. Berlin, Heidelberg: Springer Berlin Heidelberg. DOI: [10.1007/978-3-642-60931-2](https://doi.org/10.1007/978-3-642-60931-2).
- PROTAS, B., B. R. NOACK, & J. ÖSTH (2015). “Optimal nonlinear eddy viscosity in Galerkin models of turbulent flows”. *Journal of Fluid Mechanics* 766, pp. 337–367. DOI: [10.1017/jfm.2015.14](https://doi.org/10.1017/jfm.2015.14).
- REISS, J., P. SCHULZE, J. SESTERHENN, & V. MEHRMANN (2018). “The Shifted Proper Orthogonal Decomposition: A Mode Decomposition for Multiple Transport Phenomena”. *SIAM Journal on Scientific Computing* 40.3, A1322–A1344. DOI: [10.1137/17M1140571](https://doi.org/10.1137/17M1140571).
- RIBEIRO, J. H. M. & W. R. WOLF (2017). “Identification of coherent structures in the flow past a NACA0012 airfoil via proper orthogonal decomposition”. *Physics of Fluids* 29.8, p. 085104. DOI: [10.1063/1.4997202](https://doi.org/10.1063/1.4997202).

- ROWLEY, C. W. & S. T. M. DAWSON (2017). "Model Reduction for Flow Analysis and Control". *Annual Review of Fluid Mechanics* 49.1, pp. 387–417. DOI: [10.1146/annurev-fluid-010816-060042](https://doi.org/10.1146/annurev-fluid-010816-060042).
- RUKES, L., M. SIEBER, C. NAYERI, & C. O. PASCHEREIT (2014). "The Impact of an Inhomogeneous Temperature Field on the Precessing Vortex Core in Swirling Jets Undergoing Vortex Breakdown". In: *52nd Aerospace Sciences Meeting, 13-17 January 2014, National Harbor, Maryland*. [Reston]: [American Institute of Aeronautics and Astronautics - AIAA]. DOI: [10.2514/6.2014-0957](https://doi.org/10.2514/6.2014-0957).
- RUKES, L., M. SIEBER, K. OBERLEITHNER, C. NAYERI, & C. O. PASCHEREIT (2015). "The influence of the inner shear layer on the suppression of the global mode in heated swirling jets". In: *53rd AIAA Aerospace Sciences Meeting 2015*. Red Hook, NY: Curran. DOI: [10.2514/6.2015-0302](https://doi.org/10.2514/6.2015-0302).
- RUKES, L., M. SIEBER, C. O. PASCHEREIT, & K. OBERLEITHNER (2016a). "Methods for the extraction and analysis of the global mode in swirling jets undergoing vortex breakdown". *Journal of Engineering for Gas Turbines and Power* 139.2, p. 022604. DOI: [10.1115/1.4034315](https://doi.org/10.1115/1.4034315).
- (2016b). "The impact of heating the breakdown bubble on the global mode of a swirling jet: Experiments and linear stability analysis". *Physics of Fluids* 28.10. DOI: [10.1063/1.4963274](https://doi.org/10.1063/1.4963274).
- (2017). "Transient evolution of the global mode in turbulent swirling jets: Experiments and modal stability analysis". *European Journal of Mechanics B-Fluids* 65, pp. 98–106. DOI: [10.1016/j.euromechflu.2017.02.010](https://doi.org/10.1016/j.euromechflu.2017.02.010).
- SCHMIDT, O. T., A. TOWNE, G. RIGAS, T. COLONIUS, & G. A. BRÈS (2018). "Spectral analysis of jet turbulence". *Journal of Fluid Mechanics* 855.arXiv:1711.06296, pp. 953–982. DOI: [10.1017/jfm.2018.675](https://doi.org/10.1017/jfm.2018.675).
- SIEBER, M., A. KUHN, H.-C. HEGE, C. O. PASCHEREIT, & K. OBERLEITHNER (2015). *A Graphical Representation of the Spectral Proper Orthogonal Decomposition*. 68th Annual Meeting of the APS Division of Fluid Dynamics (November 22, 2015 — November 24, 2015). DOI: [10.1103/APS.DFD.2015.GFM.P0007](https://doi.org/10.1103/APS.DFD.2015.GFM.P0007).
- SIEBER, M., F. OSTERMANN, R. WOSZIDLO, K. OBERLEITHNER, & C. O. PASCHEREIT (2016a). "Lagrangian coherent structures in the flow field of a fluidic oscillator". *Phys. Rev. Fluids* 1.5, p. 050509. DOI: [10.1103/PhysRevFluids.1.050509](https://doi.org/10.1103/PhysRevFluids.1.050509).
- SIEBER, M., C. O. PASCHEREIT, & K. OBERLEITHNER (2017). "On the nature of spectral proper orthogonal decomposition and related modal decompositions". *arXiv preprint arXiv:1712.08054*.
- (2021a). "Stochastic modelling of a noise-driven global instability in a turbulent swirling jet". *Journal of Fluid Mechanics* 916, A7. DOI: [10.1017/jfm.2021.133](https://doi.org/10.1017/jfm.2021.133).
- SIEBER, M., C. O. PASCHEREIT, & K. OBERLEITHNER (2016b). "Advanced Identification of Coherent Structures in Swirl-Stabilized Combustors". *Journal of Engineering for Gas Turbines and Power* 139.2, p. 021503. DOI: [10.1115/1.4034261](https://doi.org/10.1115/1.4034261).

- (2016c). “Identification of unstable coherent modes in reacting swirling flows and their control”. In: *54th AIAA Aerospace Sciences Meeting*. AIAA SciTech. American Institute of Aeronautics and Astronautics. DOI: [10.2514/6.2016-1840](https://doi.org/10.2514/6.2016-1840).
- (2016d). “Spectral proper orthogonal decomposition”. *Journal of Fluid Mechanics* 792, pp. 798–828. DOI: [10.1017/jfm.2016.103](https://doi.org/10.1017/jfm.2016.103).
- SIEBER, M., C. O. PASCHEREIT, & K. OBERLEITHNER (2021b). “Impact of density stratification on the global mode in a swirling jet: Stochastic modelling and Lagrangian coherent structures”. *International Journal of Heat and Fluid Flow* 90, p. 108820. DOI: <https://doi.org/10.1016/j.ijheatfluidflow.2021.108820>.
- SIROVICH, L. (1987). “Turbulence and the dynamics of coherent structures: Part I: Coherent Structures”. *Quarterly of Applied Mathematics* 45.3, pp. 561–571.
- SONNENBERGER, R., K. GRAICHEN, & P. ERK (2000). “Fourier averaging: a phase-averaging method for periodic flow”. *Experiments in Fluids* 28.3, pp. 217–224. DOI: [10.1007/s003480050381](https://doi.org/10.1007/s003480050381).
- STÖHR, M., K. OBERLEITHNER, M. SIEBER, Z. YIN, & W. MEIER (2017). “Experimental Study Of Transient Mechanisms Of Bi-Stable Flame Shape Transitions In A Swirl Combustor”. *Journal of Engineering for Gas Turbines and Power*, V04BT04A063. DOI: [10.1115/1.4037724](https://doi.org/10.1115/1.4037724).
- TAIRA, K., S. L. BRUNTON, S. T. M. DAWSON, C. W. ROWLEY, T. COLONIUS, B. J. MCKEON, O. T. SCHMIDT, S. GORDEYEV, V. THEOFILIS, & L. S. UKEILEY (2017). “Modal Analysis of Fluid Flows: An Overview”. *AIAA J* 55.12, pp. 4013–4041. DOI: [10.2514/1.J056060](https://doi.org/10.2514/1.J056060).
- TAKENS, F. (1981). “Detecting strange attractors in turbulence”. In: *Dynamical Systems and Turbulence, Warwick 1980: Proceedings of a Symposium Held at the University of Warwick 1979/80*. Ed. by D. RAND & L.-S. YOUNG. Berlin, Heidelberg: Springer Berlin Heidelberg, pp. 366–381. DOI: [10.1007/BFb0091924](https://doi.org/10.1007/BFb0091924).
- TOWNE, A., O. T. SCHMIDT, & T. COLONIUS (2018). “Spectral proper orthogonal decomposition and its relationship to dynamic mode decomposition and resolvent analysis”. *Journal of Fluid Mechanics* 847, pp. 821–867. DOI: [10.1017/jfm.2018.283](https://doi.org/10.1017/jfm.2018.283).
- VANIERSCHOT, M., J. S. MÜLLER, M. SIEBER, M. PERCIN, B. W. VAN OUDHEUSDEN, & K. OBERLEITHNER (2020). “Single- and double-helix vortex breakdown as two dominant global modes in turbulent swirling jet flow”. *Journal of Fluid Mechanics* 883. DOI: [10.1017/jfm.2019.872](https://doi.org/10.1017/jfm.2019.872).
- WELCH, P. (1967). “The use of fast Fourier transform for the estimation of power spectra: A method based on time averaging over short, modified periodograms”. *IEEE Transactions on Audio and Electroacoustics* 15.2, pp. 70–73. DOI: [10.1109/TAU.1967.1161901](https://doi.org/10.1109/TAU.1967.1161901).
- YE, S., Z. ZHANG, X. SONG, Y. WANG, Y. CHEN, & C. HUANG (2020). “A flow feature detection method for modeling pressure distribution around a cylinder in non-uniform flows by using a convolutional neural network”. *Scientific reports* 10.1, p. 4459. DOI: [10.1038/s41598-020-61450-z](https://doi.org/10.1038/s41598-020-61450-z).

ZHU, Y., V. GUPTA, & L. K. B. LI (2019). "Coherence resonance in low-density jets". *Journal of Fluid Mechanics* 881, p. 55. DOI: [10.1017/jfm.2019.782](https://doi.org/10.1017/jfm.2019.782).

## Associated Publications

The list below gives the publications that are associated with the thesis in chronological order.

1. L. Rukes, M. Sieber, C. Nayeri, & C. O. Paschereit (2014). "The Impact of an Inhomogeneous Temperature Field on the Precessing Vortex Core in Swirling Jets Undergoing Vortex Breakdown". In: *52nd Aerospace Sciences Meeting, 13-17 January 2014, National Harbor, Maryland*. [Reston]: [American Institute of Aeronautics and Astronautics - AIAA]. DOI: [10.2514/6.2014-0957](https://doi.org/10.2514/6.2014-0957)
2. L. Rukes, M. Sieber, K. Oberleithner, C. Nayeri, & C. O. Paschereit (2015). "The influence of the inner shear layer on the suppression of the global mode in heated swirling jets". In: *53rd AIAA Aerospace Sciences Meeting 2015*. Red Hook, NY: Curran. DOI: [10.2514/6.2015-0302](https://doi.org/10.2514/6.2015-0302)
3. M. Sieber, A. Kuhn, H.-C. Hege, C. O. Paschereit, & K. Oberleithner (2015). *A Graphical Representation of the Spectral Proper Orthogonal Decomposition*. 68th Annual Meeting of the APS Division of Fluid Dynamics (November 22, 2015 — November 24, 2015). DOI: [10.1103/APS.DFD.2015.GFM.P0007](https://doi.org/10.1103/APS.DFD.2015.GFM.P0007)
4. L. Rukes, M. Sieber, K. Oberleithner, C. Nayeri, & C. O. Paschereit (2015). "The influence of the inner shear layer on the suppression of the global mode in heated swirling jets". In: *53rd AIAA Aerospace Sciences Meeting 2015*. Red Hook, NY: Curran. DOI: [10.2514/6.2015-0302](https://doi.org/10.2514/6.2015-0302)
5. L. Rukes, M. Sieber, C. O. Paschereit, & K. Oberleithner (2016a). "Methods for the extraction and analysis of the global mode in swirling jets undergoing vortex breakdown". *Journal of Engineering for Gas Turbines and Power* 139.2, p. 022604. DOI: [10.1115/1.4034315](https://doi.org/10.1115/1.4034315)
6. L. Rukes, M. Sieber, C. O. Paschereit, & K. Oberleithner (2016b). "The impact of heating the breakdown bubble on the global mode of a swirling jet: Experiments and linear stability analysis". *Physics of Fluids* 28.10. DOI: [10.1063/1.4963274](https://doi.org/10.1063/1.4963274)
7. M. Sieber, F. Ostermann, R. Wosidlo, K. Oberleithner, & C. O. Paschereit (2016a). "Lagrangian coherent structures in the flow field of a fluidic oscillator". *Phys. Rev. Fluids* 1.5, p. 050509. DOI: [10.1103/PhysRevFluids.1.050509](https://doi.org/10.1103/PhysRevFluids.1.050509)
8. M. Sieber, C. O. Paschereit, & K. Oberleithner (2016b). "Advanced Identification of Coherent Structures in Swirl-Stabilized Combustors". *Journal of Engineering for Gas Turbines and Power* 139.2, p. 021503. DOI: [10.1115/1.4034261](https://doi.org/10.1115/1.4034261)
9. M. Sieber, C. O. Paschereit, & K. Oberleithner (2016c). "Identification of unstable coherent modes in reacting swirling flows and their control". In: *54th AIAA Aerospace Sciences Meeting*. AIAA SciTech. American Institute of Aeronautics and Astronautics. DOI: [10.2514/6.2016-1840](https://doi.org/10.2514/6.2016-1840)
10. M. Sieber, C. O. Paschereit, & K. Oberleithner (2016d). "Spectral proper orthogonal decomposition". *Journal of Fluid Mechanics* 792, pp. 798–828. DOI: [10.1017/jfm.2016.103](https://doi.org/10.1017/jfm.2016.103)
11. L. Rukes, M. Sieber, C. O. Paschereit, & K. Oberleithner (2017). "Transient evolution of the global mode in turbulent swirling jets: Experiments and modal stability

- analysis". *European Journal of Mechanics B-Fluids* 65, pp. 98–106. DOI: [10.1016/j.euromechflu.2017.02.010](https://doi.org/10.1016/j.euromechflu.2017.02.010)
12. H. M. Lang, K. Oberleithner, C. O. Paschereit, & M. Sieber (2017). "Measurement of the fluctuating temperature field in a heated swirling jet with BOS tomography". *Experiments in Fluids* 58.7, p. 88. DOI: [10.1007/s00348-017-2367-1](https://doi.org/10.1007/s00348-017-2367-1)
  13. M. Stöhr, K. Oberleithner, M. Sieber, Z. Yin, & W. Meier (2017). "Experimental Study Of Transient Mechanisms Of Bi-Stable Flame Shape Transitions In A Swirl Combustor". *Journal of Engineering for Gas Turbines and Power*, V04BT04A063. DOI: [10.1115/1.4037724](https://doi.org/10.1115/1.4037724)
  14. F. Lückoff, M. Sieber, C. O. Paschereit, & K. Oberleithner (2018). "Characterization of Different Actuator Designs for the Control of the Precessing Vortex Core in a Swirl-Stabilized Combustor". *Journal of Engineering for Gas Turbines and Power* 140.4, p. 041503. DOI: [10.1115/1.4038039](https://doi.org/10.1115/1.4038039)
  15. F. Lückoff, M. Sieber, C. O. Paschereit, & K. Oberleithner (2019). "Phase-Opposition Control of the Precessing Vortex Core in Turbulent Swirl Flames for Investigation of Mixing and Flame Stability". *Journal of Engineering for Gas Turbines and Power* 141.11. DOI: [10.1115/1.4044469](https://doi.org/10.1115/1.4044469)
  16. M. Vanierschot, J. S. Müller, M. Sieber, M. Percin, B. W. van Oudheusden, & K. Oberleithner (2020). "Single- and double-helix vortex breakdown as two dominant global modes in turbulent swirling jet flow". *Journal of Fluid Mechanics* 883. DOI: [10.1017/jfm.2019.872](https://doi.org/10.1017/jfm.2019.872)
  17. F. Lückoff, M. Sieber, C. O. Paschereit, & K. Oberleithner (2020). "Impact of the Precessing Vortex Core on NO<sub>x</sub> Emissions in Premixed Swirl-Stabilized Flames—An Experimental Study". *Journal of Engineering for Gas Turbines and Power* 142.11. 111010. DOI: [10.1115/1.4048603](https://doi.org/10.1115/1.4048603)
  18. J. S. Müller, M. Sieber, I. Litvinov, S. Shtork, S. Alekseenko, & K. Oberleithner (2020). "Prediction of vortex precession in the draft tube of a model hydro turbine using mean field stability theory and stochastic modelling". In: *30th Symposium on Hydraulic Machinery and Systems 2020*. Lausanne, Switzerland
  19. M. Sieber, C. O. Paschereit, & K. Oberleithner (2021b). "Impact of density stratification on the global mode in a swirling jet: Stochastic modelling and Lagrangian coherent structures". *International Journal of Heat and Fluid Flow* 90, p. 108820. DOI: <https://doi.org/10.1016/j.ijheatfluidflow.2021.108820>
  20. M. Sieber, C. O. Paschereit, & K. Oberleithner (2021a). "Stochastic modelling of a noise-driven global instability in a turbulent swirling jet". *Journal of Fluid Mechanics* 916, A7. DOI: [10.1017/jfm.2021.133](https://doi.org/10.1017/jfm.2021.133)